

# Applications of Advanced Nanomaterials to Microelectronic and Photonic Devices

Guest Editors: Shoou-Jinn Chang, Teen-Hang Meen, Stephen D. Prior, Liang-Wen Ji, and Sheng-Joue Young





---

# **Applications of Advanced Nanomaterials to Microelectronic and Photonic Devices**

# **Applications of Advanced Nanomaterials to Microelectronic and Photonic Devices**

Guest Editors: Shoou-Jinn Chang, Teen-Hang Meen,  
Stephen D. Prior, Liang-Wen Ji, and Sheng-Joue Young



---

Copyright © 2015 Hindawi Publishing Corporation. All rights reserved.

This is a special issue published in "Journal of Nanomaterials." All articles are open access articles distributed under the Creative Commons Attribution License, which permits unrestricted use, distribution, and reproduction in any medium, provided the original work is properly cited.

## Editorial Board

- Domenico Acierno, Italy  
Katerina Aifantis, USA  
Sheikh Akbar, USA  
Nageh K. Allam, USA  
Margarida Amaral, Portugal  
Raul Arenal, Spain  
Ilaria Armentano, Italy  
Lavinia Balan, France  
Thierry Baron, France  
Andrew R. Barron, USA  
Reza Bayati, USA  
Hongbin Bei, USA  
Stefano Bellucci, Italy  
Enrico Bergamaschi, Italy  
Debes Bhattacharyya, New Zealand  
Giovanni Bongiovanni, Italy  
Theodorian Borca-Tasciuc, USA  
Mohamed Bououdina, Bahrain  
Torsten Brezesinski, Germany  
C. Jeffrey Brinker, USA  
Christian Brosseau, France  
Victor M. Castaño, Mexico  
Albano Cavaleiro, Portugal  
Bhanu P. S. Chauhan, USA  
Shafiq Chowdhury, USA  
Jin-Ho Choy, Korea  
Kwang-Leong Choy, UK  
Yu-Lun Chueh, Taiwan  
Elisabetta Comini, Italy  
Giuseppe Compagnini, Italy  
David Cornu, France  
Miguel A. Correa-Duarte, Spain  
P. Davide Cozzoli, Italy  
Shadi A. Dayeh, USA  
Luca Deseri, USA  
Yong Ding, USA  
Zehra Durmus, Turkey  
Joydeep Dutta, Oman  
Ali Eftekhari, USA  
Jeffrey Elam, USA  
Samy El-Shall, USA  
Ovidiu Ersen, France  
Claude Estournès, France  
Andrea Falqui, KSA  
Matteo Ferroni, Italy
- Wolfgang Fritzsche, Germany  
Alan Fuchs, USA  
Miguel A. Garcia, Spain  
Siddhartha Ghosh, Singapore  
P. K. Giri, India  
Russell E. Gorga, USA  
Jihua Gou, USA  
Jean M. Greneche, France  
John Zhanhu Guo, USA  
Smrati Gupta, Germany  
Kimberly Hamad-Schifferli, USA  
Michael Harris, USA  
Michael Z. Hu, USA  
Nay Ming Huang, Malaysia  
Shaoming Huang, China  
David Hui, USA  
Zafar Iqbal, USA  
Balachandran Jeyadevan, Japan  
Xin Jiang, Germany  
Rakesh Joshi, Australia  
Jeong-won Kang, Korea  
Hassan Karimi-Maleh, Iran  
Antonios Kelarakis, UK  
Alireza Khataee, Iran  
Ali Khorsand Zak, Iran  
Philippe Knauth, France  
Ralph Krupke, Germany  
Christian Kübel, Germany  
Prashant Kumar, UK  
Michele Laus, Italy  
Eric Le Bourhis, France  
Burtrand Lee, USA  
Jun Li, Singapore  
Shijun Liao, China  
Meiyong Liao, Japan  
Silvia Licocchia, Italy  
Wei Lin, USA  
Jun Liu, USA  
Zainovia Lockman, Malaysia  
Jim Low, Australia  
Songwei Lu, USA  
Jue Lu, USA  
Ed Ma, USA  
Gaurav Mago, USA  
Muhamamd A. Malik, UK
- Devanesan Mangalaraj, India  
Sanjay R. Mathur, Germany  
Tony McNally, UK  
Paulo Cesar Morais, Brazil  
Paul Munroe, Australia  
Jae-Min Myoung, Korea  
Rajesh R. Naik, USA  
Albert Nasibulin, Russia  
Toshiaki Natsuki, Japan  
Koichi Niihara, Japan  
Sherine Obare, USA  
Won-Chun Oh, Republic of Korea  
Atsuto Okamoto, Japan  
Abdelwahab Omri, Canada  
Ungyu Paik, Republic of Korea  
Edward A. Payzant, USA  
Alessandro Pegoretti, Italy  
Ton Peijs, UK  
Oscar Perales-Pérez, Puerto Rico  
Jorge Pérez-Juste, Spain  
Peter Reiss, France  
Orlando Rojas, USA  
Marco Rossi, Italy  
Cengiz S. Ozkan, USA  
Vladimir Šepelák, Germany  
Huaiyu Shao, Japan  
Prashant Sharma, USA  
Donglu Shi, USA  
Bhanu P. Singh, India  
Surinder Singh, USA  
Vladimir Sivakov, Germany  
Ashok Sood, USA  
Marinella Striccoli, Italy  
Xuping Sun, KSA  
Ashok K. Sundramoorthy, USA  
Bo Tan, Canada  
Valeri P. Tolstoy, Russia  
Muhammet S. Toprak, Sweden  
Ramon Torrecillas, Spain  
Takuya Tsuzuki, Australia  
Tamer Uyar, Turkey  
Bala Vaidhyanathan, UK  
Luca Valentini, Italy  
Rajender S. Varma, USA  
Ester Vazquez, Spain



---

Antonio Villaverde, Spain  
Ajayan Vinu, Australia  
Ruibing Wang, Macau  
Shiren Wang, USA  
Yong Wang, USA

Magnus Willander, Sweden  
Ping Xiao, UK  
Zhi Li Xiao, USA  
Yangchuan Xing, USA  
Doron Yadlovker, Israel

Yoke K. Yap, USA  
William W. Yu, USA  
Kui Yu, Canada  
Renyun Zhang, Sweden

# Contents

**Applications of Advanced Nanomaterials to Microelectronic and Photonic Devices**, Shoou-Jinn Chang, Teen-Hang Meen, Stephen D. Prior, Liang-Wen Ji, and Sheng-Joue Young  
Volume 2015, Article ID 451503, 1 page

**Study of Reduced Graphene Oxide Preparation by Hummers' Method and Related Characterization**, Ning Cao and Yuan Zhang  
Volume 2015, Article ID 168125, 5 pages

**Improvement of Lighting Uniformity and Phosphor Life in Field Emission Lamps Using Carbon Nanocoils**, Kun-Ju Chung, Nen-Wen Pu, Meng-Jey Youh, Yih-Ming Liu, Ming-Der Ger, and Wen-Ko Huang  
Volume 2015, Article ID 373549, 9 pages

**Effect of Substrate Temperature on the Thermoelectric Properties of the  $Sb_2Te_3$  Thin Films Deposition by Using Thermal Evaporation Method**, Jyun-Min Lin, Ying-Chung Chen, Cheng-Fu Yang, and Wei Chen  
Volume 2015, Article ID 135130, 6 pages

**Surface Patterning of PEDOT:PSS by Photolithography for Organic Electronic Devices**, Shihong Ouyang, Yingtao Xie, Dongping Wang, Dalong Zhu, Xin Xu, Te Tan, and Hon Hang Fong  
Volume 2015, Article ID 603148, 9 pages

**Memory and Electrical Properties of (100)-Oriented AlN Thin Films Prepared by Radio Frequency Magnetron Sputtering**, Maw-Shung Lee, Sean Wu, Shih-Bin Jhong, Kai-Huang Chen, and Kuan-Ting Liu  
Volume 2014, Article ID 250439, 6 pages

**The Influence of Electrophoretic Deposition for Fabricating Dye-Sensitized Solar Cell**, Jung-Chuan Chou, Shen-Chang Lin, Yi-Hung Liao, Jui-En Hu, Shen-Wei Chuang, and Chin-Hui Huang  
Volume 2014, Article ID 126053, 7 pages

**Oxidized Nano-Porous-Silicon Buffer Layers for Suppressing the Visible Photoresponsivity of ZnO Ultraviolet Photodetectors on Si Substrates**, Kuen-Hsien Wu  
Volume 2014, Article ID 756527, 4 pages

**AlGa<sub>N</sub>/Ga<sub>N</sub> High Electron Mobility Transistors with Multi-Mg<sub>x</sub>N<sub>y</sub>/Ga<sub>N</sub> Buffer**, P. C. Chang, K. H. Lee, Z. H. Wang, and S. J. Chang  
Volume 2014, Article ID 623043, 4 pages

**Investigation of the Optimal Parameters in Hydrothermal Method for the Synthesis of ZnO Nanorods**, Ying-Chung Chen, Huan-Yi Cheng, Cheng-Fu Yang, and Yuan-Tai Hsieh  
Volume 2014, Article ID 430164, 6 pages

**Metallurgical Mechanism and Optical Properties of CuSnZnS<sub>2</sub> Powders Using a 2-Step Sintering Process**, Tai-Hsiang Liu, Fei-Yi Hung, Truan-Sheng Lui, and Kuan-Jen Chen  
Volume 2014, Article ID 101958, 8 pages

**Thermal Effect on the Structural, Electrical, and Optical Properties of In-Line Sputtered Aluminum Doped Zinc Oxide Films Explored with Thermal Desorption Spectroscopy**, Shang-Chou Chang, Tien-Chai Lin, and To-Sing Li  
Volume 2014, Article ID 690498, 6 pages



---

**Self-Excited Single-Stage Power Factor Correction Driving Circuit for LED Lighting**, Yong-Nong Chang  
Volume 2014, Article ID 107939, 8 pages

**Optimization of Biohydrogen Production with Biomechatronics**, Shao-Yi Hsia and Yu-Tuan Chou  
Volume 2014, Article ID 721267, 11 pages

## *Editorial*

# **Applications of Advanced Nanomaterials to Microelectronic and Photonic Devices**

**Shoou-Jinn Chang,<sup>1</sup> Teen-Hang Meen,<sup>2</sup> Stephen D. Prior,<sup>3</sup>  
Liang-Wen Ji,<sup>4</sup> and Sheng-Joue Young<sup>2</sup>**

<sup>1</sup>*Institute of Microelectronics and Department of Electrical Engineering, National Cheng Kung University, Tainan 701, Taiwan*

<sup>2</sup>*Department of Electronic Engineering, National Formosa University, Yunlin 632, Taiwan*

<sup>3</sup>*Aeronautics, Astronautics and Computational Engineering, University of Southampton, Southampton SO17 1BJ, UK*

<sup>4</sup>*Institute of Electro-Optical and Materials Science, National Formosa University, Yunlin 632, Taiwan*

Correspondence should be addressed to Shoou-Jinn Chang; [changsj@mail.ncku.edu.tw](mailto:changsj@mail.ncku.edu.tw)

Received 12 May 2015; Accepted 12 May 2015

Copyright © 2015 Shoou-Jinn Chang et al. This is an open access article distributed under the Creative Commons Attribution License, which permits unrestricted use, distribution, and reproduction in any medium, provided the original work is properly cited.

The scope of the special issue is as follows. Nanomaterials which provide one of the greatest potentials for improving performance and extended capabilities of products in a number of industrial sectors are a new class of materials, having dimensions in the 1~100 nm range. Nanostructures can be divided into zero-dimensional, one-dimensional, and two-dimensional based on their shapes. The recent emphasis in the nanomaterials research is put on 1D nanostructures at the expense of 0D and 2D ones, perhaps due to the intriguing possibility of using them in a majority of short-term future applications. The most successful examples are seen in the microelectronics, where “smaller” has always meant a greater performance ever since the invention of transistors: for example, higher density of integration, faster response, lower cost, and less power consumption. In recent years, applications of advanced nanomaterials on microelectronic and photonic devices have been a highly developing field, due to the flexibility and light weight for daily use, which has the potential to be deployable. This special issue selects many papers about advanced nanomaterials on microelectronic and photonic devices topics. It enables interdisciplinary collaboration between science and engineering technologists in the academic and industrial fields.

*Shoou-Jinn Chang  
Teen-Hang Meen  
Stephen D. Prior  
Liang-Wen Ji  
Sheng-Joue Young*

## Research Article

# Study of Reduced Graphene Oxide Preparation by Hummers' Method and Related Characterization

**Ning Cao and Yuan Zhang**

*College of Mechanical and Electrical Engineering, China University of Petroleum, Qingdao 266580, China*

Correspondence should be addressed to Ning Cao; [caoning1982@gmail.com](mailto:caoning1982@gmail.com)

Received 13 August 2014; Accepted 25 September 2014

Academic Editor: Liang-Wen Ji

Copyright © 2015 N. Cao and Y. Zhang. This is an open access article distributed under the Creative Commons Attribution License, which permits unrestricted use, distribution, and reproduction in any medium, provided the original work is properly cited.

As a novel two-dimensional carbon material, graphene has fine potential applications in the fields of electron transfer agent and supercapacitor material for its excellent electronic and optical property. However, the challenge is to synthesize graphene in a bulk quantity. In this paper, graphite oxide was prepared from natural flake graphite by Hummers' method through liquid oxidization, and the reduced graphene oxide was obtained by chemical reduction of graphene oxide using  $\text{NH}_3 \cdot \text{H}_2\text{O}$  aqueous solution and hydrazine hydrate. The raw material graphite, graphite oxide, and reduced graphene oxide were characterized by X-ray diffraction (XRD), attenuated total reflectance-infrared spectroscopy (ATR-IR), and field emission scanning electron microscope (SEM). The results indicated that the distance spacing of graphite oxide was longer than that of graphite and the crystal structure of graphite was changed. The flake graphite was oxidized to graphite oxide and lots of oxygen-containing groups were found in the graphite oxide. In the morphologies of samples, fold structure was found on both the surface and the edge of reduced graphene oxide.

## 1. Introduction

Graphene is a novel 2-dimensional material which was first separated from graphite by mechanical stripping method in 2004 [1]. As an allotrope of element carbon, it is a planar sheet of carbon atoms arranged into hexagon [2]. The "thinnest" known material graphene can be used for biosensors [3], transparent electrodes [4], hydrogen storage, composites [5], and high energy supercapacitors [6] for its high optical and electron transparency and excellent mechanical properties [7].

There are many ways to synthesize graphene [1, 8, 9], such as exfoliation and cleavage, chemical vapor deposition (CVD), thermal decomposition, and electrochemical reduction. Among these preparation methods, solution-based reduction of graphite oxide (GO) is attractive for its easy operation in recent years. It includes three typical steps in this method. They are graphite oxidation, GO aqueous dispersion, and GO reduction. The methods invented by Brodie, Staudenmaier, and Hummers are widely used for graphite oxidation [10]. And Hummers' method is popular for the following reasons. First,  $\text{KClO}_3$  was replaced by  $\text{KMnO}_4$  as the oxidation agent. In this condition, the byproducts of toxic

gas were eliminated and the securities of experiments were improved. Moreover, the oxidation time was shortened, and last it was easy to exfoliate the resulted product in water. In this paper, Hummers' method was employed to prepare GO and reduced GO (rGO) was obtained with the aid of  $\text{NH}_3 \cdot \text{H}_2\text{O}$  aqueous and hydrazine hydrate.

## 2. Experimental

**2.1. Raw Materials.** Flake graphite powder, 98 wt.%  $\text{H}_2\text{SO}_4$ ,  $\text{KMnO}_4$ ,  $\text{NaNO}_3$ , deionized water,  $\text{NH}_3 \cdot \text{H}_2\text{O}$  aqueous, dilute HCl aqueous, 30%  $\text{H}_2\text{O}_2$  aqueous, and 80% hydrazine hydrate aqueous.

### 2.2. Graphene Preparation

**2.2.1. GO Preparation.** The mixture of flake graphite/ $\text{NaNO}_3$  was prepared in weight ratio of 2:1. The mixture was added into a beaker with a certain amount of 98 wt.%  $\text{H}_2\text{SO}_4$  at  $15^\circ\text{C}$  and a suspension was obtained. Then,  $\text{KMnO}_4$  powder which acted as an oxidation agent was gradually added into the suspension with continuous stirring. The weight of the  $\text{KMnO}_4$  powder is 3 times as much as the one of the mixture.

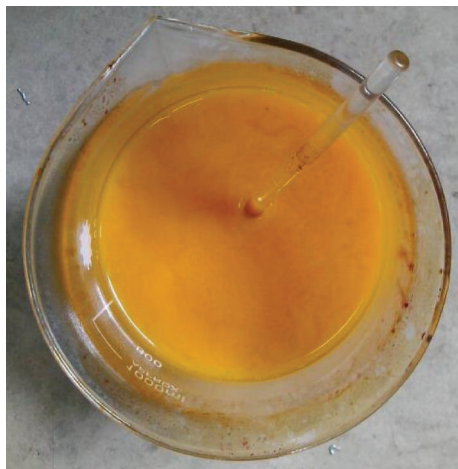


FIGURE 1: Pattern of resulting suspension.

There were 3 steps for the following process. First of all, it is the low temperature reaction. The temperature of the mixture was controlled below  $20^{\circ}\text{C}$  for 2 hours; at the same time, the suspension should be stirred continuously. The second step is the mid temperature reaction. The temperature of the mixture was maintained at  $35^{\circ}\text{C}$  for 30 minutes after  $\text{KMnO}_4$  was totally dissolved. Finally, it is the high temperature reaction. A certain amount of deionized water was added into the mixture slowly; therefore a large amount of heat was released when concentrated  $\text{H}_2\text{SO}_4$  was diluted. 15 minutes later, certain amounts of hot water and 30%  $\text{H}_2\text{O}_2$  aqueous were added into the mixture, respectively, with continuously stirring. As Figure 1 shows, the bright yellow resulted suspension was filtered by the qualitative filter paper when it was still hot, and the solid mixture was washed with dilute  $\text{HCl}$  aqueous and distilled water and dried in vacuum oven at  $70^{\circ}\text{C}$  for 24 h.

**2.2.2. rGO Preparation.** 400 mg GO was dispersed in 400 mL water by means of 30 minutes' ultrasonic treatment. As a result, a homogeneous brown GO aqueous suspension was obtained. The pH of the suspension was adjusted to 10 by dropping  $\text{NH}_3\cdot\text{H}_2\text{O}$ . A mount of hydrazine hydrate was added into suspension and heated at  $80^{\circ}\text{C}$  for 24 hours, and the weight ratio of hydrazine hydrate and GO was controlled at 10:7. A kind of black flocculent substance was gradually precipitated out of the solution. The product was obtained by filtered with the qualitative filter paper. Finally, the resulting black product was washed with methanol and water and dried at  $80^{\circ}\text{C}$  for 24 h.

**2.3. Characterization of Materials.** Crystal features of flake graphite, GO, and rGO were obtained by XRD [10] (AXS cooperation, Germany), with a scan speed of  $4^{\circ}/\text{min}$  from  $5$  to  $60^{\circ}$  of  $2\theta$  angles. The layer spacing ( $d$  spacing) could be calculated with the aid of Bragg equation, and the change of diffraction peak could also be observed. The micromorphology of rGO was observed by SEM (JSM-6700F, Japan), with the acceleration voltage from 0.5 to 30 KV. Spectra of dried GO and rGO were obtained by Tensor 27 FTIR-ATR (Bruker

cooperation, Germany), with the resolution of  $4\text{ cm}^{-1}$  from  $3700$  to  $500\text{ cm}^{-1}$  of spectral region, and functional groups of GO and rGO can be observed.

### 3. Result and Discussion

**3.1. X-Ray Diffraction.** As shown in Figure 2(a). Flake graphite exhibits a basal diffraction peak (002) at  $2\theta = 26.5^{\circ}$  ( $d$  spacing =  $0.33630\text{ nm}$ ), which is very sharp. There is also a very weak diffraction peak (004) at  $2\theta = 54.8^{\circ}$  ( $d$  spacing =  $0.16738\text{ nm}$ ). The diffraction peak (004) is the second diffraction [11] of the diffraction peak (002) according to layer spatial arrangement rules of microcrystals; thus diffraction peak (004) intensity is much weaker than that of diffraction peak (002). The diffraction peak at about  $2\theta = 9.8^{\circ}$  is very typical for GO; no apparent diffraction peak could be found for rGO in its XRD pattern. This result is similar to that of Tapas Kuila [2], who had already described the structure of GO and rGO by XRD. Figures 2(b) and 2(c) show the enlarged XRD patterns of GO and rGO. Diffraction peak becomes broader in the enlarged pattern of GO at  $2\theta = 9.8^{\circ}$  ( $d$  spacing =  $0.88160$ ) and the significant increase in  $d$  spacing is believed due to the following reason: oxygen functional groups intercalate in the interlayer of graphite. There is a very weak diffraction peak at  $2\theta = 42.3^{\circ}$ , which is believed due to the incomplete oxidation. As is shown in Figure 2(c), a very weak and broad diffraction peak can be observed in the XRD pattern of rGO at  $2\theta = 25\text{--}30^{\circ}$ ; the diffraction peak of rGO is so weak that it cannot be visible when drawn together in the XRD pattern with graphite and GO (Figure 2(a)). There is also a weak diffraction peak at  $2\theta = 42.3^{\circ}$ .

**3.2. FTIR-ATR.** FTIR-ATR spectra of GO and rGO are shown in Figures 3 and 4. Some carbon-oxygen functional groups of GO are observed in Figure 3, such as O-H, C=O, C-OH, and C-O. Characteristic peak ( $\sim 3464\text{ cm}^{-1}$ ) [12] is believed to be attributed to O-H stretching of hydroxyl and carboxyl groups, and characteristic peaks of C=O ( $\sim 1639\text{ cm}^{-1}$ ), C-OH ( $\sim 1288\text{ cm}^{-1}$ ), and C-O ( $\sim 1003\text{ cm}^{-1}$ ) are also believed to be attributed to carboxylic acid and carbonyl groups [13]. And the characteristic peak at  $1493\text{ cm}^{-1}$  is corresponding to the C=C skeletal vibration of unoxidized graphitic domain. These oxygen functional groups indicate that the flake graphite powder has been oxidized to GO. As shown in Figure 4, no obvious peak could be observed, which means that full reduction of GO was made. While carbon-oxygen functional groups all existed, their characteristic peaks are just very weak.

**3.3. Scanning Electron Microscope.** Figure 5 shows SEM morphologies of rGO which was dried at  $80^{\circ}\text{C}$  for 1 day. As is shown in Figure 5, 2-dimensional material can be observed. Fold structure can be found on both the surface and the edge of rGO powder. They are the typical morphologies of few-layer rGo [14]. The thickness of rGO may be 10 nm and it is obviously that rGO layers have fairly large dimension (much larger than 100 nm), and rGO retacked together. The reason of the reaggregate may be the long-time high temperature

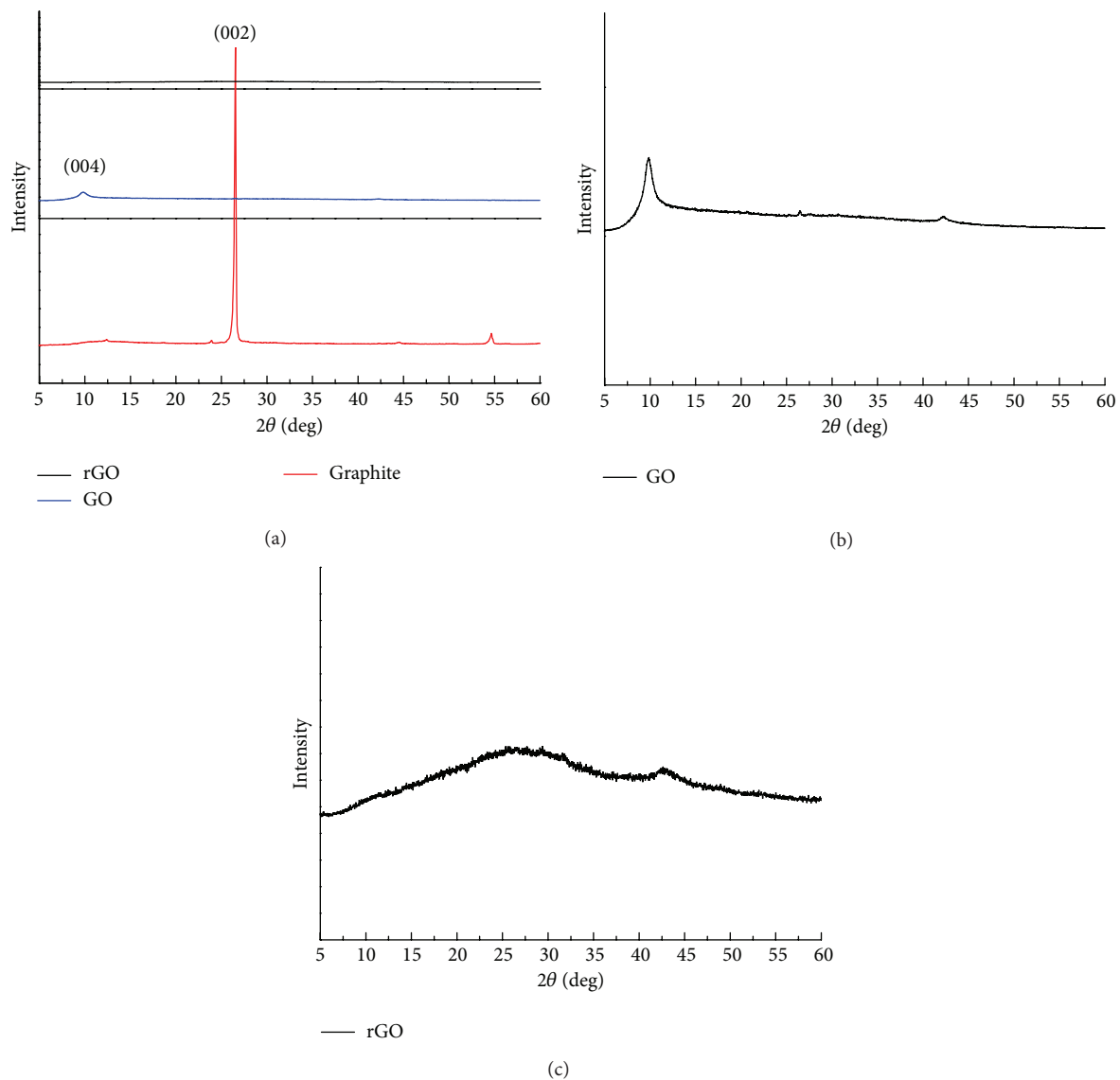


FIGURE 2: X-ray diffraction patterns. (a) graphite, GO, and rGO; (b) enlarged view of GO; (c) enlarged view of rGO.

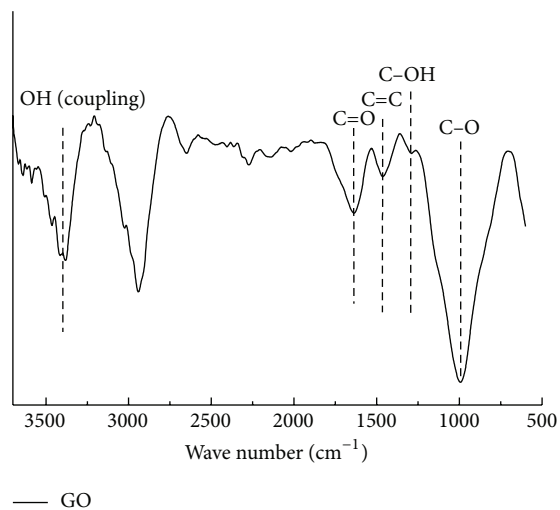


FIGURE 3: FTIR-ATR spectra of GO.

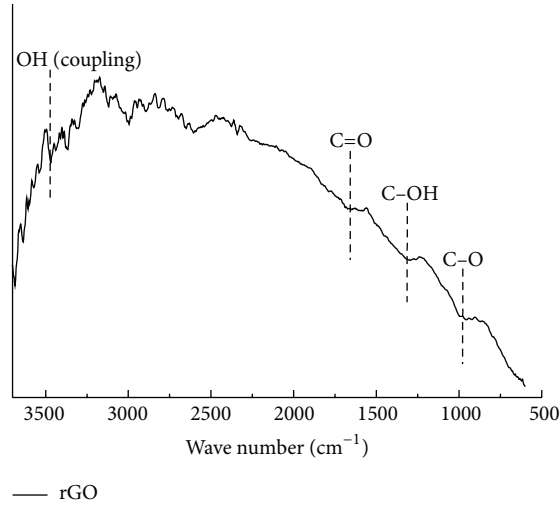


FIGURE 4: FTIR-ATR spectra of rGO.

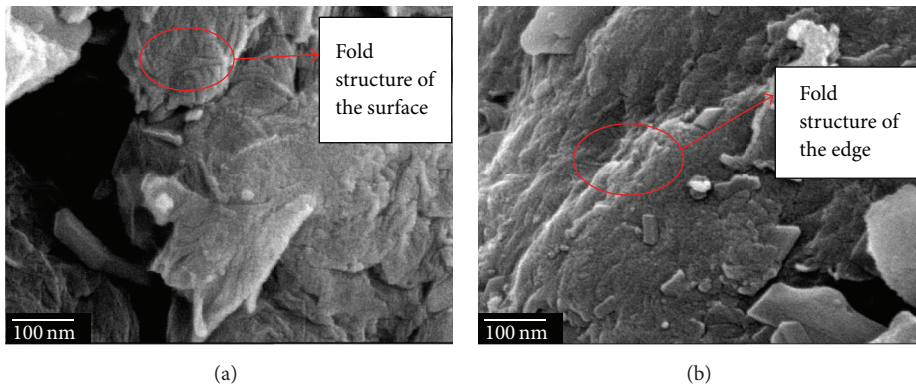
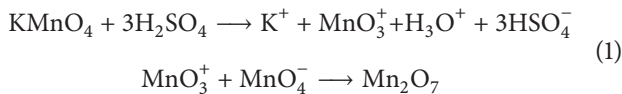


FIGURE 5: SEM morphology of rGO.

treatment. The morphology of graphite (fold structure) can also be found in Figure 5.

Reaction mechanism of solution-based reduction of graphite oxide will be discussed, to begin with the mechanism of Hummers, though  $\text{KMnO}_4$  is used as a kind of oxidizing agent. Dreyer et al. [15] believed that the active species was  $\text{Mn}_2\text{O}_7$ . The following equation gives the reaction between  $\text{KMnO}_4$  and  $\text{H}_2\text{SO}_4$ :



In low temperature reaction, the edge of graphite was oxidized and intercalated with the aid of oxidizing agent.  $-\text{OH}$  was formed during this process. In mid temperature reaction, with the increasing of temperature, the oxidation ability improves furthermore. More oxygen functional groups are formed in this process, and the oxidizing agent penetrates into the internal of graphite layer; therefore this process results in the increasing of  $d$  spacing. In the high temperature reaction, concentrated  $\text{H}_2\text{SO}_4$  releases large amount of heat during the process of watering. Force between layers is

destroyed and finally the GO could be fully exfoliated to single layers. Secondly, the fully exfoliated GO will be reduced to rGO with the help of  $\text{NH}_3\cdot\text{H}_2\text{O}$  aqueous and hydrazine hydrate.

The mechanism of solution-based reduction of GO is quite different with that of the traditional CVD ones. The formation of graphene on bulk metal through CVD includes three steps [1, 16, 17]. First, a hydrocarbon could be dissociated through dehydrogenation; second, the carbon species diffuse and dissolve into the bulk metal at the growth temperature; the reason why transition metals could serve as an electron acceptor is because of the empty  $d$ -shell; third, carbon species precipitate out of the bulk metal onto the metal surface upon the rapid quenching, start the segregation process, and build up honeycomb lattice because the solubility decreases during the cooling process.

#### 4. Conclusion

GO was prepared by Hummers' method and rGO was prepared with the aid of  $\text{NH}_3\cdot\text{H}_2\text{O}$  aqueous and hydrazine hydrate successfully. The characterization results indicate that

the layer spacing of graphite oxide was longer than that of graphite. The crystal structure of graphite was changed. Graphite was oxidized to GO and lots of oxygen-containing groups were found in the GO. The typical fold morphologies were found on both the surface and the edge of rGO.

Compared with the traditional CVD method, Hummers' method can synthesize GO in large scale, then rGO can be prepared with the help of reduced agent, and this process costs a little. Meanwhile, the prepared GO is dispersed easily in solution. In this case, the modification of the GO is easy and it is suitable for GO application in composites and energy storage devices.

### Conflict of Interests

The authors declare that there is no conflict of interests regarding the publishing of this paper.

### Acknowledgments

The authors acknowledge funding from the National Natural Science Foundation of China (no. 51302320) and the Fundamental Research Funds for the Central Universities (no. 14CX05094A).

### References

- [1] V. Singh, D. Joung, L. Zhai, S. Das, S. I. Khondaker, and S. Seal, "Graphene based materials: past, present and future," *Progress in Materials Science*, vol. 56, no. 8, pp. 1178–1271, 2011.
- [2] M. I. Katsnelson, "Graphene: carbon in two dimensions," *Materials Today*, vol. 10, no. 1-2, pp. 20–27, 2007.
- [3] T. Kuila, S. Bose, P. Khanra, A. K. Mishra, N. H. Kim, and J. H. Lee, "Recent advances in graphene-based biosensors," *Biosensors and Bioelectronics*, vol. 26, no. 12, pp. 4637–4648, 2011.
- [4] G. Eda, G. Fanchini, and M. Chhowalla, "Large-area ultrathin films of reduced graphene oxide as a transparent and flexible electronic material," *Nature Nanotechnology*, vol. 3, no. 5, pp. 270–274, 2008.
- [5] T. Kuilla, S. Bhadra, D. Yao, N. H. Kim, S. Bose, and J. H. Lee, "Recent advances in graphene based polymer composites," *Progress in Polymer Science*, vol. 35, no. 11, pp. 1350–1375, 2010.
- [6] B. G. Choi, M. Yang, W. H. Hong, J. W. Choi, and Y. S. Huh, "3D macroporous graphene frameworks for supercapacitors with high energy and power densities," *ACS Nano*, vol. 6, no. 5, pp. 4020–4028, 2012.
- [7] Y. Zhu, S. Murali, W. Cai et al., "Graphene and graphene oxide: synthesis, properties, and applications," *Advanced Materials*, vol. 22, no. 35, pp. 3906–3924, 2010.
- [8] T. Kuila, S. Bose, A. K. Mishra, P. Khanra, N. H. Kim, and J. H. Lee, "Chemical functionalization of graphene and its applications," *Progress in Materials Science*, vol. 57, no. 7, pp. 1061–1105, 2012.
- [9] S. Y. Toh, K. S. Loh, S. K. Kamarudin, and W. R. Wan Daud, "Graphene production via electrochemical reduction of graphene oxide: synthesis and characterisation," *Chemical Engineering Journal*, vol. 251, pp. 422–434, 2014.
- [10] C. Bao, L. Song, W. Xing et al., "Preparation of graphene by pressurized oxidation and multiplex reduction and its polymer nanocomposites by masterbatch-based melt blending," *Journal of Materials Chemistry*, vol. 22, no. 13, pp. 6088–6096, 2012.
- [11] A. Bagri, C. Mattevi, M. Acik, Y. J. Chabal, M. Chhowalla, and V. B. Shenoy, "Structural evolution during the reduction of chemically derived graphene oxide," *Nature Chemistry*, vol. 2, no. 7, pp. 581–587, 2010.
- [12] Y. Jin, S. Sun, and X. Qi National Defense Industry Press, 2008, (Chinese).
- [13] Q. Deng, L. Liu, and H. Deng, *Spectrum Analysis Tutorial*, Science Press, 2007, (Chinese).
- [14] F. Hong, L. Zhou, and Y. Huang, "Synthesis and characterization of graphene by improved hummers method," *Chemical & Biomolecular Engineering*, vol. 29, pp. 31–33, 2012 (Chinese).
- [15] D. R. Dreyer, S. Park, C. W. Bielawski, and R. S. Ruoff, "The chemistry of graphene oxide," *Chemical Society Reviews*, vol. 39, no. 1, pp. 228–240, 2010.
- [16] Y. Kai, F. Lei, L. P. Hai, and F. L. Zhong, "Designed CVD growth of graphene via process engineering," *Accounts of Chemical Research*, vol. 46, pp. 2263–2274, 2013.
- [17] C.-M. Seah, S.-P. Chai, and A. R. Mohamed, "Mechanisms of graphene growth by chemical vapour deposition on transition metals," *Carbon*, vol. 70, pp. 1–21, 2014.

## Research Article

# Improvement of Lighting Uniformity and Phosphor Life in Field Emission Lamps Using Carbon Nanocoils

Kun-Ju Chung,<sup>1</sup> Nen-Wen Pu,<sup>2</sup> Meng-Jey Youh,<sup>3</sup> Yih-Ming Liu,<sup>4</sup>  
Ming-Der Ger,<sup>4</sup> and Wen-Ko Huang<sup>1</sup>

<sup>1</sup>School of Defense Science, Chung Cheng Institute of Technology, National Defense University, Dasi, Taoyuan 335, Taiwan

<sup>2</sup>Department of Photonics Engineering, Yuan Ze University, Chung-Li, Taoyuan 320, Taiwan

<sup>3</sup>Department of Information Technology, Hsing Wu University, Linkou, New Taipei City 244, Taiwan

<sup>4</sup>Department of Chemical and Materials Engineering, Chung Cheng Institute of Technology, National Defense University, Dasi, Taoyuan 335, Taiwan

Correspondence should be addressed to Meng-Jey Youh; 095063@mail.hwu.edu.tw and Yih-Ming Liu; takululiu@gmail.com

Received 25 July 2014; Accepted 12 April 2015

Academic Editor: Teen-Hang Meen

Copyright © 2015 Kun-Ju Chung et al. This is an open access article distributed under the Creative Commons Attribution License, which permits unrestricted use, distribution, and reproduction in any medium, provided the original work is properly cited.

The lighting performances and phosphor degradation in field emission lamps (FELs) with two different kinds of cathode materials—multiwalled carbon nanotubes (MWCNTs) and carbon nanocoils (CNCs)—were compared. The MWCNTs and CNCs were selectively synthesized on 304 stainless steel wire substrates dip-coated with nanosized Pd catalysts by controlling the growth temperature in thermal chemical vapor deposition, and the film uniformity can be optimized by adjusting the growth time. FELs were successfully fabricated by assembling these cathode filaments with a glass bulb-type anode. The FEL with the CNC cathode showed much higher lighting uniformity and light-spot density and a lower current at the same voltage than that with the MWCNT cathode filament, and its best luminous efficiency was as high as 75 lm/W at 8 kV. We also found that, for P22, the phosphor degradation can be effectively suppressed by replacing MWCNTs with CNCs in the cathode, due to the much larger total bright spot area and hence much lower current density loading on the anode.

## 1. Introduction

The phenomenon of field emission (FE) was proposed by Fowler and Nordheim in 1928 [1]. This phenomenon has been used in a variety of applications such as display panels [2–5], backlight in flat panel displays [6, 7], field emission lamps (FELs) [8–11], and X-ray tubes [12]. FEL devices have numerous advantages such as short switching times, low power consumption, high brightness, and low heat generation. In addition, they are also free of mercury. Compared with light-emitting diodes and cold cathode fluorescent lamps, FELs have an edge as a new-generation environment-friendly light source [13].

Carbon nanotubes (CNTs) have been widely used as the cathode material in most FELs that were recently developed because they are characterized by a high aspect ratio and a low turn-on electric field [14]. Hence, the voltage required

for operating these FELs is lower than those of conventional cathode materials. In 2001, Bonard et al. fabricated a prototype of cold illumination device with CNTs as the cathode material [15]. They directly grew CNTs on metal wires using thermal chemical vapor deposition (TCVD) and then used the CNT-coated wires as the cathode emitter set in the middle of a vacuum tube. The inner side of the vacuum tube was coated with an ITO film and phosphor and served as the anode of the tubular FEL, which has brightness higher than  $1 \times 10^4$  cd/m<sup>2</sup> under an applied voltage of 5.4 kV. Huang et al. also successfully fabricated an FEL device in 2008 using a CNT wire cathode, which was also prepared by TCVD growth of CNTs on a stainless steel wire with a diameter of 0.7 mm and a length of 30 mm, and an anode coated with blue and green phosphors [16]. Fu et al. blended multiwalled CNTs (MWCNTs) and silver glue and then applied the mixture on a stainless ball with a diameter of 2 mm to fabricate a spherical

FE light bulb in 2008 [17]. The bulb they made can achieve an emission current density as high as  $300 \text{ mA/cm}^2$  and a luminous efficiency of  $26.4 \text{ lm/W}$ .

However, compared to those commonly used lamps such as CCFLs, these CNT-FELs have not shown significantly higher luminous efficiency or brightness. To achieve high luminous efficiency or brightness, the characteristics of the cathode material are crucial. The choice of cathode material not only directly affects lighting uniformity and light-spot density, but also is very important for the anode performance and phosphor lifetime in FELs. This is because ZnS-based types of phosphors, P22, which have become the primary fluorescent material in FELs currently, suffer from many unsolved problems, including Coulombic damage (aging), charge accumulation, and thermal quenching, despite their high efficiency and brightness in high-voltage or high current operation [18].

In particular, in high current density operation with intense electron bombardment, the phenomenon of Coulombic damage and charge accumulation were quite severe since for the P22 phosphors the maximum Coulombic loading per stimulated phosphor area ( $\text{C/cm}^2$ ) is limited to  $\sim 200$  [19–21]. The luminescent brightness increases with the current density at low current density for a short term, but the lifetime of the phosphor rapidly decreases at high current density. Therefore, increasing the voltage (hence the kinetic energy of electrons) to improve the brightness of FELs is considered more suitable than increasing the current.

In addition, even at a moderate current level, poor lighting uniformity and low light-spot density, which are common in FEL devices, will result in excessive concentration of current density at local phosphor particles, easily causing phosphor degradation and brightness declination. Generally, to control the lighting uniformity and light-spot density is difficult because electron emission only occurs at the tip of CNTs. Many researchers have synthesized vertically aligned CNT arrays to enhance the uniformity of electron emission using various different methods, but they usually require complicated or expensive processes.

Carbon nanocoils (CNCs) were first synthesized by Motojima and coworkers [22] using TCVD. Pan et al. pointed out that CNCs can be a better candidate for an effective FEL material. Because of the special helical morphology of CNCs, they have sharp edges (graphene edge) all over the surface, which offer numerous electron emission sites on one single CNC [23], and this will significantly increase the light spots on the phosphor. In previous studies [24, 25], it has been demonstrated that the FELs with CNC cathodes exhibited much better light-spot density and uniformity than those with CNT counterparts. The emission from a carbon nanocoil occurs not only at its tip, but also on its top surface, where the electric field is concentrated [25]. These results indicated that CNCs are a great potential material for FEL cathodes.

In this study, we grew CNTs and CNCs separately on 304 stainless steel (304-SS) wires utilizing a poly(styrene-co-NIPAAm)/Pd catalyst (reported in our previous study [26, 27]) as the FEL cathode and compare their FE characteristics. Higher lighting uniformity and light-spot density at lower

current density, as well as greater luminescence efficiency and a longer anode phosphor life, were observed in the FEL with a CNC cathode.

## 2. Experimental

The substrates used for the FEL cathodes were 304-SS wires with a length of 6 cm and a diameter of 1 mm. The substrate was first cleaned with acetone and ultrasonicated for 30 min. The substrate surface was then roughened by sand blasting with 220-grit sands. Before TCVD, Pd catalyst was deposited on the wire substrates by dipping the wires into a poly(styrene-co-NIPAAm)/Pd solution (see [26, 27] for the details of preparation) and then drying at  $80^\circ\text{C}$  in air. Figure 1 shows a schematic of cathode preparation. The wires were placed at the center of a quartz tube, which was heated by a furnace and equipped with a gas-flow controlling system. Subsequently, 5 sccm of acetylene, 100 sccm of argon, and 20 sccm of hydrogen were introduced into the furnace as the carbon source, carrier gas, and reductive gas, respectively.

To fabricate separately the two different types of electron emitters, two process temperatures— $600$  and  $800^\circ\text{C}$ —were used. A heating ramp lasting for 30–40 min was used to reach the desired process temperature, and acetylene was introduced into the reaction tube for 0–30 min. After cooling the reaction system to room temperature, CNC or MWCNT cathode filaments were obtained. The morphologies of the cathodes were examined using a field emission scanning electron microscope (FE-SEM) (model: JEOL JSM-7600F) and a transmission electron microscope (TEM) (model: FEI Tecnai F30).

The bulb-type FE anode adopted in this study is shown in Figure 1. The diameter of the glass bulb was 6 cm, and the lower hemisphere of the inner surface was coated with an aluminum film. 10 g of P22 phosphor, 9.8 g of butyl acetate, and 0.25 g of ethyl cellulose (EC) were mixed together to form the phosphor slurry, which was then coated on the aluminum film to act as the anode. Then the anode with the phosphor slurry was baked at  $500^\circ\text{C}$  to remove the butyl acetate and EC.

A cathode filament was fused with the glass bulb-type anode and pumped to a  $3 \times 10^{-6}$  Torr vacuum to form an FEL bulb. The FEL bulb was tested in a vacuum chamber at high voltages (0–8 kV). The characteristics for the FELs with two different cathode materials, including their current density versus applied voltage and emission uniformity, were investigated. Also, the performances of anode phosphor for the FELs with the two different cathode materials were also evaluated.

## 3. Results and Discussion

Figures 2 and 3 show the SEM images with various magnifications for the two distinct types of carbonaceous materials synthesized on Pd-nanoparticle-containing substrate wires at the two process temperatures. MWCNTs and CNCs were synthesized in the samples processed at  $800$  and  $600^\circ\text{C}$ , respectively. Figures 2(a)–2(c) show the MWCNTs grown on 304-SS for various growth times: 5, 8, and 10 min.

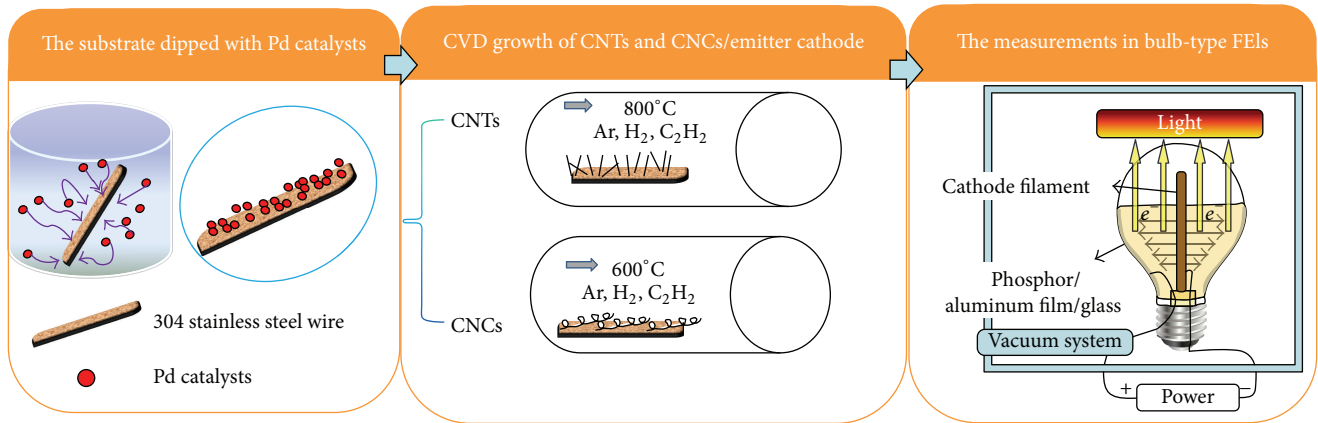


FIGURE 1: Schematic depicting the experimental process for FEL cathode preparation and device fabrication: dip coating of Pd catalysts; TCVD growth of MWCNTs and CNCs; the assembly of a bulb FEL and the FE measurements.

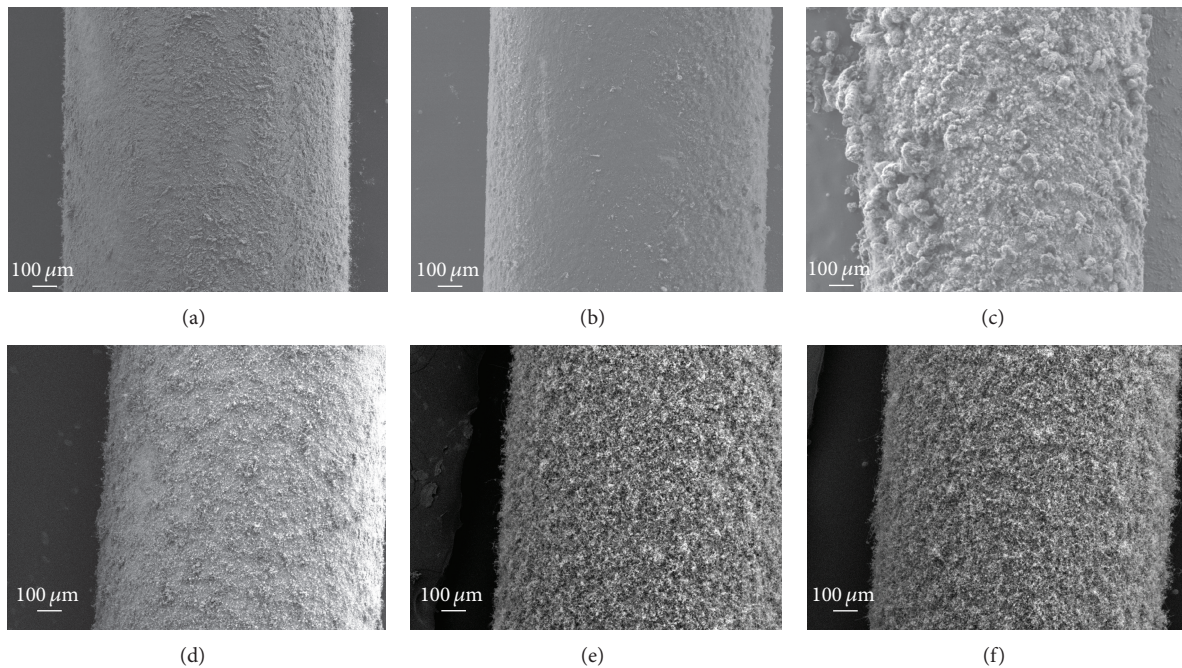


FIGURE 2: SEM images of MWCNT cathode filaments grown for various periods of time: (a) 5, (b) 8, and (c) 10 min and CNC cathode filaments grown for various periods of time: (d) 10, (e) 20, and (f) 30 min.

Figures 2(d), 2(e), and 2(f) show the CNCs grown on 304-SS for 10, 20, and 30 min, respectively. The reason we grew CNTs and CNCs with different periods is that the growth rates of CNTs and CNCs are quite different. Proper lengths of CNTs or CNCs are needed to achieve good field emission efficiency, so the ranges for their synthesis time for a better field emission effect are different. For example, as shown in Figures 2(a) and 2(c), an uneven CNT film was obtained for growth times of 5 and 10 min. The optimum growth time for MWCNTs was about 8 min at 800°C. In contrast, the optimum growth time for the CNCs prepared at 600°C was about 20 min, as revealed in Figures 2(d)–2(f). So, for the subsequent research including the FE measurements and material analysis, the growth times of MWCNT and CNC cathode filaments were fixed at 8 and 20 min, respectively.

According to Baker's hypothesis [28], the decomposition of the carbon source and the diffusion of carbon atoms in the catalyst involve thermally activated reactions that obey the Arrhenius equation, so they are very sensitive to the reaction temperature. In Figures 3(a) and 3(c), acetylene decomposed quickly at 800°C and the fast diffusion and high deposition rate of these carbon atoms resulted in the formation of MWCNTs. The reason is that, at higher diffusion rates, the diffusion of carbon atoms became increasingly isotropic, and their precipitation rates on various catalyst planes were almost identical, leading to the uniform growth of CNTs. In contrast, at 600°C acetylene decomposed slowly and the diffusion of carbon atoms was not only slow but also anisotropic, resulting in the formation of a coiled or helical structure in Figures 3(b) and 3(d). In our previous work [29], carbonaceous materials

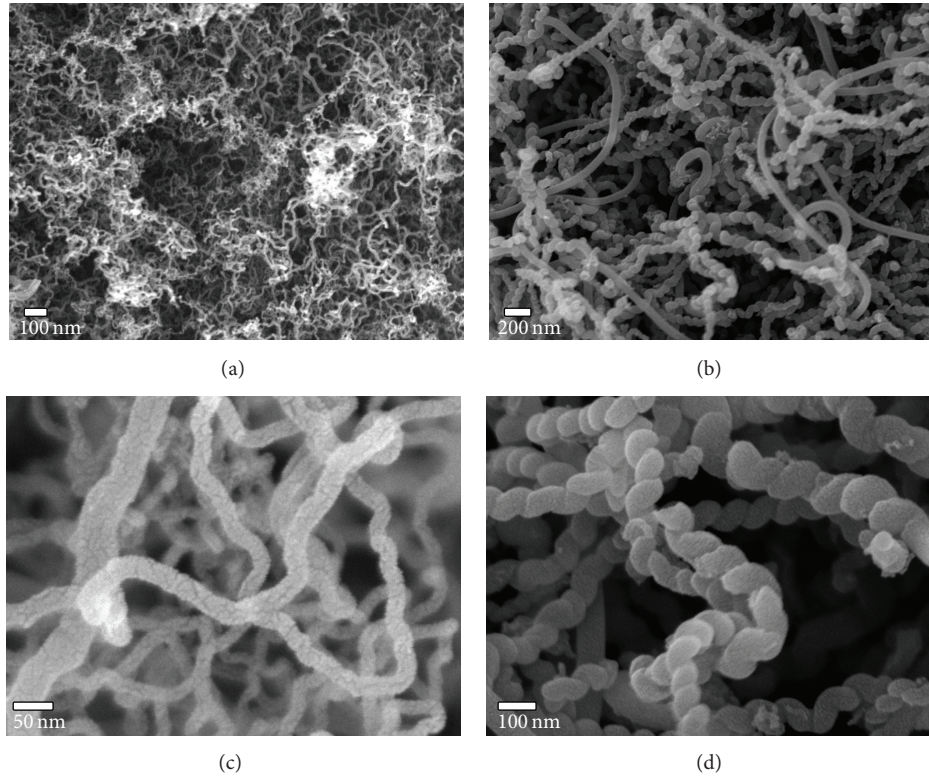


FIGURE 3: SEM images of carbon nanomaterials grown at different temperatures in low magnification, (a) 800°C and (b) 600°C, and in high magnification, (c) 800°C and (d) 600°C.

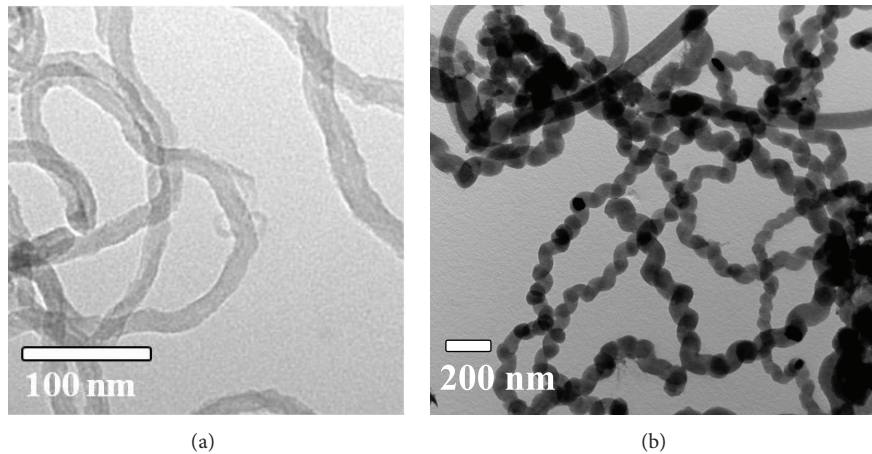


FIGURE 4: TEM images of the (a) MWCNTs and (b) CNCs.

synthesized on Pd-nanoparticle-containing substrate wires at various temperatures (500–800°C) have been studied. The results showed that CNCs and MWCNTs were the major synthesized carbonaceous products at 600 and 800°C, respectively, using our Pd catalysts. Similar carbon products were synthesized using Pd catalysts by Nitze et al. [30] and Segura et al. [31]. These observations indicated that the growth temperature determines the morphology of carbon nanostructures. So the growth temperatures of MWCNT and CNC cathode filaments were fixed at 800°C and 600°C, respectively, in this research.

The TEM images of the MWCNTs and CNCs synthesized in this study are shown in Figure 4. The MWCNTs grown at 800°C had a hollow structure and smaller diameters of 20–50 nm as shown in Figure 4(a). By contrast, in Figure 4(b) the CNCs grown at 600°C showed a solid amorphous helical structure and had considerably larger diameters of 80–150 nm.

Figure 5 shows the  $I$ - $V$  curves for the FELs with (a) MWCNT and (b) CNC cathode filaments. The FE  $I$ - $V$  curves were measured in a vacuum chamber using a bulb-type anode and a CNC or MWCNT filament cathode. The FE currents

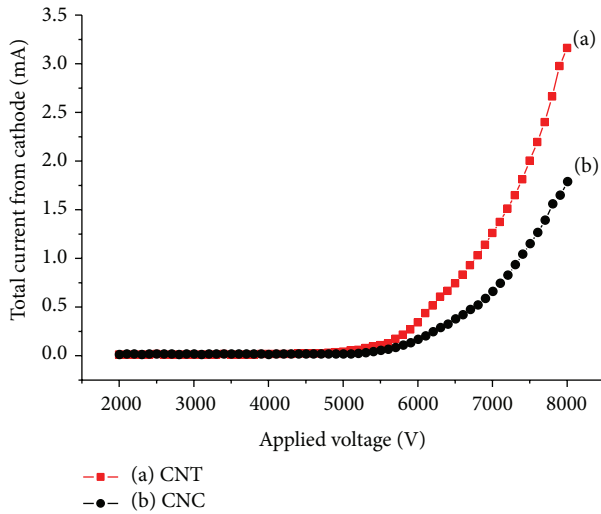


FIGURE 5:  $I$ - $V$  curves for the FELs with (a) MWCNT and (b) CNC cathodes.

at a voltage of 8 kV with MWCNT and CNC cathodes were 3.2 and 1.7 mA, respectively. The current emitted from the MWCNT cathode filament was considerably higher than that from the CNC counterpart. This is reasonable because MWCNTs have a higher aspect ratio and hence a lower turn-on electric field than CNCs.

Furthermore, Figures 6(a) and 6(b) show the photos of FELs in operation (operated at dc 8 kV) using the same (a) MWCNT and (b) CNC cathode filaments in Figure 5 ((a) and (b)), respectively. It reveals that the MWCNT cathode FEL had much poorer lighting uniformity (see Figure 6(a)) despite its higher FE current. In contrast, Figure 6(b) shows that the CNC cathode FEL was brighter and had excellent bright spot density and uniformity, which can be attributed to the numerous emission sites on a single CNC, as opposed to the only emission site at the tip of a MWCNT.

In addition, Pan et al. [23] have pointed out that 5-ring or 7-ring carbon bond defects in the nanocoil-structure can serve as the FE sites (electrons are emitted from these points). Compared with a CNT of the same length, a CNC has considerably more FE sites and efficiency [24, 32]. In accordance with Pan's study, our study showed that the CNC cathode FEL was brighter than the CNT one and had excellent lighting-spot density and uniformity, which can be attributed to the numerous emission sites on the single CNC, as opposed to the only one emission site at the tip of a MWCNT. According to the measurements with an integrating sphere, the best luminous efficiency from our CNC cathode filament was as high as 75 lm/W.

For P22, a higher electron kinetic energy and hence a higher working voltage are needed to achieve a high CL efficiency, but this will be detrimental for exceedingly high emission current density. In high current density operation with intense electron bombardment, the phenomenon of Coulombic damage and charge accumulation were quite severe since for the P22 phosphors the maximum Coulombic loading per stimulated phosphor area ( $C/cm^2$ ) is limited to

$\sim 200 C/cm^2$  [19–21]. Thus if we raise the current to improve the brightness, the phosphor would be damaged more quickly and so the number of bright spots and the luminous efficiency would decay faster.

Moreover, after 1 h of operation the FEL with the MWCNT cathode showed evident yellowing of the phosphor (Figure 6(c)) due to the much higher FE current. To make the situation even worse, this higher current converged on the much smaller area of the sparse bright spots on the phosphor, as shown in Figure 6(a). The high-density electric bombardment on the anode caused fast degradation of the P22 phosphor, which was evidenced by the yellowing. The CNC cathode FEL, in contrast, showed no clear sign of phosphor degradation (Figure 6(d)).

Because the MWCNTs have lower turn-on and threshold voltages than our CNCs, MWCNTs tend to emit higher current density than CNCs at the same operation voltage. In addition, the total bright spot areas on the anode for the CNC FEL were much larger due to the numerous emission sites per CNC. Therefore the Coulombic loading ( $C/cm^2$ ) on the phosphor can be significantly lower in the CNC FEL. To quantitatively estimate this effect, the actual loading current density on the anode versus the applied voltage ( $J$ - $V$  curve) was calculated by dividing the current by the total bright spot area, and the result is shown in Figure 7. The total bright spot areas calculated by the software ImageJ were 49.6 and 93.7% of the anode area for Figures 6(a) and 6(b), respectively. Evidently, the loading current density can be significantly reduced—from 0.23 to 0.03  $mA/cm^2$  at 8 kV—by replacing the MWCNTs with CNCs. In this work, for P22, the phosphor life estimated from the current density can reach about 810 h for the CNC cathode FEL, while for the MWCNT cathode FEL it is only about 115 h. Therefore, an operation regime at low emission current density, rather than high emission current density, is preferred because it leads to higher lighting efficiency and longer life of the anode phosphors.

To reveal the damage on the phosphors, the SEM morphologies of the phosphor for the FELs with (a) the MWCNT cathode (high current density) and (b) the CNC cathode (low current density) after 1 h of operation were displayed in Figure 8. The phosphor particle in Figure 8(a) (the MWCNT cathode FEL) had a severely roughened surface morphology due to the numerous eroded defects. In comparison, the phosphor in Figure 8(b) (the CNC cathode FEL) showed no sign of morphological changes. We think the eroded defects came from the electron bombardment at high current density. High-energy electron bombardment can produce changes in the surface chemical composition on the ZnS phosphors [18, 33] and may also create a nonluminescent layer on the surface of the phosphor.

The changes in the surface chemical composition on the ZnS phosphors can be analyzed with electron spectroscopy for chemical analysis (ESCA). Figure 9 shows the  $S_{2p_{3/2}}$  (Figure 9(a)) and  $Zn_{2p_{3/2}}$  (Figure 9(b)) photoelectron spectra for the FELs with (A) the MWCNT cathode (high current density) and (B) the CNC cathode (low current density) after 1 h of FE operation. After the high current density electron bombardment (curve (A)), the sulfur signals (at about 152 eV)

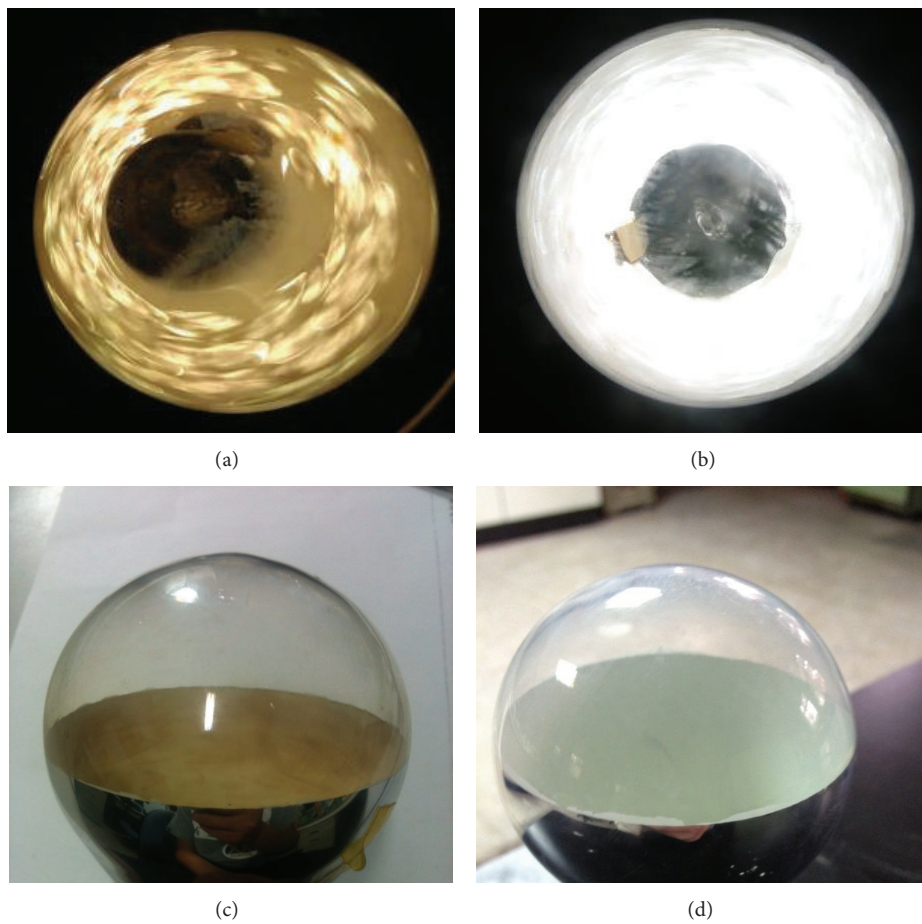


FIGURE 6: Top: FELs with (a) MWCNT and (b) CNC cathodes in operation. Bottom: phosphor on the anodes after 1 h of FE measurement for FELs with (c) MWCNT and (d) CNC cathodes.

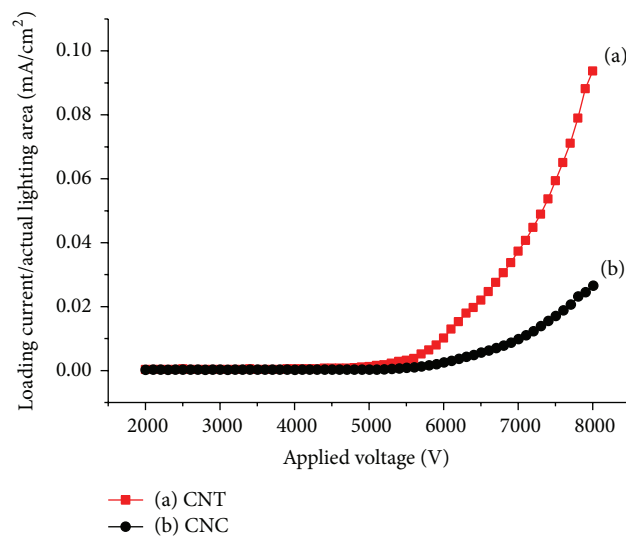


FIGURE 7:  $J$ - $V$  curves for FELs with (a) MWCNT and (b) CNC cathodes, where  $J$  is the averaged loading current density on the anode.

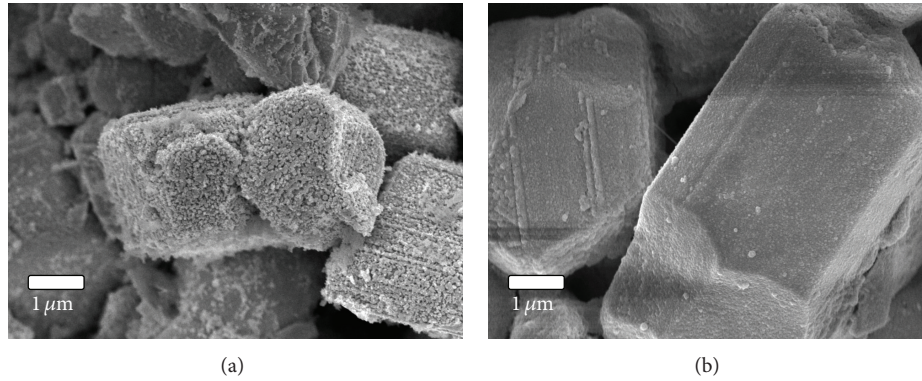


FIGURE 8: SEM morphologies of phosphor for the FELs with (a) MWCNT and (b) CNC cathodes after 1 h of FE operation.

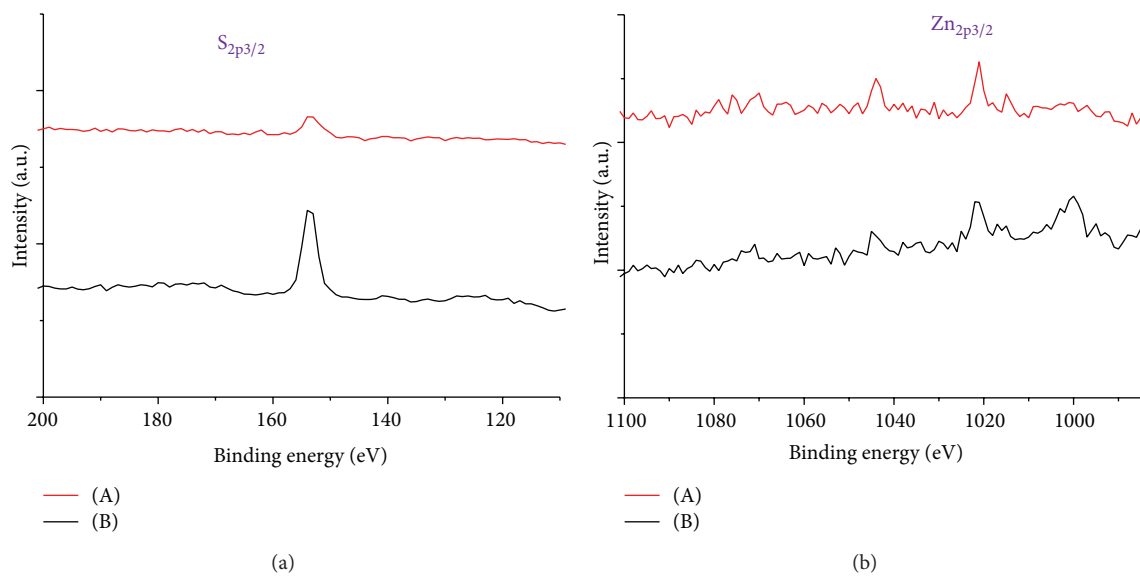


FIGURE 9: ESCA  $S_{2p_{3/2}}$  (a) and  $Zn_{2p_{3/2}}$  (b) photoelectron spectra of P22 phosphor for FELs with (A) MWCNT and (B) CNC cathodes after 1 h of FE operation.

decreased very obviously. The work in [21] and [33] indicated that sulfur was severely depleted from ZnS on the phosphor surface. The phenomenon is not observed in the low current density CNC cathode FEL. It suggests that using CNC as the cathode can effectively decelerate the degradation of P22 phosphors.

#### 4. Conclusions

In this paper, MWCNTs and CNCs were separately synthesized by TCVD at growth temperatures of 800 and 600°C, respectively, using nanosized Pd catalysts. The film uniformity can be optimized by adjusting the growth time. We successfully fabricated high-uniformity bulb-type FELs using CNCs on a 304-SS wire as field emitters. The P22 phosphor prefers high-voltage and low current density operation. Our results showed that the best luminous efficiency from our FEL with the CNC cathode can reach 75 lm/W at an applied DC voltage of 8 kV and low loading current density (on the anode) of 0.03 mA/cm<sup>2</sup>. For P22, the phosphor life estimated from the current density can reach about 810 h for the CNC

cathode FEL, as opposed to 115 h for the MWCNT cathode counterpart. Our results showed that using CNC as the FE cathode material can effectively decelerate the degradation of P22 phosphors.

#### Conflict of Interests

The authors declare that there is no conflict of interests regarding the publication of this paper.

#### Authors' Contribution

Nen-Wen Pu and Kun-Ju Chung contributed equally to this work.

#### Acknowledgments

This work is sponsored by the Ministry of Science Technology, Taiwan, under Grant no. MOST-102-2221-E-606-005 and the Ministry of Economic Affairs, Taiwan, under Academic TDP no. 100-EC-17-A-07-S1-167.

## References

- [1] R. H. Fowler and L. Nordheim, "Electron emission in intense electric fields," *Proceedings of the Royal Society of London Series A*, vol. 119, no. 781, pp. 173–181, 1928.
- [2] N. S. Lee, D. S. Chung, I. T. Han et al., "Application of carbon nanotubes to field emission displays," *Diamond and Related Materials*, vol. 10, no. 2, pp. 265–270, 2001.
- [3] J. E. Jung, Y. W. Jin, J. H. Choi et al., "Fabrication of triode-type field emission displays with high-density carbon-nanotube emitter arrays," *Physica B*, vol. 323, no. 1–4, pp. 71–77, 2002.
- [4] F. G. Zeng, C. C. Zhu, W. Liu, and X. Liu, "The fabrication and operation of fully printed Carbon nanotube field emission displays," *Microelectronics Journal*, vol. 37, no. 6, pp. 495–499, 2006.
- [5] A. A. Kuznetsov, S. B. Lee, M. Zhang, R. H. Baughman, and A. A. Zakhidov, "Electron field emission from transparent multiwalled carbon nanotube sheets for inverted field emission displays," *Carbon*, vol. 48, no. 1, pp. 41–46, 2010.
- [6] Y. C. Choi, J. W. Lee, S. K. Lee et al., "The high contrast ratio and fast response time of a liquid crystal display lit by a carbon nanotube field emission backlight unit," *Nanotechnology*, vol. 19, no. 23, Article ID 235306, 2008.
- [7] Y. Zhang, S. Z. Deng, N. S. Xu, and J. Chen, "Fully sealed carbon nanotube flat-panel light source and its application as thin film transistor-liquid-crystal display backlight," *Journal of Vacuum Science and Technology B: Microelectronics and Nanometer Structures*, vol. 26, no. 3, pp. 1033–1037, 2008.
- [8] N. Y. Bae, W. M. Bae, A. N. Ha, M. Nakamoto, J. Jang, and K. C. Park, "Low-voltage driven carbon nanotube field emission lamp," *Current Applied Physics*, vol. 11, no. 4, pp. S86–S89, 2011.
- [9] H. S. Yoo, W. Y. Sung, S. J. Yoon, Y. H. Kim, and S. K. Joo, "Novel triode-type field emission arrays and appropriate driving method for flat lamp using carbon nanofibers grown by plasma enhanced chemical vapor deposition," *Japanese Journal of Applied Physics*, vol. 26, no. 7, p. 4381, 2007.
- [10] L. Wei, X. Zhang, B. Wang et al., "A stable field-emission light source with ZnO nanoemitters," *IEEE Electron Device Letters*, vol. 29, no. 5, pp. 452–455, 2008.
- [11] X.-X. Zhang and C.-C. Zhu, "Field-emission lighting tube with CNT film cathode," *Microelectronics Journal*, vol. 37, no. 11, pp. 1358–1360, 2006.
- [12] S. Wang, X. Calderon, R. Peng, E. C. Schreiber, O. Zhou, and S. Chang, "A carbon nanotube field emission multipixel X-ray array source for microradiotherapy application," *Applied Physics Letters*, vol. 98, no. 21, Article ID 213701, 2011.
- [13] H.-C. Wu, M.-J. Youh, W.-H. Lin et al., "Fabrication of double-sided field-emission light source using a mixture of carbon nanotubes and phosphor sandwiched between two electrode layers," *Carbon*, vol. 50, no. 13, pp. 4781–4786, 2012.
- [14] Y. Saito, K. Hamaguchi, R. Mizushima et al., "Field emission from carbon nanotubes and its application to cathode ray tube lighting elements," *Applied Surface Science*, vol. 146, no. 1, pp. 305–311, 1999.
- [15] J.-M. Bonard, T. Stöckli, O. Noury, and A. Châtelain, "Field emission from cylindrical carbon nanotube cathodes: possibilities for luminescent tubes," *Applied Physics Letters*, vol. 78, no. 18, pp. 2775–2777, 2001.
- [16] J. X. Huang, J. Chen, S. Z. Deng, J. C. She, and N. S. Xu, "Field-emission fluorescent lamp using carbon nanotubes on a wire-type cold cathode and a reflecting anode," *Journal of Vacuum Science and Technology B: Microelectronics and Nanometer Structures*, vol. 26, no. 5, pp. 1700–1704, 2008.
- [17] W. Fu, P. Liu, J. Tang, L. Liu, and S. Fan, "Spherical field emission cathode based on carbon nanotube paste and its application in luminescent bulbs," *Journal of Vacuum Science and Technology B*, vol. 26, no. 4, pp. 1404–1406, 2008.
- [18] J. S. Sebastian, H. C. Swart, T. A. Trottier, S. L. Jones, and P. H. Holloway, "Degradation of ZnS field-emission display phosphors during electron-beam bombardment," *Journal of Vacuum Science and Technology A: Vacuum, Surfaces and Films*, vol. 15, no. 4, pp. 2349–2353, 1997.
- [19] L. E. Tannas, *Flat-Panel Displays and CRT's*, Van Nostrand Reinhold, New York, NY, USA, 1982.
- [20] T. Hase, T. Kano, E. Nakazawa, and H. Yamamoto, "Phosphor materials for cathode-ray tubes," *Advances in Electronics and Electron Physics*, vol. 79, pp. 1819–1823, 1990.
- [21] S. Itoh, T. Kimizuka, and T. Tonegawa, "Degradation mechanism for low voltage cathodoluminescence of sulfide phosphors," *Journal of the Electrochemical Society*, vol. 136, no. 6, pp. 1819–1823, 1989.
- [22] S. Motojima, M. Kawaguchi, K. Nozaki, and H. Iwanaga, "Growth of regularly coiled carbon filaments by Ni catalyzed pyrolysis of acetylene, and their morphology and extension characteristics," *Applied Physics Letters*, vol. 56, no. 4, pp. 321–323, 1990.
- [23] L. Pan, T. Hayashida, M. Zhang, and Y. Nakayama, "Field emission properties of carbon tubule nanocoils," *Japanese Journal of Applied Physics*, vol. 40, no. 3B, pp. L235–L237, 2001.
- [24] Z. Zhang, P. He, Z. Sun et al., "Growth and field emission property of coiled carbon nanostructure using copper as catalyst," *Applied Surface Science*, vol. 256, no. 14, pp. 4417–4422, 2010.
- [25] S. Hokushin, L. Pan, Y. Konishi, H. Tanaka, and Y. Nakayama, "Field emission properties and structural changes of a stand-alone carbon nanocoil," *Japanese Journal of Applied Physics*, vol. 46, no. 23, pp. L565–L567, 2007.
- [26] W.-D. Chen, Y. Sung, C.-P. Chang, Y.-C. Chen, and M.-D. Ger, "The preparation of thermo-responsive palladium catalyst with high activity for electroless nickel deposition," *Surface and Coatings Technology*, vol. 204, no. 14, pp. 2130–2135, 2010.
- [27] Y. M. Liu, N. W. Pu, W. D. Chen et al., "Low temperature fabrication of Ni-P metallic patterns on ITO substrates utilizing inkjet printing," *Microelectronics Reliability*, vol. 52, no. 2, pp. 398–404, 2012.
- [28] R. T. K. Baker, M. A. Barber, P. S. Harris, F. S. Feates, and R. J. Waite, "Nucleation and growth of carbon deposits from the nickel catalyzed decomposition of acetylene," *Journal of Catalysis*, vol. 26, no. 1, pp. 51–62, 1972.
- [29] K. J. Chung, N. W. Pu, M. Y. Youh et al., "Improvement of field-emission-lamp characteristics using nitrogen-doped carbon nanocoils," *Diamond & Related Materials*, vol. 53, pp. 1–10, 2015.
- [30] F. Nitze, E. Abou-Hamad, and T. Wgberg, "Carbon nanotubes and helical carbon nanofibers grown by chemical vapour deposition on C60 fullerene supported Pd nanoparticles," *Carbon*, vol. 49, no. 4, pp. 1101–1107, 2011.
- [31] R. Segura, A. Tello, G. Cardenas, and P. Häberle, "Synthesis of carbon nanotubes and nanofibers by decomposition of acetylene over a SMAD palladium catalyst," *Physica Status Solidi A*, vol. 204, no. 2, pp. 513–517, 2007.

- [32] S. Hokushin, L. Pan, Y. Konishi, H. Tanaka, and Y. Nakayama, "Field emission properties and structural changes of a stand-alone carbon nanocoil," *Japanese Journal of Applied Physics, Part 2: Letters*, vol. 46, no. 20-24, pp. L565–L567, 2007.
- [33] H. C. Swart, J. S. Sebastian, T. A. Trottier, S. L. Jones, and P. H. Holloway, "Degradation of zinc sulfide phosphors under electron bombardment," *Journal of Vacuum Science and Technology A*, vol. 14, no. 3, pp. 1697–1703, 1996.

## Research Article

# Effect of Substrate Temperature on the Thermoelectric Properties of the $\text{Sb}_2\text{Te}_3$ Thin Films Deposition by Using Thermal Evaporation Method

Jyun-Min Lin,<sup>1</sup> Ying-Chung Chen,<sup>1</sup> Cheng-Fu Yang,<sup>2</sup> and Wei Chen<sup>1</sup>

<sup>1</sup>Department of Electrical Engineering, National Sun Yat-Sen University, Kaohsiung 804, Taiwan

<sup>2</sup>Department of Chemical and Materials Engineering, National University of Kaohsiung, Kaohsiung 811, Taiwan

Correspondence should be addressed to Cheng-Fu Yang; [cfyang@nuk.edu.tw](mailto:cfyang@nuk.edu.tw)

Received 13 August 2014; Revised 15 October 2014; Accepted 15 October 2014

Academic Editor: Teen-Hang Meen

Copyright © 2015 Jyun-Min Lin et al. This is an open access article distributed under the Creative Commons Attribution License, which permits unrestricted use, distribution, and reproduction in any medium, provided the original work is properly cited.

The antimony-telluride ( $\text{Sb}_2\text{Te}_3$ ) thermoelectric thin films were prepared on  $\text{SiO}_2/\text{Si}$  substrates by thermal evaporation method. The substrate temperature that ranged from room temperature to  $150^\circ\text{C}$  was adopted to deposit the  $\text{Sb}_2\text{Te}_3$  thin films. The effects of substrate temperature on the microstructures and thermoelectric properties of the  $\text{Sb}_2\text{Te}_3$  thin films were investigated. The crystal structure and surface morphology of the  $\text{Sb}_2\text{Te}_3$  thin films were characterized by X-ray diffraction analyses and field emission scanning electron microscope observation. The RT-deposited  $\text{Sb}_2\text{Te}_3$  thin films showed the amorphous phase. Te and  $\text{Sb}_2\text{Te}_3$  phases were coexisted in the  $\text{Sb}_2\text{Te}_3$ -based thin films as the substrate temperature was higher than room temperature. The average grain sizes of the  $\text{Sb}_2\text{Te}_3$ -based thin films were 39 nm, 45 nm, 62 nm, 84 nm, and 108 nm, as the substrate temperatures were  $50^\circ\text{C}$ ,  $75^\circ\text{C}$ ,  $100^\circ\text{C}$ ,  $125^\circ\text{C}$ , and  $150^\circ\text{C}$ , respectively. The Seebeck coefficients, electrical conductivity, and power factor were measured at room temperature; we had found that they were critically dependent on the substrate temperature.

## 1. Introduction

Facing the impact of the energy shortage and global warming problem, much attention to the issues of energy saving and reduction of carbon emission has been paid. The green technology is getting more and more attention, of which thermoelectric (TE) effect is one of the simplest technologies to convert energy by temperature difference and has recently attracted much attention. Thermoelectric materials can directly convert electricity from heat and vice versa. Hence, the application of thermoelectric materials is very promising for power generator and cooler [1, 2]. The energy conversion efficiency of the thermoelectric materials is judged by the figure of merit  $ZT$ ,  $ZT = (S^2\sigma/\kappa)T$ , where  $T$  is defined as absolute temperature and  $S$ ,  $\sigma$ , and  $\kappa$  are defined as Seebeck coefficient ( $\Delta V/\Delta T$ ), electrical conductivity, and thermal conductivity, respectively [3, 4]. For that, the characteristics of TE materials depend on their  $S$ ,  $\sigma$ , and  $\kappa$ , and the  $S^2\sigma$  is defined as the power factor (PF). According to the

formula, the enhancement of thermoelectric figure of merit  $ZT$  can be obtained by raising the  $S^2\sigma$  and the decrease of the thermal conductivity. Till now, the bismuth telluride- (Bi-Te-) and antimony-telluride- (Sb-Te-) based compounds are known to be the state-of-the-art thermoelectric materials for the applications near room temperature region. Furthermore, the Bi-Te- and Sb-Te-based thermoelectric materials show the highest figure of merit  $ZT$  and can be extensively utilized for the commercially available thermoelectric generators and coolers. For that, the  $\text{Sb}_2\text{Te}_3$  alloy was used as the compound to investigate its thermoelectric characteristics.

Currently, the thermoelectric devices are manufactured by sintering blocks of the materials. So far, the thermoelectric materials used in applications have all been in bulk (3D), thin film (2D), and nanowire (1D) forms. However, the figure of merit ( $ZT$ ) is low for the bulk materials. In order to improve the thermoelectric performance, the low-dimensional thermoelectric materials have been researched. Hicks and Dresselhaus had pointed out that low-dimensional

materials have better efficiency than bulk ones due to low-dimensional effects on both charge carriers and lattice waves [5]. Through the low-dimensional nanostructure, the thermoelectric materials can increase their density of states of Fermi level and enhance the phonon scattering of the materials [5]. However, it is difficult to miniaturize the thermoelectric devices by sintering blocks. Therefore, various deposition techniques have been proposed to obtain the thermoelectric thin films, such as flash evaporation [6, 7], ion-beam sputtering [8, 9], pulse laser deposition (PLD) [10, 11], sputtering [12, 13], electrochemical deposition [14, 15], metal organic chemical vapor deposition (MOCVD) [16, 17], and molecular beam epitaxy (MBE) [18, 19]. The electrochemical deposition was also a useful method to deposit thermoelectric materials in different morphologies, including thin films and nanowires [20, 21]. However, some processes need long time and expensive facilities to prepare the materials. In this paper, the thermal evaporation method is adopted to prepare  $\text{Sb}_2\text{Te}_3$  thin films, because it is an attractive technology and offers some advantages, such as lower fabricating expenses and short processing time. In this work, the influence of substrate temperature on the microstructures and thermoelectric properties of the thermal evaporated thin films on silicon substrates was investigated.

## 2. Experimental

The p-type (1 0 0) silicon (Si) substrates were cleaned with standard RCA cleaning processes to remove the native oxide and particles. After that, a 400 nm thermally grown silicon dioxide ( $\text{SiO}_2$ ) layer was deposited on the Si substrate by atmospheric pressure chemical vapor deposition (APCVD) method. Then, the thermoelectric thin films were deposited on  $\text{SiO}_2/\text{Si}$  substrates by the thermal evaporation method. The high-purity (99.99%)  $\text{Sb}_2\text{Te}_3$  powder was used as evaporation source and evaporated from a tungsten boat. The size of the powders was in the range of 1 mm–10 mm, which was obtained by smashing the  $\text{Sb}_2\text{Te}_3$  ingot. During the deposition process, a 60 A current was applied to the tungsten boat to evaporate the  $\text{Sb}_2\text{Te}_3$  powder. The deposition rate of the  $\text{Sb}_2\text{Te}_3$  thin films was estimated to be 16 Å/s. In this study, the thermoelectric thin films were prepared at the substrate temperature that ranged from room temperature to 150°C with chamber pressure of about  $3.75 \times 10^{-5}$  torr. As we know, the substrate temperature is the most important factor to affect the characteristics of the  $\text{Sb}_2\text{Te}_3$  thin films, including thickness, crystalline structure, grain size, and pore ratio. For that, the substrate temperature will be the most important factor to affect the electrical characteristics of the  $\text{Sb}_2\text{Te}_3$  thin films. As the substrate temperature was higher than 150°C, the  $\text{Sb}_2\text{Te}_3$  thin films were hard to deposit on the Si substrates, for the fact that the substrate temperature was ranged from room temperature to 150°C. The thickness of the  $\text{Sb}_2\text{Te}_3$  thin films was approximately 0.4  $\mu\text{m}$ , independent of the substrate temperature.

The surface morphologies, deposition rate, and the thickness of thermoelectric thin films were observed by scanning electron microscopy (FE-SEM, JEOL JSM6700) with an

accelerating voltage of 10 kV. The crystalline structures of the thermoelectric thin films were determined by means of X-ray diffraction (XRD) (Cu-K $\alpha$ , Bruker D8). The diffraction angles ( $2\theta$ ) of thermoelectric  $\text{Sb}_2\text{Te}_3$  thin films were revealed by scanning between 20° and 60° at the speed of 0.05° per second. For the investigation of thermoelectric properties, Seebeck coefficient ( $S$ ) and electrical conductivity ( $\sigma$ ) were measured at the room temperature. The Seebeck coefficient could be obtained by measuring the resulted Seebeck voltage as applying a temperature gradient across the sample, in which, the data was acquired by a Keithley 2700 system. As measured temperature was changed in a small range, for example, approximately 5°C, the Seebeck coefficient of the device under test (DUT) could be considered as a fixed value. Because the output voltage was not a steady value within the measuring time, the calculated Seebeck coefficient comprising the measured temperature gradient and output voltage could nearly be the constant values. During the measurement process, we used 10 seconds as the measurement time and ten Seebeck coefficient values could be obtained. Then, the average value of the ten data was taken as Seebeck coefficient value. The electrical conductivity of the specimens was measured by a conventional four-point probe method at room temperature. From  $S$  and  $\sigma$ , the thermoelectric power factor ( $S^2\sigma$ ) was obtained.

## 3. Results and Discussion

Figure 1 shows the X-ray diffraction patterns of the standard  $\text{Sb}_2\text{Te}_3$  alloy from the JCPD card and the raw  $\text{Sb}_2\text{Te}_3$  alloy powder. The XRD diffraction peaks of the raw alloy powder were coincided with those of JCPDS card for  $\text{Sb}_2\text{Te}_3$  alloy. This result indicates that the used alloy material for evaporation was single phase  $\text{Sb}_2\text{Te}_3$  compound. For the raw  $\text{Sb}_2\text{Te}_3$  alloy powder, four major diffraction peaks of 28.24°, 38.29°, 42.35°, and 44.58°, which are corresponding to (0 1 5), (1 0 10), (1 1 0), and (0 0 15) diffraction planes, were observed in Figure 1. Meanwhile, the raw  $\text{Sb}_2\text{Te}_3$  alloy powder shows a preferred orientation corresponding to the (0 1 5) diffraction plane.

Figure 2 shows the X-ray diffraction patterns of the  $\text{Sb}_2\text{Te}_3$  thin films deposited at various substrate temperatures. The crystalline properties of the  $\text{Sb}_2\text{Te}_3$  thin films are apparently affected by the substrate temperature. The diffraction peaks in Figure 2 show that as the substrate temperature was changed; different alloy compounds were deposited during the evaporation process. As room temperature (RT) was used to deposit thin films, only the amorphous phase was observed. The reason is that the atoms did not have enough energy to proliferate and cluster on the substrate at room temperature. As the substrate temperature was higher than RT, the Te ((1 0 1) and (0 1 2)) and  $\text{Sb}_2\text{Te}_3$  ((0 1 5), (1 0 10), (1 1 0), and (0 0 15)) phases were really observed in the XRD patterns. As the substrate temperature was increased from 50°C to 100°C, the diffraction intensities of the Te and  $\text{Sb}_2\text{Te}_3$  phases increased with substrate temperature, showing that the crystallinity of the thin films was improved.

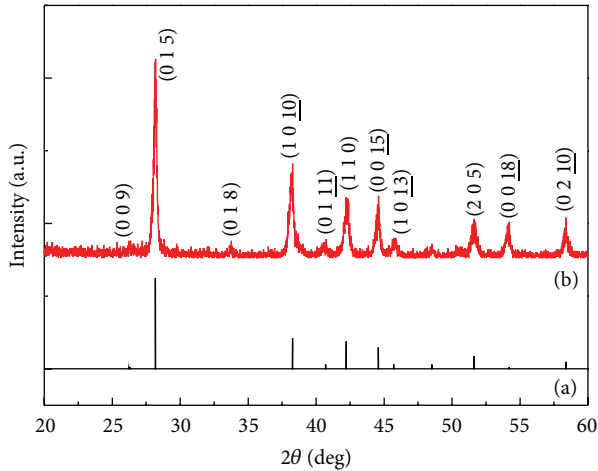


FIGURE 1: XRD patterns of (a) JCPDS card for  $\text{Sb}_2\text{Te}_3$  material and (b) raw  $\text{Sb}_2\text{Te}_3$  alloy powder.

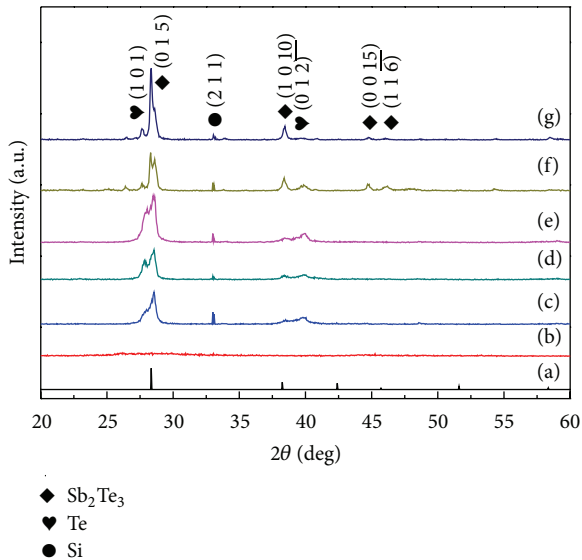


FIGURE 2: XRD patterns of the  $\text{Sb}_2\text{Te}_3$  thin films deposited on  $\text{SiO}_2/\text{Si}$  substrates at various substrate temperatures: (a) JCPDS card, (b) room temperature, (c)  $50^\circ\text{C}$ , (d)  $75^\circ\text{C}$ , (e)  $100^\circ\text{C}$ , (f)  $125^\circ\text{C}$ , and (g)  $150^\circ\text{C}$ , respectively.

As  $125^\circ\text{C}$  was used as substrate temperature, the diffraction intensity of Te phase critically decreased and (0 1 5) plane of  $\text{Sb}_2\text{Te}_3$  phase showed a splitting peak; as  $150^\circ\text{C}$  was used as substrate temperature, the diffraction intensity of (0 1 5) plane of  $\text{Sb}_2\text{Te}_3$  phase critically increased and the full width at half maximum (FWHM) value of (0 1 5) plane decreased and a preferred orientation of (0 1 5) existed. The FWHM values of (0 1 5) plane were  $0.525^\circ$ ,  $0.512^\circ$ ,  $0.478^\circ$ ,  $0.385^\circ$ , and  $0.298^\circ$  as the substrate temperatures were  $50^\circ\text{C}$ ,  $75^\circ\text{C}$ ,  $100^\circ\text{C}$ ,  $125^\circ\text{C}$ , and  $150^\circ\text{C}$ , respectively. However, as the substrate temperature was higher than  $150^\circ\text{C}$ , the raw  $\text{Sb}_2\text{Te}_3$  material was hard to deposit on the  $\text{SiO}_2/\text{Si}$  substrates. In this study, the optimum  $\text{Sb}_2\text{Te}_3$  (0 1 5) plane of thin films was obtained at the substrate temperature of  $150^\circ\text{C}$ . The XRD

patterns shown in Figure 2 also suggest that the substrate temperature had large effect on the characteristics of the deposited  $\text{Sb}_2\text{Te}_3$  thin films.

The SEM top-viewed images of the  $\text{Sb}_2\text{Te}_3$  thin films deposited at various substrate temperatures are shown in Figure 3. As R.T. was used as substrate temperature, a continuous and smooth surface morphology was obtained; the deposited thin films with amorphous phase are the reason to cause this result. The figure also shows that as the substrate temperature was raised, the grain sizes increased with increasing substrate temperature. The average grain sizes were 39 nm, 45 nm, 62 nm, 84 nm, and 108 nm, as the substrate temperature was  $50^\circ\text{C}$ ,  $75^\circ\text{C}$ ,  $100^\circ\text{C}$ ,  $125^\circ\text{C}$ , and  $150^\circ\text{C}$ , respectively. Those results prove that the polycrystalline structure, as XRD patterns in Figure 2 show, was obtained as the substrate temperature was equal to and higher than  $50^\circ\text{C}$ . Figure 4 shows the SEM cross-sectional microstructures of the deposited  $\text{Sb}_2\text{Te}_3$  thin films under various substrate temperatures. As the substrate temperature was changed from R.T. to  $100^\circ\text{C}$ , the cross-sections of the deposited  $\text{Sb}_2\text{Te}_3$  thin films showed a flat morphology and their thickness was around 400 nm; as the substrate temperature was higher than  $100^\circ\text{C}$ , the thickness was decreased and the size of pores increased with increasing substrate temperature. The increase in the size of pores is caused by the fact that the large grains grow at the expense of small ones, which result in the formation of new and larger voids where the small grains are originally located. As Figure 4 shows, the pores mainly grow in the vertical direction of the  $\text{Sb}_2\text{Te}_3$  thin films as higher substrate temperature is used. As we know, the main composition of pores is air, which has very low conductivity. For that, even the electrical conductivity characteristic is mainly determined by the lateral structure of the  $\text{Sb}_2\text{Te}_3$  thin films, the decrease in the conductivity of the  $\text{Sb}_2\text{Te}_3$  thin films with increasing in the size of pores is expectable.

Figure 5 shows the variations of the electrical conductivity with various substrate temperatures. As the substrate temperature increased, the electrical conductivity of the deposited  $\text{Sb}_2\text{Te}_3$  thin films first increased, reached a maximum at  $100^\circ\text{C}$ , and then decreased. The lower electrical conductivity of the RT-deposited thin films could be attributed to the poor crystallization, as confirmed by XRD analysis in Figure 2 and SEM surface observation in Figure 3. The electrical conductivity increased from  $2.14 \times 10^2 \text{ S/cm}$  to  $6.81 \times 10^2 \text{ S/cm}$  as the substrate temperature increased from R.T. to  $100^\circ\text{C}$ . With an increased substrate temperature from  $100^\circ\text{C}$  to  $150^\circ\text{C}$ , the electrical conductivity decreased from  $6.81 \times 10^2$  to  $3.11 \times 10^2 \text{ S/cm}$ . The electrical conductivity of the  $\text{Sb}_2\text{Te}_3$  thin films was enhanced as the substrate temperature is higher than RT. The improvement in the crystallization, as proven by XRD analysis in Figure 2 and SEM surface observation in Figure 3, is believed as the reason. As the substrate temperature is higher than  $100^\circ\text{C}$ , the pores increased with increasing temperature. Also, this is the reason to cause the decrease in conductivity.

Figure 6 shows the variation of the Seebeck coefficient with different substrate temperature. The results show that all samples have a positive Seebeck coefficient, which means that

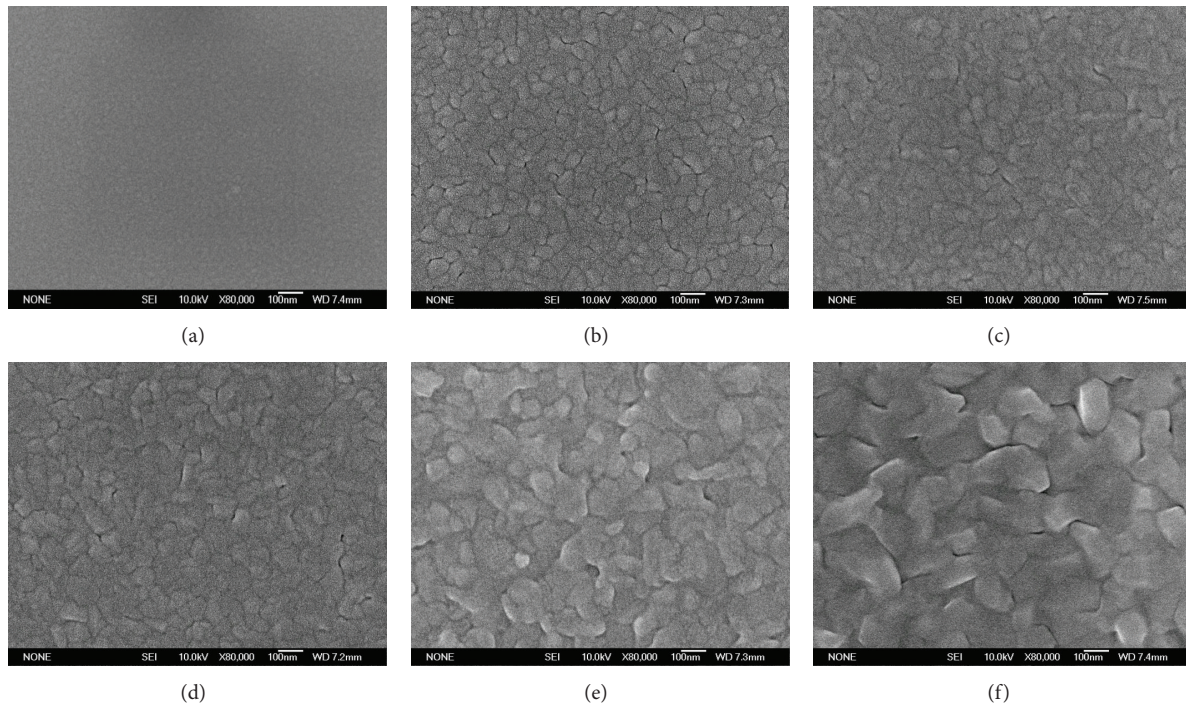


FIGURE 3: FE-SEM top-viewed morphologies of the  $\text{Sb}_2\text{Te}_3$  thin films deposited under various substrate temperatures: (a) room temperature, (b)  $50^\circ\text{C}$ , (c)  $75^\circ\text{C}$ , (d)  $100^\circ\text{C}$ , (e)  $125^\circ\text{C}$ , and (f)  $150^\circ\text{C}$ , respectively.

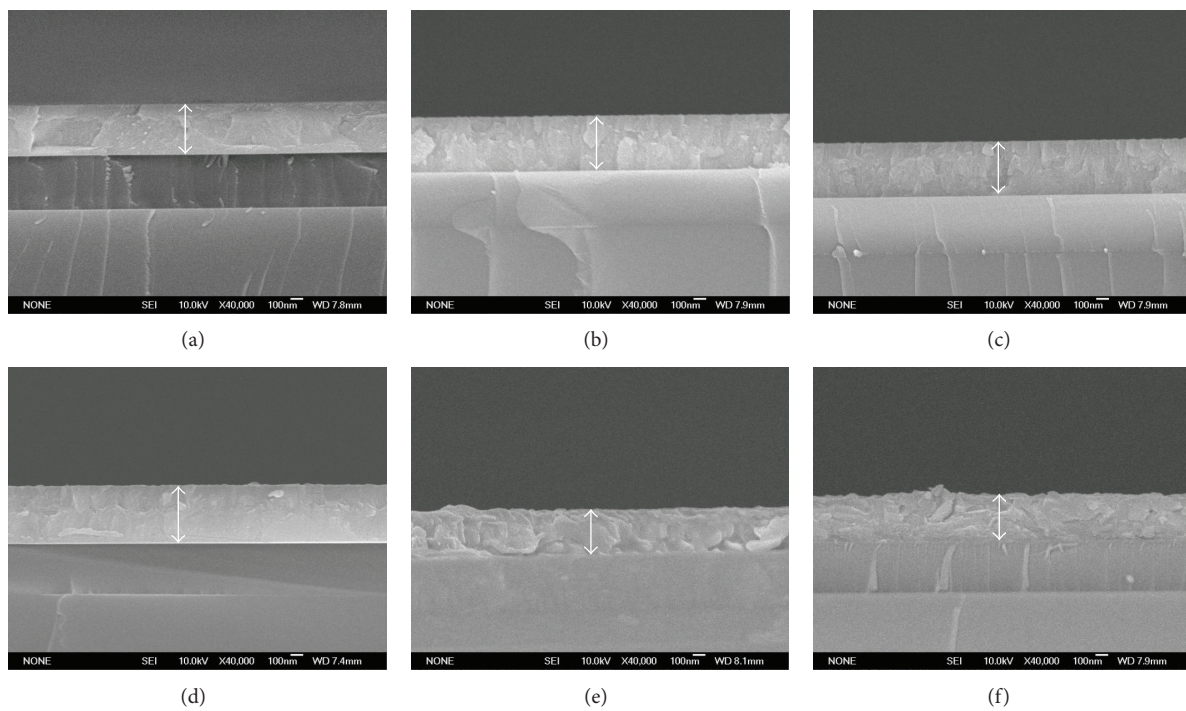


FIGURE 4: FE-SEM cross-sectional morphologies of the  $\text{Sb}_2\text{Te}_3$  thin films deposited under various substrate temperatures: (a) room temperature, (b)  $50^\circ\text{C}$ , (c)  $75^\circ\text{C}$ , (d)  $100^\circ\text{C}$ , (e)  $125^\circ\text{C}$ , and (f)  $150^\circ\text{C}$ , respectively.

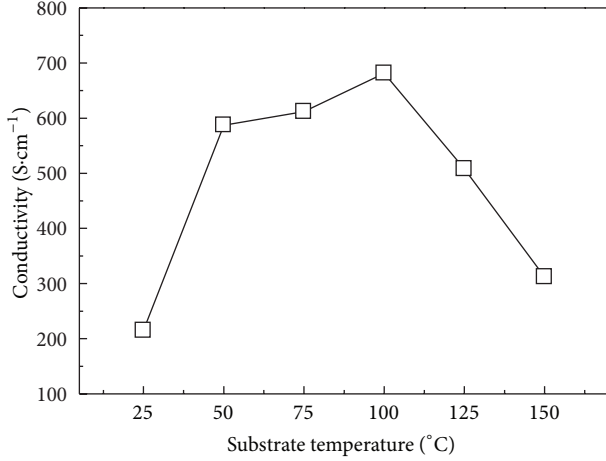


FIGURE 5: Variations of electrical conductivity for  $\text{Sb}_2\text{Te}_3$  thin films deposited at various substrate temperatures.

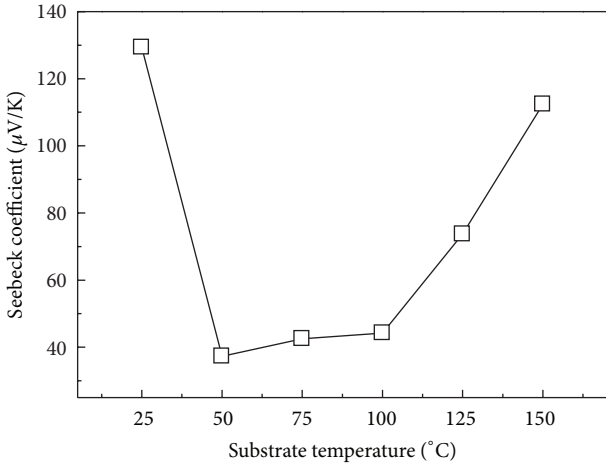


FIGURE 6: Variations of Seebeck coefficient for  $\text{Sb}_2\text{Te}_3$  thin films deposited at various substrate temperatures.

the  $\text{Sb}_2\text{Te}_3$  thin films are p-type semiconductors. According to the results, the samples deposited at R.T. show a large Seebeck coefficient ( $\sim 129.3 \mu\text{V/K}$ ). The Seebeck coefficient decreased from  $129.3 \mu\text{V/K}$  to  $37.3 \mu\text{V/K}$  as the substrate temperature varied from R.T. to  $50^\circ\text{C}$ . After that, the Seebeck coefficient was enhanced as the substrate temperature increased from  $50$  to  $150^\circ\text{C}$ . The sample deposited at  $150^\circ\text{C}$  exhibited the large Seebeck coefficient of  $112.4 \mu\text{V/K}$ . It is well known that the Seebeck coefficient is closely related to the carrier concentration. In the case of p-type semiconductor crystals obeying Boltzmann statistics, the Seebeck coefficient ( $S$ ) is given by the following equation [22]:

$$S = \pm \frac{k_B}{e} \left( (\gamma + 2) + \ln \frac{2(2\pi m^* < k_B T)^{3/2}}{h^3 n} \right), \quad (1)$$

$$\sigma = ne\mu, \quad (2)$$

where  $k_B$  is Boltzmann's constant,  $e$  is the electron charge,  $r$  is the scattering factor,  $m^*$  is effective mass,  $h$  is Planck's

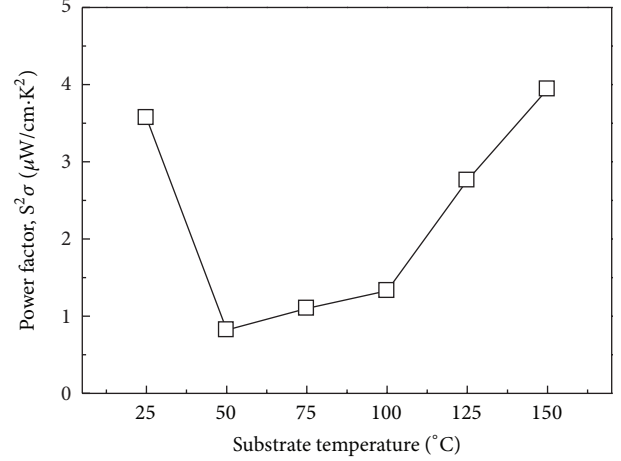


FIGURE 7: Variations of power factor for  $\text{Sb}_2\text{Te}_3$  thin films deposited at various substrate temperatures.

constant,  $n$  is the carrier concentration, and  $\mu$  is the carrier mobility, respectively. From (1), the Seebeck coefficient was found to be inversely proportional to the logarithmic scale of the carrier concentration. From (2) the conductivity is proportional to the carrier concentration, which may be caused by decreasing the number of defects. For that, the Seebeck coefficient of the thermoelectric thin films might be enhanced owing to the reduction of the conductivity. The results in Figures 5 and 6 prove that the Seebeck coefficient is inversely proportional to the electrical conductivity.

According to the results of Seebeck coefficient and electrical conductivity, the power factor can be calculated. The power factor is a significant thermoelectric parameter, which determines the performance of the thermoelectric converter. Figure 7 shows the power factors obtained for the  $\text{Sb}_2\text{Te}_3$  thin films deposited at various substrate temperatures. Figure 7 shows that the power factor first drastically decreased as the substrate temperature increased from R.T. to  $50^\circ\text{C}$ ; then it increased as the substrate temperature was further increased from  $50^\circ\text{C}$  to  $150^\circ\text{C}$ . The thermoelectric properties for  $\text{Sb}_2\text{Te}_3$  thin films deposited at various substrate temperatures are summarized in Table 1. Table 1 shows an important result that we can use the cheap evaporation equipment to deposit the  $\text{Sb}_2\text{Te}_3$  thin films with high Seebeck coefficient and acceptable power factor. It also shows that the optimized Seebeck coefficient and power factor of the  $\text{Sb}_2\text{Te}_3$  p-type thin films were found to be about  $112.4 \mu\text{V/K}$  and  $3.94 \mu\text{W/cm}\cdot\text{K}^2$  at the substrate temperature of  $150^\circ\text{C}$ , respectively.

#### 4. Conclusion

In this study, a thermal evaporation method was successfully utilized for the deposition of the  $\text{Sb}_2\text{Te}_3$ -based thermoelectric thin films from R.T. to  $150^\circ\text{C}$  on  $\text{SiO}_2/\text{Si}$  substrates with low-cost. We found that as the substrate temperature was higher than  $150^\circ\text{C}$ , the raw  $\text{Sb}_2\text{Te}_3$  material was hard to deposit on the  $\text{SiO}_2/\text{Si}$  substrates. The electrical conductivity increased from  $2.14 \times 10^2 \text{ S/cm}$  to  $6.81 \times 10^2 \text{ S/cm}$  as the substrate

TABLE 1: Thermoelectric properties of the  $\text{Sb}_2\text{Te}_3$  thin films deposited at various substrate temperatures.

| Substrate temperature (°C) | Seebeck coefficient ( $\mu\text{W}/\text{K}$ ) | Conductivity ( $\text{S}\cdot\text{cm}^{-1}$ ) | Power factor ( $\mu\text{W}/\text{cm}\cdot\text{K}^2$ ) |
|----------------------------|--|--|---|
| R.T.                       | 129.3  | 214.75   | 3.57  |
| 50                         | 37.3   | 587.30   | 0.80  |
| 75                         | 42.5   | 611.80   | 1.10  |
| 100                        | 44.2   | 681.57   | 1.33  |
| 125                        | 73.7   | 508.20   | 2.76  |
| 150                        | 112.4  | 311.99   | 3.94  |

temperature increased from R.T. to 100°C. With an increased substrate temperature from 100°C to 150°C, the electrical conductivity decreased from  $6.81 \times 10^2$  to  $3.11 \times 10^2$  S/cm. The Seebeck coefficient decreased from 129.3  $\mu\text{V}/\text{K}$  to 37.3  $\mu\text{V}/\text{K}$  as the substrate temperature varied from R.T. to 50°C. After that, the Seebeck coefficient was enhanced as the substrate temperature increased from 50 to 150°C. As the substrate temperature increased to 150°C, the Seebeck coefficient and power factor of p-type  $\text{Sb}_2\text{Te}_3$ -based thin films were found to be about 112.4  $\mu\text{V}/\text{K}$  and 3.94  $\mu\text{W}/\text{cm}\cdot\text{K}^2$ , respectively.

## Conflict of Interests

The authors declare that there is no conflict of interests regarding the publication of this paper.

## Acknowledgment

The authors gratefully acknowledge the financial support from the Contract of MOST 103-2221-E-110-075-MY2.

## References

- [1] W. L. Luan and S. T. Tu, "Recent development of thermoelectric generation," *Chinese Science Bulletin*, vol. 49, pp. 1-8, 2004.
- [2] K. H. Lee and O. J. Kim, "Analysis on the cooling performance of the thermoelectric micro-cooler," *International Journal of Heat and Mass Transfer*, vol. 50, no. 9-10, pp. 1982-1992, 2007.
- [3] D. M. Rowe, *Thermoelectrics Handbook: Macro to Nano*, CRC & Taylor & Francis, Boca Raton, Fla, USA, 2006.
- [4] T. M. Tritt, "Holey and unholey semiconductors," *Science*, vol. 283, no. 5403, pp. 804-805, 1999.
- [5] L. D. Hicks and M. S. Dresselhaus, "Effect of quantum-well structures on the thermoelectric figure of merit," *Physical Review B*, vol. 47, no. 19, pp. 12727-12731, 1993.
- [6] A. Foucaran, A. Sackda, A. Giani, F. Pascal-Delannoy, and A. Boyer, "Flash evaporated layers of  $(\text{Bi}_2\text{Te}_3\text{-Bi}_2\text{Se}_3)(\text{N})$  and  $(\text{Bi}_2\text{Te}_3\text{-Sb}_2\text{Te}_3)(\text{P})$ ," *Materials Science and Engineering B*, vol. 52, no. 2-3, pp. 154-161, 1998.
- [7] M. Takashiri, T. Shirakawa, K. Miyazaki, and H. Tsukamoto, "Fabrication and characterization of bismuth-telluride-based alloy thin film thermoelectric generators by flash evaporation method," *Sensors and Actuators A*, vol. 138, no. 2, pp. 329-334, 2007.
- [8] H. Noro, K. Sato, and H. Kagechika, "The thermoelectric properties and crystallography of Bi-Sb-Te-Se thin films grown by ion beam sputtering," *Journal of Applied Physics*, vol. 73, no. 3, pp. 1252-1260, 1993.
- [9] P. Fan, Z. H. Zheng, G. X. Liang, D. P. Zhang, and X. M. Cai, "Thermoelectric characterization of ion beam sputtered  $\text{Sb}_2\text{Te}_3$  thin films," *Journal of Alloys and Compounds*, vol. 505, no. 1, pp. 278-280, 2010.
- [10] R. S. Makala, K. Jagannadham, and B. C. Sales, "Pulsed laser deposition of  $\text{Bi}_2\text{Te}_3$ -based thermoelectric thin films," *Journal of Applied Physics*, vol. 94, no. 6, pp. 3907-3918, 2003.
- [11] H. Obara, S. Higomo, M. Ohta, A. Yamamoto, K. Ueno, and T. Iida, "Thermoelectric properties of  $\text{Bi}_2\text{Te}_3$ -based thin films with fine grains fabricated by pulsed laser deposition," *Japanese Journal of Applied Physics*, vol. 48, no. 8, Article ID 085506, 2009.
- [12] H. Huang, W.-L. Luan, and S.-T. Tu, "Influence of annealing on thermoelectric properties of bismuth telluride films grown via radio frequency magnetron sputtering," *Thin Solid Films*, vol. 517, no. 13, pp. 3731-3734, 2009.
- [13] B. Fang, Z. Zeng, X. Yan, and Z. Hu, "Effects of annealing on thermoelectric properties of  $\text{Sb}_2\text{Te}_3$  thin films prepared by radio frequency magnetron sputtering," *Journal of Materials Science: Materials in Electronics*, vol. 24, no. 4, pp. 1105-1111, 2013.
- [14] F. Xiao, C. Hangarter, B. Yoo, Y. Rheem, K.-H. Lee, and N. V. Myung, "Recent progress in electrodeposition of thermoelectric thin films and nanostructures," *Electrochimica Acta*, vol. 53, no. 28, pp. 8103-8117, 2008.
- [15] Y. Ma, E. Ahlberg, Y. Sun, B. B. Iversen, and A. E. C. Palmqvist, "Thermoelectric characteristics of electrochemically deposited  $\text{Bi}_2\text{Te}_3$  and  $\text{Sb}_2\text{Te}_3$  thin films of relevance to multilayer preparation," *Journal of the Electrochemical Society*, vol. 159, no. 2, pp. D50-D58, 2012.
- [16] A. Giani, A. Boulouz, F. Pascal-Delannoy, A. Foucaran, E. Charles, and A. Boyer, "Growth of  $\text{Bi}_2\text{Te}_3$  and  $\text{Sb}_2\text{Te}_3$  thin films by MOCVD," *Materials Science and Engineering B: Solid-State Materials for Advanced Technology*, vol. 64, no. 1, pp. 19-24, 1999.
- [17] A. Giani, A. Boulouz, F. Pascal-Delannoy et al., "Electrical and thermoelectrical properties of  $\text{Sb}_2\text{Te}_3$  prepared by the metal-organic chemical vapor deposition technique," *Journal of Materials Science Letters*, vol. 18, no. 7, pp. 541-543, 1999.
- [18] H. Cao, R. Venkatasubramanian, C. Liu et al., "Topological insulator  $\text{Bi}_2\text{Te}_3$  films synthesized by metal organic chemical vapor deposition," *Applied Physics Letters*, vol. 101, no. 16, Article ID 162104, 2012.
- [19] Y. Kim, A. Divenere, G. K. L. Wong, J. B. Ketterson, S. Cho, and J. R. Meyer, "Structural and thermoelectric transport properties of  $\text{Sb}_2\text{Te}_3$  thin films grown by molecular beam epitaxy," *Journal of Applied Physics*, vol. 91, no. 2, pp. 715-718, 2002.
- [20] Y. Jia, D. Yang, B. Luo, S. Liu, M. O. Tade, and L. Zhi, "One-pot synthesis of Bi-Ni nanowire and nanocable arrays by coelectrodeposition approach," *Nanoscale Research Letters*, vol. 7, article 130, 2012.
- [21] C.-G. Kuo, Y.-T. Hsieh, C.-F. Yang, C.-H. Huang, and C.-Y. Yen, "Growth of anodic aluminum oxide templates and the application in fabrication of the  $\text{BiSbTe}$ -based thermoelectric nanowires," *International Journal of Photoenergy*, vol. 2014, Article ID 978184, 7 pages, 2014.
- [22] G. S. Nolas, J. Sharp, and H. J. Goldsmid, *Thermoelectrics: Basic Principles and New Materials Developments*, Springer, Berlin, Germany, 2001.

## Review Article

# Surface Patterning of PEDOT:PSS by Photolithography for Organic Electronic Devices

**Shihong Ouyang, Yingtao Xie, Dongping Wang, Dalong Zhu, Xin Xu, Te Tan, and Hon Hang Fong**

*National Engineering Lab for TFT-LCD Materials and Technologies, Department of Electronic Engineering, Shanghai Jiao Tong University, Shanghai 200240, China*

Correspondence should be addressed to Hon Hang Fong; [hhfong@sjtu.edu.cn](mailto:hhfong@sjtu.edu.cn)

Received 25 July 2014; Accepted 23 December 2014

Academic Editor: Teen-Hang Meen

Copyright © 2015 Shihong Ouyang et al. This is an open access article distributed under the Creative Commons Attribution License, which permits unrestricted use, distribution, and reproduction in any medium, provided the original work is properly cited.

Along with the development of organic electronics, conductive polymer of PEDOT:PSS has been attracting more and more attention because they possess various novel electrical, optical, and mechanical properties, which render them useful in modern organic optoelectronic devices. Due to its organic nature, it is lightweight and can be fabricated into flexible devices. For better device processing and integrating, it is essential to tune their surface morphologies, and photolithography is the best choice at present. In this paper, current PEDOT:PSS patterning approaches using photolithography are reviewed, and some of our works are also briefly introduced. Appropriate photolithographic patterning process for PEDOT:PSS will enable its application in future organic electronics.

## 1. Introduction

Organic electronics is a fast developing branch of modern science and technology. It has received enormous attention as a technology platform that enables lightweight, inexpensive, mechanically flexible and large-scale devices by exploiting the unique properties of organic materials. Devices such as organic light emitting diodes (OLEDs) [1], organic thin film transistors (OTFTs) [2, 3], organic solar cell [4, 5], and sensors [6, 7] have been demonstrated, and tremendous progress in the performance was realized through the past two decades.

Along with the development of organic electronics, commercially available poly(3,4-ethylenedioxythiophene):poly(styrenesulfonate) (PEDOT:PSS) is emerging as a promising material for its electrical, optical, and mechanical property [8]. PEDOT:PSS is a flexible, transparent, and intrinsically conductive polymer which can reach a high conductivity above 1000 S/cm and has a high transmission above 90% in visible spectrum [9, 10]. It is also biocompatible and has high chemical stability. As the commonly used indium tin oxide (ITO) is brittle and will lose its conductivity during bending, PEDOT:PSS is much suitable for flexible applications. Compared with other materials like carbon

nanotubes, graphene, silver nanowires, PEDOT:PSS is low-cost and can be easily deposited onto various substrates via spin-coating or printing. Moreover, PEDOT:PSS has a high work function of about 5.2 eV, which is beneficial for charge injection [1]. Due to its property, PEDOT:PSS found various applications and exhibited good performance in organic electronics including OLEDs [1, 11, 12], OTFT [2, 3], OPV [4], batteries and bioelectronics [6, 7], and so forth.

For practical applications, it is essential to develop general patterning procedures for integrating PEDOT:PSS into microscale devices. However, micropatterning and processing of organic materials for electronic and optoelectronic systems remain a challenging issue to be addressed. Organic materials, including small molecular and polymer that can be dissolved in water or organic solvents, are usually mechanically soft and chemically sensitive. Their surface morphology and electrical property will be adversely influenced during the patterning processes. Thus, it has stimulated numerous attempts and approaches in different micro- and nanopatterning techniques for making patterned structures with fine features. Ink-jet printing involves a modified inkjet or bubble jet printer that delivers small droplets of PEDOT:PSS to selected places on the substrate [13]. It is a directly writing

approach without any mask, and its material utilization is very high. However, it has certain resolution limitations (10–20  $\mu\text{m}$ ) as well as problems with resulting film uniformity. For imprint technique [14], it can achieve extremely high resolution possibilities ( $\sim 10$  nm) using a nanostructured mold. However, due to its complexity, imprint technique still remains on the research laboratory scale level. Furthermore, for the two aforementioned methods, fabrication of multi-layer devices is exceptionally challenging, and they require the use of new equipment. Photolithography, in contrast, remains the most attractive thin film patterning technique for the patterning of inorganic electronic materials to date in modern silicon-based semiconductor industry. It uses UV radiation to change the solubility of light-sensitive imaging materials in certain solutions, and the patterned imaging materials are used as a contact mask to pattern the electronic materials. However, the techniques used in the mature and entrenched industry of silicon processing have made little impact in patterning of PEDOT:PSS which is mainly due to a lack of chemical compatibility. Overcoming these incompatibilities promises a breakthrough in the application of PEDOT:PSS since it would provide for massively parallel output along with process knowledge and equipment already available from a very successful silicon industry.

In this paper, photolithographic patterning approaches of PEDOT:PSS are reviewed, and our relevant works are also briefly introduced. Using appropriate materials and processes, fine PEDOT:PSS patterns are achieved by photolithography and are applied into various organic electronics devices. These results indicate the promising applications of PEDOT:PSS in future organic electronics devices.

## 2. Traditional Photolithography for PEDOT:PSS Patterning

Photolithography has many advantages, including ultrahigh resolution ability, straightforward scaling to large area substrates, availability of a broad basis of equipment and expertise, and the high throughput associated with its inherently parallel nature. As photolithography is widely used, it will be favorable to still use materials and facilities of traditional photolithography to pattern organic material of PEDOT:PSS, especially for cost concern from industry. In spite of its technical advantages, conventional photolithography has not been recognized as a suitable technique for patterning PEDOT:PSS. It is presently hindered by concerns of chemical deterioration upon exposure to process materials for photolithography. Specifically, PEDOT:PSS films are damaged during the photoresist deposition, development, and removal steps due to interaction with aggressive chemical reagents, especially the aqueous alkaline solutions, which are standard developers in conventional photolithography. Moreover, due to the acidity of PEDOT:PSS films, the cross-linking of traditional acid-sensitive photoresists is adversely affected. For positive-tone photoresist, acidic PEDOT:PSS films cause uncontrolled decomposition. For negative-tone photoresist, the resist films are cross-linked without UV radiation, and residuals are left on the surface. Accordingly, various practical

photolithographic approaches have been demonstrated to minimize or eliminate damage by careful choice of processes and relevant materials. These efforts include the utilization of physical lift-off processes and the employment of protective interlayers between PEDOT:PSS and photoresist films during etching.

In lift-off processes, shown in Figures 1(a)–1(e), photoresist is first spin-coated and patterned on a substrate, and PEDOT:PSS to be patterned are subsequently deposited on it. Appropriate solvents are used to dissolve parts of photoresist, removing PEDOT:PSS film that was deposited on it. By coating PEDOT:PSS on patterned photoresist and then performing lift-off, exposure of UV radiation and alkaline developer was prohibited, and there was also less contamination on the surface, which will be very important for ensuring good performance of electronics devices. Chan et al. used positive photoresist to perform these processes [15] and achieved micrometer-scale patterns. As positive photoresist is usually acidic sensitive and PEDOT:PSS is acidic, there is a risk that photoresist is decomposed by PEDOT:PSS solution during its spin coating. Processes like hard baking of the resist patterns may be utilized to prevent the decomposition.

Leem et al. and Huang et al. used negative photoresist SU8 [16, 17], as shown in Figure 2. PEDOT:PSS can be spin-coated either before or after UV exposure, corresponding to route 1 and route 2 in Figure 2. Using developer of propylene glycol monomethyl ether acetate (PGMEA), unexposed parts were removed, leaving PEDOT:PSS patterns. As it is very hard to remove UV exposed SU8, cross-linked resists were left beneath PEDOT:PSS. For devices with complex structures, this will be inconvenient.

For aforementioned processes, solvents were used to remove parts of photoresist, and this may impact PEDOT:PSS films. Therefore, Takamatsu et al. and Defranco et al. performed a dry lift-off process with parylene [18, 19], as shown in Figure 3. PEDOT:PSS was spin-coated on patterned parylene, and parylene films were mechanically delaminated, avoiding the contact of solvents with PEDOT:PSS. Parylene is a chemical vapor deposited (CVD) polymer and nearly inert (resist solvents, strong acids and bases), which is useful as a barrier layer in electronic devices. It is deposited near room temperature and can be applied on chemically sensitive materials without damaging them. Most importantly, parylene has conformal and pinhole-free coating, and it shows relatively weak adhesion to substrate, which makes it easily peeled off.

For lift-off of inorganic materials, the undercut profile at the edges of patterned photoresist will ensure a discontinuous film, which results in successful lift-off, as shown in Figures 4(a) and 4(b). For a spin-coated PEDOT:PSS, however, the film is generally continuous across the edges of the patterned photoresist, shown in Figure 4(c), and this will make a rough edge of PEDOT:PSS film after peeling-off. Moreover, there may be sharp peaks at the edge, shown in Figure 4(d), which may greatly influence the device performance.

In traditional etching processes for inorganic materials, photoresist is spin-coated on the film to be patterned. After exposure and developing, photoresist patterns are formed and used as a contact mask for later etching. Finally,

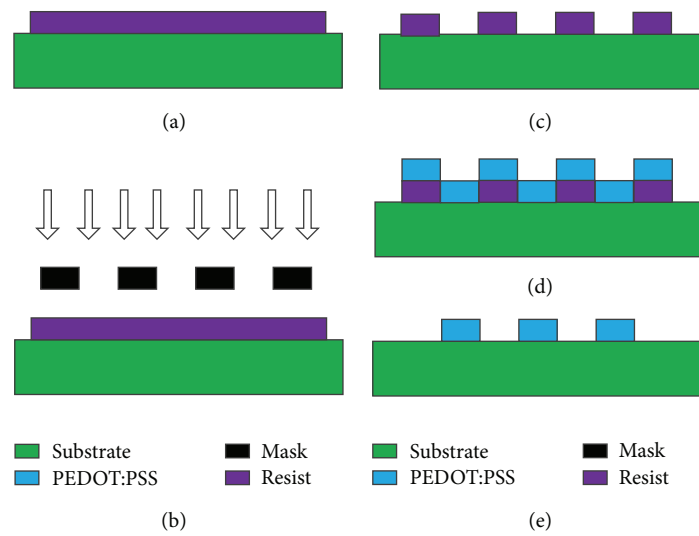


FIGURE 1: Lift-off processes of photolithographic patterning of PEDOT:PSS. Photoresist was first spin-coated (a) and patterned (b), (c) on a substrate. Then, PEDOT:PSS was subsequently deposited (d). After lift-off of left resist, PEDOT:PSS patterns are left on the substrate (e).

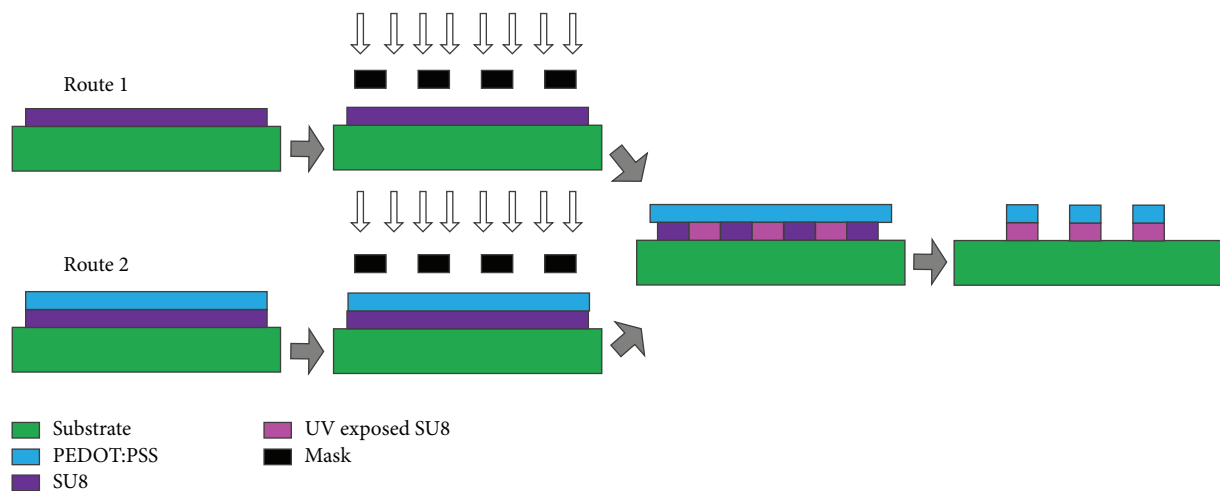


FIGURE 2: Photolithographic patterning of PEDOT:PSS using SU8. Here are two routes, in which PEDOT:PSS can be deposited either before or after UV exposure. After developing in PGMEA, PEDOT:PSS patterns are left on cross-linked SU8.

the photoresist is stripped off. For acidic PEDOT:PSS, the solvents used during the processes (especially the alkaline developer) usually have detrimental effect. Khodagholy et al. and Defranco et al. used a parylene film to protect PEDOT:PSS films [6, 19], as shown in Figure 5, and  $1\ \mu\text{m}$  PEDOT:PSS lines were demonstrated. Parylene shows relatively weak adhesion to PEDOT:PSS, which makes it easily peeled off after etching. Although the conductivity of PEDOT:PSS films was proved to be unchanged during the processes, there is a risk for the surface of PEDOT:PSS to get damaged while peeling off.

As published by Xia et al., the conductivity of PEDOT:PSS can be enhanced using strong acid [10]. It is concluded that acidic PEDOT:PSS possesses strong stability in acid solution. Thus, we proposed an approach using acid as processing

solvent [20]. Silver thin films were used as protective layer, and traditional photolithographic etching of PEDOT:PSS can be achieved. Shown in Figure 6, resist was first formed on silver. Using acidic silver etchant, silver interlayer was etched, followed by oxygen plasma etching of PEDOT:PSS. After resist striping and silver removal, PEDOT:PSS patterns were formed on substrate. Commonly used silver and traditional photoresist can be utilized, and this process was proved to have no obvious influence towards PEDOT:PSS.

Using processes in Figure 6, patterns down to several micrometers were achieved on a 4-inch PET substrate (Figure 7(a)), and notably the resolution limit here is the photo mask and exposure system. With the patterned conductive PEDOT:PSS as electrode, OLEDs showed comparable performance as those with ITO anode (Figure 7(b)).

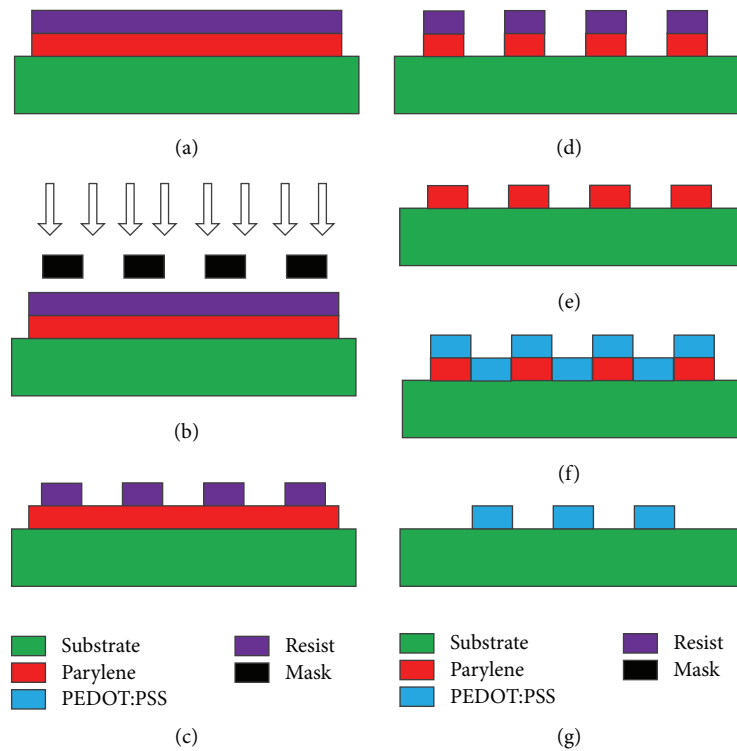


FIGURE 3: Lift-off processes with parylene. Resist was spin-coated (a), UV exposed (b), and developed (c) on parylene. With etching (d), patterns were transferred to parylene (e). PEDOT:PSS was deposited on patterned parylene (f), and after mechanical peel-off, PEDOT:PSS patterns were left on substrate (g).

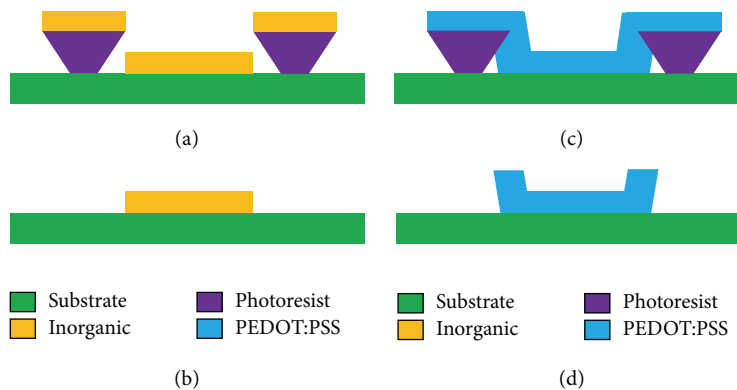


FIGURE 4: Lift-off processes of inorganic material and PEDOT:PSS. (a) Inorganic materials on photoresist, (b) inorganic material patterns on substrate after photoresist removal, (c) PEDOT:PSS on photoresist, and (d) PEDOT:PSS patterns on substrate.

### 3. Orthogonal Solvents and Specially Tailored Photo Imaging Materials for PEDOT:PSS Patterning

For photolithography in inorganic semiconductor industry, the concept of chemical orthogonality has long been practiced, and it is necessary to deposit and remove a layer of photoresist without damaging the underlying layers. However, deterioration of PEDOT:PSS occurs during the photoresist deposition and removal stages due to aggressive organic

solvents, especially in the pattern development steps by aqueous base solutions. It is a major challenge in chemical processing of PEDOT:PSS films to find orthogonal solvents, that is, solvents that do not dissolve or adversely damage PEDOT:PSS. Here, two kinds of such solvents are introduced, supercritical carbon dioxide ( $\text{scCO}_2$ ) and fluorosolvents.

$\text{scCO}_2$  is a kind of fluid which exists above the critical temperature and pressure of  $\text{CO}_2$  ( $T_c = 31.1^\circ\text{C}$ ;  $P_c = 73.8$  bar). This  $\text{scCO}_2$  fluid is a poor solvent for most ionic, high molecular weight and low vapor pressure organic

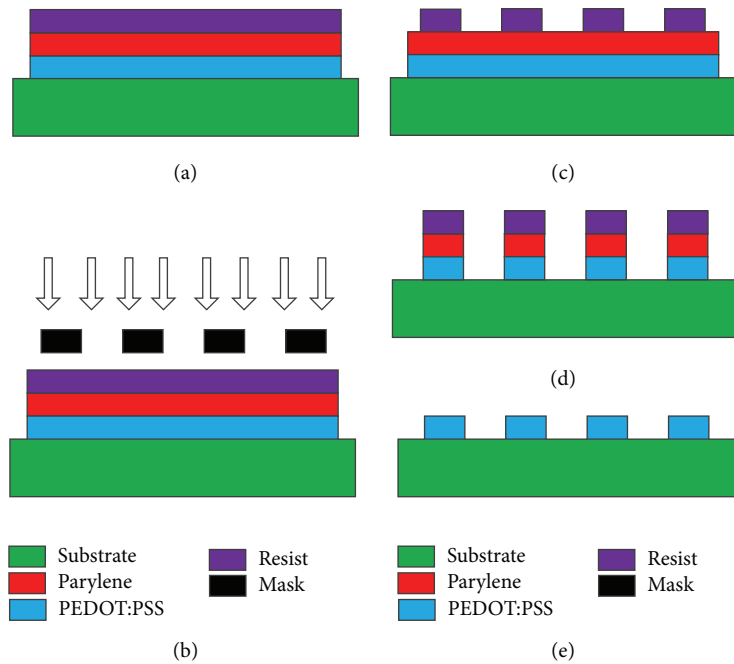


FIGURE 5: Etching process with parylene for PEDOT:PSS. (a) Spin-coating of PEDOT:PSS, parylene and resist, (b) UV exposure, (c) resist developing, (d) dry etching, and (e) parylene peeling-off.

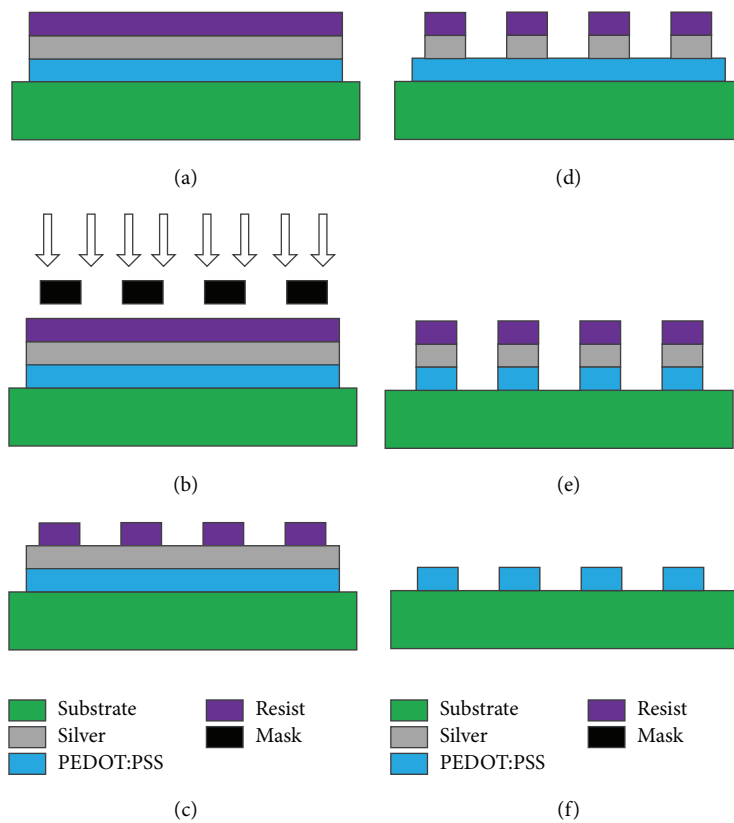
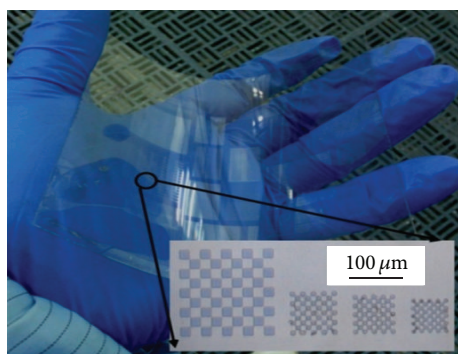
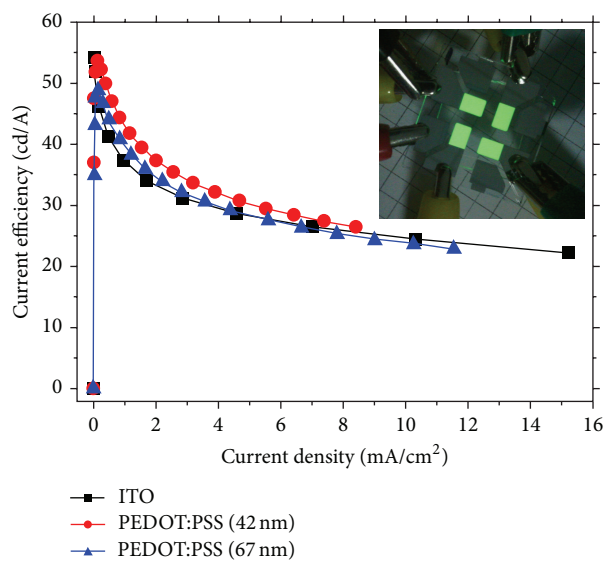


FIGURE 6: Photolithography with silver interlayer for PEDOT:PSS patterning. (a) Deposition of PEDOT:PSS, silver film and parylene. (b) UV exposure, (c) developing of resist. (d) Silver etching with silver etchant. (e) Oxygen plasma etching of PEDOT:PSS, (f) removal of resist and silver.



(a)



(b)

FIGURE 7: Photolithographic patterning of PEDOT:PSS using silver as protective interlayer. (a) Small patterns down to micrometer scale were fabricated on flexible substrate. (b) OLEDs using the patterned conductive PEDOT:PSS anodes had comparable performance as those using ITO anode.

compounds, which makes it an extremely promising nondestructive developing medium for vast majority of materials utilized in organic electronics. Another very important aspect is that  $\text{scCO}_2$  is a nontoxic, nonflammable, environmentally friendly fluid, which is proposed as a key driver in the new field of “green” chemistry. In recent years,  $\text{scCO}_2$  is being considered as a low-cost substitute solvent in microelectronics processing such as wafer cleaning, spin coating, etching, and resist stripping, based on its physical and chemical advantages. Utilizing dry  $\text{scCO}_2$  media as a developing solvent to dissolve resists in photolithography, Hwang et al. and Lee et al. introduced a chemically benign dry photolithographic approach without interfering with the active material, and appropriate copolymers with high fluorine content were developed (shown in Figure 8) as effective negative photoresists for development with  $\text{scCO}_2$  [21, 22]. Patterned PEDOT:PSS is demonstrated with fine features as small as  $1.3 \mu\text{m}$ . No delamination, distortion, or cracking of the PEDOT:PSS patterns was observed over larger scale.

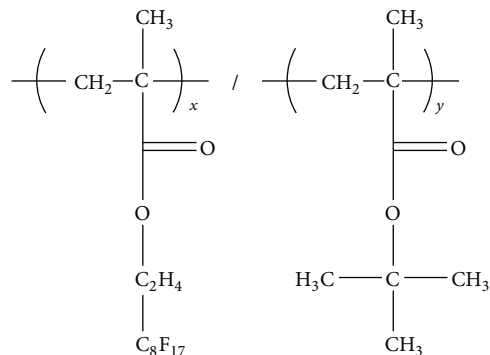


FIGURE 8: Chemical structure of photoresist for  $\text{scCO}_2$ .

Fluorous solvents are perfluorinated or very highly fluorinated liquids, which are typically immiscible with organic solvents and water. They are poor solvents for nonfluorinated organic materials and benign to a wide variety of organic electronic materials, and only materials with higher F content dissolve well in fluorous solvents. Therefore, they naturally extend options for solvent orthogonality. Since hydrofluoroethers (HFEs) are well known to be highly environmentally friendly, “green” solvents, they were chosen out of the variety of other available fluorous solvents. HFEs are nonflammable, have zero ozone-depletion potential, low global warming potential, and show very low toxicity to humans. Typical commercially available HFEs are HFE 7100 (Figure 9(a)) and HFE 7500 (Figure 9(b)). Based on the HFEs solvents combined and specifically tailored, highly fluorinated photoresist (Figures 9(c) and 9(d)), Ober et al. demonstrated facile photolithographic patterning for organic electronics [23–25]. Highly fluorinated chemicals are used, including the specifically designed resist material, the resist developer solvent, and the resist stripper solvent. Any possible damage to the organic semiconductor film associated with processing the photoresist is minimized. It should be emphasized that the photosensitive resist was carefully selected to enable nonchemically amplified patterning: an imaging mechanism that does not rely on acid-catalyzed deprotection reactions. The advantages of this pathway are substantial for the patterning of acidic PEDOT:PSS films. No residual layers of decomposed resist were found, as with chemically amplified resists. The PEDOT:PSS interface is left clean and unaffected following resist removal. After photolithography processing, PEDOT:PSS films showed essentially the same resistance as the reference devices, which indicates that the photoresist has no detrimental effects on device performance. Optical and atomic force microscopy on PEDOT:PSS were also performed, before and after immersion in boiling HFE 7100. No significant change of morphology and no pinhole formation, cracking, or delamination were observed, confirming the orthogonality of HFEs even under extreme conditions. Submicrometer patterning of PEDOT:PSS was also demonstrated.

Using fluorinated provided by Orthogonal Inc., we systematically studied the influence of the patterning processes towards PEDOT:SS [26]. Both the conductivity and surface



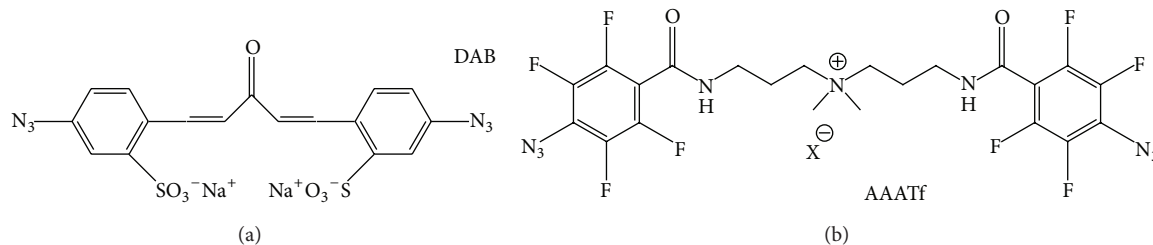


FIGURE 11: Photoinitiator for direct cross-linking of PEDOT:PSS. (a) DAB, (b) AAATf.

They used water-soluble ionic photoinitiators of 4,4'-diazido-2,2'-disulfonic acid benzalacetone disodium salt (DAB) and bis(fluorinated phenyl azide) (AAATf), shown in Figures 11(a) and 11(b). The minimum feature size of PEDOT:PSS patterns realized comprises 2.5  $\mu\text{m}$  wide lines separated by 1  $\mu\text{m}$  spacing. Atomic force microscope (AFM) images of the cross-linked PEDOT:PSS films showed no significant difference in surface roughness compared to the non-cross-linked films. However, their thickness is reduced, corresponding to a retention factor of 0.7-0.8. Conductivity enhancement was also observed after PEDOT:PSS cross-linking which could be due to the chemical doping. The cross-linking was also found to cause a work function deviation (about 0.1 eV to 0.2 eV) from the original PEDOT:PSS films, and the mechanism is still not fully understood. This approach is promising, and to improve the performance of this direct cross-linking approach of PEDOT:PSS, there needs to be more research involving both materials and processes.

## 5. Discussion

For photolithographic patterning of PEDOT:PSS, different approaches can be adopted, as reviewed in above sections. For lift-off processes using conventional resist, it is convenient to obtain resists and related solvents. However, as PEDOT:PSS films are usually continuous at the edge of resist, it influences the resolution and pattern fineness. Although limit resolution also happens to lift-off with parylene, peeling-off of parylene prevents the contact of PEDOT:PSS with stripping solvents, which results in unchanged PEDOT:PSS film. However, the peeling-off processes add a little complexity. For etching with parylene as a protective layer, it can achieve very good resolution except for a little complexity by the peeling-off processes. Changing parylene with Ag films as a protective layer during etching, it can achieve both good resolution and simplicity, for Ag can be easily removed by acid solution, and PEDOT:PSS is acid-stable. Photolithography using orthogonal solvents and specially tailored imaging materials realized submicron PEDOT:PSS patterns, and this approach is believed to be very promising, for it can be directly transferred to conventional photolithography facilities, only to change processing materials. If adding proper photoinitiators, PEDOT:PSS can be directly cross-linked which is very convenient. However, the resolution is limited to several micrometers, and more researches on materials and processing are needed.

## 6. Conclusion

Through properly selecting materials and processes, PEDOT:PSS can be patterned using photolithography processes. With lift-off processes, traditional photolithography materials and processes can be used. If protected by interlayer, PEDOT:PSS can be patterned using traditional photolithography. Utilizing orthogonal solvents and corresponding photoresist, nanoscale PEDOT:PSS patterns are realized. PEDOT:PSS can also be directly cross-linked by UV radiation if adding proper photoinitiators. To integrated PEDOT:PSS into future organic electronic devices, however, more researches concerning both materials and processes are needed for the patterning of PEDOT:PSS.

## Conflict of Interests

The authors declare that there is no conflict of interests regarding the publication of this paper.

## References

- [1] M. Cai, Z. Ye, T. Xiao et al., "Extremely efficient indium-tin-oxide-free green phosphorescent organic light-emitting diodes," *Advanced Materials*, vol. 24, no. 31, pp. 4337-4342, 2012.
- [2] K. Hong, S. H. Kim, C. Yang et al., "Photopatternable, highly conductive and low work function polymer electrodes for high-performance n-type bottom contact organic transistors," *Organic Electronics*, vol. 12, no. 3, pp. 516-519, 2011.
- [3] P. A. Ersman, D. Nilsson, J. Kawahara, G. Gustafsson, and M. Berggren, "Fast-switching all-printed organic electrochemical transistors," *Organic Electronics*, vol. 14, no. 5, pp. 1276-1280, 2013.
- [4] S.-I. Na, S.-S. Kim, J. Jo, and D.-Y. Kim, "Efficient and flexible ITO-free organic solar cells using highly conductive polymer anodes," *Advanced Materials*, vol. 20, no. 21, pp. 4061-4067, 2008.
- [5] M. C. Barr, C. Carbonera, R. Po, V. Bulović, and K. K. Gleason, "Cathode buffer layers based on vacuum and solution deposited poly(3,4-ethylenedioxythiophene) for efficient inverted organic solar cells," *Applied Physics Letters*, vol. 100, no. 18, Article ID 183301, 2012.
- [6] D. Khodagholy, T. Doublet, M. Gurfinkel et al., "Highly conformable conducting polymer electrodes for in vivo recordings," *Advanced Materials*, vol. 23, no. 36, pp. H268-H272, 2011.
- [7] D. Khodagholy, T. Doublet, P. Quilichini et al., "In vivo recordings of brain activity using organic transistors," *Nature Communications*, vol. 4, article 1575, 2013.

- [8] A. Elschner, S. Kirchmeyer, W. Lövenich, U. Merker, and K. Reuter, *PEDOT: Principles and Applications of an Intrinsically Conductive Polymer*, Taylor & Francis, New York, NY, USA, 2010.
- [9] N. Kim, S. Kee, S. H. Lee et al., "Highly conductive PEDOT:PSS nanofibrils induced by solution-processed crystallization," *Advanced Materials*, vol. 26, no. 14, pp. 2268–2272, 2014.
- [10] Y. Xia, K. Sun, and J. Ouyang, "Solution-processed metallic conducting polymer films as transparent electrode of optoelectronic devices," *Advanced Materials*, vol. 24, no. 18, pp. 2436–2440, 2012.
- [11] W. Gaynor, S. Hofmann, M. G. Christoforo et al., "Color in the corners: ITO-free white OLEDs with angular color stability," *Advanced Materials*, vol. 25, no. 29, pp. 4006–4013, 2013.
- [12] Y. H. Kim, J. Lee, S. Hofmann, M. C. Gather, L. Müller-Meskamp, and K. Leo, "Achieving high efficiency and improved stability in ITO-free transparent organic light-emitting diodes with conductive polymer electrodes," *Advanced Functional Materials*, vol. 23, no. 30, pp. 3763–3769, 2013.
- [13] Z. Xiong and C. Liu, "Optimization of inkjet printed PEDOT:PSS thin films through annealing processes," *Organic Electronics*, vol. 13, no. 9, pp. 1532–1540, 2012.
- [14] H. J. Lee, T. H. Park, J. H. Choi et al., "Negative mold transfer patterned conductive polymer electrode for flexible organic light-emitting diodes," *Organic Electronics*, vol. 14, no. 1, pp. 416–422, 2013.
- [15] J. R. Chan, X. Q. Huang, and A. M. Song, "Nondestructive photolithography of conducting polymer structures," *Journal of Applied Physics*, vol. 99, no. 2, Article ID 023710, 2006.
- [16] D.-S. Leem, P. H. Wöbkenberg, J. Huang, T. D. Anthopoulos, D. D. C. Bradley, and J. C. de Mello, "Micron-scale patterning of high conductivity poly(3,4-ethylenedioxythiophene):poly(styrenesulfonate) for organic field-effect transistors," *Organic Electronics*, vol. 11, no. 7, pp. 1307–1312, 2010.
- [17] J. Huang, R. Xia, Y. Kim et al., "Patterning of organic devices by interlayer lithography," *Journal of Materials Chemistry*, vol. 17, no. 11, pp. 1043–1049, 2007.
- [18] S. Takamatsu, T. Takahata, K. Matsumoto, and I. Shimoyama, "Micro-patterning of a conductive polymer and an insulation polymer using the Parylene lift-off method for electrochromic displays," *Journal of Micromechanics and Microengineering*, vol. 21, no. 7, Article ID 075021, 2011.
- [19] J. A. DeFranco, B. S. Schmidt, M. Lipson, and G. G. Malliaras, "Photolithographic patterning of organic electronic materials," *Organic Electronics: Physics, Materials, Applications*, vol. 7, no. 1, pp. 22–28, 2006.
- [20] S. Ouyang, Y. Xie, D. Zhu et al., "Photolithographic patterning of PEDOT:PSS with a silver interlayer and its application in organic light emitting diodes," *Organic Electronics*, vol. 15, pp. 1822–1827, 2014.
- [21] H. S. Hwang, A. A. Zakhidov, J.-K. Lee et al., "Dry photolithographic patterning process for organic electronic devices using supercritical carbon dioxide as a solvent," *Journal of Materials Chemistry*, vol. 18, no. 26, pp. 3087–3090, 2008.
- [22] J. K. Lee, P. G. Taylor, A. A. Zakhidov et al., "Orthogonal processing: a novel photolithographic patterning method for organic electronics," *Journal of Photopolymer Science and Technology*, vol. 22, no. 5, pp. 565–569, 2009.
- [23] J. K. Lee, M. Chatzichristidi, A. A. Zakhidov et al., "Acid-sensitive semiperfluoroalkyl resorcinarene: an imaging material for organic electronics," *The Journal of the American Chemical Society*, vol. 130, no. 35, pp. 11564–11565, 2008.
- [24] P. G. Taylor, J.-K. Lee, A. A. Zakhidov et al., "Orthogonal patterning of PEDOT:PSS for organic electronics using hydrofluoroether solvents," *Advanced Materials*, vol. 21, no. 22, pp. 2314–2317, 2009.
- [25] A. A. Zakhidov, J.-K. Lee, J. A. DeFranco et al., "Orthogonal processing: a new strategy for organic electronics," *Chemical Science*, vol. 2, no. 6, pp. 1178–1182, 2011.
- [26] S. Ouyang, Y. Xie, D. Wang et al., "Photolithographic patterning of highly conductive PEDOT:PSS and its application in organic light-emitting diodes," *Journal of Polymer Science Part B: Polymer Physics*, vol. 52, no. 18, pp. 1221–1226, 2014.
- [27] S.-H. Khong, S. Sivaramakrishnan, R.-Q. Png et al., "General photo-patterning of polyelectrolyte thin films via efficient ionic bis(fluorinated phenyl azide) photo-crosslinkers and their post-deposition modification," *Advanced Functional Materials*, vol. 17, no. 14, pp. 2490–2499, 2007.
- [28] F. J. Touwslager, N. P. Willard, and D. M. de Leeuw, "I-line lithography of poly-(3,4-ethylenedioxythiophene) electrodes and application in all-polymer integrated circuits," *Applied Physics Letters*, vol. 81, no. 24, pp. 4556–4558, 2002.
- [29] O. Fenwick, K. Oliver, and F. Cacialli, "Cross-linking of a poly(3,4-ethylene dioxythiophene):(polystyrene sulfonic acid) hole injection layer with a bis-azide salt and the effect of atmospheric processing conditions on device properties," *Applied Physics Letters*, vol. 100, no. 5, Article ID 053309, 2012.
- [30] G. Winroth, G. Latini, D. Credginton et al., "Polyfluorene-based light-emitting diodes with an azide photocross-linked poly(3,4-ethylene dioxythiophene):(polystyrene sulfonic acid) hole-injecting layer," *Applied Physics Letters*, vol. 92, no. 10, Article ID 103308, 2008.

## Research Article

# Memory and Electrical Properties of (100)-Oriented AlN Thin Films Prepared by Radio Frequency Magnetron Sputtering

Maw-Shung Lee,<sup>1</sup> Sean Wu,<sup>2</sup> Shih-Bin Jhong,<sup>1</sup> Kai-Huang Chen,<sup>3</sup> and Kuan-Ting Liu<sup>4</sup>

<sup>1</sup> Department of Electronics Engineering, National Kaohsiung University of Applied Sciences, Kaohsiung 807, Taiwan

<sup>2</sup> Department of Electronics Engineering and Computer Science, Tung Fang Design Institute, Kaohsiung 829, Taiwan

<sup>3</sup> Department of Animation and Multimedia Design, Tung Fang Design Institute, Kaohsiung 829, Taiwan

<sup>4</sup> Department of Electronics Engineering, Cheng-Shiu University, Kaohsiung 833, Taiwan

Correspondence should be addressed to Sean Wu; wusean.tw@gmail.com

Received 19 June 2014; Accepted 18 July 2014; Published 11 September 2014

Academic Editor: Teen-Hang Meen

Copyright © 2014 Maw-Shung Lee et al. This is an open access article distributed under the Creative Commons Attribution License, which permits unrestricted use, distribution, and reproduction in any medium, provided the original work is properly cited.

The (100)-oriented aluminum nitride (AlN) thin films were well deposited onto p-type Si substrate by radio frequency (RF) magnetron sputtering method. The optimal deposition parameters were the RF power of 350 W, chamber pressure of 9 mTorr, and nitrogen concentration of 50%. Regarding the physical properties, the microstructure of as-deposited (002)- and (100)-oriented AlN thin films were obtained and compared by XRD patterns and TEM images. For electrical properties analysis, we found that the memory windows of (100)-oriented AlN thin films are better than those of (002)-oriented thin films. Besides, the interface and interaction between the silicon and (100)-oriented AlN thin films was serious important problem. Finally, the current transport models of the as-deposited and annealed (100)-oriented AlN thin films were also discussed. From the results, we suggested and investigated that large memory window of the annealed (100)-oriented AlN thin films was induced by many dipoles and large electric field applied.

## 1. Instructions

Recently, the various functional thin films were widely focused on the applications in nonvolatile random access memory (NvRAM), such as smart cards and portable electrical devices, utilizing excellent memory characteristics, high storage capacity, long retention cycles, low electric consumption, nonvolatility, and high speed readout. Additionally, the various nonvolatile random access memory devices such as ferroelectric random access memory (FeRAM), magnetron memory (MRAM), resistance random access memory (RRAM), and flash memory were widely discussed and investigated [1–9]. However, the high volatile pollution elements and high fabrication cost of the complex composition material were serious difficult problems for applications in integrated circuit semiconductor processing. For this reason, the simple binary metal oxide materials such as ZnO, Al<sub>2</sub>O<sub>3</sub>, TiO<sub>2</sub>, and Ta<sub>2</sub>O<sub>5</sub> were widely considered and investigated for the various functional electronic product applications in resistance of random access memory devices [10–12].

The AlN thin film was promising piezoelectric materials for GHz-band surface acoustic wave SAW devices because of its high ultrasonic velocity, piezoelectricity, and thermal stability. In addition, AlN thin films exhibited (002)-, (100)-, and (103)-oriented hexagonal wurtzite structure and wide band gap in the range 5.9–6.2 eV [13]. For the ultrasonic velocity properties, the coupling coefficient was an important parameter and was chosen for the SAW devices. According to previous study, the coupling coefficient of the (100)-oriented AlN thin films is larger than the (002)-oriented thin films. However, it was difficult to prepare the (100)-oriented AlN thin films by PVD method [14, 15].

In this report, the subject of this work was to study the possible application of (100)-oriented AlN thin films deposited onto p-type silicon substrate using the RF magnetron sputtering. In addition, the physical and electrical characteristics of (100)-oriented AlN thin films were well developed and investigated in the metal-insulator-semiconductor (MIS) structure. The leakage current density, current transport mechanism, and the memory window of

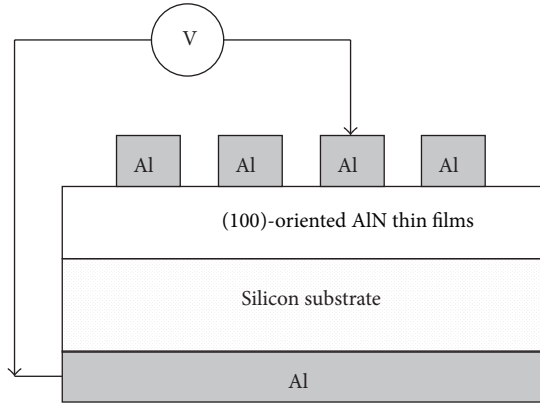


FIGURE 1: Metal insulator semiconductor (MIS) structure using as-deposited (100)-oriented AlN thin films.

(100)-oriented AlN thin films will be characterized. We will show that (100)-oriented AlN thin film is a candidate for fabrication of the memory devices.

## 2. Experimental Details

Metal insulator semiconductor (MIS) device, schematically shown in Figure 1, was fabricated over a polished p-Si wafer of nominal resistivity  $\sim 1.0$  ohm-cm. To overcome the existence of native-oxide on p-type silicon wafer, the particle and metal ion on p-type silicon wafer were removed during RCA clean process. The Al target was placed near 9.5 cm away from the substrate. The AlN thin films were deposited on a p-type Si substrate by RF magnetron sputtering method. The thin films were deposited on silicon substrate at  $200^\circ\text{C}$  under the optimal deposition parameters such as the RF power of 350 W, chamber pressure of 9 mTorr, and nitrogen concentration of 50%. The XRD patterns of the AlN thin films were recorded to find the crystallographic structure of thin film in the  $2\theta$ -degree range of  $20^\circ\sim 60^\circ$  using SIEMENS D5000. To complete the MIS structure, an array of circular top contacts with a diameter of 0.1 cm was formed by depositing an Al film with thickness of 500 nm through a metal mask by thermal evaporation in a vacuum system operating at  $1 \times 10^{-5}$  Torr. The capacitance and leakage of current characteristics of AlN thin films were measured by a gain phase analyzer (HP 4194A) and a semiconductor parameter analyzer (HP 4156).

## 3. Results and Discussion

To determine and investigated the difference preferred phase on AlN thin films in this study, the XRD pattern of the (100)- and (002)-oriented AlN thin films was studied and discussed. According to a few reports; the (100) and (001) preferential orientation of AlN thin films were controlled and prepared, because electromechanical coupling coefficient of the (100)-oriented thin films was suitable for that of the (001)-oriented thin films. However, it was difficult to prepare the (100)-oriented AlN thin films by sputtering and other technologies [14, 15]. Ishihara et al. already reported that the (100) and

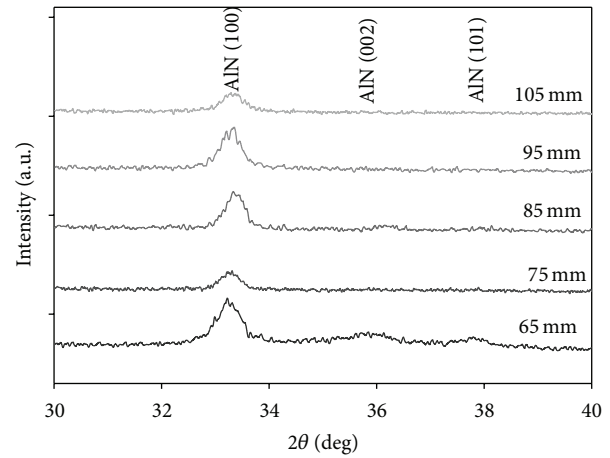


FIGURE 2: The XRD patterns of as-deposited (100)-oriented AlN thin films for different sputtering distance.

(001) preferential orientation of AlN films were prepared and controlled by the reactive sputtering method. A long distance between the Al target and substrate and the high sputtering pressures prepared and deposited for (100)-oriented AlN thin films were also found and discussed [13].

Figure 2 shows X-ray diffraction patterns of (100)-oriented AlN thin films for different distance between the Al target and substrate on a p-type silicon substrate. From the XRD pattern, we found that the AlN thin films exhibited polycrystalline structure. All of AlN thin films exhibited well *a*-axis orientation. According to Joint Committee for Powder Diffraction Studies (JCPDS) card of AlN material (number 25-1133), the (100), (002), and (101) peaks were observed in the XRD pattern. For the distance of 95 mm, the AlN thin films exhibited the preferred (100) orientation. At the distance of 95 mm, the intensity of the AlN (002) and (101) peak disappeared and the peaks of the AlN (100) appear. We found and suggested that (100)-oriented AlN thin films were prepare by making the suitable distance from the experimental results. The optimal deposition conditions such as the RF power of 350 W, chamber pressure of 9 mTorr, and nitrogen concentration of 50%. In addition, the  $2\theta$  diffraction peak of (101)- and (002)-oriented AlN thin film were  $37.925^\circ$  and  $36.039^\circ$ , respectively. In addition,  $d_{101}$  and  $d_{002}$  lattice constant of the AlN thin films were 0.2371 and 0.249 nm.

The high resolution transmission electron microscopy (HRTEM) image shows the (100)-oriented structure in the AlN thin films, as shown in Figure 3. The thickness of (100)-oriented AlN thin films was about  $1\ \mu\text{m}$  in Figure 3(a). The  $d_{100}$  lattice constant of the (100)-oriented AlN thin films was calculated and it was about 0.27 nm using the following Bragg diffraction equation:

$$n\lambda = 2d \cdot \sin \theta, \quad (1)$$

where  $n$  is the diffraction time. The  $\lambda$  is the wavelength of the X-ray diffraction. The  $\theta$  is injection angle of the X-ray diffraction. The  $d$  is the spacing of lattice. Therefore, these results proved that the AlN thin films exhibited (100)-oriented structure in Figure 3(b).

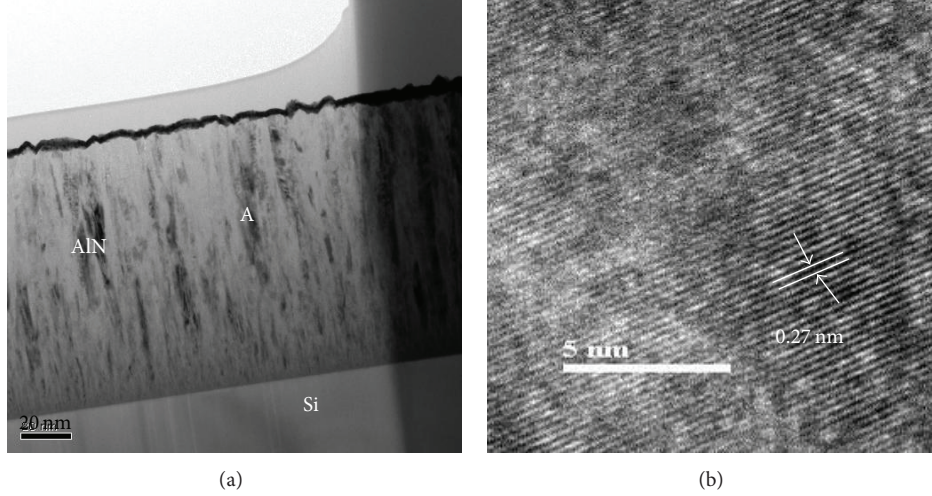


FIGURE 3: The (a) cross-sectional images and (b)  $d_{100}$  lattice distance of as-deposited (100)-oriented AlN thin films.

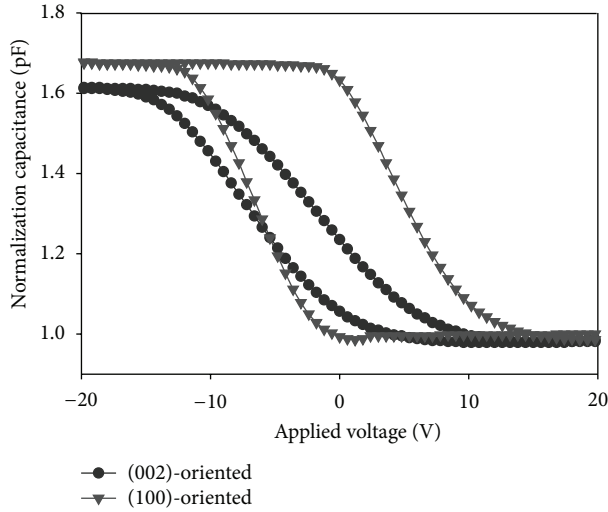


FIGURE 4: The normalization capacitance versus applied voltage curves of as-deposited (002)- and (100)-oriented AlN thin films.

Figure 4 shows the normalization capacitance versus the applied voltage ( $C$ - $V$ ) curves of the (100)- and (002)-oriented AlN thin films in MIS structure measured at 1 MHz. The applied voltages, which were first changed from  $-20$  V to  $20$  V and then returned to  $-20$  V, were used to measure the capacitance voltage characteristics ( $C$ - $V$ ) curves. We found that the normalization capacitances of (002)- and (100)-oriented AlN thin films were  $1.61$  and  $1.67$  pF, respectively. However, the (100)-oriented AlN thin films exhibited high normalization capacitance than those of (002)-oriented AlN thin films. As shown in Figure 4, the normalization capacitances of the (100)-oriented AlN thin films appear to increase due to its  $a$ -axis orientation structure. From the experimental results obtained, the oxide trap charges ( $Q_{ot}$ ) number was calculated and found using the following:

$$Q_{ot} = \frac{\Delta V_{FB} \cdot C}{q \cdot A}, \quad (2)$$

where the  $C$  and  $A$  value are capacitance and area of the AlN capacitor, respectively. The elementary charge  $q = 1.60218 \times 10^{-19}$  C. The  $\Delta V_{FB}$  is the flat-band voltage. The  $Q_{ot}$  is the oxide trap charges numbers.

As shown in Figure 4, the  $Q_{ot}$  number for the as-deposited (100)-oriented AlN thin films was  $1 \times 10^3$ . Additionally, the threshold voltage of (002)- and (100)-oriented AlN thin films was  $10$  V and  $13$  V, respectively. We suggested that the high threshold voltage of AlN thin films for (100)-oriented structure caused by many defects and vacancies in  $C$ - $V$  curves. In a previous study, the threshold voltage of dielectric thin films was attributed by defects and vacancies [9]. These  $C$ - $V$  experimental results were proved and discussed from the  $JE$  properties of AlN thin films. In addition, the memory window of the (002)- and (100)-oriented AlN thin films was observed and found. They were about  $10$  V and  $13$  V, respectively. The memory window of (100)-oriented AlN thin films was larger than those (002)-oriented thin films. In addition, the memory window of (100)-oriented AlN thin films was changed by the sweeping speed in Figure 5. The threshold voltage of (100)-oriented AlN thin films in MIS structure decreases as the sweeping speed increases. That was influenced by the mobile ions and charge injection between as-deposited (100)-oriented AlN thin films and metal electrode as the sweeping speed increased [9].

For MIS structure, the interface and interaction between the silicon and dielectric films was serious important problem. From the leakage current density versus electrical field ( $JE$ ) curves, the conduction mechanism of as-deposited (002)- and (100)-oriented AlN thin films also proved the defect and vacancy results. Figure 6 shows the  $JE$  characteristics of as-deposited (100)-oriented AlN thin films for the different deposited time. The leakage current density of the as-deposited AlN thin films for 1 hr deposited time was lower than those of other thin films. The few defects and vacancies were also proved and found from the  $Q_{ot}$  charges number of the as-deposited AlN thin films for 1 hr time in  $C$ - $V$  curves. To discuss the oxide charge  $Q_{ot}$  effect, the leakage current versus

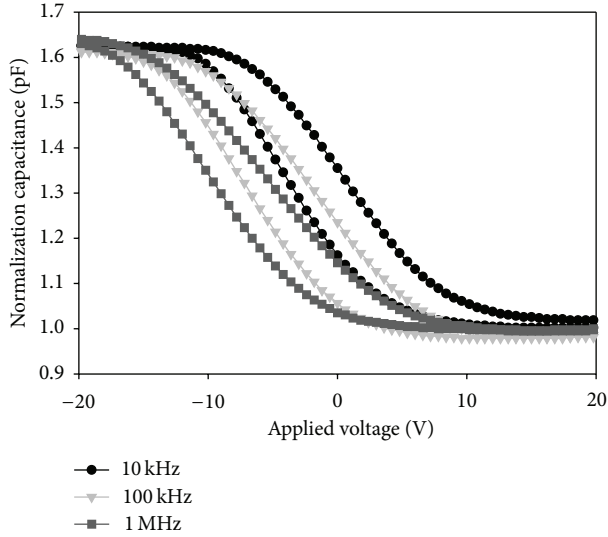


FIGURE 5: The normalization capacitance versus applied voltage curves of as-deposited (100)-oriented AlN thin films for different sweeping speed.

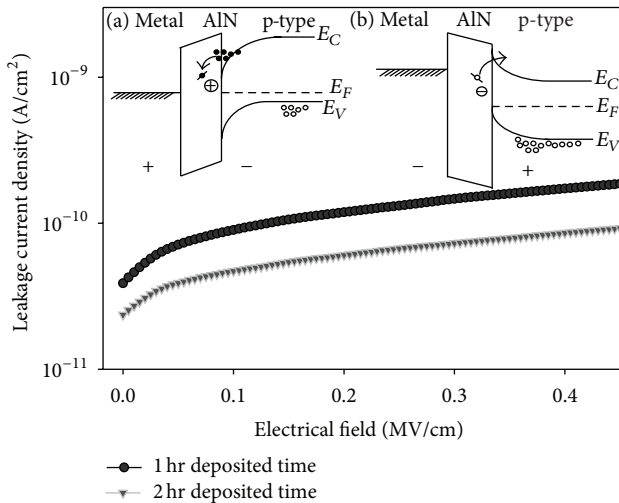


FIGURE 6: The leakage current versus applied voltage characteristics of as-deposited (100)-oriented AlN thin films for the different deposited time.

electrical field curves of the as-deposited AlN thin films were fitted to Schottky emission, Poole-Frankel, and space charge limit conduction (SCLC) transport models. As shown in insert of Figure 6, the schematic energy band diagrams under positive and negative bias conditions were discussed and found, respectively. For positive bias, the electrons were attracted from the p-type Si substrate to the as-deposited (100)-oriented AlN thin films and captured by deep traps of the AlN thin films (Figure 6(a)). For negative bias, the trapped electrons of as-deposited AlN thin films emit from the traps to the p-type Si substrate, corresponding to the left shift of the C-V curve (Figure 6(b)). The large memory window of the as-deposited AlN thin films might be caused by defects and vacancies.

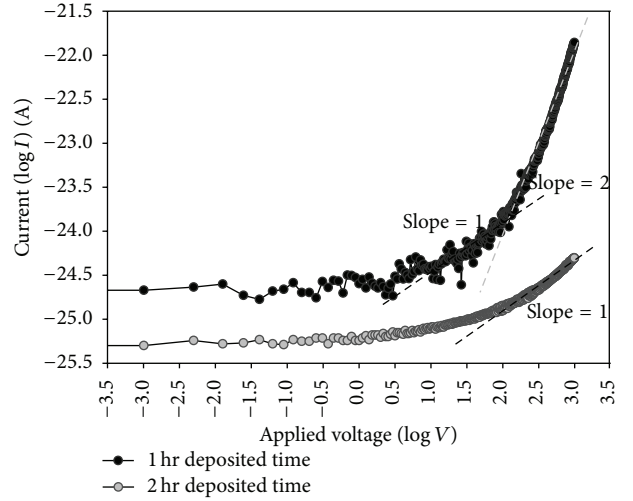


FIGURE 7: The leakage current versus applied voltage characteristics of as-deposited (100)-oriented AlN thin films for the different deposited time.

Figure 7 shows the  $JE$  characteristics for the as-deposited AlN thin films in terms of  $\log I$  as vertical axis and  $\log V$  as horizontal axis. The fitting curves were straight and had different slope in this figure and  $JE$  curve of AlN thin films was the SCLC theory [16].

The child's law equation of space charge limit conduction is as follows:

$$J_{\text{child}} = \frac{9}{8} \epsilon \mu_n \frac{V^2}{d_s^3}, \quad (3)$$

where the  $\epsilon$ ,  $\mu_n$ , and  $d_s$  value of the AlN capacitor are dielectric constant, electronic mobility, and thickness, respectively. For the slope = 1, the as-deposited AlN thin films exhibited the ohmic conduction in low applied voltage, and it was from 0.7 V to 3 V. For the slope = 2, the as-deposited AlN thin films exhibited child's law in high applied voltage and it was trap center region. The results were proved and caused by the carrier filling the trap and defect of the as-deposited AlN thin films. However, the as-deposited AlN thin films for 2 hr time did not exhibited the child's law in high applied voltage applied. The high leakage current was also attributed to the vacancies and defects of as-deposited thin films.

Figure 8 shows the same  $JE$  characteristics in terms of  $J/T^2$  as vertical axis and applied electrical filed  $E^{1/2}$  as horizontal axis. The fitting curves were straight in this figure, and the  $JE$  curves obey the Schottky emission model [17–19]. For as-deposited thin films, the  $JE$  current of AlN thin films was fitted well by straight lines in low applied electrical filed. According to fitting curves in  $JE$  current, we found and suggested that the as-deposited AlN thin films exhibited the Schottky emission model in high applied electrical filed. Additionally, we found that the as-deposited AlN thin films for 2 hr deposited time only exhibited the Schottky emission model. In this study, the as-deposited (100)-oriented AlN thin films exhibited excellent memory and electrical properties were found.

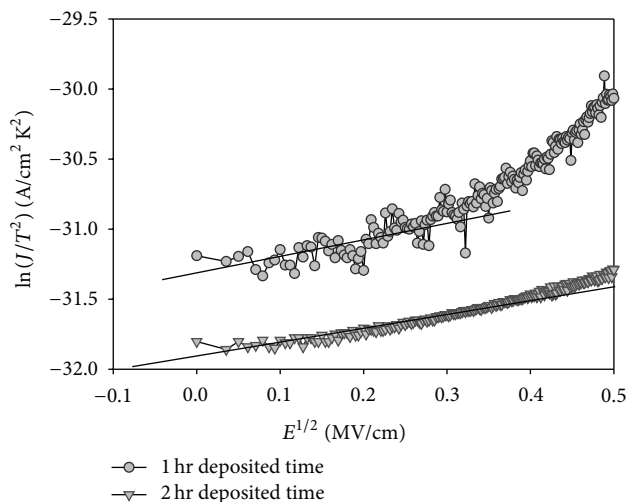


FIGURE 8: The  $(J/T^2)$  versus  $E^{1/2}$  curves of as-deposited (100)-oriented AlN thin films for the different deposited time.

#### 4. Conclusion

In summary, the (100)-oriented AlN thin films were prepared by RF magnetron sputtering technology. From the XRD patterns, all oriented AlN thin films on p-type substrate crystallized well. The  $d_{100}$  lattice constant of the (100)-oriented AlN thin films was calculated and it was about 0.27 nm using the Bragg diffraction equation. From the  $C$ - $V$  curves, the  $Q_{ot}$  charge number of the as-deposited (100)-oriented AlN thin films was  $1 \times 10^3$ . The memory window effect, electrical properties, and depletion delay of the MIS structure may be caused by oxide charge of the as-deposited AlN thin films in  $C$ - $V$  curves. The conduction mechanism of as-deposited (100)-oriented AlN thin films also proved these results in  $JE$  curves.

#### Conflict of Interests

The authors declare that there is no conflict of interests regarding the publication of this paper.

#### Acknowledgment

This work acknowledges the financial support of the Ministry of Science and Technology of the Republic of China (NSC 102-2221-E-151-054-).

#### References

- [1] S. R. Shannigrahi and H. M. Jang, "Fatigue-free lead zirconate titanate-based capacitors for nonvolatile memories," *Applied Physics Letters*, vol. 79, p. 1051, 2001.
- [2] S. K. Hong, C. W. Suh, C. G. Lee, S. W. Lee, E. Y. Hang, and N. S. Kang, "Protection of  $\text{SrBi}_2\text{Ta}_2\text{O}_9$  ferroelectric capacitors from hydrogen damage by optimized metallization for memory applications," *Applied Physics Letters*, vol. 77, p. 76, 2000.
- [3] S. B. Xiong and S. Sakai, "Memory properties of  $\text{SrBi}_2\text{Ta}_2\text{O}_9$  thin films prepared on  $\text{SiO}_2/\text{Si}$  substrates," *Applied Physics Letters*, vol. 75, p. 1613, 1999.
- [4] J. S. Kim and S. G. Yoon, "High dielectric constant  $(\text{Ba}_{0.65}\text{Sr}_{0.35})(\text{Ti}_{0.41}\text{Zr}_{0.59})\text{O}_3$  capacitors for Gbit-scale dynamic random access memory devices," *Journal of Vacuum Science & Technology B*, vol. 18, pp. 216–220, 2000.
- [5] T. B. Wu, C. M. Wu, and M. L. Chen, "Highly insulative barium zirconate-titanate thin films prepared by rf magnetron sputtering for dynamic random access memory applications," *Applied Physics Letters*, vol. 69, p. 2659, 1996.
- [6] K. H. Chen, Y. C. Chen, C. F. Yang, and T. C. Chang, "Fabrication and characteristics of  $\text{Ba}(\text{Zr}_{0.1}\text{Ti}_{0.9})\text{O}_3$  thin films on glass substrate," *Journal of Physics and Chemistry of Solids*, vol. 69, no. 2-3, pp. 461–464, 2008.
- [7] C. F. Yang, K. H. Chen, Y. C. Chen, and T. C. Chang, "Fabrication of one-transistor-capacitor structure of nonvolatile TFT ferroelectric RAM devices using  $\text{Ba}(\text{Zr}_{0.1}\text{Ti}_{0.9})\text{O}_3$  gated oxide film," *IEEE Transactions on Ultrasonics, Ferroelectrics and Frequency Control*, vol. 54, no. 9, pp. 1726–1730, 2007.
- [8] C. F. Yang, K. H. Chen, Y. C. Chen, and T. C. Chang, "Physical and electrical characteristics of  $\text{Ba}(\text{Zr}_{0.1}\text{Ti}_{0.9})\text{O}_3$  thin films under oxygen plasma treatment for applications in nonvolatile memory devices," *Applied Physics A: Materials Science & Processing*, vol. 90, no. 2, pp. 329–331, 2008.
- [9] K. H. Chen, Y. C. Chen, Z. S. Chen, C. F. Yang, and T. C. Chang, "Temperature and frequency dependence of the ferroelectric characteristics of  $\text{BaTiO}_3$  thin films for nonvolatile memory applications," *Applied Physics A*, vol. 89, no. 2, pp. 533–536, 2007.
- [10] S. Wu, Z. X. Lin, M. S. Lee, and R. Ro, "Bulk acoustic wave analysis of crystalline plane oriented ZnO films," *Applied Physics Letters*, vol. 102, Article ID 084908, 2007.
- [11] S. Lee, E. B. Song, S. Kim et al., "Impact of gate work-function on memory characteristics in  $\text{Al}_2\text{O}_3/\text{HfO}_x/\text{Al}_2\text{O}_3/\text{graphene}$  charge-trap memory devices," *Applied Physics Letters*, vol. 100, Article ID 023109, 2012.
- [12] Y. Yang, L. Jin, X. Ma, and D. Yang, "Low-voltage driven visible and infrared electroluminescence from light-emitting device based on Er-doped  $\text{TiO}_2/p^+-\text{Si}$  heterostructure," *Applied Physics Letters*, vol. 100, Article ID 031103, 2012.
- [13] M. Ishihara, S. J. Li, H. Yumoto, K. Akashi, and Y. Ide, "Control of preferential orientation of AlN films prepared by the reactive sputtering method," *Thin Solid Films*, vol. 316, no. 1-2, pp. 152–157, 1998.
- [14] M. Ishihara, H. Yumoto, T. Tsuchiya, and K. Akashi, "AlN thin films prepared by the electron shower method," *Journal of the Surface Finishing Society of Japan*, vol. 47, no. 2, pp. 152–156, 1996.
- [15] M. Ishihara, H. Yumoto, T. Tsuchiya, and K. Akashi, "Effect of bias voltage on AlN thin films prepared by electron shower method," *Thin Solid Films*, vol. 281-282, no. 1-2, pp. 321–323, 1996.
- [16] A. Lampert and P. Mark, *Current Injection in Solids*, Academic, New York, NY, USA, 1970.
- [17] S. Fleischer, P. T. Lai, and Y. C. Cheng, "Trap-assisted conduction in nitrided-oxide and re-oxidized nitrided-oxide n-channel metal-oxide-semiconductor field-effect transistors," *Journal of Applied Physics*, vol. 73, p. 8353, 1994.

- [18] T. Mihara and H. Watanabe, "Electronic conduction characteristics of sol-gel ferroelectric  $\text{Pb}(\text{Zr}_{0.4}\text{Ti}_{0.6})\text{O}_3$  thin-film capacitors: part I," *Japanese Journal of Applied Physics*, vol. 34, pp. 5664–5673, 1995.
- [19] Y. B. Lin and J. Y. Lee, "The temperature dependence of the conduction current in  $\text{Ba}_{0.5}\text{Sr}_{0.5}\text{TiO}_3$  thin-film capacitors for memory device applications," *Journal of Applied Physics*, vol. 87, p. 1841, 2000.

## Research Article

# The Influence of Electrophoretic Deposition for Fabricating Dye-Sensitized Solar Cell

Jung-Chuan Chou,<sup>1,2</sup> Shen-Chang Lin,<sup>1</sup> Yi-Hung Liao,<sup>3</sup>  
Jui-En Hu,<sup>2</sup> Shen-Wei Chuang,<sup>2</sup> and Chin-Hui Huang<sup>2</sup>

<sup>1</sup> Department of Electronic Engineering, National Yunlin University of Science and Technology, Douliou, Yunlin 64002, Taiwan

<sup>2</sup> Department of Electronic Engineering and Graduate School of Electronic Engineering, National Yunlin University of Science and Technology, Douliou, Yunlin, Taiwan

<sup>3</sup> Department of Information Management, TransWorld University, Yunlin 64063, Taiwan

Correspondence should be addressed to Jung-Chuan Chou; [choujc@yuntech.edu.tw](mailto:choujc@yuntech.edu.tw)

Received 9 May 2014; Revised 18 August 2014; Accepted 18 August 2014; Published 28 August 2014

Academic Editor: Teen-Hang Meen

Copyright © 2014 Jung-Chuan Chou et al. This is an open access article distributed under the Creative Commons Attribution License, which permits unrestricted use, distribution, and reproduction in any medium, provided the original work is properly cited.

Titanium dioxide (TiO<sub>2</sub>) film was deposited on fluorine-doped tin oxide (FTO) glass substrate by electrophoretic deposition method (EPD). TiO<sub>2</sub> films were prepared with different I<sub>2</sub> dosages, electric field intensities and deposition time (D.T.), electrophoretic deposition times. By different I<sub>2</sub> dosages, electric field intensities, deposition time, electrophoretic deposition times fabricated TiO<sub>2</sub> films and compared photoelectric characteristics of TiO<sub>2</sub> films to find optimal parameters which were the highest photovoltaic conversion efficiency. And use electrochemical impedance spectroscopy (EIS) to measure the Nyquist plots under different conditions and analyze the impedance of dye-sensitized solar cells at the internal heterojunction. According to the experimental results, the I<sub>2</sub> dosage was 0.025 g which obtained the optimal characteristic parameters. Thickness of TiO<sub>2</sub> film was 10.6 μm, the open-circuit voltage (V<sub>oc</sub>) was 0.77 V, the short-circuit current density (J<sub>sc</sub>) was 7.20 mA/cm<sup>2</sup>, the fill factor (F.F.) was 53.41%, and photovoltaic conversion efficiency (η) was 2.96%.

## 1. Introduction

Solar energy has been considered as a renewable energy of the next generation since fossil fuel was getting less and less. And dye-sensitized solar cell (DSSC), which was developed by O'Regan and Graetzel in 1991 [1], is highly potential in the solar energy. Titanium dioxide (TiO<sub>2</sub>) had several advantages such as easily tunable bandgap and great absorption dye ability, so it has been a widely used material in many fields, such as photocatalysis, gas sensor, sunscreen, dye-sensitized solar cell, and other applications [2]. Titanium dioxide exists naturally in three nanocrystallines, namely, rutile (tetragonal, E<sub>g</sub> = 3.05 eV), anatase (tetragonal, E<sub>g</sub> = 3.23 eV), and brookite (orthorhombic, E<sub>g</sub> = 3.26 eV).

There are several methods to manufacture titanium dioxide films, such as sputtering [3], hydrothermal method [4], doctor-blade [5], spin coating [6], chemical bath [7], electrophoretic deposition [8], and screen printing [9].

Electrophoretic deposition method has several advantages, such as high deposition rate, simple apparatus, and no binder required. And it also allows us to prepare any kind of conductive substrate shape. In addition, the electrophoretic deposition does not limit to the deposition temperature during processing of depositing TiO<sub>2</sub> film [10].

In this study, TiO<sub>2</sub> films were prepared by electrophoretic deposition method. Electrophoretic deposition was an attractive technique for the fabrication of films [11, 12]. Electrophoretic deposition was achieved via electrophoretic motion of charged particles in a suspension toward an electrode which depended on the particle charge and formation under the influence of an applied electric field [3].

Recently, for improving the photovoltaic conversion efficiency of dye-sensitized solar cell, the structure of TiO<sub>2</sub> has been developed in several forms such as nanosheet [8], nanowire [5], and nanopores [9].

## 2. Experimental Details

**2.1. Material.** Titanium dioxide ( $\text{TiO}_2$ ) powder (P25) which was purchased from Degussa, Germany, contained 80% of anatase and 20% of rutile. The ruthenium-535 (N3) was purchased from UniRegion Bio-Tech, USA. The absolute ethanol was purchased from Katayama Chemical, Japan. The Acetylacetone (AcAc) was purchased from Acros Organics, Belgium. The lithium iodide (LiI) and 4-tert-butylpyridine (TBP) were purchased from Sigma-Aldrich, USA. The iodine ( $\text{I}_2$ ) was purchased from Riedel-deHaen, USA. The 1-propyl-2,3-dimethylimidazolium iodide (DMPII) was purchased from Tokyo Chemical, Japan. And fluorine-doped tin oxide (FTO) glass substrate was purchased from C. P. Solar, Co., Ltd., Taiwan.

**2.2. Preparation of  $\text{TiO}_2$  Suspension and Electrophoretic Deposition.** In this experiment, fluorine-doped tin oxide glass substrate was used as the cathode electrode, and platinum (Pt) was used as the anode electrode. The  $\text{TiO}_2$  suspension consists of 0.25 g  $\text{TiO}_2$  powder and 0.02 g  $\text{I}_2$  in 25 mL of Acetylacetone. Before the cathode deposition, the  $\text{TiO}_2$  suspension was placed in an ultrasonic vibrator to vibrate for 30 minutes. The distance between the cathode and the anode was fixed at 1 cm and 2 cm. After depositing the  $\text{TiO}_2$  on FTO glass substrate,  $\text{TiO}_2$  films were annealed at  $450^\circ\text{C}$  for 30 minutes. The purpose of annealing is to improve the connection between  $\text{TiO}_2$  film and substrate. The postannealed electrodes were immediately immersed in an absolute ethanol solution of  $3 \times 10^{-4}$  M N3 dye for 24 h at room temperature.

**2.3. Fabrication of Dye-Sensitized Solar Cell.** The Pt film was fabricated on FTO glass substrate by R.F. sputtering for 90 sec as the counterelectrode. The working electrode and counterelectrode were filled with the liquid electrolyte which consisted of 0.6 M DMPII, 0.5 M LiI, 0.05 M  $\text{I}_2$ , and 0.5 M TBP in 15 mL MPN. Finally, DSSC was sealed as the sandwich structure of DSSC device. The active area of the solar cell was  $0.8 \text{ cm} \times 0.8 \text{ cm}$ .

**2.4. Measurement.** Surface morphology of  $\text{TiO}_2$  film was measured by scanning electron microscope (SEM). The short-circuit current density ( $J_{sc}$ ), the open-circuit voltage ( $V_{oc}$ ), the fill factor (F.F.), and the photovoltaic conversion efficiency ( $\eta$ ) of DSSC were measured by Keithley 2400 digital source meter under one sun illumination ( $\text{AM } 1.5 \text{ G}$ ,  $100 \text{ mW/cm}^2$ ).

## 3. Results and Discussion

**3.1. Electrophoretic Kinetics.** According to the Hamaker equation [16, 17], the relation between the deposited weight ( $w$ ) and the electric field intensity ( $E$ ) is

$$\text{Mass} = \int_0^t AC\mu E dt, \quad (1)$$

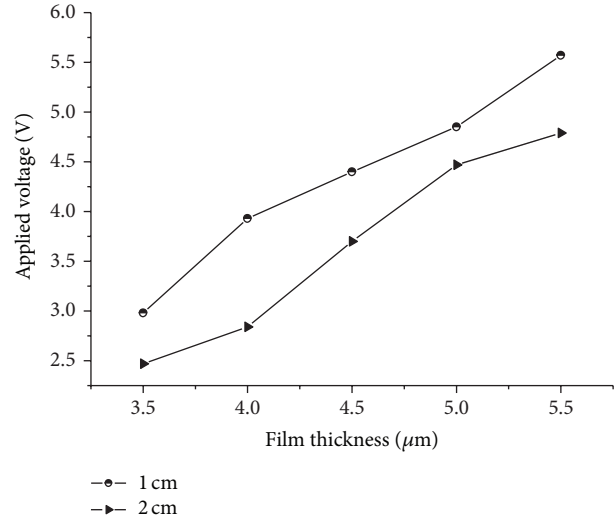


FIGURE 1: The  $\text{TiO}_2$  films fabricated by different applied voltages and electrode distances.

where  $\mu$  is the electrophoretic mobility,  $A$  is the surface area of the electrode,  $C$  is the concentration of the suspension, and  $t$  is the time.

The  $\text{TiO}_2$  films were fabricated with different voltages. The larger applied voltage was applied, which could increase  $\text{TiO}_2$  film thickness. The experimental results were as shown in Figure 1. The  $\text{TiO}_2$  film thickness was a function of increasing applied voltage. Increasing the voltage could provide larger dragging force, so  $\text{TiO}_2$  nanoparticles could obtain faster deposition rate. And we also increased the distance between two electrodes from 1 cm to 2 cm; the  $\text{TiO}_2$  film thicknesses were thinner with increasing distance between two electrodes, which could lead the higher possibility for  $\text{TiO}_2$  nanoparticles to collide each other that led to the deceleration and decreased deposition rate. In addition, the larger voltage generated faster deposition rate and formed the thicker  $\text{TiO}_2$  film thickness, but it also led to the bigger crack on  $\text{TiO}_2$  film, as shown in Figures 2(a)–2(f).

The numbers of crack seemed to depend on deposition electric field intensity. In the microstructure of  $\text{TiO}_2$  film which deposited at  $4.0 \text{ V/cm}$  for 1 min,  $\text{TiO}_2$  particles seemed to be separated, as shown in Figures 2(a) and 2(b), respectively. The microstructure of  $\text{TiO}_2$  film which deposited at  $4.50 \text{ V/cm}$  for 1 min became more concentrated, as shown in Figures 2(c) and 2(d), respectively. And the  $\text{TiO}_2$  film which was prepared at  $5.0 \text{ V/cm}$  has larger crack as shown in Figures 2(e) and 2(f), respectively. The main reason of crack was that the inorganic solvent rapidly was evaporated from the film surface during the drying process. The presence of nanopores on the film could be a great advantage of absorbing dye.

**3.2. J-V Characterization of DSSC.** There were few factors that could influence  $\text{TiO}_2$  films in the preparing process, such as (a) the limitation of distance between two electrodes [16], (b) the decreasing of the suspension concentration [18],

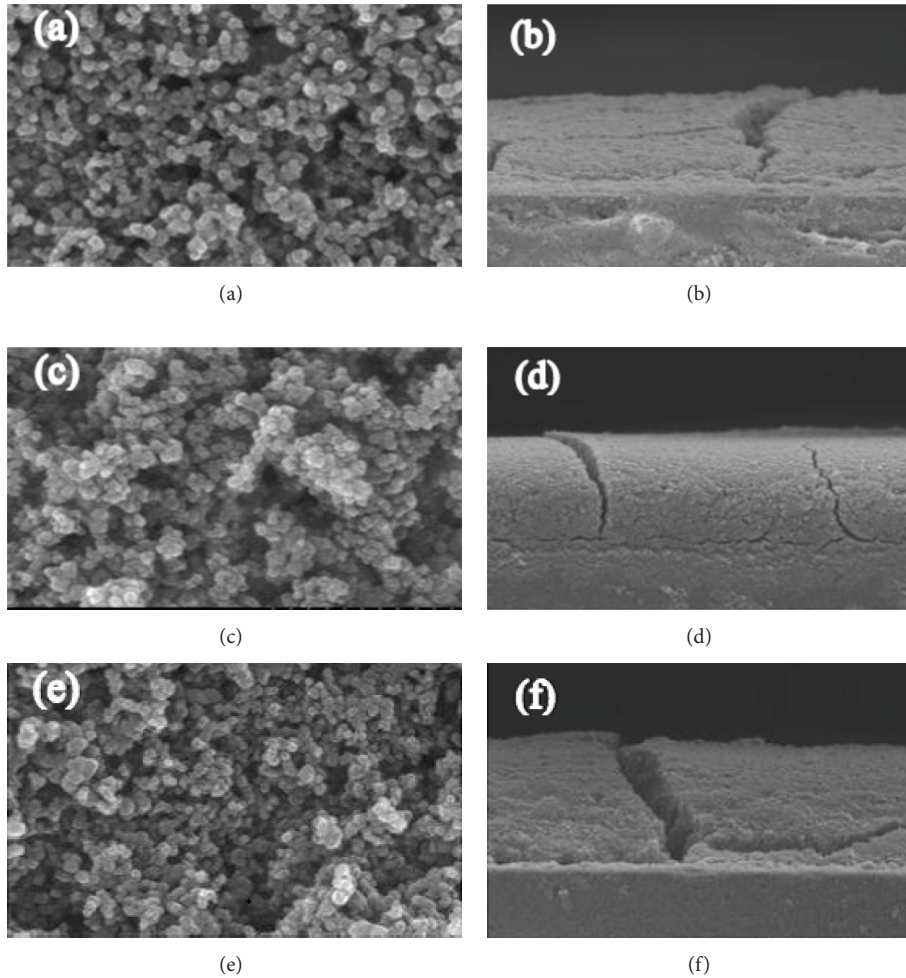


FIGURE 2: The SEM images of (a) TiO<sub>2</sub> film and (b) cross-section deposited at 4.0 V/m. (c) TiO<sub>2</sub> film and (d) cross-section deposited at 4.50 V/cm, (e) TiO<sub>2</sub> film, and (f) cross-section deposited at 5.0 V/m.

(c) the increasing of deposition resistance [19], and (d) the mobility of TiO<sub>2</sub> nanoparticles in the electrophoretic solution [20]. In this experiment, the TiO<sub>2</sub> films were fabricated by different deposition time, as shown in Figure 3. We found optimal properties of DSSC in deposition time at 60 s. Moreover, the more I<sub>2</sub> dosages at the same deposition time could lead TiO<sub>2</sub> nanoparticle (TNP) to carry more electric charges on the TiO<sub>2</sub> nanoparticle surface. So the mobility of TiO<sub>2</sub> nanoparticle could increase by increasing electric charge at TiO<sub>2</sub> nanoparticle surface [19]; the deposition rate and the thickness of TiO<sub>2</sub> film were increased by increasing I<sub>2</sub> dosages. The experimental results were shown as listed in Table 1.

Figure 4 showed *J-V* curves of DSSCs, which were prepared with different weights dosages of iodine (I<sub>2</sub>). The optimal I<sub>2</sub> dosage was 0.025 g and the thickness was 10.6 μm. In comparison with TiO<sub>2</sub> films which have been prepared with different I<sub>2</sub> dosages, both the short-circuit current density and TiO<sub>2</sub> film thickness were proportional. The thicker thickness of TiO<sub>2</sub> film could increase the amount of

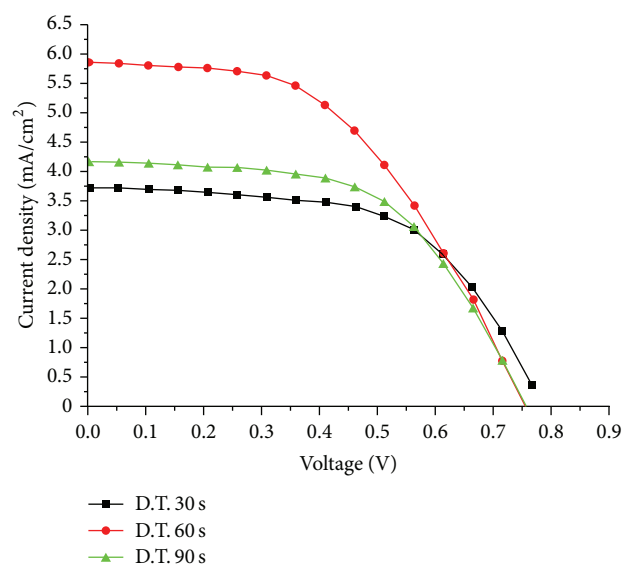


FIGURE 3: The TiO<sub>2</sub> films fabricated by different deposition time.

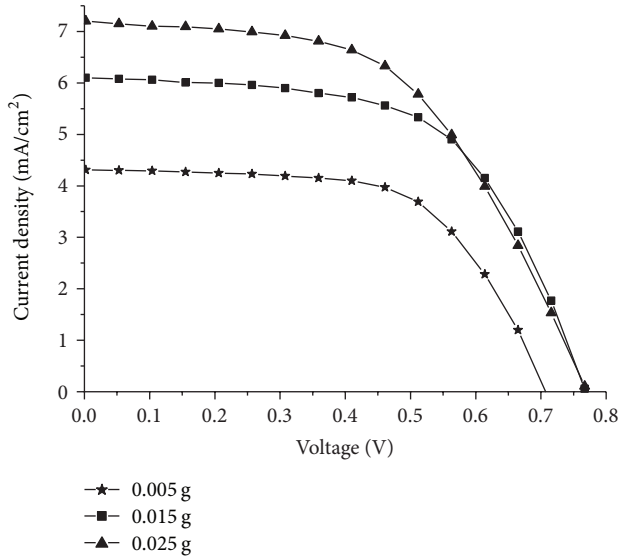


FIGURE 4: The TiO<sub>2</sub> films fabricated by different I<sub>2</sub> dosages.

TABLE 1: The thicknesses and deposition rates with different I<sub>2</sub> dosages.

| I <sub>2</sub> dosage (g) | Deposition rate ( $\mu\text{m}/\text{sec}$ ) | Thickness ( $\mu\text{m}$ ) |
|---------------------------|--|-----------------------------|
| 0.025                     | 0.177  | 10.6                        |
| 0.015                     | 0.150  | 9.0                         |
| 0.005                     | 0.125  | 7.5                         |

dye absorption which could generate more photoelectrons. Zhang et al. [21, 22] reported that the thicker thickness of TiO<sub>2</sub> film could increase dye desorption and the current density value was dependent on the light absorption which is strongly related to the amount of dye molecules being adsorbed. And, the TiO<sub>2</sub> nanoparticles deposited on the conductive substrate were due to an electrostatic attraction force between nanoparticles and FTO glass surface. Nanoparticles were formed by the electrostatic force with the cathode surface, because TiO<sub>2</sub> nanoparticles were accumulated with H<sup>+</sup> ions [23, 24].

Table 2 showed the comparison of DSSCs parameters with other references [3, 13–15]; we found that the suspension amount could affect the thickness of TiO<sub>2</sub> film; larger suspension amount had longer distance effect, so the TiO<sub>2</sub> film thickness could be thinner.

The increasing TiO<sub>2</sub> film thickness could increase dye loading of DSSC to generate more photoexcited electrons under the sun irradiation 100 mW/cm<sup>2</sup>, so the current density was increased by 18% (from 6.09 mA to 7.02 mA) [13].

The photovoltaic conversion efficiency could influence not only the thickness of TiO<sub>2</sub> layer but also the structure of TiO<sub>2</sub> layer. In this study, the structure of photoelectrode was nanopores which were stacked by TiO<sub>2</sub> nanoparticles. In the other hand, there were many studies about the structure of TiO<sub>2</sub> layer in the photoelectrode which was TiO<sub>2</sub> nanotube (TNT). Since the structure of TiO<sub>2</sub> nanotube had greater specific surface area than nanoparticles, and

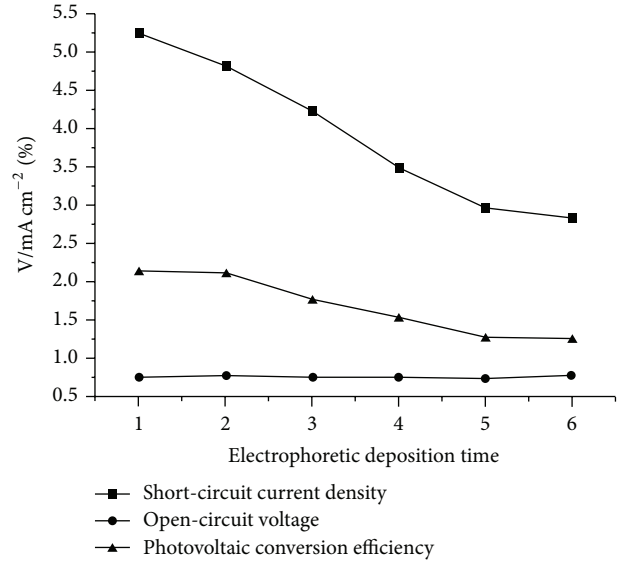


FIGURE 5: The effect of electrophoretic deposition times on properties of DSSC.

effectively enhance the absorption amount of dye and the photoelectric conversion efficiency can be further enhanced [25, 26]. The nanotube structure fabricated by anodizing method is best arrayed, simple, and easy for fabrication and has low equipment cost. Through parameters, the fabricated nanoporous structure can be adjusted to achieve neatly arrayed nanoporous structure with pores in appropriate size. The photovoltaic conversion efficiency (2.96%) of DSSC thickness 10.6  $\mu\text{m}$  was higher than the DSSC (2.60%) thickness 10.0  $\mu\text{m}$  in [3]. The electrical field intensity during the deposited TiO<sub>2</sub> films caused nonuniform film, so it has lower absorption amount of dye and the photovoltaic conversion efficiency.

For the same structure of photoelectrode [14, 15], the thickness of TiO<sub>2</sub> film could be observed as an important relationship between short current density and photovoltaic conversion efficiency. If the thickness was 6.0  $\mu\text{m}$ , the TNT-TNP mixed structure of photoelectrode had performance higher than TNT or TNP, because the TNT-TNP mixed structure had enlarged specific surface area at the same active area with better current density and photovoltaic conversion efficiency of DSSC.

From Figure 5, the  $J_{\text{sc}}$  and  $\eta$  were decreased with increasing electrophoretic deposition times. But, the  $V_{\text{oc}}$  was not significantly change with increasing electrophoretic deposition times. The results explained that effect of electrophoretic deposition times on photovoltaic properties was dramatic, which resulted from suspension concentration which was changed, compared with initial suspension concentration, which led to nonuniform TiO<sub>2</sub> charge quantity in TiO<sub>2</sub> suspension in repeated process of electrophoretic deposition.

3.3. Analysis of the Electrochemical Impedance Spectroscopy. Electrochemical impedance spectroscopy (EIS) is an electrochemical measurement method which inputs sinusoidal

TABLE 2: The comparison of DSSCs parameters with other references [3, 13–15].

| Sample structure | Thickness ( $\mu\text{m}$ ) | $V_{oc}$ (V) | $J_{sc}$ ( $\text{mA}/\text{cm}^2$ ) | F.F. (%) | $\eta$ (%) | Reference     |
|------------------|-----------------------------|--------------|--------------------------------------|----------|------------|---------------|
| TNP              | 6.6                         | 0.80         | 5.17                                 | 55.5     | 2.30       |               |
| TNP              | 7.5                         | 0.71         | 4.31                                 | 62.0     | 1.89       |               |
| TNP              | 7.9                         | 0.72         | 3.30                                 | 62.1     | 1.49       |               |
| TNP              | 9.0                         | 0.77         | 6.09                                 | 58.9     | 2.76       | In this study |
| TNP              | 10.6                        | 0.77         | 7.20                                 | 53.4     | 2.96       |               |
| TNP              | 12.9                        | 0.74         | 4.44                                 | 46.8     | 1.55       |               |
| TNP              | 15.9                        | 0.75         | 6.31                                 | 53.4     | 2.54       |               |
| TNP              | 10.0                        | 0.69         | 5.70                                 | 66.00    | 2.60       | [3]           |
| TNT              | 22.0                        | 0.70         | 13.90                                | 47.7     | 5.43       | [13]          |
| TNT-TNP          | 6.0                         | 0.75         | 11.50                                | 53.3     | 4.89       | [13]          |
| TNT-TNP          | 15.5                        | 0.75         | 19.50                                | 49.6     | 7.40       | [13]          |
| TNP              | 1.5                         | 0.30         | 0.49                                 | 50.0     | 0.07       | [14]          |
| TNP              | 4.2                         | 2.20         | 0.74                                 | 53.0     | 0.87       | [14]          |
| TNP              | 6.0                         | 0.75         | 7.95                                 | 74.0     | 4.37       | [15]          |

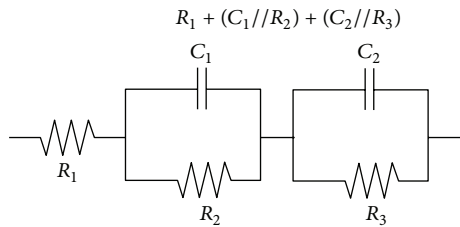


FIGURE 6: The equivalent circuit model of DSSC.

wave alternating current and the equivalent circuit model. The equivalent circuit model can describe the junction impedance, and the EIS measurement system can compute the value of junction impedance by Ohm's law. In the electrochemical system, the dye-sensitized solar cell consists of the anode electrode, the cathode electrode, and the electrolyte. Figure 6 showed the equivalent circuit model in the study. Table 3 described the physical meaning of each symbol in equivalent circuit model. Figure 7 showed the Nyquist plots of DSSCs which were prepared with different  $I_2$  dosages. The Nyquist plots were formed by real part impedance ( $\text{Re}(Z)/\text{Ohm}$ ) and imaginary impedance ( $-\text{Im}(Z)/\text{Ohm}$ ). And Table 4 showed the resistance and capacitance values which were measured by EIS. The experimental results showed increasing  $R_3$  value with increasing  $I_2$  dosage. The larger  $R_3$  value led to the fact that the electrons were more difficult to transmit at  $\text{TiO}_2/\text{dye}$  and electrolyte interface. However, the amount of absorbed dye increased with increasing the  $\text{TiO}_2$  thickness [26]. And the photovoltaic conversion efficiency had been improved.

#### 4. Conclusions

Nanocrystalline  $\text{TiO}_2$  films were deposited on FTO substrates by the electrophoretic deposition method. The film thickness and crevices numbers of  $\text{TiO}_2$  film were increased with the deposition electric field intensity. And the thickness of

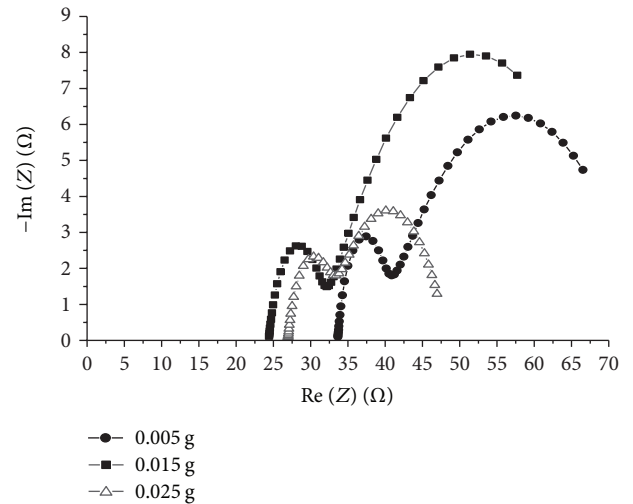
FIGURE 7: The Nyquist plots of DSSCs prepared with different  $I_2$  dosages.

TABLE 3: The physical meaning of resistances and capacitances symbols.

| Symbol     | Physical meaning   |
|------------|--|
| $R_1$      | Serial resistance of FTO glass/wire.                                 |
| $C_1//R_2$ | Impedance at Pt/electrolyte interface.                               |
| $C_2//R_3$ | Impedance at $\text{TiO}_2/\text{dye}/\text{electrolyte}$ interface. |

$\text{TiO}_2$  film increased with increasing deposition time and  $I_2$  dosage. By controlling the  $I_2$  dosages which could increase the surface electric charge of  $\text{TiO}_2$  particles, so the photovoltaic efficiency of DSSC was improved. The amount of absorbed dye was found to increase  $\text{TiO}_2$  thickness so as to improve the photovoltaic conversion efficiency of DSSC. However, the thicker  $\text{TiO}_2$  films could obtain the larger impedance at  $\text{TiO}_2$  layer. The experimental results showed that the  $\text{TiO}_2$  film deposited for 60 sec which had the optimal  $\text{TiO}_2$

TABLE 4: The resistances and capacitances values of TiO<sub>2</sub> films prepared at 60 sec with different I<sub>2</sub> dosages.

| I <sub>2</sub> dosage (g) | R <sub>1</sub> (Ω) | C <sub>1</sub> (mF) | R <sub>2</sub> (Ω) | C <sub>2</sub> (mF) | R <sub>3</sub> (Ω) |
|---------------------------|--------------------|---------------------|--------------------|---------------------|--------------------|
| 0.005                     | 33                 | 16.00               | 35                 | 0.018               | 6                  |
| 0.015                     | 24                 | 25.00               | 41                 | 0.062               | 7                  |
| 0.025                     | 27                 | 1.67                | 8                  | 0.530               | 17                 |

film thickness of 10.6 μm, the open-circuit voltage ( $V_{oc}$ ) was 0.77 V, short-circuit current density ( $J_{sc}$ ) was 7.20 mA/cm<sup>2</sup>, fill factor (F.F.) was 53.41%, and photovoltaic conversion efficiency ( $\eta$ ) was 2.96%.

## Conflict of Interests

The authors declare that there is no conflict of interests regarding the publication of this paper.

## Acknowledgment

This study has been supported by National Science Council, Taiwan, under the Contracts NSC 102-2221-E-224-075 and MOST 103-2221-E-224-073.

## References

- B. O'Regan and M. Graetzel, "Low-cost, high-efficiency solar cell based on dye-sensitized colloidal TiO<sub>2</sub> films," *Nature*, vol. 353, no. 6346, pp. 737–740, 1991.
- N. J. Smith, K. J. Emmett, and S. J. Rosenthal, "Photovoltaic cells fabricated by electrophoretic deposition of CdSe nanocrystals," *Applied Physics Letters*, vol. 93, no. 4, Article ID 043504, 2008.
- W. Jarernboon, S. Pimanpang, S. Maensiri, E. Swatsitang, and V. Amornkitbamrung, "Optimization of titanium dioxide film prepared by electrophoretic deposition for dye-sensitized solar cell application," *Thin Solid Films*, vol. 517, no. 16, pp. 4663–4667, 2009.
- J.-A. Jeong and H.-K. Kim, "Thickness effect of RF sputtered TiO<sub>2</sub> passivating layer on the performance of dye-sensitized solar cells," *Solar Energy Materials & Solar Cells*, vol. 95, no. 1, pp. 344–348, 2011.
- C.-M. Lin, Y.-C. Chang, J. Yao, C. Wang, C. Luo, and S. Yin, "Multi-step hydrothermally synthesized TiO<sub>2</sub> nanoforests and its application to dye-sensitized solar cells," *Materials Chemistry and Physics*, vol. 135, no. 2-3, pp. 723–727, 2012.
- A. I. Kontos, A. G. Kontos, D. S. Tsoukleris, M.-C. Bernard, N. Spyrellis, and P. Falaras, "Nanostructured TiO<sub>2</sub> films for DSSCs prepared by combining doctor-blade and sol-gel techniques," *Journal of Materials Processing Technology*, vol. 196, no. 1–3, pp. 243–248, 2008.
- W. A. Daoud and M. L. Turner, "Effect of interfacial properties and film thickness on device performance of bilayer TiO<sub>2</sub>-poly(1,4-phenylenevinylene) solar cells prepared by spin coating," *Reactive and Functional Polymers*, vol. 66, no. 1, pp. 13–20, 2006.
- H. Zhu, J. Yang, S. Feng, M. Liu, J. Zhang, and G. Li, "Growth of TiO<sub>2</sub> nanosheet-array thin films by quick chemical bath deposition for dye-sensitized solar cells," *Applied Physics A*, vol. 105, no. 3, pp. 769–774, 2011.
- A. Chávez-Valdez, M. Herrmann, and A. R. Boccaccini, "Alternating current electrophoretic deposition (EPD) of TiO<sub>2</sub> nanoparticles in aqueous suspensions," *Journal of Colloid and Interface Science*, vol. 375, no. 1, pp. 102–105, 2012.
- J.-E. Hu, S.-Y. Yang, J.-C. Chou, and P.-H. Shih, "Fabrication of flexible dye-sensitized solar cells with titanium dioxide thin films based on screen-printing technique," *Micro and Nano Letters*, vol. 7, no. 12, pp. 1162–1165, 2012.
- H. Chang, T. L. Chen, K. D. Huang, S. H. Chien, and K. C. Hung, "Fabrication of highly efficient flexible dye-sensitized solar cells," *Journal of Alloys and Compounds*, vol. 504, supplement 1, pp. S435–S438, 2010.
- I. Corni, M. P. Ryan, and A. R. Boccaccini, "Electrophoretic deposition: from traditional ceramics to nanotechnology," *Journal of the European Ceramic Society*, vol. 28, no. 7, pp. 1353–1367, 2008.
- H. Chang, C.-H. Chen, M.-J. Kao, S.-H. Chien, and C.-Y. Chou, "Photoelectrode thin film of dye-sensitized solar cell fabricated by anodizing method and spin coating and electrochemical impedance properties of DSSC," *Applied Surface Science*, vol. 275, pp. 252–257, 2013.
- M. Hamadani, A. Gravand, and V. Jabbari, "High performance dye-sensitized solar cells (DSSCs) achieved via electrophoretic technique by optimizing of photoelectrode properties," *Materials Science in Semiconductor Processing*, vol. 16, no. 5, pp. 1352–1359, 2013.
- I. Shin, H. Seo, M.-K. Son, J.-K. Kim, K. Prabakar, and H.-J. Kim, "Analysis of TiO<sub>2</sub> thickness effect on characteristic of a dye-sensitized solar cell by using electrochemical impedance spectroscopy," *Current Applied Physics*, vol. 10, no. 3, pp. S422–S424, 2010.
- A. R. Gardeshzadeh, B. Raissi, and E. Marzbanrad, "Electrophoretic deposition of SnO<sub>2</sub> nanoparticles using low frequency AC electric fields," *Materials Letters*, vol. 62, no. 10-11, pp. 1697–1699, 2008.
- L. Besra and M. Liu, "A review on fundamentals and applications of electrophoretic deposition (EPD)," *Progress in Materials Science*, vol. 52, no. 1, pp. 1–61, 2007.
- H. Morgan and N. G. Green, *AC Electrokinetics: Colloids and Nanoparticles*, Research Studies Press, 1st edition, 2002.
- P. Sarkar and P. S. Nicholson, "Electrophoretic deposition (EPD): mechanisms, kinetics, and application to ceramics," *Journal of the American Ceramic Society*, vol. 79, no. 8, pp. 1987–2002, 1996.
- E. V. Shevchenko, D. V. Talapin, N. A. Kotov, S. O'Brien, and C. B. Murray, "Structural diversity in binary nanoparticle superlattices," *Nature*, vol. 439, no. 7072, pp. 55–59, 2006.
- J. Zhang, S. Li, H. Ding et al., "Transfer and assembly of large area TiO<sub>2</sub> nanotube arrays onto conductive glass for dye sensitized solar cells," *Journal of Power Sources*, vol. 247, pp. 807–812, 2014.

- [22] B.-X. Lei, J.-Y. Liao, R. Zhang, J. Wang, C.-Y. Su, and D.-B. Kuang, "Ordered crystalline  $\text{TiO}_2$  nanotube arrays on transparent FTO glass for efficient dye-sensitized solar cells," *Journal of Physical Chemistry C*, vol. 114, no. 35, pp. 15228–15233, 2010.
- [23] T. Y. Lee, P. S. Alegaonkar, and J.-B. Yoo, "Fabrication of dye sensitized solar cell using  $\text{TiO}_2$  coated carbon nanotubes," *Thin Solid Films*, vol. 515, no. 12, pp. 5131–5135, 2007.
- [24] C. Randall and J. V. Tassel, "Electrophoretic deposition," in *Encyclopedia of Materials: Science and Technology*, pp. 2733–2738, Bernhard Ilshner, 2001.
- [25] B. Tan and Y. Wu, "Dye-sensitized solar cells based on anatase  $\text{TiO}_2$  nanoparticle/nanowire composites," *Journal of Physical Chemistry B*, vol. 110, no. 32, pp. 15932–15938, 2006.
- [26] L. Zhao, J. Yu, J. Fan, P. Zhai, and S. Wang, "Dye-sensitized solar cells based on ordered titanate nanotube films fabricated by electrophoretic deposition method," *Electrochemistry Communications*, vol. 11, no. 10, pp. 2052–2055, 2009.

## Research Article

# Oxidized Nano-Porous-Silicon Buffer Layers for Suppressing the Visible Photoresponsivity of ZnO Ultraviolet Photodetectors on Si Substrates

**Kuen-Hsien Wu**

*Department of Electro-Optical Engineering, Southern Taiwan University of Science and Technology, Tainan 710, Taiwan*

Correspondence should be addressed to Kuen-Hsien Wu; [khwu@mail.stust.edu.tw](mailto:khwu@mail.stust.edu.tw)

Received 20 July 2014; Accepted 16 August 2014; Published 26 August 2014

Academic Editor: Teen-Hang Meen

Copyright © 2014 Kuen-Hsien Wu. This is an open access article distributed under the Creative Commons Attribution License, which permits unrestricted use, distribution, and reproduction in any medium, provided the original work is properly cited.

This paper demonstrated the fabrication and optoelectronic characteristics of ZnO ultraviolet (UV) photodetectors fabricated on Si substrates with oxidized nano-porous-Si (ONPS) buffer layers. ONPS layers were prepared on the surfaces of Si substrates by use of an electrochemical anodization technique following a rapid-thermal-oxidation process. Experimental results indicated that application of ONPS buffer layers not only improved the crystallinity of the deposited ZnO thin films but also greatly restricted the visible-to-infrared photoresponse that was generated from the light absorption of Si substrates. The developed ZnO-on-ONPS photodiodes achieved high photoresponsivity for the incident UV light of 300 ~ 400 nm and got a large photo-to-dark current ratio up to 104 at wavelength of 375 nm under a bias of 5 V. Therefore, ZnO on ONPS provides a highly potential approach for the development of low-cost visible-blind UV photodetectors.

## 1. Introduction

Ultraviolet (UV) photodetectors are important devices due to their various applications including ozone layer monitoring, solar astronomy, missile plume detection, space communications, fire alarm, and combustion monitoring [1, 2]. Of particular value are visible-blind and solar-blind UV detectors, whose low sensitivity for visible and infrared (IR) light can ensure accurate measurement in the UV with minimal background. At present, commercial solid-state UV photodetectors still mostly use Si-based optical devices. Nevertheless, these devices are sensitive to visible and infrared radiation and have small responsivity in UV regions because of the low bandgap energy of Si. Current researches on visible-blind UV photodetectors mainly concentrated on the III-nitride materials [3, 4]. However, epitaxial processing of III-nitride thin films is quite difficult and is not compatible with the Si integrated circuit process. Therefore, it is not easy to reduce the cost of related products for commercial applications.

As a wide- and direct-bandgap semiconductor material, zinc oxide (ZnO) has been considered a promising candidate for UV detecting applications [5, 6]. But, it is difficult

to obtain high-quality ZnO films directly growing on Si substrates due to the large differences in the lattice constant and the thermal expansion coefficient between ZnO and Si. Hence, the applications of ZnO-on-Si devices were limited.

In recent year, owing to the low price and ready availability of Si substrates as well as the compatibility with Si integrated-circuit fabrication process, hetero growth of ZnO films on porous Si (PS) has become an important method for the development of novel devices [7–10]. Many studies pointed out that the special sponge-like structures of PS can assist nucleation reaction and reduce the stress in the hetero-epitaxial films. Some materials grown on PS got better film crystallinity and film quality than those grown directly on silicon substrates [11–13]. Furthermore, preparation process of PS from Si wafers is quite simple by using an electrochemical anodization technique. Therefore, the combination of ZnO and PS is very potential for development of low-cost UV photodetectors [14, 15]. Unfortunately, ZnO-on-PS UV photodetectors are still not visible-blind because PS materials are sensitive to visible and IR radiation.

In this work, ZnO UV photodetectors with highly restricted photoresponsivity to visible and IR light were

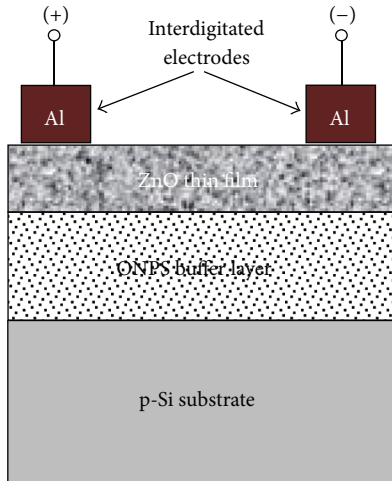


FIGURE 1: Schematic device structure of the ZnO photodiode fabricated on a Si substrate with an oxidized nano-porous-Si (ONPS) buffer layer.

fabricated on Si substrates by introducing oxidized nano-porous-Si (ONPS) as the buffer layers.

## 2. Materials and Methods

Heavily doped ( $3\sim 5\text{ m}\Omega\text{-cm}$ )  $p^+$ -type (100) Si wafers were used as the starting substrates. After a standard RCA cleaning process, nano-porous-Si (NPS) layers were prepared on Si substrates by an electrochemically anodic etching technique. The anodization was carried out in an etching solution with concentration ratio of  $\text{HF}:\text{ethanol}:\text{H}_2\text{O} = 3:1:1$ , under etching current density of  $10\text{ mA/cm}^2$ . Then, NPS layers were transformed into ONPS layers through a rapid-thermal-oxidation (RTO) process. According to Lee et al. [16], the photoconductance of an oxidized PS layer increased with the oxidation time ( $t_{\text{ox}}$ ) or oxidation temperature ( $T_{\text{ox}}$ ) to a maximum value and then reduced for higher  $t_{\text{ox}}$  or  $T_{\text{ox}}$ . To obtain high photoresponsivity of devices, a  $t_{\text{ox}}$  of 60 s and a  $T_{\text{ox}}$  of  $800^\circ\text{C}$  were employed in the RTO process based on the empirical results of experiments. After the formation of ONPS buffer layers, ZnO thin films were deposited on the samples by sputtering under RF power of 100 W and Ar pressure of 12.6 mTorr at room temperature. The samples were then annealed under different temperatures in  $\text{N}_2$  ambient to improve the crystallinity of ZnO films. Finally, aluminum (Al) interdigitated electrodes were deposited on the top of the samples by an e-beam evaporator to complete the device structure of a metal-semiconductor-metal (MSM) photodiode, as shown in Figure 1. The structure of the developed ZnO UV photodiode contained, from top to bottom, 500 nm Al interdigitated electrodes, a 100 nm ZnO film, a  $3.5\ \mu\text{m}$  ONPS layer, and a 300 mm p-Si substrate.

The morphology of ZnO films and ONPS layers was observed by field-emission scanning electron microscopy (FE-SEM). The crystallinity of ZnO thin films was characterized by X-ray diffraction (XRD). Analysis of optoelectronic

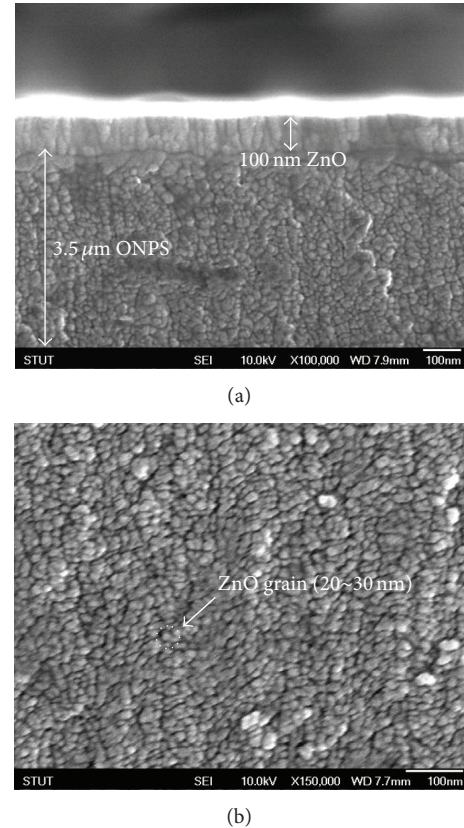


FIGURE 2: SEM images of the as-deposited ZnO thin films on the ONPS layer. (a) The cross-sectional view and (b) the top view.

characteristics of photodiodes was carried out by a photoresponse measurement system with a TRIAX320 spectrometer. The current-voltage characteristics of devices were measured by an HP-4155A semiconductor parameter analyzer.

## 3. Results and Discussion

Figure 2 showed the SEM images of samples with the as-deposited ZnO thin films on ONPS buffer layers. From Figure 2(a), the cross-sectional view of the sample, we can observe that a ZnO thin film with thickness of about 100 nm was deposited on a  $3.5\ \mu\text{m}$  ONPS layer that was prepared on a Si substrate. As shown in Figure 2(b), the top view of the sample, the deposited ZnO film had a smooth surface and contained uniformly distributed grains with average sizes of about 20 nm~30 nm.

X-ray diffraction (XRD) patterns of the deposited ZnO film on ONPS at different annealing temperatures were shown in Figure 3. The obtained ZnO film had a polycrystalline structure with two obvious diffraction peaks at  $34.395^\circ$  and  $62.78^\circ$ , which are corresponding to ZnO (002) and ZnO (103), respectively. The intensity of diffraction peak increased with the annealing temperature, indicating that the crystallinity of the ZnO films was improved at higher annealing temperatures.

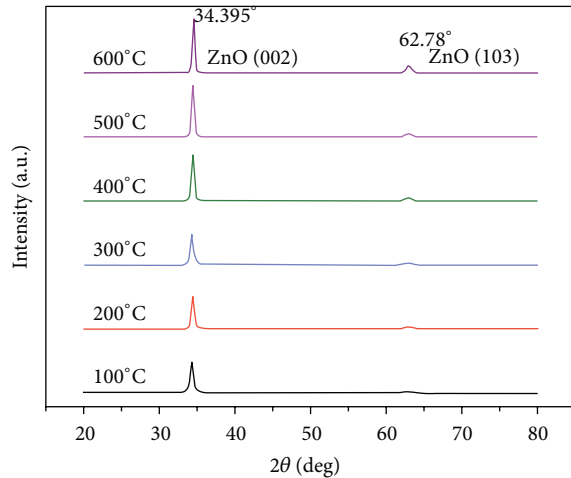


FIGURE 3: X-ray diffraction patterns of ZnO films deposited on ONPS layers of Si substrates for different annealing temperatures.

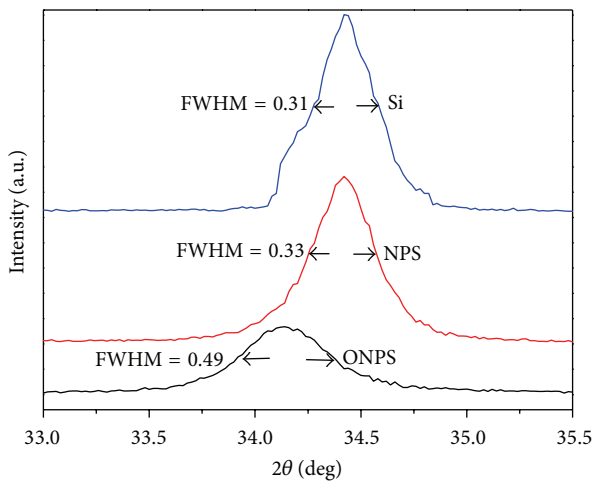


FIGURE 4: Selected X-ray diffraction patterns of ZnO films deposited on different substrates.

Figure 4 showed the selected X-ray diffraction patterns of ZnO films deposited on different substrates for  $2\theta = 33^\circ \sim 35.5^\circ$ . We can observe that the value of full width at half maximum (FWHM) of the main peak for the ZnO film deposited on ONPS was approximately equal to that of the ZnO on NPS, while it was lower than that of ZnO on Si. This result confirmed that the film quality of ZnO deposited on NPS or ONPS was better than that on a bare Si substrate and indicated both NPS and ONPS buffer layers can help to improve the film crystallinity of ZnO hetero growth on a Si substrate.

Figure 5 illustrated the photoresponse spectra of ZnO photodiodes fabricated on Si substrates with NPS or ONPS buffer layers. It was found that ZnO-on-NPS devices had high responsivity to the 300~400 nm UV light, but they also strongly respond to the 600~1000 nm irradiation which

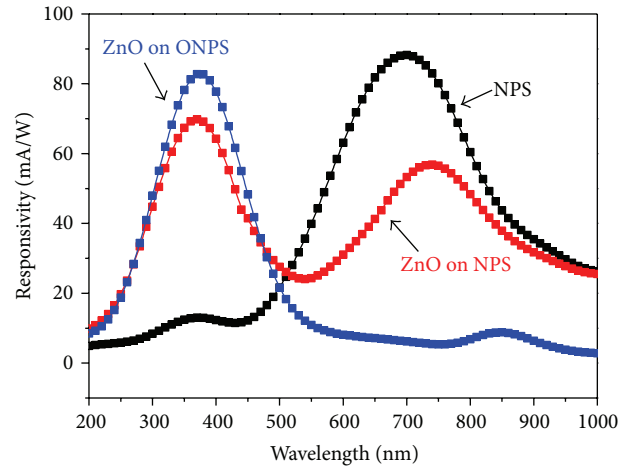


FIGURE 5: Photoresponse spectra of ZnO photodiodes prepared on Si substrates with NPS and ONPS buffer layers, respectively. For comparison purpose, the photoresponse spectra of a bare NPS layer on a Si substrate were also included in the figure.

corresponded to the visible-to-IR light. It is disadvantageous to exhibit visible and IR response for a UV photodetector for some special purposes. To clarify the origin of the non-UV photoresponse, the photoresponse spectra of a bare NPS layer prepared on a Si substrate were also measured and also shown in Figure 5. It was observed that the photoresponse of NPS-on-Si mostly appeared within visible-to-IR regions. In addition, the optical bandgap of the prepared NPS and ZnO films that was measured from Tauc's plots was 1.6 eV and 3.2 eV, respectively. Thus, it can be inferred that the visible-to-IR response of a ZnO-on-NPS device mainly came from the light absorption of NPS layers. In order to restrict the non-UV absorption, NPS layers were converted into ONPS with a RTO process before the ZnO deposition. It was found the ZnO-on-ONPS device achieved high 300~400 nm UV photoresponsivity as shown in Figure 5. Most importantly, the visible-to-IR photoresponse above 500 nm almost disappeared in these devices. Because the optical bandgap of ONPS measured from Tauc's plots was about 3.5 eV that corresponded to an absorption wavelength of 350 nm, an ONPS layer was only sensitive to UV light. That is, the ONPS buffer layer not only contributed UV response to devices but also largely suppressed the visible-to-IR response originating from the light absorption of Si substrates. Therefore, UV-to-visible/IR rejection ratio of the developed ZnO photodiode fabricated on a Si substrate can be greatly enhanced by introduction of an ONPS buffer layer.

Current-voltage characteristics of the ZnO-on-ONPS photodiode with and without UV illumination were shown in Figure 6. The photocurrent was measured under irradiating light with wavelength of 375 nm and power of  $0.08 \text{ mW/cm}^2$ . At a 5-V bias, the measured photocurrent was  $4.74 \text{ mA/cm}^2$  and the dark current was  $4.56 \times 10^{-2} \text{ mA/cm}^2$ . The photo-to-dark current ratio (PDCR) was calculated up to about 104, indicating that the developed device was highly sensitive to UV light.

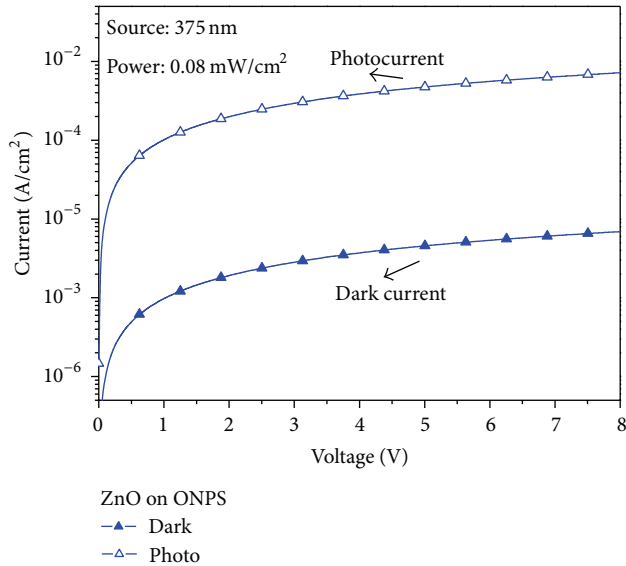


FIGURE 6: Current-voltage characteristics of the ZnO photodiode fabricated on a Si substrate with an ONPS buffer layer.

#### 4. Conclusions

ZnO thin films with smooth surfaces and uniformly distributed grains had been successfully deposited on Si substrates with NPS and ONPS buffer layers. XRD measurement showed that the crystallinity of the deposited ZnO thin films on both buffer layers was better than that deposited directly on Si substrates. ZnO-on-NPS devices exhibited high UV and visible-to-IR photoresponsivity. The undesirable visible-to-IR response above 500 nm was almost eliminated in ZnO-on-ONPS devices. The developed ZnO-on-ONPS photodiodes achieved high photocurrent and high PDCR, demonstrating that ZnO on ONPS had high potential in the development of low-cost UV photodetectors.

#### Conflict of Interests

The author declares that he has no competing interests.

#### Acknowledgments

The author acknowledges financial support from the Ministry of Science and Technology of R. O. C under Contract no. NSC 102-2221-E-218-038.

#### References

- [1] M. Razeghi and A. Rogalski, "Semiconductor ultraviolet detectors," *Journal of Applied Physics*, vol. 79, no. 10, pp. 7433–7473, 1996.
- [2] E. Monroy, F. Omnes, and F. Calle, "Wide-bandgap semiconductor ultraviolet photodetectors," *Semiconductor Science and Technology*, vol. 18, no. 4, pp. R33–R51, 2003.
- [3] M. Razeghi, "III-nitride optoelectronic devices: from ultraviolet toward terahertz," *IEEE Photonics Journal*, vol. 3, no. 2, pp. 263–267, 2011.

- [4] G. Wang, H. Lu, D. Chen, F. Ren, R. Zhang, and Y. Zheng, "High quantum efficiency GaN-based p-i-n ultraviolet photodetectors prepared on patterned sapphire substrates," *IEEE Photonics Technology Letters*, vol. 25, no. 7, pp. 652–654, 2013.
- [5] S. J. Young, L. W. Ji, S. J. Chang, and Y. K. Su, "ZnO metal-semiconductor-metal ultraviolet sensors with various contact electrodes," *Journal of Crystal Growth*, vol. 293, no. 1, pp. 43–47, 2006.
- [6] L. Luo, Y. F. Zhang, S. S. Mao, and L. W. Lin, "Fabrication and characterization of ZnO nanowires based UV photodiodes," *Sensors and Actuators A*, vol. 127, no. 2, pp. 201–206, 2006.
- [7] H.-C. Hsu, C.-S. Cheng, C.-C. Chang, S. Yang, C.-S. Chang, and W.-F. Hsieh, "Orientation-enhanced growth and optical properties of ZnO nanowires grown on porous silicon substrates," *Nanotechnology*, vol. 16, no. 2, pp. 297–301, 2005.
- [8] E. Kayahan, "White light luminescence from annealed thin ZnO deposited porous silicon," *Journal of Luminescence*, vol. 130, no. 7, pp. 1295–1299, 2010.
- [9] B. Zhao, Q.-S. Li, H.-X. Qi, and N. Zhang, "White light emission from the composite system of ZnO/porous Si," *Chinese Physics Letters*, vol. 23, no. 5, pp. 1299–1301, 2006.
- [10] R. G. Singh, F. Singh, V. Agarwal, and R. M. Mehra, "Photoluminescence studies of ZnO/porous silicon nanocomposites," *Journal of Physics D: Applied Physics*, vol. 40, no. 10, article 012, pp. 3090–3093, 2007.
- [11] T. W. Kang, J. Y. Leem, and T. W. Kim, "Growth of GaAs epitaxial layers on porous silicon," *Microelectronics Journal*, vol. 27, no. 4–5, pp. 423–436, 1996.
- [12] A. Matoussi, T. Boufaden, A. Missaoui et al., "Porous silicon as an intermediate buffer layer for GaN growth on (100) Si," *Microelectronics Journal*, vol. 32, no. 12, pp. 995–998, 2011.
- [13] Y. Liao, F. Ye, Q. Y. Shao, C. Chang, G. Z. Wang, and R. C. Fang, "Study of diamond film growth mechanism on porous silicon during hot-filament chemical vapor deposition," *Thin Solid Films*, vol. 368, no. 2, pp. 211–215, 2000.
- [14] M. Rajabi, R. S. Dariani, and A. Iraj Zad, "UV photodetection of laterally connected ZnO rods grown on porous silicon substrate," *Sensors and Actuators A: Physical*, vol. 180, pp. 11–14, 2012.
- [15] A. M. Suhail, S. Salman, F. E. Naoum, H. A. Thjeel, and Q. G. Al zaidi, "ZnO/Porous-silicon photovoltaic UV detector," *Journal of Electron Devices*, vol. 13, pp. 900–909, 2012.
- [16] M. K. Lee, Y. H. Wang, and C. H. Chu, "High-sensitivity porous silicon photodetectors fabricated through rapid thermal oxidation and rapid thermal annealing," *IEEE Journal of Quantum Electronics*, vol. 33, no. 12, pp. 2199–2202, 1997.

## Research Article

# AlGa<sub>N</sub>/Ga<sub>N</sub> High Electron Mobility Transistors with Multi-Mg<sub>x</sub>N<sub>y</sub>/Ga<sub>N</sub> Buffer

P. C. Chang,<sup>1</sup> K. H. Lee,<sup>2</sup> Z. H. Wang,<sup>1</sup> and S. J. Chang<sup>3</sup>

<sup>1</sup> Department of Electro-Optical Engineering, Kun Shan University, Yong-Kang District, Tainan 71003, Taiwan

<sup>2</sup> National Synchrotron Radiation Research Center, Hsinchu 30076, Taiwan

<sup>3</sup> Department of Electrical Engineering and Institute of Microelectronics, Center for Micro/Nano Science and Technology, Advanced Optoelectronic Technology Center, National Cheng Kung University, Tainan 70101, Taiwan

Correspondence should be addressed to P. C. Chang; [pcchang@mail.ksu.edu.tw](mailto:pcchang@mail.ksu.edu.tw)

Received 27 March 2014; Revised 28 April 2014; Accepted 9 May 2014; Published 20 July 2014

Academic Editor: Liang-Wen Ji

Copyright © 2014 P. C. Chang et al. This is an open access article distributed under the Creative Commons Attribution License, which permits unrestricted use, distribution, and reproduction in any medium, provided the original work is properly cited.

We report the fabrication of AlGa<sub>N</sub>/Ga<sub>N</sub> high electron mobility transistors with multi-Mg<sub>x</sub>N<sub>y</sub>/Ga<sub>N</sub> buffer. Compared with conventional HEMT devices with a low-temperature Ga<sub>N</sub> buffer, smaller gate and source-drain leakage current could be achieved with this new buffer design. Consequently, the electron mobility was larger for the proposed device due to the reduction of defect density and the corresponding improvement of crystalline quality as result of using the multi-Mg<sub>x</sub>N<sub>y</sub>/Ga<sub>N</sub> buffer.

## 1. Introduction

GaN-based materials demonstrate an outstanding potential for significantly advancing the solid-state electronic and optoelectronic technologies. However, there are still no suitable substrates that are commercially available for homoepitaxial growth of GaN thin films. Instead, devices must be grown heteroepitaxially on sapphire or other substrates with an expense of high lattice mismatch. As of result, extremely high threading dislocation (TD) densities are thus generated. Very recently, it was found that GaN epitaxial layer prepared on multi-Mg<sub>x</sub>N<sub>y</sub>/Ga<sub>N</sub> buffer exhibited a reduced TD density and better crystalline quality. In addition, we have also reported high performance Schottky barrier diodes or photodetectors on multi-Mg<sub>x</sub>N<sub>y</sub>/Ga<sub>N</sub> buffer [1]. In this paper, we extend the applicability of this buffer scheme by fabricating AlGa<sub>N</sub>/Ga<sub>N</sub> high electron mobility transistors (HEMTs) on multi-Mg<sub>x</sub>N<sub>y</sub>/Ga<sub>N</sub> buffer. Physical and electrical properties of the fabricated HEMTs will also be discussed afterward.

## 2. Materials and Methods

All of the samples used in this study were grown on c-face (0001) sapphire substrates by metalorganic vapor phase epitaxy (MOVPE) system. Al<sub>0.22</sub>Ga<sub>0.78</sub>N/GaN HEMTs structure

with a conventional low temperature Ga<sub>N</sub> buffer layer (i.e., sample A) and a multi-Mg<sub>x</sub>N<sub>y</sub>/Ga<sub>N</sub> buffer (i.e., sample B) were both prepared. Detailed growth procedures of these HEMT structures can be found elsewhere [2]. Device fabrication started with mesa isolation using BCl<sub>3</sub> etchants from the reactive ion etching system. Ohmic contacts were formed by thermal evaporation of Ti/Al/Ti/Au (13/80/13/60 nm) metals, which were subsequently annealed at 800°C for 8 min in N<sub>2</sub> ambient. Finally, Ni and Au (40/100 nm) were used for gate electrodes with a dimension of 1 × 50 μm<sup>2</sup>. The schematic device structure can be found in Table 1. Device performance was measured at room temperature by using an HP-4155B semiconductor parameter analyzer for DC characteristics, an HP-4284A LCR meter for capacitance-voltage (C-V) measurements.

## 3. Results and Discussion

Electron mobility ( $\mu$ ) of sample A and sample B was measured at temperatures from 120 K to 500 K using Hall-effect measurement technique with van der Pauw configuration. As shown in Figures 1(a) and 1(b), the theoretical  $\mu$  is limited by the various scattering mechanisms, such as piezoelectric, acoustic-mode deformation potential, and polar optical

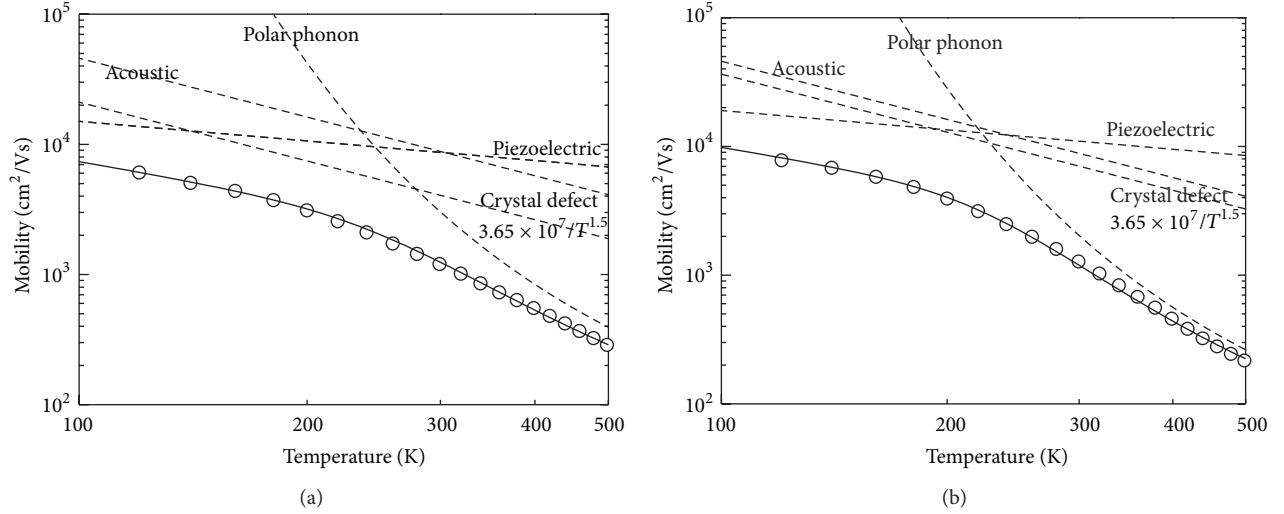


FIGURE 1: Temperature-dependent mobility of (a) sample A and (b) sample B.

TABLE I: The schematic device structures of samples A and B.

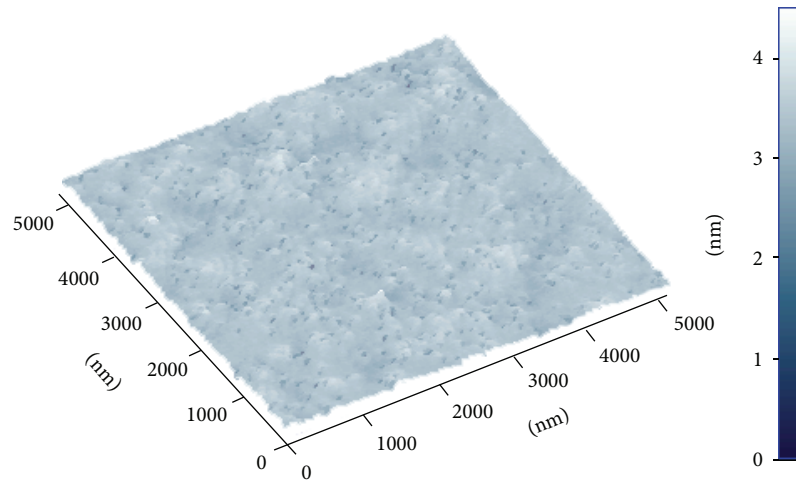
| Sample A  | Sample B  |
|---|---|
| 20 nm $n\text{-Al}_{0.22}\text{Ga}_{0.78}\text{N}$ ( $1 \times 10^{17} \text{ cm}^{-3}$ ) | 20 nm $n\text{-Al}_{0.22}\text{Ga}_{0.78}\text{N}$ ( $1 \times 10^{17} \text{ cm}^{-3}$ ) |
| 2.2 $\mu\text{m}$ un-GaN  | 2.2 $\mu\text{m}$ un-GaN  |
| LT-GaN buffer   | multi-Mg <sub>x</sub> N <sub>y</sub> /GaN buffer  |
| Sapphire  | Sapphire  |

phonon, assuming that Matthiessen's rule [3] is applied. A good fit is obtainable at low temperature, while a large deviation occurs at high temperature. Therefore, besides the aforementioned scattering mechanisms, scattering due to extended crystalline defects such as TDs and planar defects may also be significant and must be taken into account in order to achieve a good fit especially at high temperature. The strain associated with and the charge collected at these defects may introduce a potential that tends to scatter electrons. In our work, the empirical limit of crystal defect function with the form of  $C/T^{1.5}$  at high temperature has to be included. It was found that the fitting parameter  $C$  is equal to  $2.11 \times 10^7$  and  $3.65 \times 10^7$  for samples A and B, respectively. It was also found that  $\mu$  below the room temperature was higher in sample B compared to that of sample A. The larger magnitudes of  $C$  and  $\mu$  observed from sample B suggest smaller defect density and better crystalline quality. On the other hand, the reason for observing sample A with lower  $\mu$  at higher temperature remains unclear. One possible cause could be due to the fields being induced by the domain boundaries or a change of strain as a result of incorporating the multi-Mg<sub>x</sub>N<sub>y</sub>/GaN buffer.

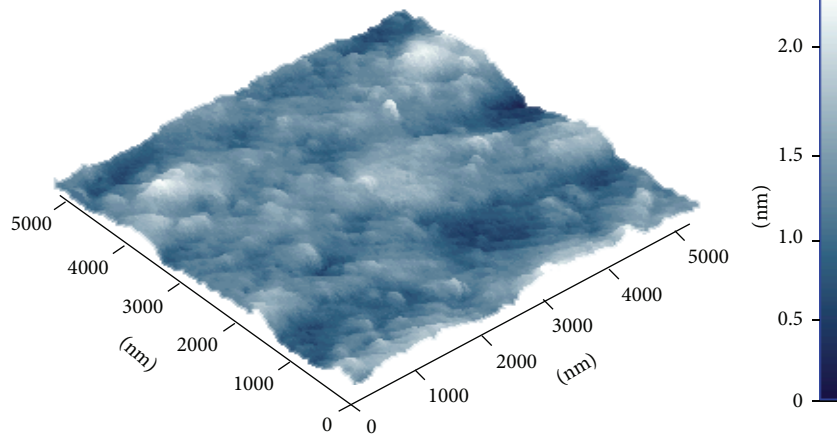
Atomic force microscopy (AFM) was also used to characterize these two samples. Figures 2(a) and 2(b) show AFM images ( $5 \times 5 \mu\text{m}^2$ ) of samples A and B, respectively. As shown in Figure 2(a), dark pits can be clearly observed from sample A. These pits generally originate from the surface

termination of TDs and are thought to be one of the leakage current sources in GaN-based devices [4]. In contrast, a more flat surface with invisible dark pits is observed from sample B. Therefore, one suggests that the multi-Mg<sub>x</sub>N<sub>y</sub>/GaN buffer could significantly improve the crystalline quality and thereby reduce the TD-related leakage paths. This agrees well with the aforementioned results obtained by Hall-effect measurement.

HEMT was fabricated as follows: mesa etching was performed by a reactive ion etcher for device isolation. Ti/Al/Ti/Au (13 nm/80 nm/13 nm/60 nm) was subsequently deposited on the samples as the source and drain contact electrodes, followed by 800°C furnace annealing in N<sub>2</sub> ambient for 8 min. Finally,  $1 \mu\text{m} \times 50 \mu\text{m}$  Ni/Au (40 nm/100 nm) gate metal was deposited on the samples. HEMT device performances were measured using an HP 4155 semiconductor parameter analyzer. Figures 3(a) and 3(b) show the drain-source current ( $I_{\text{DS}}$ ) as a function of the drain-source voltage ( $V_{\text{DS}}$ ) when the gate-source voltage ( $V_{\text{GS}}$ ) was varied from 1 to  $-5 \text{ V}$  with a step of  $-0.5 \text{ V}$  for sample A and sample B, respectively. As shown in Figure 3(b), sample B is completely pinched off at  $V_{\text{GS}}$  of  $-1 \text{ V}$ . On the other hand, the source-drain (S-D) leakage current of sample A was relatively large. For example, with  $V_{\text{DS}} = 10 \text{ V}$  and  $V_{\text{GS}} = -5 \text{ V}$  applied, the resultant S-D leakage current was as high as 6.9 mA/mm for sample A, as shown in Figure 3(a). In other words, the transistor corresponding to sample A could not be turned off completely, even with a large negative gate bias applied. It has been reported that nonisolated channel or poor Schottky gate contact could result in a large S-D leakage current in HEMT devices [5]. However, since the same processing condition was implemented on both samples, we believe that the large S-D leakage current was originated instead from the 2.2  $\mu\text{m}$  thick unintentionally doped GaN layer. It was found that GaN epitaxial layer prepared on multi-Mg<sub>x</sub>N<sub>y</sub>/GaN buffer exhibited higher carrier mobility and lower background concentration, which lead to lower S-D leakage current and better pinch-off characteristic.

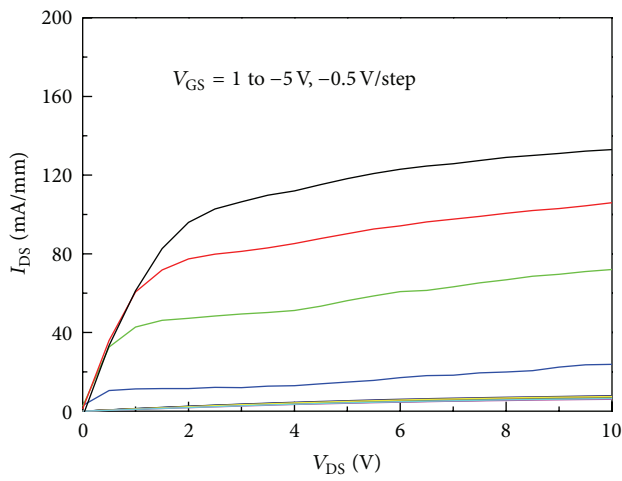


(a)

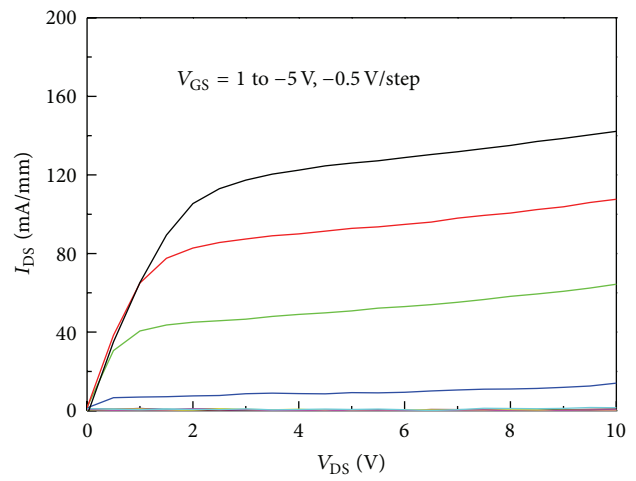


(b)

FIGURE 2: AFM images of (a) sample A and (b) sample B.



(a)



(b)

FIGURE 3: Output characteristics of drain-source current ( $I_{DS}$ ) as a function of drain-source voltage ( $V_{DS}$ ) of (a) sample A and (b) sample B. Gate-source voltage ( $V_{GS}$ ) varied from 1 V to -5 V with step of -0.5 V.

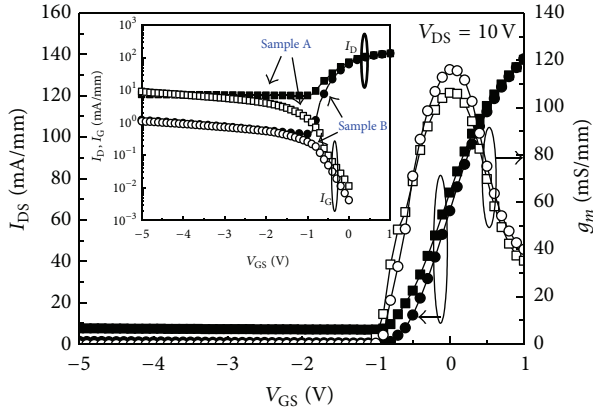


FIGURE 4: Drain-source current ( $I_{DS}$ ) and transconductance ( $g_m$ ) as a function of gate-source voltage ( $V_{GS}$ ) of both samples. The inset shows pinch-off characteristics of both samples at  $V_{DS} = 10$  V.

The  $I_{DS}$  and the transconductance ( $g_m$ ) as a function of  $V_{GS}$  at  $V_{DS} = 10$  V are shown in Figure 4. It was found that the maximum extrinsic  $g_m$  values were 106 and 116 mS/mm for samples A and B, respectively. The enhancement of  $g_m$  could be attributed to the higher carrier mobility and better pinch-off characteristic obtained from sample B with multi-Mg<sub>x</sub>N<sub>y</sub>/GaN buffer. The inset of Figure 4 shows pinch-off characteristics at  $V_{DS} = 10$  V of both samples, including sub-threshold  $I_D$ - $V_{GS}$  and gate leakage current ( $I_G$ )- $V_{GS}$  curves. Sample B demonstrated a larger subthreshold slope compared to that of sample A. Furthermore, sample B also showed larger  $I_{on}/I_{off}$  ratio compared to that of sample A. These results were attributed to the lower pinch-off current associated with sample B. In addition, we also found that  $I_G$  of sample B was one order of magnitude lower than that of sample A. Lower gate and S-D leakage currents thus obtained both suggest that the pinch-off characteristics of HEMT could be substantially improved through the incorporation of the multi-Mg<sub>x</sub>N<sub>y</sub>/GaN buffer.

#### 4. Conclusions

In summary, AlGaIn/GaN HEMTs with conventional low temperature GaN buffer and with multi-Mg<sub>x</sub>N<sub>y</sub>/GaN buffer were both fabricated. It was found that the gate and S-D leakage current of the HEMTs could be substantially reduced by using multi-Mg<sub>x</sub>N<sub>y</sub>/GaN buffer. The improvements in transfer and pinch-off characteristics of the HEMTs were also realized by the adoption of the multi-Mg<sub>x</sub>N<sub>y</sub>/GaN buffer scheme.

#### Conflict of Interests

The authors declare that there is no conflict of interests regarding the publication of this paper.

#### Acknowledgments

This work was financially supported by the National Science Council under Contract nos. NSC NSC 101-2221-E-168-024 and NSC 102-2221-E-168-027.

#### References

- [1] K. H. Lee, S. J. Chang, P. C. Chang, Y. C. Wang, and C. H. Kuo, "High quality GaN-based Schottky barrier diodes," *Applied Physics Letters*, vol. 93, no. 13, Article ID 132110, 2008.
- [2] S. J. Chang, K. H. Lee, P. C. Chang et al., "AlGaIn/GaN Schottky barrier photodetector with multi-Mg<sub>x</sub>N<sub>y</sub>/GaN buffer," *IEEE Sensors Journal*, vol. 9, no. 2, pp. 87–92, 2009.
- [3] H. Tang, W. Kim, A. Botchkarev, G. Popovici, F. Hamdani, and H. Morkoç, "Analysis of carrier mobility and concentration in Si-doped GaN grown by reactive molecular beam epitaxy," *Solid-State Electronics*, vol. 42, no. 5, pp. 839–847, 1998.
- [4] J. K. Sheu, M. L. Lee, and W. C. Lai, "Effect of low-temperature-grown GaN cap layer on reduced leakage current of GaN Schottky diodes," *Applied Physics Letters*, vol. 86, Article ID 052103, 2005.
- [5] Y. S. Lin, Y. W. Lian, J. M. Yang et al., "Contact engineering of GaN-on-silicon power devices for breakdown voltage enhancement," *Semiconductor Science and Technology*, vol. 28, no. 7, Article ID 074018, 2013.

## Research Article

# Investigation of the Optimal Parameters in Hydrothermal Method for the Synthesis of ZnO Nanorods

Ying-Chung Chen,<sup>1</sup> Huan-Yi Cheng,<sup>1</sup> Cheng-Fu Yang,<sup>2</sup> and Yuan-Tai Hsieh<sup>3</sup>

<sup>1</sup> Department of Electrical Engineering, National Sun Yat-Sen University, Kaohsiung 80424, Taiwan

<sup>2</sup> Department of Chemical and Materials Engineering, National University of Kaohsiung, Kaohsiung 81147, Taiwan

<sup>3</sup> Department of Electronic Engineering, Southern Taiwan University, Tainan 71005, Taiwan

Correspondence should be addressed to Cheng-Fu Yang; [cfyang@nuk.edu.tw](mailto:cfyang@nuk.edu.tw)

Received 7 May 2014; Accepted 16 June 2014; Published 25 June 2014

Academic Editor: Teen-Hang Meen

Copyright © 2014 Ying-Chung Chen et al. This is an open access article distributed under the Creative Commons Attribution License, which permits unrestricted use, distribution, and reproduction in any medium, provided the original work is properly cited.

We investigated a two-step method to deposit the ZnO-based nanostructure films, including nanorods and nanoflowers. In the first step, sputtering method was used to deposit the ZnO films on SiO<sub>2</sub>/Si substrates as the seed layer. In the second step, Zn(NO<sub>3</sub>)<sub>2</sub>·6H<sub>2</sub>O and C<sub>6</sub>H<sub>12</sub>N<sub>4</sub> were used as precursors and hydrothermal process was used as the method to synthesize the ZnO films. After that, the ZnO films were measured by an X-ray diffraction pattern and a FESEM to analyze their crystallization and morphology. We had found that the ZnO films had three different morphologies synthesized on ZnO/SiO<sub>2</sub>/Si substrates, including irregular-plate structure films, nanorod films, and beautiful chrysanthemum-like clusters (nanoflower films). We would prove that the face direction of ZnO/SiO<sub>2</sub>/Si substrates in the hydrothermal bottle and deposition time were two important factors to influence the synthesized results of the ZnO films.

## 1. Introduction

Transparent conducting oxide (TCO) films based on zinc oxide (ZnO) are promising candidates for applications in various optoelectronic devices. However, ZnO-based films present a lot of advantages such as higher transparency in infrared region and high chemical stability under the hydrogen plasma as compared to tin-doped indium oxide (ITO). For that, transparent conducting ZnO-based films have already been extensively used in solar cells, light-emitting diodes, and liquid crystal displays as a substitute for ITO [1]. ZnO nanorods have attracted much attention of researchers due to their various applications such as solar cells [2], light-emitting diodes [3], and super hydrophobic surfaces [4]. ZnO nanorods are also considered as a promising material of gas sensors because of its high electrochemical stability, nontoxicity, suitability to doping, and low material cost [5]. The sensing characteristics of a sensor depend on the shape and dimensionality of the sensing material a lot, so that multiply ZnO nanostructures have been synthesized

and studied in the past decade. Those researches have shown that one-dimensional (1D) ZnO nanostructures possess a large surface-to-volume ratio, which can absorb more tested molecules on the surface and have high gas-sensing efficiency [5–7].

Up to now, 1D ZnO-based nanotubes, nanowires, nanorods, and nanotetrapods have been synthesized by various physical and chemical methods and used to fabricate gas sensors. Synthesis of the ZnO nanorods based on vapor phase deposition, such as metal-organic chemical vapor deposition, vapor-liquid-solid reaction, vapor-solid reaction, chemical vapor deposition, and pulsed laser deposition are expensive methods because of the sophisticated equipment or high temperature required [8]. In contrast to the above growth techniques, the aqueous solution growth method can be a simple and cost-effective technique because it has no drawbacks of expensive apparatus, rigorous condition, complex process, low yield, and high temperature needed. Recently, a hydrothermal method has also been developed to fabricate 1D ZnO nanostructures. Jiaqiang et al. had

prepared ZnO nanorods by a hydrothermal process with cetyltrimethyl ammonium bromide and zinc powder at 182°C [9]; Li et al. had synthesized ultralong ZnO nanowires by a hydrothermal reaction of Zn foil and aqueous  $\text{Na}_2\text{C}_2\text{O}_4$  solution at 140°C [6]; Kim and Yong had synthesized ZnO nanorod-bundle powders by a hydrothermal reaction using zinc chloride and ammonium hydroxide solution at 150°C [7]. Those results prove that the hydrothermal method provides a convenient and low cost route for the construction of rod- or wire-typed ZnO nanostructures. Herein, we used  $\text{SiO}_2/\text{Si}$  as substrates and investigated a two-step method to find a simple process for growing ZnO-based nanorods. In the first step, the ZnO seed layer was deposited using sputter method. In the second step, we used  $\text{Zn}(\text{NO}_3)_2 \cdot 6\text{H}_2\text{O}$  and  $\text{C}_6\text{H}_{12}\text{N}_4$  (Hexamethylenetetramine, HMTA) as precursors to develop a low-temperature hydrothermal route (at 100°C) for synthesizing the nanorod-typed ZnO nanostructures. We would show that faces' direction of ZnO/ $\text{SiO}_2/\text{Si}$  substrates in the hydrothermal bottle and deposition time were two important factors to grow the ZnO nanorods.

## 2. Experimental

ZnO powder was mixed with polyvinylalcohol (PVA) as binder, and then the mixed powder was uniaxially pressed into pellets of 5 mm thickness and 54 mm diameter using a steel die. After debinding, the ZnO pellets were sintered at 1200°C for 2 h.  $\text{SiO}_2/\text{Si}$  substrates with an area of  $2 \times 2 \text{ cm}^2$  were cleaned ultrasonically with isopropyl alcohol (IPA) and deionized (DI) water and then dried under a blown nitrogen gas. Our growth procedure for ZnO-based nanostructures consisted of two steps. At the first step, ZnO targets were used to deposit ZnO films with a thickness of  $\sim 300 \text{ nm}$  by sputtering deposition technique to form the ZnO/ $\text{SiO}_2/\text{Si}$  substrates. ZnO films were subsequently used as seed layer for the growth of ZnO nanostructures. The deposition parameters for seed layer were RF power of 85 W, working pressure of  $15 \times 10^{-3} \text{ Torr}$  in pure Ar (99.99%) ambient, deposition at room temperature (RT), and the deposition time of 30 min, respectively. In the second step, ZnO nanostructures were grown on seed-deposition ZnO/ $\text{SiO}_2/\text{Si}$  substrates from an equimolar aqueous solution of  $\text{Zn}(\text{NO}_3)_2 \cdot 6\text{H}_2\text{O}$  (99.9% purity) and  $\text{C}_6\text{H}_{12}\text{N}_4$  (99.9% purity, Hexamethylenetetramine, HMTA) in deionized water [10–12]. In order to fabricate ZnO nanorods,  $\text{Zn}(\text{NO}_3)_2 \cdot 6\text{H}_2\text{O}$  and  $\text{C}_6\text{H}_{12}\text{N}_4$  were used as reagents, the diluted solution with concentration of 0.1 M in DI water, and volume of DI water was 20 g. After mixing at 65°C for 40 min the diluted solution was put into a bottle and the ZnO nanostructures were synthesized on the seed ZnO/ $\text{SiO}_2/\text{Si}$  layer by using hydrothermal process at 100°C for 1 h, 3 h, and 5 h, respectively. The sketch of the experimental set for growing ZnO nanostructure films was shown in Figure 1, two different directions were compared in this study, and ZnO films were deposited on both up and down faces of ZnO/ $\text{SiO}_2/\text{Si}$  substrates. Surface morphology of ZnO films was observed using a field emission scanning electron microscopy (FESEM), and their crystalline structures were

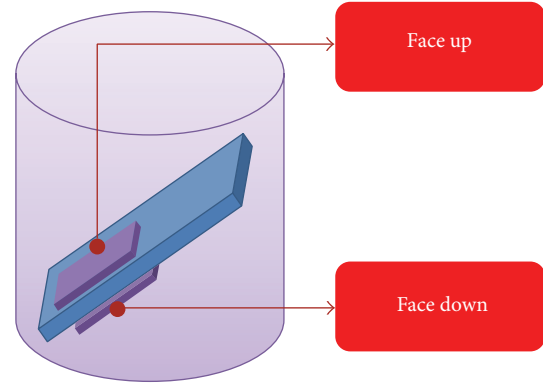


FIGURE 1: Structure for growing nanostructure ZnO films.

measured using X-ray diffraction (XRD) patterns with Cu  $K\alpha$  radiation ( $\lambda = 1.5418 \text{ \AA}$ ).

## 3. Results and Discussion

To investigate the general morphologies of hydrothermal-deposited ZnO nanostructures, the synthesized products are first examined by FESEM and demonstrated in Figure 2 under lower magnifications. The hydrothermal process is based on the formation of solid phase from a solution, which involves two steps as nucleation and growth [12]. At first in the nucleation process, the clusters of molecules formed undergo rapid decomposition ( $\text{Zn}(\text{NO}_3)_2 \cdot 6\text{H}_2\text{O}$  is used as source) and particles combine to grow up on the substrate surface of the ZnO seed layer by nonheterogeneous reactions. Figure 2(a) shows the down-face morphology of the 1 h deposited ZnO films; there are no nanorods or nanoflowers that appeared on the ZnO/ $\text{SiO}_2/\text{Si}$  substrates in the first 1 h growth and only irregular-plate structure films were observed, which was identical to the up-face morphology. In the past, Liu et al. explained that the different morphology of the deposited ZnO films on different substrates should be related to the lattice structure and defects on the substrates' surfaces, which were key factors for chemical adsorption and subsequent nucleation and growth [12]. However, we will show that the deposition time and the face of substrates are two important factors to synthesize the ZnO nanorods on ZnO/ $\text{SiO}_2/\text{Si}$  substrates.

From the obtained FESEM observations in Figure 2(b), it is confirmed that as deposition time was 3 h, the synthesized products were only ZnO nanorods with a diameter ranging from 65 to 200 nm, grown in very large quantity, and the irregular-plate structure shown in Figure 2(a) was not observed. As the ZnO nanorods are synthesized in large quantity and densely populated, hence it is seen that many nanorods are not joined with each other at each side of the nanorods, which suggests that the ZnO nanorods can have enough space to detect gas and act as a sensor. When deposition time was increased to 5 h, as Figure 2(c) shows, the synthesized products were not only nanorods, but also beautiful chrysanthemum- (flower-) like clusters grown above the nanorods in very large quantity. The flower-like

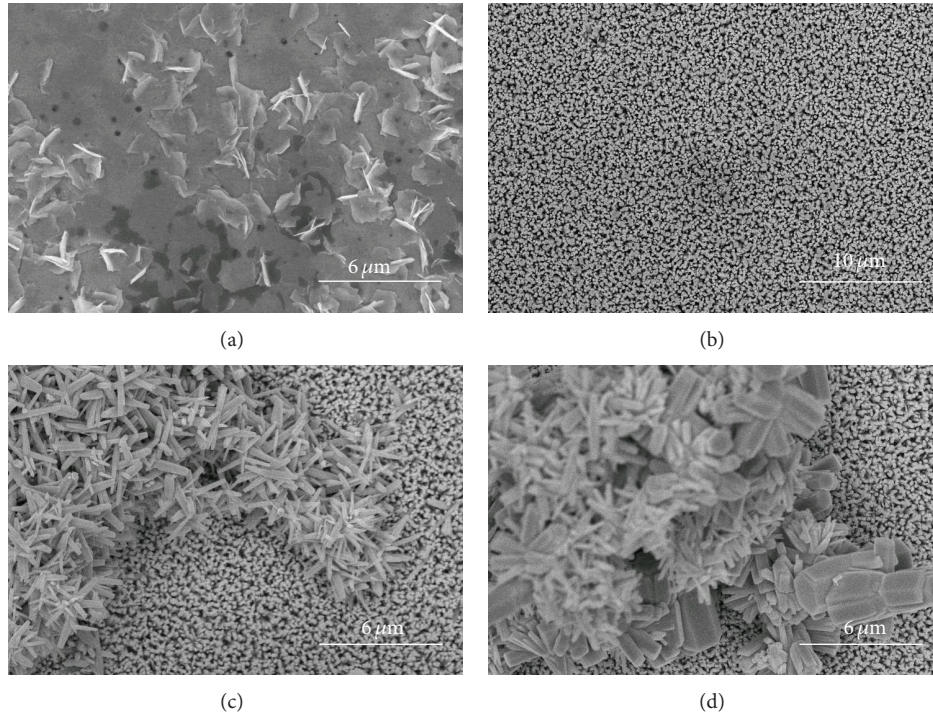


FIGURE 2: Surface morphologies of the deposited ZnO films synthesized at different faces and time and under different magnifications. Down face (a) 1 h, (b) 3 h, and (c) 5 h; up face (d) 5 h, respectively.

microstructures also consist of nanorods with a diameter ranging from 200 to 350 nm and length of 1.5–3  $\mu\text{m}$ , and the flower-like architectures become dominant with substrate coverage of about 50%. However, as the surface morphology in up face was observed, as Figure 2(d) shows, the size of the flower-like nanostructures was not uniform, while a few of the large rods with different diameters and lengths were also present. The flower-like and large-rod architectures developed further and became dominant with substrate coverage of about 80%. Those results suggest that the ZnO deposition rate of up-face substrates is quicker than that of down-face substrates and 3 h is the optimal time to grow the ZnO nanorods as the gas sensors.

The XRD results in Figure 3 reveal that all the ZnO-deposited films were of hexagonal wurtzite structure, and the three patterns of the ZnO-deposited films were in agreement with but different from the diffraction data from standard card (JCPDS 36-1451). The mainly crystalline peak of ZnO in JCPDS 36-1451 is (101), which is located around  $2\theta \sim 36.25^\circ$ . By comparison, the stronger intensity of (002) diffraction peak was found in Figure 3 for all deposited ZnO films, suggesting that all the films exist in high *c*-axis orientation. Accordingly, the tendency of *c*-orientation (200) peak was increased as the deposition time increased from 1 h to 3 h. The increase of the full width at half maximum (FWHM) values of (200) peak indicates that the crystallization of ZnO films increases as the synthesized time increases.

Results in Figure 3 indicate that 1 h deposited ZnO films had a (002) peak and two weak (100) and (110) peaks; 3 h deposited ZnO films only had a strong (002) peak; and 5 h

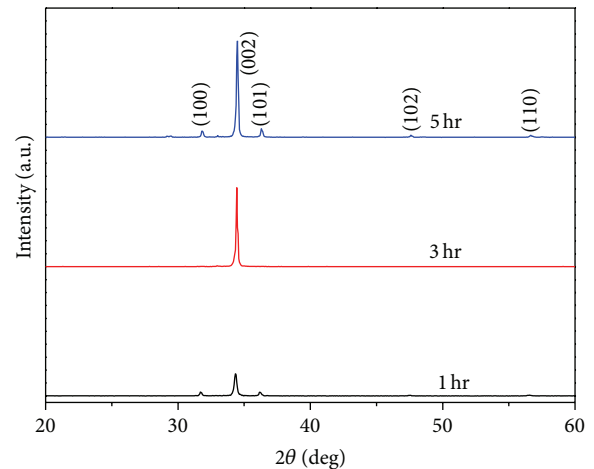


FIGURE 3: XRD patterns of the down-face ZnO films synthesized at different deposition time.

deposited ZnO films had a strong (002) peak and two weak (100) and (110) peaks. The (002), (100), and (110) peaks are preferred orientation with the *c*-axis perpendicular to the substrate. Those results illustrate that the diffraction data on the surface match the morphology as well as crystal orientation of the resultant films. An energy dispersive spectroscopic (EDS) analysis of the ZnO films in Figure 4 (up-face and deposition time was 3 h) shows that the products were composed mainly of Zn and O elements, consistent with

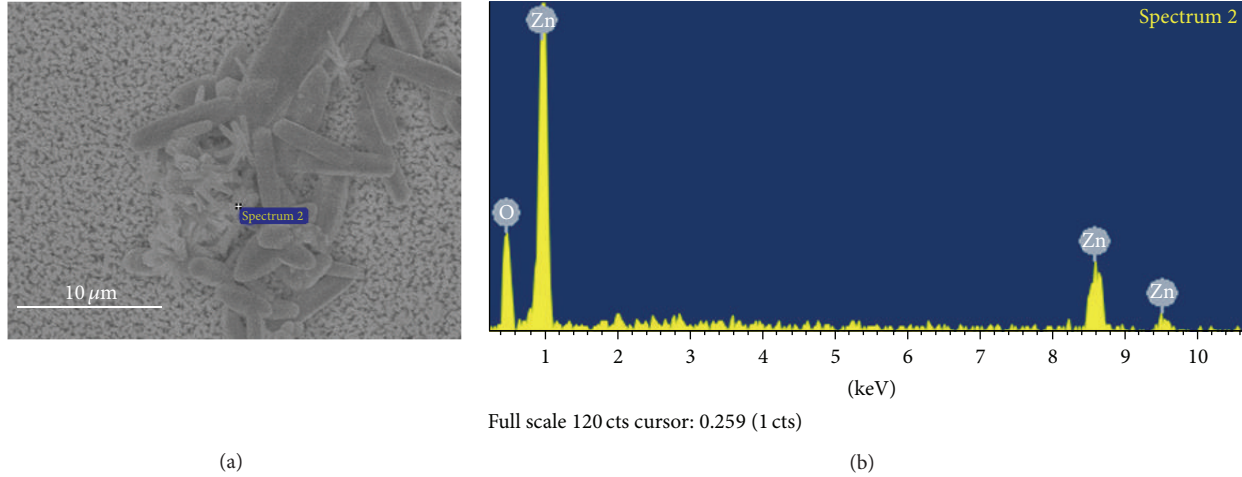


FIGURE 4: EDS analysis of the up-face ZnO films synthesized at 3 h.

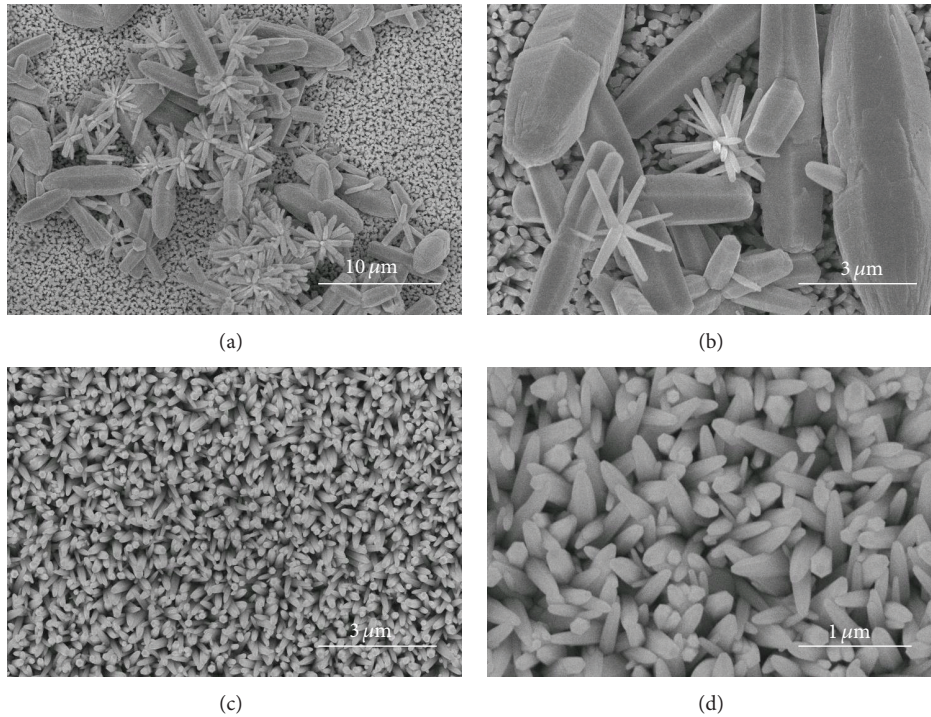


FIGURE 5: Surface morphologies of the ZnO films synthesized at different faces and different magnifications; the deposition time was 3 h. Up face with (a) lower magnification and (b) higher magnification; down face with (c) lower magnification and (d) higher magnification, respectively.

the results of XRD in Figure 3. The results in Figures 3 and 4 illustrate that the different lattice mismatches and defects affect the morphology as well as crystal orientation of the deposited ZnO films.

To investigate the general morphologies of as-synthesized ZnO nanorods and nanoflowers, the synthesized products are examined by FESEM and demonstrated in lower and higher magnification FESEM images, and the results are shown in Figure 5. The SEM images in Figures 5(a) and 5(b) clearly show that the up-face surfaces of the 3 h deposited

ZnO/SiO<sub>2</sub>/Si substrates had been coated with non-uniform-sized ZnO nanorods, nanoflowers, and large hexagonal bars. The SEM images in Figures 5(c) and 5(d) clearly show that the down-face surfaces of the 3 h deposited ZnO/SiO<sub>2</sub>/Si substrates had been coated with uniform-sized and quasi-oriented ZnO nanorods. As we know, crystallization exists in two different successive stages: nucleation and crystal growth. The interaction between these two steps determines the crystal characteristics, including size, distribution, and morphology of the crystals. When the solutions are used to

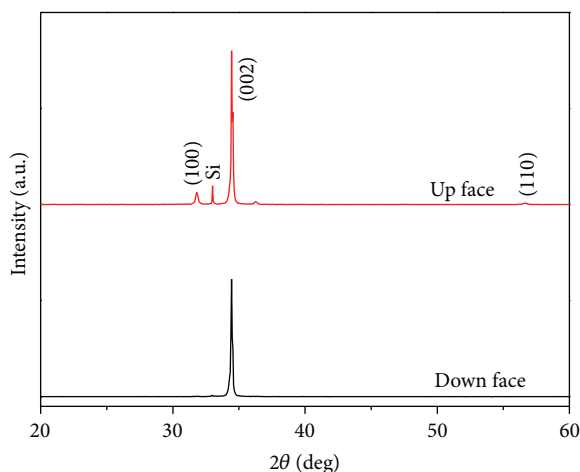


FIGURE 6: XRD patterns of the ZnO films synthesized at different faces; the deposition time was 3 h.

synthesize or deposit films, there are two different nucleation mechanisms in the solution: heterogeneous nucleation and homogenous nucleation [13]. Homogenous nucleation takes place when primary nucleation proceeds in a nucleation free solution; this is when the solution contains no foreign particles. Heterogeneous nucleation takes place if primary nucleation proceeds when foreign particles are present in the solution.

The reason for the different morphology of the synthesized ZnO films obtained on the two faces should be related to the different nucleation mechanisms in the solution. In our case, the growth of ZnO films on ZnO/SiO<sub>2</sub>/Si substrates at different faces was controlled by the two nucleation mechanisms. Li et al. have successfully grown large scale arrays of ZnO nanorods on zinc foil without the assistance of any template, oxidant, or coating of metal oxide layers, simply by dipping the foil into a 25% aqueous solution of ammonia (NH<sub>4</sub>OH) and heating at a temperature 80°C in a Teflon-lined stainless steel autoclave [14]. They prepared four different samples by varying the concentration of ammonia in an 80 mL growth bath and the growth duration. They found that the thickness, density, and morphology of the ZnO nanorods are affected by the alkalinity of the solution in the growth bath. However, in this study we prove that with the addition of ZnO films as seed layer on SiO<sub>2</sub>/Si substrates we can synthesize the nanorods and nanoflowers at 100°C. Those results also suggest that we can control the number of the irregular-plate type ZnO, ZnO nanorods, and ZnO nanoflowers on 2 × 2 cm<sup>2</sup> sample by controlling the deposition time and direction (down face or up face) of ZnO/SiO<sub>2</sub>/Si substrates.

Figure 6 shows the XRD spectra of the 3 h deposited ZnO films prepared at different faces. Results indicate that down-face ZnO films only had a strong (002) peak and up-face ZnO films had a strong (002) peak and two weak (100) and (110) peaks preferred orientation with the *c*-axis perpendicular to the substrate. All the (002) peaks in Figure 6

were found at  $2\theta \sim 34.45^\circ$ , which was the same as the stoichiometric ZnO crystal ( $2\theta \sim 34.45^\circ$ ). These results imply that the parameter of lattice constant *c* is unchanged as different faces of ZnO/SiO<sub>2</sub>/Si substrates are used in the synthesizing process. The results for XRD patterns of the ZnO films in Figures 4 and 6 can be described as a number of alternating planes composed of tetrahedrally coordinated O<sup>2-</sup> and Zn<sup>2+</sup> stacked alternately along the *c*-axis. Also, the ZnO films exhibit a varied range of novel structures. These structures can be grown by tuning the growth rates along different fast growing directions. As those results in SEM images and XRD patterns, changing the face of the ZnO/SiO<sub>2</sub>/Si substrates will change the nucleation mechanisms and then change the synthesizing results of the ZnO films, because homogenous nucleation produces undesired ZnO particles and heterogeneous nucleation produces nanorods. As the ZnO seed layer is grown on the SiO<sub>2</sub>/Si substrates, we think the irregular-plate type ZnO is grown under the heterogeneous nucleation, which is much more common than homogeneous nucleation. Heterogeneous nucleation is typically much faster than homogeneous nucleation because the nucleation barrier ( $\Delta G^*$ ) is much lower at a surface. For that, the irregular-plate type ZnO is grown first. However, ZnO nanorods are limited by homogenous nucleation of ZnO particles that align the *c*-axis and ZnO nanoflowers are homogenous nucleation in a different crystalline direction as the nanorods are grown too long.

#### 4. Conclusions

As the synthesized time was 1 h, 3 h, and 5 h, the down-face morphologies of ZnO films on ZnO/SiO<sub>2</sub>/Si substrates were irregular-plate structure films, ZnO nanorods with a diameter ranging from 65 to 200 nm, and beautiful chrysanthemum- (flower-) like clusters grown above the nanorods in very large quantity, respectively. As the synthesized time was 1 h, 3 h, and 5 h, the pure ZnO nanorods could not be obtained in up-face ZnO films. XRD patterns indicated that 1 h and 5 h deposited ZnO films had a (002) peak and two weak (100) and (110) peaks and 3 h deposited ZnO films only had a strong (002) peak. The reason for different morphologies of the ZnO films obtained on the two faces should be related to the two nucleation mechanisms, heterogeneous nucleation and homogenous nucleation, in the solution. As deposition time was 3 h, the down-face morphology of ZnO films was only ZnO nanorods with a diameter ranging from 65 to 200 nm and in very large quantity, which could be investigated as gas sensors.

#### Conflict of Interests

The authors have no financial competing interests.

#### Acknowledgments

The authors acknowledge financial supports of NSC 102-2221-E-218-036, NSC 102-2622-E-390-002-CC3, and NSC 102-2221-E-390-027.

## References

- [1] F. H. Wang, C. F. Yang, and Y. H. Lee, "Deposition of F-doped ZnO transparent thin films using ZnF<sub>2</sub>-doped ZnO target under different sputtering substrate temperatures," *Nanoscale Research Letters*, vol. 9, article 97, 2014.
- [2] J. Chung, J. Lee, and S. Lim, "Annealing effects of ZnO nanorods on dye-sensitized solar cell efficiency," *Physica B*, vol. 405, no. 11, pp. 2593–2598, 2010.
- [3] N. Saito, H. Haneda, T. Sekiguchi, N. Ohashi, I. Sakaguchi, and K. Koumoto, "Low-temperature fabrication of light-emitting zinc oxide micropatterns using self-assembled monolayers," *Advanced Materials*, vol. 14, no. 6, pp. 418–421, 2002.
- [4] G. Kwak, M. Seol, Y. Tak, and K. Yong, "Superhydrophobic ZnO nanowire surface: chemical modification and effects of UV irradiation," *Journal of Physical Chemistry C*, vol. 113, no. 28, pp. 12085–12089, 2009.
- [5] L. Wang, Y. Kang, X. Liu, S. Zhang, W. Huang, and S. Wang, "ZnO nanorod gas sensor for ethanol detection," *Sensors and Actuators, B: Chemical*, vol. 162, no. 1, pp. 237–243, 2012.
- [6] L. Li, H. Yang, H. Zhao et al., "Hydrothermal synthesis and gas sensing properties of single-crystalline ultralong ZnO nanowires," *Applied Physics A*, vol. 98, no. 3, pp. 635–641, 2010.
- [7] J. Kim and K. Yong, "Mechanism study of ZnO nanorod-bundle sensors for H<sub>2</sub>S gas sensing," *Journal of Physical Chemistry C*, vol. 115, no. 15, pp. 7218–7224, 2011.
- [8] H. Ghayour, H. R. Rezaie, S. Mirdamadi, and A. A. Nourbakhsh, "The effect of seed layer thickness on alignment and morphology of ZnO nanorods," *Vacuum*, vol. 86, no. 1, pp. 101–105, 2011.
- [9] X. Jiaqiang, C. Yuping, C. Daoyong, and S. Jianian, "Hydrothermal synthesis and gas sensing characters of ZnO nanorods," *Sensors and Actuators, B: Chemical*, vol. 113, no. 1, pp. 526–531, 2006.
- [10] L. Vayssieres, "Growth of arrayed nanorods and nanowires of ZnO from aqueous solutions," *Advanced Materials*, vol. 15, no. 5, pp. 464–466, 2003.
- [11] G. Kenanakis, D. Vernardou, E. Koudoumas, and N. Katsarakis, "Growth of c-axis oriented ZnO nanowires from aqueous solution: The decisive role of a seed layer for controlling the wires' diameter," *Journal of Crystal Growth*, vol. 311, no. 23–24, pp. 4799–4804, 2009.
- [12] X. Liu, Z. Jin, S. Bu, J. Zhao, and Z. Liu, "Effect of buffer layer on solution deposited ZnO films," *Materials Letters*, vol. 59, no. 29–30, pp. 3994–3999, 2005.
- [13] V. L. Snoeyink and D. Jenkins, *Water Chemistry*, John Wiley & Sons, 1980.
- [14] Z. Li, X. Huang, J. Liu, Y. Li, X. Ji, and G. Li, "Growth and comparison of different morphologic ZnO nanorod arrays by a simple aqueous solution route," *Materials Letters*, vol. 61, no. 22, pp. 4362–4365, 2007.

## Research Article

# Metallurgical Mechanism and Optical Properties of CuSnZnSSe Powders Using a 2-Step Sintering Process

Tai-Hsiang Liu,<sup>1</sup> Fei-Yi Hung,<sup>1</sup> Truan-Sheng Lui,<sup>1</sup> and Kuan-Jen Chen<sup>2</sup>

<sup>1</sup> Department of Materials Science and Engineering, Center for Micro/Nano Science and Engineering, National Cheng Kung University, Tainan 701, Taiwan

<sup>2</sup> The Instrument Center, National Cheng Kung University, Tainan 701, Taiwan

Correspondence should be addressed to Fei-Yi Hung; fyhung@mail.ncku.edu.tw

Received 3 April 2014; Accepted 14 May 2014; Published 5 June 2014

Academic Editor: Liang-Wen Ji

Copyright © 2014 Tai-Hsiang Liu et al. This is an open access article distributed under the Creative Commons Attribution License, which permits unrestricted use, distribution, and reproduction in any medium, provided the original work is properly cited.

$\text{Cu}_2\text{SnZn}(\text{S} + \text{Se})_4$  is an excellent absorber material for solar cells. This study obtained  $\text{Cu}_2\text{SnZn}(\text{S} + \text{Se})_4$  powders through solid state reaction by the ball milling and sintering processes from elemental Cu, Zn, Sn, S, and Se without using either polluting chemicals or expensive vacuum facilities. Ratios of S/S + Se in CuSnZnSSe were controlled from 0 to 1. The results showed that the 2-step sintering process (400°C for 12 hrs and then 700°C for 1 hr) was able to stabilize the composition and structure of the CuSnZnSSe powders. The crystallized intensity of the CuSnZnS matrix decreased with increasing the Se content. Raising the Se content restrained the SnS phase and reduced the resistance of the absorber layer. In addition, Raman data confirmed that Se caused a Raman shift in the CuSnZnSSe matrix and enhanced the optical properties of the CuSnZnSSe powders. For the interface of CuSnZnSSe film and Mo substrate, Mo could diffuse into CuSnZnSSe matrix after 200°C annealing. The interface thermal diffusion of CuSnZnSSe/ZnS improved the effects of stack to enhance the stability of structure.

## 1. Introduction

The development of CZTS ( $\text{Cu}_2\text{Zn}_1\text{Sn}_1\text{S}_4$ ) has been a subject of focus in recent years [1, 2]. Due to the lower cost of Zn and Sn element compared with In and Ga in the CIGS system, CZTS is considered a potential substitute for CIGS in the future. In the literature [3–5], CZTS thin film has been formed in many ways such as cosputtering [3], electroplated deposition [4], and pulsed laser deposition (PLD) [5]. But the cost of manufacturing is high, so the development is slow.

In this research, we used mechanical milling on the solid powders to synthesize CZTSSe powders and it was low-cost with a stable structure. Cu, Zn, Sn, and S have been used to form CZTS powders, but the low boiling point of S [6] makes it hard to control the composition of CZTS when the S vaporizes at higher temperatures. The boiling point of Se is higher than that of S, and Se can stabilize the CZTS powders. Therefore, this research controlled the Cu, Zn, and Sn = 2:1:1 at.%, and then mixed S and Se in different ratios to combine with Cu, Zn, and Sn precursor to form the  $\text{Cu}_2\text{SnZn}(\text{S} + \text{Se})_4$  powders. During mixing,

a 2-step sintering process was performed (400°C for 12 hrs controlled the concentrations of S and Sn; 700°C for 1 hr controlled the concentration of Se) to adjust the ratios of  $x = \text{S}/\text{S} + \text{Se}$ . The 2-step sintering process is not only a continuous method, but also the metallurgical efficiency [7, 8] which helps to homogenize the compound powders. This study used the 2-step sintering process without using either polluting chemicals or expensive vacuum facilities to investigate the metallurgical mechanism of the CZTSSe powders. In addition, the morphology, crystalline structure, and optical properties of the CZTSSe powders were measured to examine the effect of Se addition. The effect of 200°C annealing in the interface diffusion of ZnS/CZTSSe/Mo structure was also explored in CZTSSe system.

## 2. Experimental Procedure

The  $\text{Cu}_2\text{SnZn}(\text{S} + \text{Se})_4$  powders were synthesized using pure Cu, Zn, Sn, S, and Se powders. The atomic ratio of Cu:Zn:Sn:(S + Se) was 2:1:1:4. The atomic ratio of

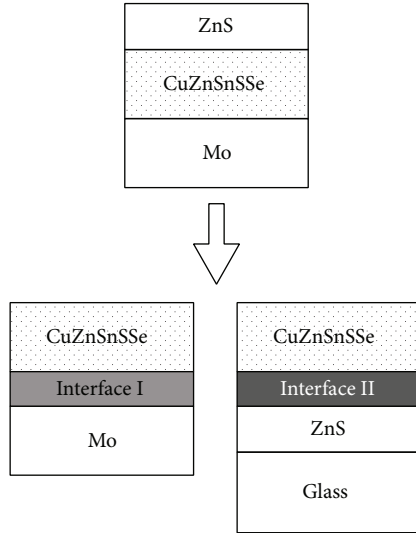


FIGURE 1: Interface I and interface II of ZnS/CZTSSe/Mo structure.

Cu : Zn : Sn was fixed. Five atomic ratios containing pure S, S : Se = 3 : 1, S : Se = 1 : 1, S : Se = 1 : 3, and pure Se were mixed to obtain 5 types of  $\text{Cu}_2\text{SnZn}(\text{S} + \text{Se})_4$  powders. The ratio value was defined as  $x = \text{S}/(\text{S} + \text{Se})$ .

The powders were milled for 1 hr in molecular ratio inside a crucible and then sintered in a stove at  $400^\circ\text{C}$  for 12 hours (1st-step sintering). During this  $400^\circ\text{C}$  sintering, S, Se, and Sn turned to liquid state and combined with Cu and Zn to form compounds. After this, the  $\text{Cu}_2\text{SnZn}(\text{S} + \text{Se})_4$  powders were sintered at  $700^\circ\text{C}$  for 1 hour (2nd-step sintering). The residual S and Se were vaporized from  $\text{Cu}_2\text{SnZn}(\text{S} + \text{Se})_4$  powders. Finally, the powders were cooled to room temperature and the measurement of crystallization and optical properties was performed.

The morphology and crystalline structure of the powders were observed using SEM (Hitachi SU8000), TEM (JEOL JEM-1400), and XRD (Bruker AXS GmbH, Karlsruhe, Germany). In addition, the compositions of the powders were determined using ICP (HEWLETT PACKARD 4500, JP) and EDS. Raman, reflection pattern and resistance of CZTSSe powders were measured to understand the contributions of S and Se ratios [6, 9]. Each analysis datum is the average of 4 test results.

In addition, the powder of S : Se = 1 : 1 was deposited by thermal evaporation and combined ZnS film (ZnS film was obtained from aqueous solution method) and Mo substrate to form CZTSSe/Mo specimen and CZTSSe/ZnS/glass specimen (Figure 1). The interface diffusion mechanisms of ZnS/CZTSSe/Mo structure were detected by TEM (JEOL JEM-1400) with EDS before and after  $200^\circ\text{C}$  annealing to explore the interface characteristics.

### 3. Results and Discussion

The SEM morphologies of the five CZTSSe powders after the 2-step sintering process are shown in Figure 2. The powders were particle-like and the agglomeration was not obvious

after mechanical milling. EDS analysis showed that the S/S + Se ratio of powders complied with the proportion and the average particle size of the powders was 160~220 nm. The powders could be applied for coating of devices and their morphologies were similar to the powders in the literature [4]. In addition, the CZTSSe powders were examined by XRD to identify the phase structure (Figure 3). It was found that the diffraction peak angle of the CZTSSe powders reduced slightly with increasing the content of Se. The main reason is that the atomic radius of Se is larger than S [10]. Thus, Se atoms replacing S would cause the lattice to expand. According to diffraction theory,  $n\lambda = 2d \sin \theta$ , we have good grounds for thinking that the addition of Se increased the value of  $d$  and then reduced the value of  $\theta$  in the CZTS system.

Notably, the combination of S and Se in the Cu-Zn-Sn matrix requires a stable sintering process. If the powders are only given the 1st-step sintering (without the 2nd step), the CZTS(S = 100%) will not only have the CZTS main diffraction planes, but also have the SnS phase (Figure 4(a)). We attempted to extend our observation in the CZTSSe (S = 50%, Se = 50%) system (only 1st-step sintering, Figure 4(b)). XRD diffractions proved clearly that some pure Se phases remained in the CZTSSe matrix, but no SnS phase was found. It is clear that both the addition of Se and the 2-step sintering process are able to improve the crystallization of the CZTSSe system.

The CZTSSe powders with a 2-step sintering process were compressed into the ingots and then their electrical resistance was measured using a 4-point probe analyzer. Figure 5 shows the electrical properties of the CZTSSe powders and the CZTS (S = 100%) powder has the highest electrical resistance. The electrical resistance of the CZTSSe (S : Se = 1 : 1,  $x = 0.5$ ) powder and the CZTSe (Se = 100%) powder were similar. Notably, the two CZTSSe powders with ratio S : Se = 3 : 1 ( $x = 0.75$ ) and S : Se = 1 : 3 ( $x = 0.25$ ) had the lowest electrical resistance. These electrical properties were closely related to the chemical composition and the phase structure. It is clear that adding Se can reduce the electrical resistance of CZTSSe powders. For the S : Se = 3 : 1 ( $x = 0.75$ ) powder, an excess of S combined with Sn to form SnS phase [10]. For the S : Se = 1 : 3 ( $x = 0.25$ ) powder, some residual Se could not enter the matrix. For this reason, their electrical resistance was lower than that of the other powders. Recent reports [11, 12] claim that the electrical resistance of CZTS powder systems has still not been explored. We have the experience in the electrical measurements of powders [13] and can confirm that SnS phase and Se in the CZTSSe powders are the main phases to affect the electrical properties.

The CZTSSe powders were subjected to Raman spectrum to observe their Raman shift characteristics. Figure 6 shows that Se addition caused a Raman shift in the CZTSSe powders (from  $334.8$  to  $323.8 \text{ cm}^{-1}$ ) and the shift frequency increased with increasing Se content. Notably, a CZTSe (Se = 100%) peak was not found at  $323\sim 335 \text{ cm}^{-1}$ , but a ZnSe peak was found at  $240.8 \text{ cm}^{-1}$ . In a word, adding Se affected the Raman results and the CZTSe (Se = 100%) powder revealed a different Raman spectrum from the CZTSSe powders. The two main reasons are as follows: (1) adding Se prevented Sn

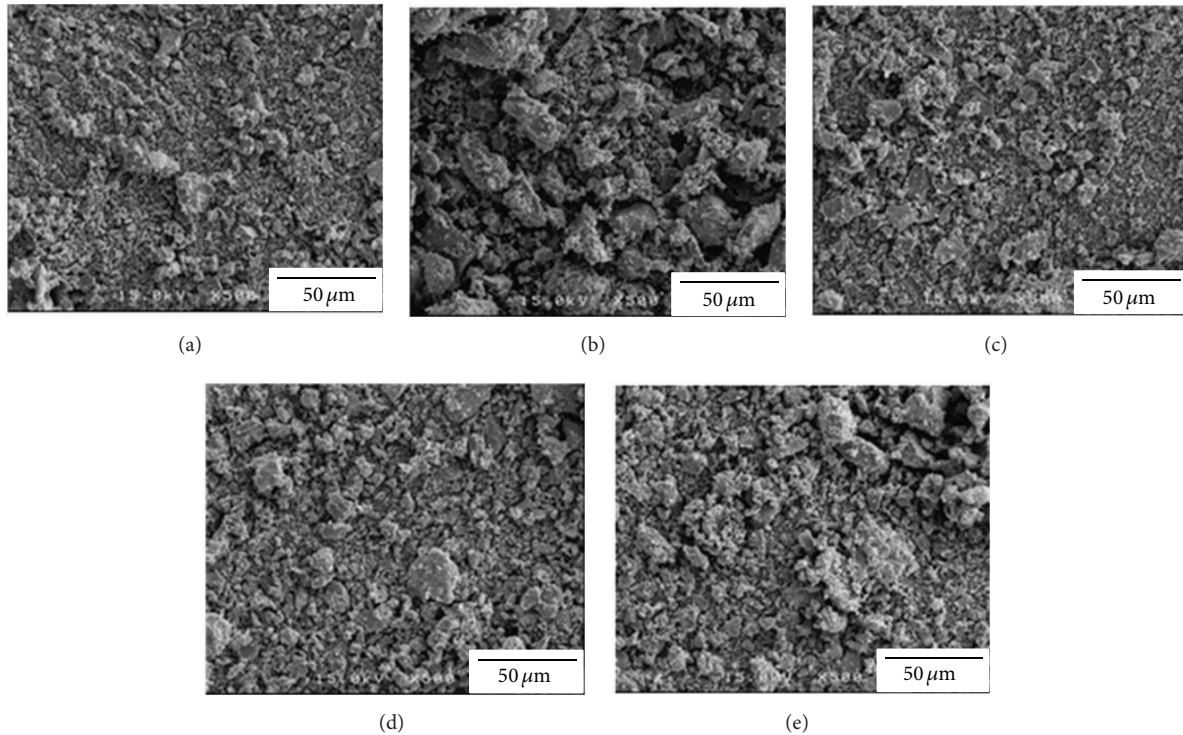


FIGURE 2: Morphology of CZTSSe powders. (a) CZTSe (Se: 100%,  $x = 0$ ), (b) CZTSSe (S: 25% + Se: 75%,  $x = 0.25$ ), (c) CZTSSe (S: 50% + Se: 50%,  $x = 0.5$ ), (d) CZTSSe (S: 75% + Se: 25%,  $x = 0.75$ ), and (e) CZTS (S: 100%,  $x = 1$ ).

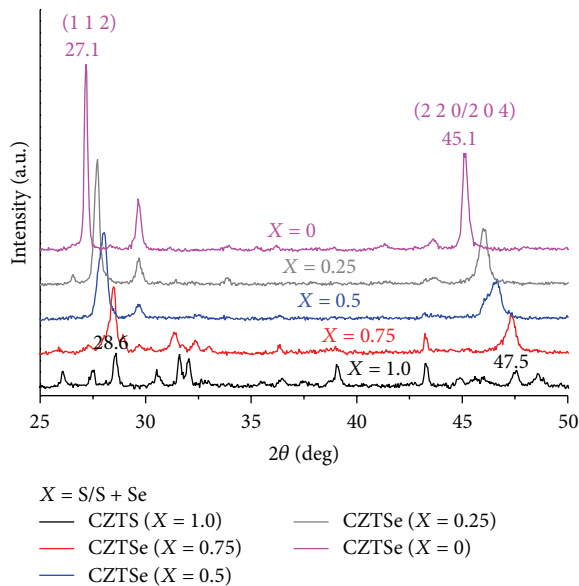


FIGURE 3: XRD of five CZTSSe powders.

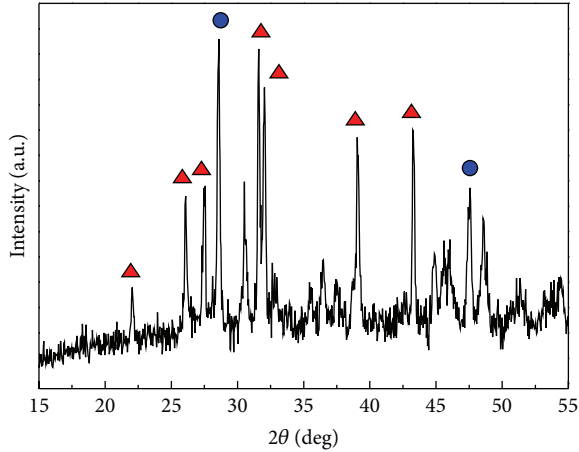
from binding with S to form SnS phase to cause structural defects and (2) some Se would inflate the lattice to cause a Raman shift in the CZTSSe powders. In a word, the random distribution of S and Se atoms in the lattice resulted in the fluctuations in the masses and force constants in the neighborhood [14, 15]. Because the electrical and optical properties

of the CZTSSe (S : Se = 1 : 1) powders were improved, CZTSSe (S : Se = 1 : 1) was selected for TEM analysis.

Figure 7 shows the TEM observations of the CZTSSe (S : Se = 1 : 1) powder. The CZTSSe powder was agglomerated and the single particle size was about 160~220 nm. According to EDS results and comparing with the literature [11, 12], the ratio S : Se = 13 : 15 (Figure 7(a)) approached the atomic ratio of 1 : 1. In addition, a bright field image (Figure 7(a)) and a dark field image (Figure 7(b)) reveal that the overlapping of powders and Se was uniform in the matrix. Figure 7(c) shows that the CZTSSe powder had a tetragonal structure which grew in the direction of C-axis.

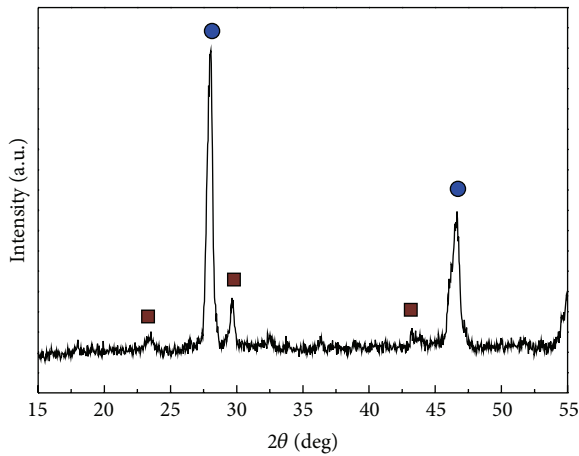
Figure 8 shows the reflection percentage of the CZTSSe powders. We can be fairly certain that the CZTS (S = 100%) powder had the highest reflection percentage. As Se was added, the reflection percentage decreased. Judging from the above, for continuous wavelength light, the absorption of the CZTSSe powder was better than that of the CZTS powder with pure sulfur. From the present data and a previous paper, it is clear that adding Se increases the absorption edge (nm) in the S-Se mixed system and then raises the reflection percentage. Therefore, when the wavelength is higher than the absorption edge, the absorption of CZTSe or CZTSSe is higher than CZTS powder with pure sulfur. Figure 8 shows that the wavelength of the absorption edge of the CZTS powder was about 300 nm; thus, the reflection ( $R\%$ ) decreased significantly below 300 nm in wavelength.

The CZTSSe (S : Se = 1 : 1) powders were deposited on Mo substrate by thermal evaporation. Both as-deposited and



● CZTS (S: 100%)  
▲ ZnS

(a)

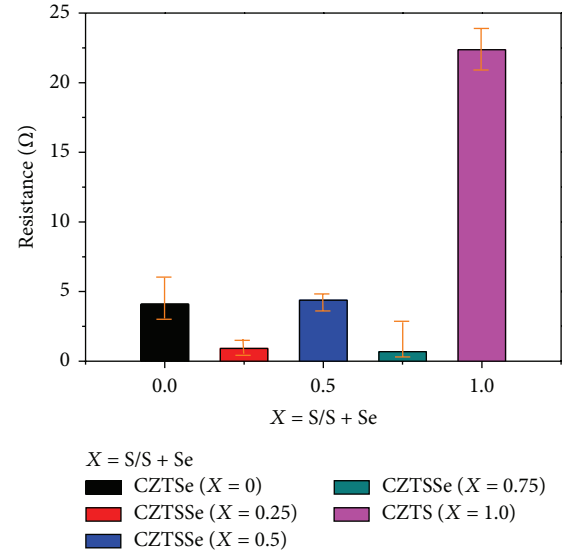


● CZTSSe  
■ Se

(b)

FIGURE 4: (a) XRD of CZTS(S: 100%), (b) XRD of CZTSSe (S: 50%, Se: 50%).

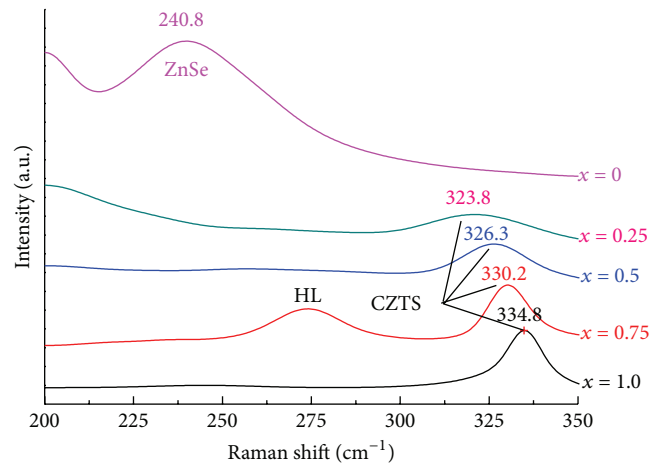
annealed CZTSSe/Mo structures were detected by TEM [16–19]. According to Figure 1, the interface I was observed in Figures 9 and 10. In fact, the Mo atom had diffused into CZTSSe matrix due to thermal diffusion induced by thermal evaporation and the concentration of Mo in the surface of CZTSSe film was about 1.5 at.%. After annealing, the concentration of Mo increased in the CZTSSe film and the zone near Mo substrate that had formed a continuous structure (EDS2~EDS3) from network structure. No doubt the CZTSSe film had the pollution of Mo atoms and it still had a tetragonal structure (see the pattern of Figure 10). The same observation applies to interface II of CZTSSe/ZnS/Glass structure (Figure 1). In Figure 11, the CZTSSe film (S:Se = 1:1) of thermal evaporation was deposited on ZnS film. The CZTSSe film represented a stacking morphology, which associated with the lower thermal conductivity of



$X = S/S + Se$

■ CZTSe (X = 0)      ■ CZTSSe (X = 0.75)  
■ CZTSSe (X = 0.25)      ■ CZTS (X = 1.0)  
■ CZTSSe (X = 0.5)

FIGURE 5: Resistance of five CZTSSe powders.



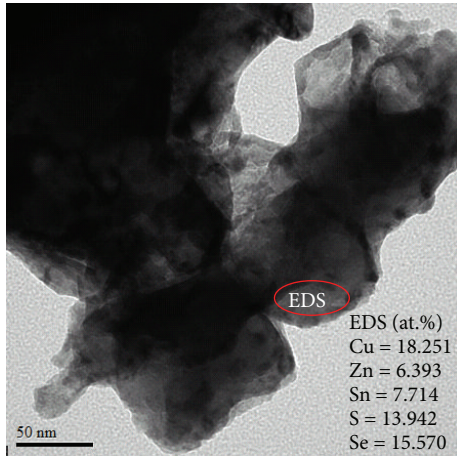
$X = S/S + Se$

— CZTS (X = 1.0)      — CZTSSe (X = 0.25)  
— CZTSSe (X = 0.75)      — CZTSe (X = 0)  
— CZTSSe (X = 0.5)

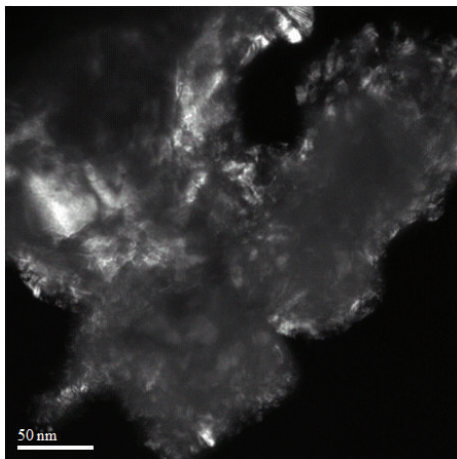
FIGURE 6: Raman of five CZTSSe powders.

ZnS/glass substrate. After annealing, the crystallization of CZTSSe film was improved to enhance the structural stability (Figure 12).

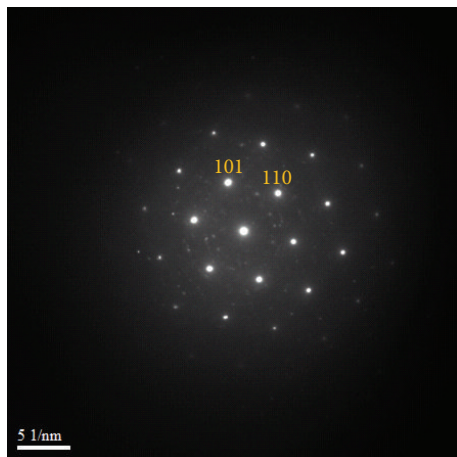
In the past, each laboratory had focused on the solar cell design for power performance. In fact, the interface of the structure is significant to affect the results of power performance. Results of this study can provide the interfacial properties of the solar cell design to assist in understanding the relationship between the power performance and materials.



(a)

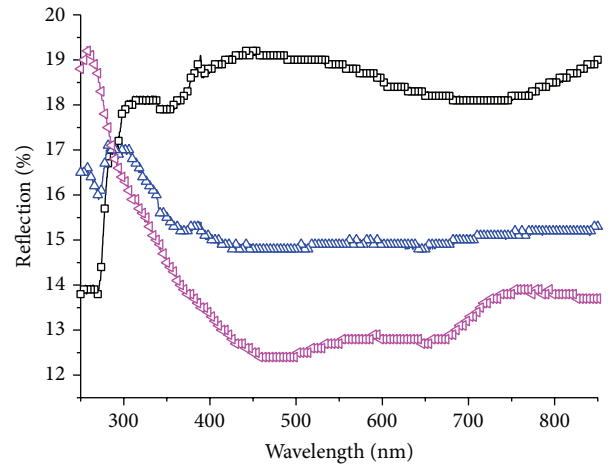


(b)



(c)

FIGURE 7: TEM observations of CZTSSe powders (S:Se = 13:17 at atomic ratio). (a) Bright field image with EDS data, (b) dark field image, and (c) SAED of CZTSSe powders.



$X = S/S + Se$   
 -□- CZTSSe ( $X = 1.0$ )  
 -△- CZTSSe ( $X = 0.5$ )  
 -◇- CZTSSe ( $X = 0$ )

FIGURE 8: Absorption-reflection detection of different ratio in CZTSSe ( $CZTSSe_xSe_{1-x}$ ,  $X = 1.0, 0.5, 0$ ).

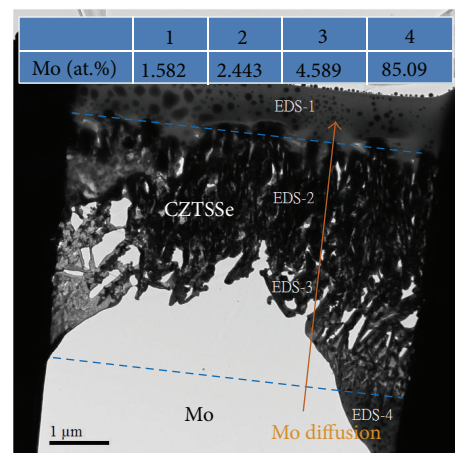


FIGURE 9: Interface observation of CZTSSe/Mo structure before annealing.

#### 4. Conclusion

Adding Se stabilized the CZTSSe phase structure. It not only improved the electrical properties, but also caused obvious shift peaks in the Raman spectrum. In addition, the absorption of the CZTSSe powder was higher than the CZTS powder.

The five-element CZTSSe powder matrix was a tetragonal crystal. Both the addition of Se and the 2-step sintering process were able to improve the crystallization. After annealing, the CZTSSe/Mo structure had an obvious thermal diffusion of Mo atoms and the stacking of CZTSSe/ZnS structure was improved. The effects can improve the design and application of the solar cells.

| EDS       | 1      | 2      | 3      | 4      | 5      | 6     |
|-----------|--------|--------|--------|--------|--------|-------|
| Mo (at.%) | 83.491 | 69.177 | 65.721 | 12.698 | 10.149 | 8.273 |

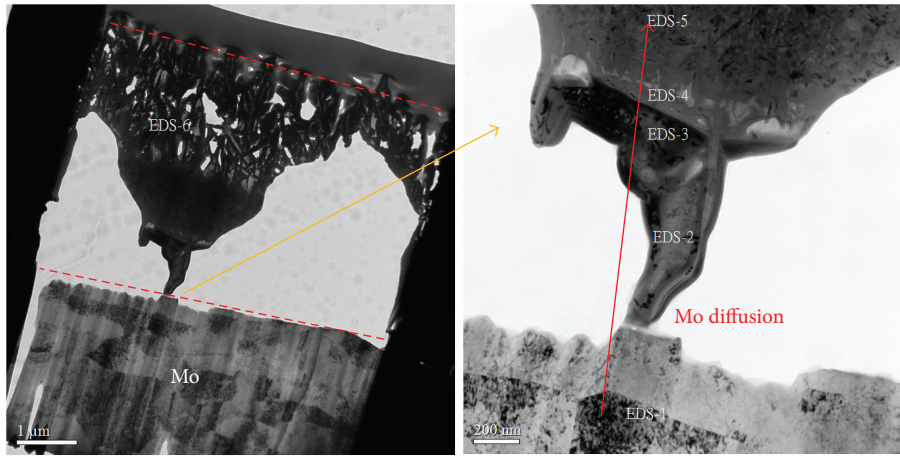


FIGURE 10: Interface characteristic of CZTSSe/Mo structure after annealing.

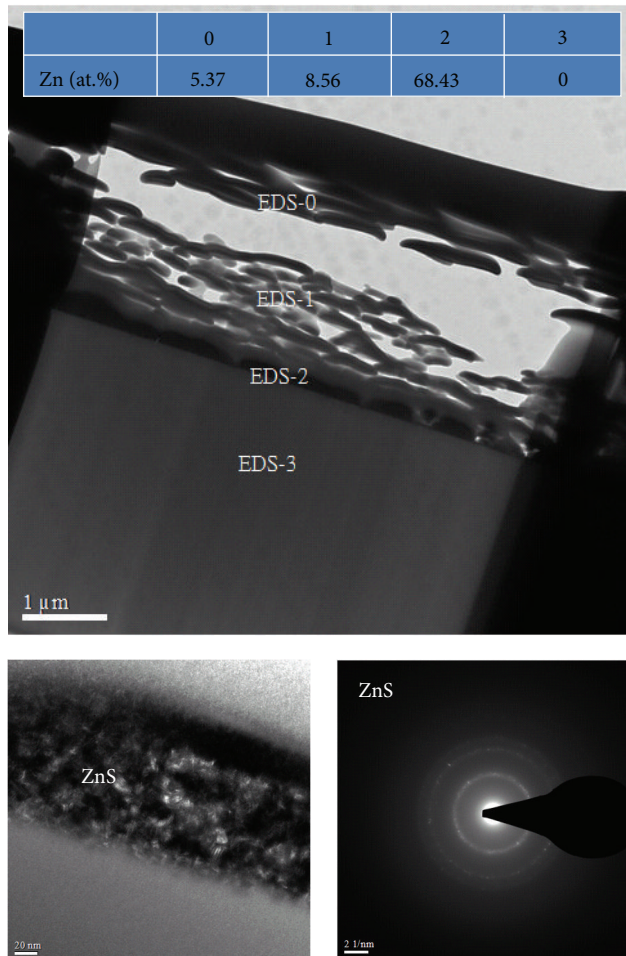


FIGURE 11: Interface observation of CZTSSe/ZnS structure before annealing.

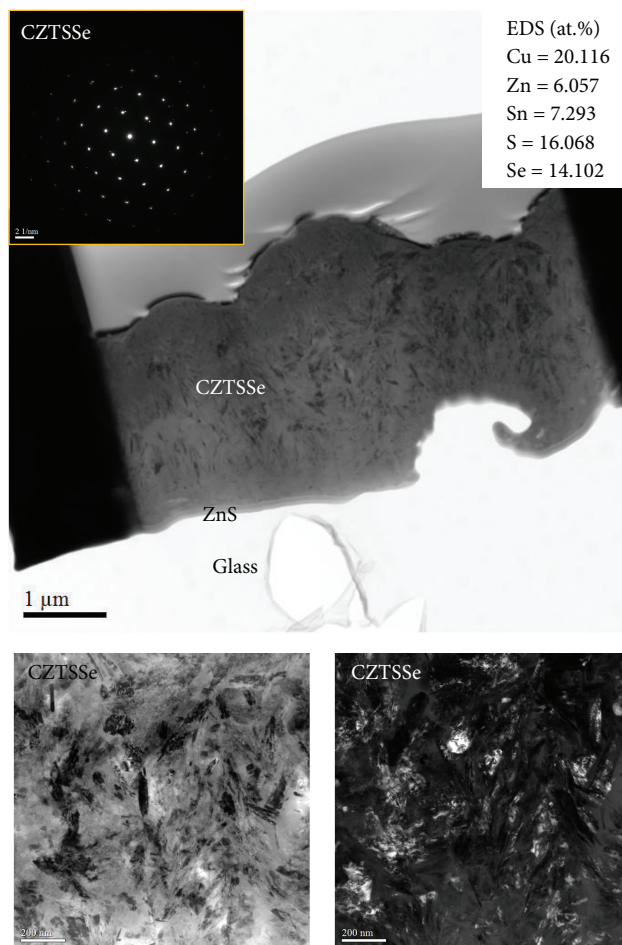


FIGURE 12: Crystallization of CZTSSe/ZnS structure after annealing.

## Conflict of Interests

The authors declare that there is no conflict of interests regarding the publication of this paper.

## Acknowledgments

The authors are grateful to National Cheng Kung University and NSC 102-2221-E-006-061 for the financial support.

## References

- [1] A. V. Moholkar, S. S. Shinde, A. R. Babar et al., "Synthesis and characterization of  $\text{Cu}_2\text{ZnSnS}_4$  thin films grown by PLD: solar cells," *Journal of Alloys and Compounds*, vol. 509, no. 27, pp. 7439–7446, 2011.
- [2] Y. Wang and H. Gong, " $\text{Cu}_2\text{ZnSnS}_4$  synthesized through a green and economic process," *Journal of Alloys and Compounds*, vol. 509, no. 40, pp. 9627–9630, 2011.
- [3] T. Prabhakar and N. Jampana, "Effect of sodium diffusion on the structural and electrical properties of  $\text{Cu}_2\text{ZnSnS}_4$  thin films," *Solar Energy Materials & Solar Cells*, vol. 95, no. 3, pp. 1001–1004, 2011.
- [4] K. Tanaka, Y. Fukui, N. Moritake, and H. Uchiki, "Chemical composition dependence of morphological and optical properties of  $\text{Cu}_2\text{ZnSnS}_4$  thin films deposited by sol-gel sulfurization and  $\text{Cu}_2\text{ZnSnS}_4$  thin film solar cell efficiency," *Solar Energy Materials & Solar Cells*, vol. 95, no. 3, pp. 838–842, 2011.
- [5] L. Sun, J. He, H. Kong, F. Yue, P. Yang, and J. Chu, "Structure, composition and optical properties of  $\text{Cu}_2\text{ZnSnS}_4$  thin films deposited by Pulsed Laser Deposition method," *Solar Energy Materials & Solar Cells*, vol. 95, no. 10, pp. 2907–2913, 2011.
- [6] A. Nagaoka, K. Yoshino, H. Taniguchi, T. Taniyama, and H. Miyake, "Preparation of  $\text{Cu}_2\text{ZnSnS}_4$  single crystals from Sn solutions," *Journal of Crystal Growth*, vol. 341, no. 1, pp. 38–41, 2012.
- [7] C.-H. Wang, F.-Y. Hung, T.-S. Lui, and L.-H. Chen, "The charge-discharge characteristics of woody carbon modified with  $\text{Fe}_3\text{O}_4$  nano phase using the hydrothermal method," *Materials Transactions*, vol. 51, no. 1, pp. 186–191, 2010.
- [8] Z.-S. Hu, F.-Y. Hung, S.-J. Chang et al., "Effects of Ag nanoshape and AgGa phase in Ag-Si nanostructure using 2-step etching process," *Journal of Alloys and Compounds*, vol. 509, no. 3, pp. 758–763, 2011.
- [9] P. K. Sarswat, M. Snure, M. L. Free, and A. Tiwari, "CZTS thin films on transparent conducting electrodes by electrochemical technique," *Thin Solid Films*, vol. 520, no. 6, pp. 1694–1697, 2012.

- [10] M. Kauk, K. Muska, M. Altosaar et al., "Effects of sulphur and tin disulphide vapour treatments of  $\text{Cu}_2\text{ZnSnS}(\text{Se})_4$  absorber materials for monograin solar cells," *Energy Procedia*, vol. 10, pp. 197–202, 2011.
- [11] G. Zha, W. Jie, T. Tan, and X. Wang, "Effect of surface treatments on the electrical and optical properties of CdZnTe single crystal," *Nuclear Instruments and Methods in Physics Research A: Accelerators, Spectrometers, Detectors and Associated Equipment*, vol. 566, no. 2, pp. 495–499, 2006.
- [12] D. B. Mitzi, O. Gunawan, T. K. Todorov, K. Wang, and S. Guha, "The path towards a high-performance solution-processed kesterite solar cell," *Solar Energy Materials & Solar Cells*, vol. 95, no. 6, pp. 1421–1436, 2011.
- [13] K. J. Chen, F. Y. Hung, S. J. Chang, and Z. S. Hu, "The crystallized mechanism and optical properties of sol-gel synthesized ZnO nanowires," *Journal of the Electrochemical Society*, vol. 157, no. 3, pp. H241–H245, 2010.
- [14] M. Grossberg, J. Krustok, J. Raudoja, K. Timmo, M. Altosaar, and T. Raadik, "Photoluminescence and Raman study of  $\text{Cu}_2\text{ZnSn}(\text{Se}_x\text{S}_{1-x})_4$  monograins for photovoltaic applications," *Thin Solid Films*, vol. 519, no. 21, pp. 7403–7406, 2011.
- [15] R. Bacewicz, W. Gebicki, and J. Filipowicz, "Raman scattering in  $\text{CuInS}_{2x}\text{Se}_{2(1-x)}$  mixed crystals," *Journal of Physics: Condensed Matter*, vol. 6, no. 49, article 003, pp. L777–L780, 1994.
- [16] N. M. Shinde, R. J. Deokate, and C. D. Lokhande, "Properties of spray deposited  $\text{Cu}_2\text{ZnSnS}_4$  (CZTS) thin films," *Journal of Analytical and Applied Pyrolysis*, vol. 100, pp. 12–16, 2013.
- [17] S. W. Shin, J. H. Han, C. Y. Park, A. V. Moholkar, J. Y. Lee, and J. H. Kim, "Quaternary  $\text{Cu}_2\text{ZnSnS}_4$  nanocrystals: facile and low cost synthesis by microwave-assisted solution method," *Journal of Alloys and Compounds*, vol. 516, pp. 96–101, 2012.
- [18] N. M. Shinde, P. R. Deshmukh, S. V. Patil, and C. D. Lokhande, "Aqueous chemical growth of  $\text{Cu}_2\text{ZnSnS}_4$  (CZTS) thin films: air annealing and photoelectrochemical properties," *Materials Research Bulletin*, vol. 48, no. 5, pp. 1760–1766, 2013.
- [19] H. Yoo, J. Kim, and L. Zhang, "Sulfurization temperature effects on the growth of  $\text{Cu}_2\text{ZnSnS}_4$  thin film," *Current Applied Physics*, vol. 12, no. 4, pp. 1052–1057, 2012.

## Research Article

# Thermal Effect on the Structural, Electrical, and Optical Properties of In-Line Sputtered Aluminum Doped Zinc Oxide Films Explored with Thermal Desorption Spectroscopy

Shang-Chou Chang, Tien-Chai Lin, and To-Sing Li

*Department of Electrical Engineering, Kun Shan University, Tainan 71003, Taiwan*

Correspondence should be addressed to Shang-Chou Chang; [jchang@mail.ksu.edu.tw](mailto:jchang@mail.ksu.edu.tw)

Received 7 May 2014; Accepted 18 May 2014; Published 29 May 2014

Academic Editor: Teen-Hang Meen

Copyright © 2014 Shang-Chou Chang et al. This is an open access article distributed under the Creative Commons Attribution License, which permits unrestricted use, distribution, and reproduction in any medium, provided the original work is properly cited.

This work investigates the thermal effect on the structural, electrical, and optical properties of aluminum doped zinc oxide (AZO) films. The AZO films deposited at different temperatures were measured using a thermal desorption system to obtain their corresponding thermal desorption spectroscopy (TDS). In addition to obtaining information of thermal desorption, the measurement of TDS also has the effect of vacuum annealing on the AZO films. The results of measuring TDS imply part of the doped aluminum atoms do not stay at substituted zinc sites in AZO films. The (002) preferential direction of the AZO films in X-ray diffraction spectra shifts to a lower angle after measurement of TDS. The grain size grows and surface becomes denser for all AZO films after measurement of TDS. The carrier concentration, mobility, and average optical transmittance increase while the electrical resistivity decreases for AZO films after measurement of TDS. These results indicate that the AZO films deposited at 200°C are appropriate selections if the AZO films are applied in device fabrication of heat-produced process.

## 1. Introduction

Zinc oxide is an old semiconductor material that dates back to the beginning of the 20th century. It has been applied in different areas like piezoelectric transducers, optical waveguides, acoustooptic media, gas sensors, varistors, and transparent conductive (TC) electrode [1]. The recent popular and hot application for zinc oxide is TC electrode. Indium tin oxide (ITO) is regularly used in TC electrode of light emitting diodes, flat panels, or solar cells industry [2]. Since indium is rare and toxic, there is a tendency to replace ITO with aluminum doped zinc oxide (AZO) for cost and safety concerns. These years, the AZO can compete with ITO due to compatible electrical and optical properties [3, 4]. In-line sputtering method can be used to produce large-area and high-throughput thin films. This work focuses on surveying in-line sputtered instead of batch-type produced AZO films. Anisotropic stress in thin films produced during in-line sputtering process has been reported [5]. The properties of AZO films produced by in-line sputtering may be different

when being compared with those produced by batch-type sputtering.

Heat generation may occur after TC electrode is produced in solar cells fabrication, such as plasma enhanced chemical vapor deposition in growing amorphous silicon films as absorption layer materials. The substrate temperature in the above process is usually around 300°C [6]. The structural, electrical, and optical properties of AZO films may change after the heat generation process. Haug et al. have reported AZO films' property alternation after thermal treatment [7]. Variation in electrical and optical properties of AZO films has to be considered if AZO films are used in heat production process.

Thermal desorption spectroscopy was firstly used in studying metal or gas desorption behavior [8]. More applications for TDS such as thermal stability [9], catalyst reaction [9], and hydrogen storage [10, 11] were developed recently. Our group has applied TDS to investigate the thermal effect on fluorine doped zinc oxide (ZnO:F) films before [12]. The results indicate ZnO:F films desorb corresponding to low

bound strength under heat treatment of 100°C. Fluorine is easily desorbed from ZnO:F films. Apparently, negative effects influence the electrical and optical properties of ZnO:F films during heating process. The electrical resistivity increases whereas the average optical transmittance in visible wavelength decreases for ZnO:F films after TDS measurement. The measurement of TDS is a heating process for ZnO:F films. This finding further motivates us to study the thermal effect on commonly used zinc oxide films: AZO films. This work applied TDS to study the thermal effect on the structural, electrical, and optical properties of AZO films deposited at different substrate temperatures. We checked whether there was any species desorbed from AZO films during measuring TDS and then calculated and compared the thermal desorption amount of AZO films. Structural, electrical, and optical properties of AZO films before and after TDS measurements were also explored.

## 2. Experimental Procedure

The substrate that AZO films were to be deposited on was the borosilicate glass. The  $2.54 \times 2.54 \text{ cm}^2$  borosilicate glass was ultrasonically cleaned with purified water and acetone in sequence three times. After that, the glass was further cleaned with purified water and dried with dry nitrogen. One in-line DC magnetron sputtering tool was applied to deposit AZO films. The ceramic AZO target was with  $\text{ZnO}/\text{Al}_2\text{O}_3 = 98:2 \text{ wt\%}$  in composition and  $95 \times 20 \text{ cm}^2$  in size. The sputtering power density was  $1.58 \text{ W}/\text{cm}^2$ . The process chamber was pumped down to  $5 \times 10^{-3} \text{ Pa}$  as base pressure. The process pressure was kept at  $3 \times 10^{-1} \text{ Pa}$  with feeding pure argon. The substrate temperature during sputtering process was at room temperature (RT), 100°C, and 200°C, respectively. The film thickness of produced AZO films was 500 nm. The TDS of prepared AZO films were measured. The measurement system of TDS was pumped down to  $10^{-5} \text{ Pa}$  range or below. Then, the AZO films were linearly heated by a proportional-integral-derivative controller at a fixed 10°C per minute heating rate from RT to 500°C. The heating of the measurement system was closed after the AZO films reached 500°C. The temperature of the TDS measurement system was naturally cooled down in vacuum. Measuring TDS of the AZO films also plays the role of vacuum annealing on the AZO films. Ion currents corresponding to ion mass to charge ratio ( $m/e$ ) 16, 27, 32, and 65 were measured with a quadruple mass spectrometer (QMS). The  $m/e$  of 16, 27, 32, and 65 corresponds to the oxygen atom, aluminum atom, oxygen molecule, and zinc atom, respectively. The TDS of the AZO films was obtained by plotting ion currents of the above four elements versus the corresponding temperature.

The crystalline structure and surface morphology of AZO films before and after measuring TDS were probed with an X-ray diffractometer (XRD) and a scanning electron microscope (SEM), respectively. The carrier concentration, mobility, and electrical resistivity of AZO films before and after measuring TDS were obtained by a hall measurement with Van-Der Pauw method. The optical transmittance of

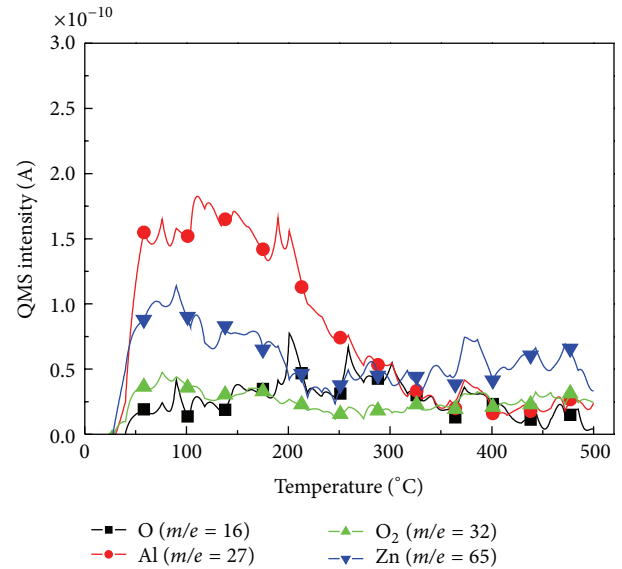


FIGURE 1: Thermal desorption spectroscopy of the AZO films deposited at 200°C.

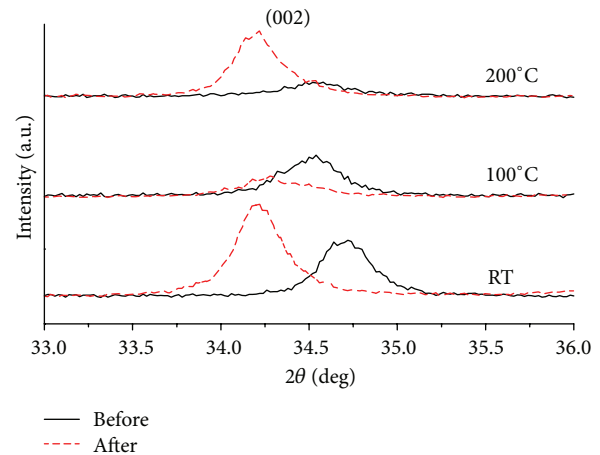


FIGURE 2: The X-ray diffraction spectra of the AZO films deposited at room temperature (RT), 100°C, and 200°C before and after measuring TDS.

AZO films before and after measuring TDS was probed by an ultraviolet-visible spectrophotometer. The percent variation of electrical resistivity and average optical transmittance in visible wavelength region for the AZO films before and after measuring TDS were calculated. The AZO films with low percent variation of electrical resistivity and optical transmittance imply they demonstrate stable electrical and optical properties when applied in heat production process.

## 3. Results and Discussion

**3.1. Thermal Desorption.** All AZO films deposited at different substrate temperatures exhibit similar curve shape but different intensity in TDS. The increasing ion current regarding

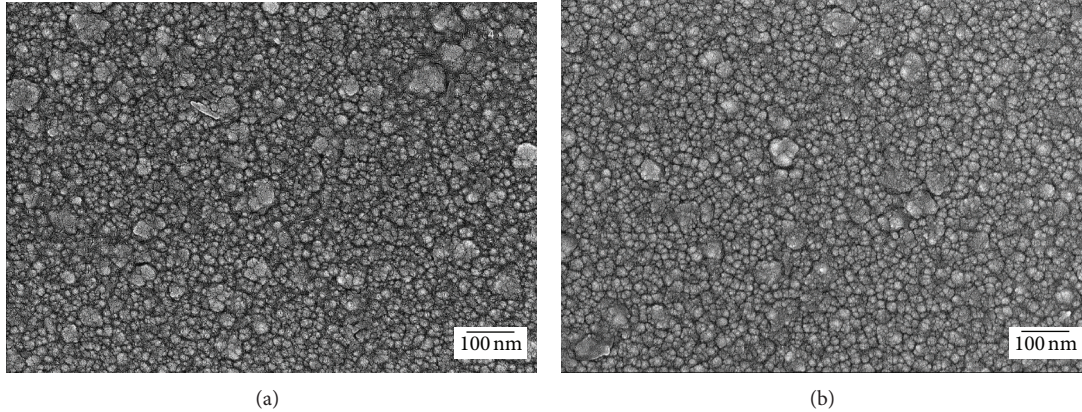


FIGURE 3: SEM micrographs of the AZO films deposited at room temperature (RT) (a) before and (b) after measuring TDS.

oxygen atom, aluminum atom, oxygen molecule, and zinc atom, respectively, can be apparently observed during TDS measurement. The TDS of the 200°C substrate produced AZO films was shown in Figure 1. The impurity metal element, aluminum atom, and the intrinsic metal element, zinc atom, both exhibit higher thermal desorption intensity than oxygen atom and oxygen molecule seen from Figure 1. The apparent increase in thermal desorption intensity of the four elements is between 60 and 200°C. High thermal desorption intensity of the aluminum atom indicates that aluminum is thermally unstable in AZO films. Haug et al. reported the thermal stability of extrinsic donors in zinc oxide like aluminum is better than that of intrinsic donors [7]. The thermal instability of aluminum found in this work may attribute that some aluminum atoms in AZO films do not exist in substituted zinc sites. They stay in other positions which make aluminum thermally unstable.

Thermal desorption amount of the elements in AZO films is proportional to integrating thermal desorption intensity with temperature derived from Polanyi-Wigner equation [8]. The ratio of desorption amount for the aluminum atom was calculated to be 39 : 26 : 22, corresponding to AZO films deposited at RT, 100°C, and 200°C substrate, respectively. This phenomenon may attribute that when AZO films deposited at high substrate temperature like 200°C, thermally unstable atoms or molecules have been thermally desorbed during sputtering. Therefore, the remaining materials on substrate after sputtering possess good adhesion. Good adhesion of the AZO films can reduce the possibility that the AZO constituents diffuse to other layer(s) during device fabrication in heat-produced process if AZO films are applied as TC electrodes. The diffusion may deteriorate the device function.

**3.2. Structural Property.** All AZO films possess (002) preferential direction obtained from measuring X-ray diffraction. The X-ray diffraction spectra for the AZO films deposited at different substrate temperatures before and after measuring TDS are shown in Figure 2. The corresponding (002) peak location and full width at half maximum of X-ray diffraction spectra are listed in Table 1. After TDS being measured,

TABLE 1: The (002) peak location and full width at half maximum of X-ray diffraction spectra of the AZO films deposited at room temperature (RT), 100°C, and 200°C before and after measuring TDS.

| Substrate temperature | $2\theta$ |        | FWMH   |       |
|-----------------------|-----------|--------|--------|-------|
|                       | Before    | After  | Before | After |
| RT                    | 34.70°    | 34.25° | 0.35°  | 0.32° |
| 100°C                 | 34.54°    | 34.20° | 0.40°  | 0.44° |
| 200°C                 | 34.56°    | 34.20° | 0.45°  | 0.36° |

the (002) peak shifts to a lower angle for all AZO films. The measurement of TDS has the effect of vacuum annealing on the AZO films. It may cause the high proportion of metallic interstitial defects in the lattice of the AZO films [13]. This increases the lattice space which makes (002) peaks shift to a lower angle for the AZO films after TDS measurement. The full width at half maximum decreases for the AZO films deposited at RT and 200°C after measuring TDS. However, the full width at half maximum increases for the AZO films deposited at 100°C after measuring TDS. The measured results on the full width at half maximum of X-ray diffraction spectra for the AZO films may be related to grain growth and release of anisotropic stress. The measurement of TDS provides thermal energy to make the grains of the AZO films grow. However, it may also release the anisotropic stress for the AZO films produced during in-line sputtering [14]. Incomplete release of the anisotropic stress may explain the increment of the full width at half maximum for AZO films deposited at 100°C.

Figure 3 shows SEM micrographs of the AZO films deposited at RT before and after measuring TDS. The film surface of the AZO films after measuring TDS becomes relatively smooth as observed from Figure 3. Figure 4 shows the SEM observation of the AZO films deposited at 100°C, before and after measuring TDS. The grains are quite even for samples deposited at 100°C compared with those deposited at RT. Figure 5 shows the SEM observation of the AZO films deposited at 200°C, before and after measuring TDS.

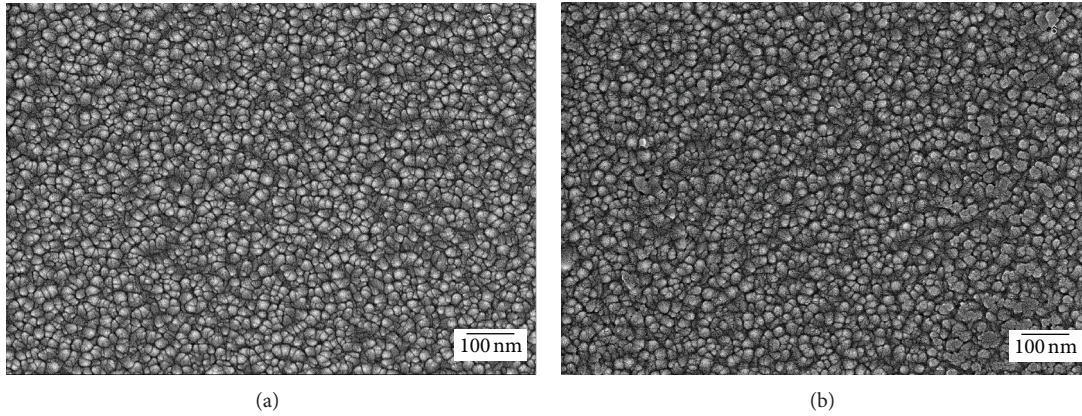


FIGURE 4: SEM micrographs of the AZO films deposited at 100°C (a) before and (b) after measuring TDS.

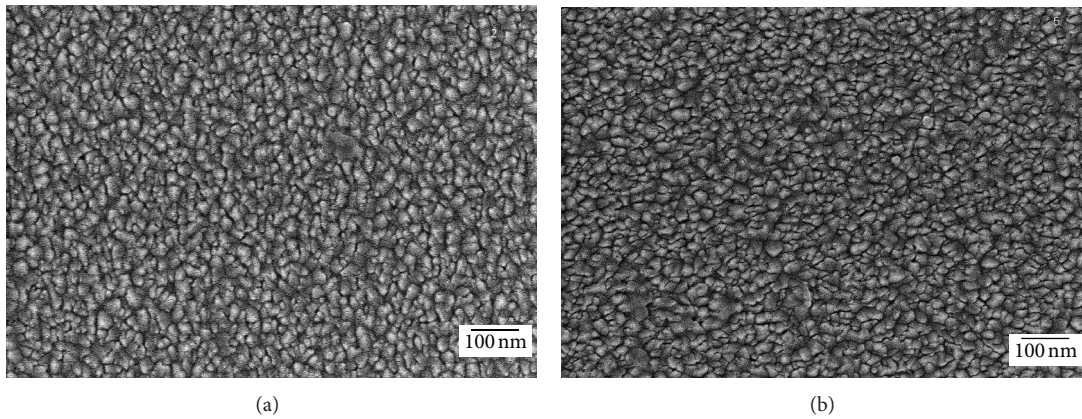


FIGURE 5: SEM micrographs of the AZO films deposited at 200°C (a) before and (b) after measuring TDS.

The surface morphology of the samples deposited at 200°C demonstrates a pyramidal shape. The grain size grows and surface becomes denser for all AZO films after measuring TDS as observed from Figures 3 to 5. The provision of thermal energy by TDS for grain growth of the AZO films is further evidenced by the results of the SEM micrographs.

**3.3. Electrical Property.** The electrical properties carrier concentration, mobility, electrical resistivity, and percent variation of electrical resistivity for the AZO films deposited at different temperatures before and after measuring TDS were shown in Table 2. The carrier concentration and mobility increase whereas the electrical resistivity decreases for the AZO films deposited at different temperatures after measuring TDS. The measurement of TDS has vacuum annealing effect on AZO films, and vacuum annealing effect causes more aluminum atoms to substitute zinc sites [15] or promotes desorption of oxygen from grain boundaries so as to increase the carrier concentration [16]. It makes AZO films increase oxygen defects, zinc interstitial atoms, and grain size [17]. Increase in oxygen defects and zinc interstitial atoms raises carrier concentration. The growth in grain size of

the AZO films results in less grain boundary scattering. The mobility of the AZO films is therefore increased.

The AZO films deposited at 200°C exhibit the lowest electrical resistivity before or after measuring TDS, as well as the lowest percent variation among the AZO films deposited at different temperatures seen from Table 2. These results indicate the AZO films deposited at 200°C are suitable selections applying in thermally treated process based on electrical properties. Poor electrical properties such as low carrier concentration and mobility and high percent variation of electrical resistivity for the AZO films deposited at 100°C before and after measuring TDS shown in Table 2 may be related with anisotropic stress in AZO films produced during in-line sputtering [14]. The stress resulted from skew incidence of sputtered ions or atoms' flux on substrate along the in-line moving direction when the substrate was entering or leaving the process chamber during sputtering. The direction perpendicular to the moving direction of substrate does not have the abovementioned stress. The anisotropic stress was trapped in AZO films when the films were deposited at RT. The anisotropic stress started to be released but incompletely when the films were deposited at 100°C. Poor crystalline structure of the AZO films deposited at 100°C was evidenced

TABLE 2: The electrical properties: carrier concentration, mobility, electrical resistivity, and percent variation of electrical resistivity of the AZO films deposited at room temperature (RT), 100°C, and 200°C before and after measuring TDS.

| Substrate temperature | Before  |  |   | After   |  |   | Electrical resistivity's percent variation (%) |
|-----------------------|---|--|---|---|--|---|--|
|                       | Carrier concentration ( $10^{20} \text{ cm}^{-3}$ ) | Mobility ( $\text{cm}^2/\text{V}\cdot\text{s}$ ) | Electrical resistivity ( $10^{-4} \Omega\cdot\text{cm}$ ) | Carrier concentration ( $10^{20} \text{ cm}^{-3}$ ) | Mobility ( $\text{cm}^2/\text{V}\cdot\text{s}$ ) | Electrical resistivity ( $10^{-4} \Omega\cdot\text{cm}$ ) |  |
| RT                    | 3.7   | 6.4  | 27  | 4.1   | 8.0  | 19  | -30  |
| 100°C                 | 0.6   | 6.6  | 160   | 1.3   | 6.9  | 69  | -57  |
| 200°C                 | 6.0   | 6.4  | 16  | 6.9   | 7.5  | 12  | -25  |

TABLE 3: The average optical transmittance in visible wavelength region and the corresponding percent variation of the AZO films deposited at room temperature (RT), 100°C, and 200°C before and after measuring TDS.

| Substrate temperature | Average optical transmittance (%) |       | Average optical transmittance's percent variation (%) |
|-----------------------|-----------------------------------|-------|---|
|                       | Before                            | After |   |
| RT                    | 70                                | 82    | 17  |
| 100°C                 | 71                                | 75    | 5.6   |
| 200°C                 | 90                                | 92    | 2.2   |

in results of the X-ray diffraction spectra in Figure 2 and Table 1. Poor crystalline structure destroys part of the carriers and lowers the mobility for the AZO films deposited at 100°C.

**3.4. Optical Property.** Figure 6 presents the optical transmittance spectra for the AZO films deposited at different temperatures before and after measuring TDS. Blue shift behavior of the optical transmittance spectra for the AZO films after measuring TDS was apparently observed in inset of Figure 6. The blue shift behavior can be ascribed to Burstein-Moss effect [18, 19]. The measurement of TDS which has the effect of vacuum annealing causes the increase of carrier concentration as shown in Table 2. The increment of carrier concentration widens the optical band gap of the AZO films. The average optical transmittance and the corresponding percent variation of the AZO films before and after measuring TDS deposited at RT, 100°C, and 200°C were shown in Table 3. The AZO films deposited at 200°C exhibit the highest average optical transmittance before or after measuring TDS and lowest percent variation among those deposited at different temperatures observed from Table 2. The measurement of TDS which has the effect of vacuum annealing reduces the materials defects of AZO films [20]; the average optical transmittance therefore increases.

## 4. Conclusion

Thermal effect on the structural, electrical, and optical properties of AZO films was studied by measuring TDS. The results of TDS imply part of the doped aluminum atoms do not stay at the substituted zinc sites in AZO films. The measurement of TDS has the effect of vacuum annealing on the AZO films. The measurement of TDS provides thermal energy to make the grains growth of the AZO films, and

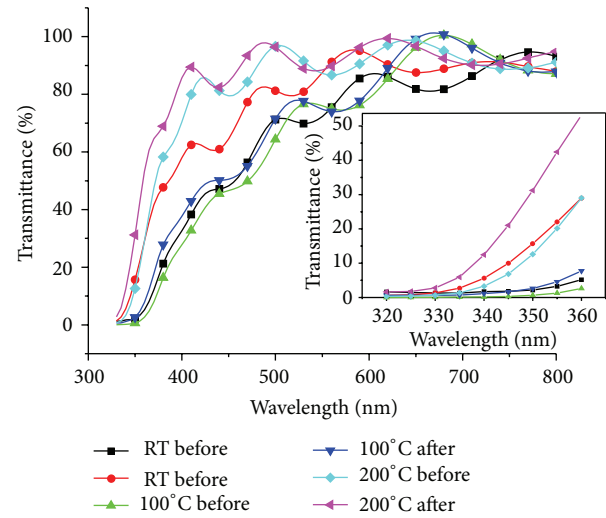


FIGURE 6: The optical transmittance spectra of the AZO films deposited at room temperature (RT), 100°C, and 200°C before and after measuring TDS.

such finding is evidenced by the results of the SEM micrographs. The carrier concentration, mobility, and average optical transmittance of the AZO films increase after measuring TDS. On the other hand, the electrical resistivity of the AZO films decreases after measuring TDS. The AZO films deposited at 200°C are appropriate selections if the AZO films are applied in device fabrication of heat-produced process. In short, the AZO films deposited at 200°C show low electrical resistivity, high average optical transmittance, low percent variation of electrical resistivity, and average optical transmittance among all tested AZO films.

## Conflict of Interests

The authors declare that there is no conflict of interests regarding the publication of this paper.

## Acknowledgments

The authors would like to thank the National Science Council of Taiwan for financial support (NSC-98-2221-E-168-005 and NSC 102-2221-E-168-037), Bay Zu Precision Corporation for providing in-line sputtering tool, and Shen-Hua Wu for carrying out part of measurements.

## References

- [1] R. Triboulet and J. Perrière, "Epitaxial growth of ZnO films," *Progress in Crystal Growth and Characterization of Materials*, vol. 47, no. 2-3, pp. 65–138, 2003.
- [2] R. G. Gordon, "Criteria for choosing transparent conductors," *MRS Bulletin*, vol. 25, no. 8, pp. 52–57, 2000.
- [3] P. Nunes, E. Fortunato, P. Tonello, F. Braz Fernandes, P. Vilarinho, and R. Martins, "Effect of different dopant elements on the properties of ZnO thin films," *Vacuum*, vol. 64, no. 3-4, pp. 281–285, 2002.
- [4] R. J. Hong, X. Jiang, B. Szyszka, V. Sittinger, and A. Pflug, "Studies on ZnO:Al thin films deposited by in-line reactive mid-frequency magnetron sputtering," *Applied Surface Science*, vol. 207, no. 1-4, pp. 341–350, 2003.
- [5] S. Suzuki, "Internal stress and adhesion of thin films sputtered onto glass by an in-line sputtering system," *Thin Solid Films*, vol. 351, no. 1-2, pp. 194–197, 1999.
- [6] J. Cárabe and J. J. Gandia, "Thin-film-silicon solar cells," *Optoelectronics Review*, vol. 12, no. 1, pp. 1–6, 2004.
- [7] F.-J. Haug, Z. Geller, H. Zogg, A. N. Tiwari, and C. Vignali, "Influence of deposition conditions on the thermal stability of ZnO:Al films grown by rf magnetron sputtering," *Journal of Vacuum Science and Technology A*, vol. 19, no. 1, pp. 171–174, 2001.
- [8] D. A. King, "Thermal desorption from metal surfaces: a review," *Surface Science*, vol. 47, no. 1, pp. 384–402, 1975.
- [9] B. Hokkanen, S. Funk, U. Burghaus, A. Ghicov, and P. Schmuki, "Adsorption kinetics of alkanes on TiO<sub>2</sub> nanotubearray—structure-activity relationship," *Surface Science*, vol. 601, no. 19, pp. 4620–4628, 2007.
- [10] K. Higuchia, K. Yamamoto, H. Kajioka et al., "Remarkable hydrogen storage properties in three-layered Pd/Mg/Pd thin films," *Journal of Alloys and Compounds*, vol. 330–332, pp. 526–530, 2002.
- [11] N. Patel, A. Kale, P. Mosaner, R. Checchetto, A. Miotello, and G. Das, "Deuterium thermal desorption from Ni-rich deuterated Mg thin films," *Renewable Energy*, vol. 33, no. 2, pp. 232–236, 2008.
- [12] S. C. Chang, T. C. Lin, T. S. Li et al., "Fluorine thermal stability of ZnO:F films investigated by thermal desorption spectroscopy," in *Proceedings of the International Conference on Electronic Materials and Packaging (EMAP '08)*, pp. 25–28, Taipei, Taiwan, October 2008.
- [13] C. Guillén and J. Herrero, "Optical, electrical and structural characteristics of Al:ZnO thin films with various thicknesses deposited by DC sputtering at room temperature and annealed in air or vacuum," *Vacuum*, vol. 84, no. 7, pp. 924–929, 2010.
- [14] S. C. Chang, G. W. Jian, S. H. Huang, T. S. Li, and T. C. Lin, "Some special phenomena observed from in-line sputtered aluminum doped zinc oxide films," in *Proceedings of the 5th International Microsystems, Packaging, Assembly and Circuits Technology Conference (IMPACT '10)*, pp. 1–4, Taipei, Taiwan, October 2010.
- [15] Y. M. Hu, C. W. Lin, and J. C. A. Huang, "Dependences of the Al thickness and annealing temperature on the structural, optical and electrical properties in ZnO/Al multilayers," *Thin Solid Films*, vol. 497, no. 1-2, pp. 130–134, 2006.
- [16] J. F. Chang, H. L. Wang, and M. H. Hon, "Studying of transparent conductive ZnO:Al thin films by RF reactive magnetron sputtering," *Journal of Crystal Growth*, vol. 211, no. 1, pp. 93–97, 2000.
- [17] M. Chen, X. Wang, Y. H. Yu et al., "X-ray photoelectron spectroscopy and auger electron spectroscopy studies of Al-doped ZnO films," *Applied Surface Science*, vol. 158, no. 1, pp. 134–140, 2000.
- [18] E. Burstein, "Anomalous optical absorption limit in InSb," *Physical Review*, vol. 93, no. 3, pp. 632–633, 1954.
- [19] T. S. Moss, "The interpretation of the properties of indium antimonide," *Proceedings of the Physical Society B*, vol. 67, no. 10, pp. 775–782, 1954.
- [20] G. Fang, D. Li, and B. L. Yao, "Fabrication and vacuum annealing of transparent conductive AZO thin films prepared by DC magnetron sputtering," *Vacuum*, vol. 68, no. 4, pp. 363–372, 2002.

## Research Article

# Self-Excited Single-Stage Power Factor Correction Driving Circuit for LED Lighting

**Yong-Nong Chang**

*Department of Electrical Engineering, National Formosa University, Yunlin County 63201, Taiwan*

Correspondence should be addressed to Yong-Nong Chang; [ynchang@nfu.edu.tw](mailto:ynchang@nfu.edu.tw)

Received 19 February 2014; Accepted 3 March 2014; Published 27 March 2014

Academic Editor: Teen-Hang Meen

Copyright © 2014 Yong-Nong Chang. This is an open access article distributed under the Creative Commons Attribution License, which permits unrestricted use, distribution, and reproduction in any medium, provided the original work is properly cited.

This paper proposes a self-excited single-stage high power factor LED lighting driving circuit. Being featured with power factor correction capability without needing any control devices, the proposed circuit structure is with low cost and suitable for commercial production. The power factor correction function is accomplished by using inductor in combination with a half-bridge quasi resonant converter to achieve active switching and yield out voltage regulation according to load requirement. Furthermore, the zero-voltage switching in the half-bridge converter can be attained to promote the overall performance efficiency of the proposed circuit. Finally, the validity and production availability of the proposed circuit will be verified as well.

## 1. Introduction

Due to the recent breakthrough in fabricating process [1–3] and progressive improvement of lighting efficiency, LED is featured with ecofriendly, free-Mercury, and low power consumption, compactness, high efficiency, and so on, thus prevailing over other lighting devices in the lighting applications. The LED (light emitting diode) lighting products are inclined toward diversified growth and application penetration. The global market scale of LED lighting products is predicted to come up to several tens of billions USA dollars in the coming year 2015. The demand of LED lighting equipment will be ever increasing.

Vast switching circuits are inevitably used in energy industry. The PFC (power factor correction) circuit is, therefore, studied and developed in the past two decades [4–6] to meet the IEC (International Electrotechnical Commission) requirements in the harmonic current standard [7]. In consequence, it is indispensable feature for the power converter to possess the power factor correction function. Power factor correction circuits can be categorized into passive type [8–12] and active type [13–15]. Passive type PFC circuit is basically composed of inductor and capacitor. It possesses the feature of low cost without needing extra control circuit. However, though active type PFC circuit possesses better power factor,

it is costly due to needing extra control circuit. In commercial applications, the cost consideration has led the extensive usage to meet PFC standard.

The power switch driving method comprises two types: self-excitation and external excitation ones. In a self-excitation circuit, resonant current feedback signal is sampled to generate driving signal without needing extra control circuit. However, the circuit performance and output characteristics are drastically affected by the device parameters, such as storage time and saturation point of transformer. The operation frequency of resonant circuit plays the key role in performance stability. The design and device selection involve more disciplines and strict conditions. Hence, the circuit parameters must be carefully envisaged. It is relatively difficult in design. Although external excitation control circuit is complex, it is both flexible and rich in design. The operating frequency of inverter and duty cycle of switch can be adjusted at will. It could, therefore, easily carry out dimming function and fault protection design. With the addition of the preceding functions, the circuit complexity inevitably increases and control IC is indispensable. Consequently, the fabricating cost will increase.

The commonly used two-stage high power factor circuit not only possesses enormous device parts and does not meet cost reduction, but also encompasses one stage to

correct power factor and another converter stage to perform voltage and current regulation. The switches therein are all hard switching basically. Therefore, the switching losses are drastically large, thus invoking heat dissipation problem. The accompanied losses in both PFC stage and conversion stage will result in poor overall efficiency [16, 17]. However, single-stage high power factor circuit structure integrates both stages into one by employing the same power switches to handle both PFC and conversion processes to reduce the power loss. Despite the fact that the switching modes turn to be complicated in nature and the determination of device parameters becomes strict [18, 19], the single-stage high power factor circuit both reduces the number of devices and avoids conversion loss between stages, thus enhancing the overall efficiency.

The self-excitation circuit structure proposed in this research utilizes resonant tank to resonate and drive the power switches. With the absence of integrated circuit and control IC, the cost can be greatly reduced. However, the traditional self-excitation circuit is inherited with poor power factor. A power correction circuit is required to promote the power factor, while it may produce low frequency noise and is bulky in size.

This research intended to design a self-excitation single-stage high power factor driving circuit for LED lighting to overcome the proceeding drawbacks. Self-excitation technique is introduced to drive control signal and, therefore, achieves the active power factor correction function. In addition, dramatic cost and circuit complexity reductions are fulfilled by the absence of integrated circuits. The usage of half-bridge resonant technique can effectively increase the operating frequency to avoid audible noise production along with output voltage and current regulations. Furthermore, the zero-voltage-switching function furnished by resonant circuit can effectively reduce the high-frequency switching loss and tackle the heat dissipation problem. Consequently, the proposed self-excitation high power factor single-stage driving circuit is featured with advantages such as simple structure, size reduction, and low complexity.

## 2. Configuration

Figure 1 is the circuit configuration of a self-excitation single-stage high power factor driving circuit for LED lighting proposed in this research. It is majorly constituted by a PFC inductor  $L_{\text{PFC}}$ , resonant inductor  $L_r$ , and resonant capacitor  $C_r$ . Besides, the self-excitation circuit comprises energy storage capacitor  $C_{\text{bus}}$ , resistor  $R_1$ , capacitor  $C_1$ , and silicon diode for alternating current (SIDAC). The self-excitation mechanism is accomplished by switching half-bridge converter to store and release energy on PFC inductor  $L_{\text{PFC}}$  to complete high power factor performance. For lack of control IC, the cost can be curtailed consequently. By utilizing self-excitation along with half-bridge resonant switching technique, the output voltage and current can meet the LED lighting load requirement. The technique of resonant converter will equip the power switch with zero-voltage-switching function and enhance the overall efficiency.

Self-excitation electronic ballast has the advantage of generating driving signal by itself without needing extra control circuit, thus saving the budget. In this research, a simple circuit using resistor  $R_1$  and capacitor  $C_1$  is applied to accomplish the self-excitation purpose. Figure 2 shows the current flow path of the first trigger operation.

As illustrated in the above figure, the half-bridge resonant switch is left open due to lack of triggering signal. Therefore, the current will pass through the intrinsic diode  $D_1$  inherited on switch to pump the energy to storage capacitor  $C_{\text{bus}}$ . Next, the energy on  $C_{\text{bus}}$  will charge energy storage capacitor  $C_1$  via resistor  $R_1$  until the voltage across  $C_1$  gets enough voltage to turn on SIDAC. After breakdown, the SIDAC starts to transfer energy to signal transformer  $T_{\text{signal}2}$  and half-bridge switches begin to switch complementarily. Through the above operation mode, the triggering signal of half-bridge resonant switching gets ready.

Figure 3 is the triangular inductor current  $i_{L_{\text{PFC}}}$  of power factor corrector. The peak value of current is proportional to the absolute value of switching-on instant of input sinusoidal voltage; that is, the dashed line waveform of current peak  $i_{p,\text{peak}}(t)$  is proportional to the absolute value  $|V_{\text{in}}|$ . This leads to source current  $i_{\text{in}}(t)$  being proportional to source voltage  $V_{\text{in}}(t)$  and in-phase each other, thus bettering the power factor.

In Figure 4, LED lighting set comprises a LED set and a high frequency transformer. In other words, the LEDs are powered by an isolated power source and the LED lighting set is equivalent to a resistor  $R_{\text{LED}}$ . A pair of power switches are triggered complementarily. The input high dc voltage will turn into a high frequency sinusoidal signal after resonant switching of the combination of half-bridge inverters,  $L_r$  and  $C_r$ . Also, the operating characteristics are controlled in the inductive region. The advantages of the preceding conversion include (1) DC high voltage being converted to high frequency sinusoidal wave (it both meets load requirement and reduces EMI due to its nearly sinusoidal form); (2) the increased frequency encompasses extra merits of increased lighting efficiency, reduced magnetic device low frequency noise, declined lamp flickering, compacted and magnetic device; (3) operating characteristics being controlled in the inductive region (the resonant current will lag behind square wave voltage). Before the conduction of resonant switch, current passes through body diode of switch, thus yielding zero-voltage stress on switch during switching action.

## 3. Circuit Operation

In this research, all power switches comprise MOSFET. Figure 5 illustrates the waveforms of triggering signal and voltage across and current through the passive devices. Trigger signals  $V_{\text{GS}1}$  and  $V_{\text{GS}2}$  are applied to control half-bridge resonant switches. The current  $i_{L_{\text{PFC}}}$  passing through power factor correction inductor can be controlled as well to arrive at power factor correction. After cautious selection of resonant inductor  $L_r$  and capacitor  $C_r$ , resonant current waveform  $i_r$  is shown in Figure 5. The voltage across on switches is controlled to zero before being turned on. Figure 5

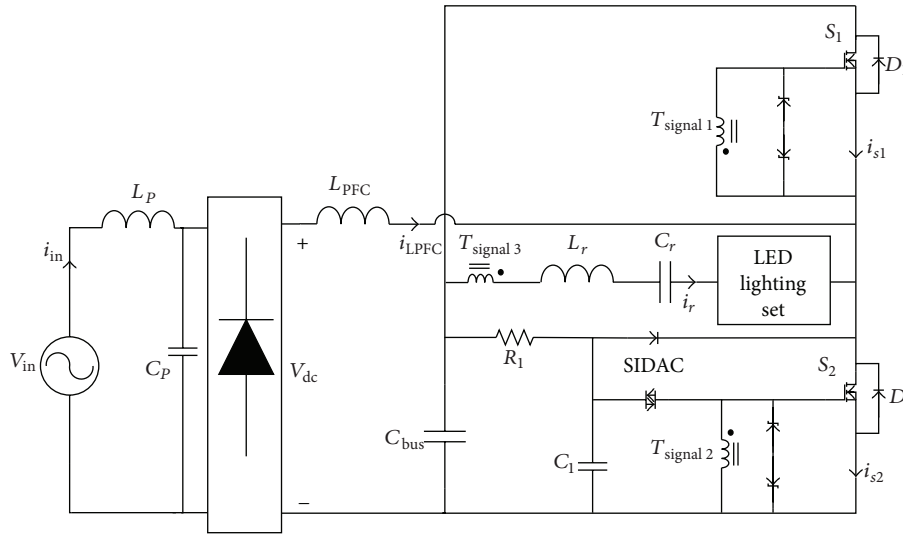


FIGURE 1: Self-excitation single-stage high PF circuit configuration.

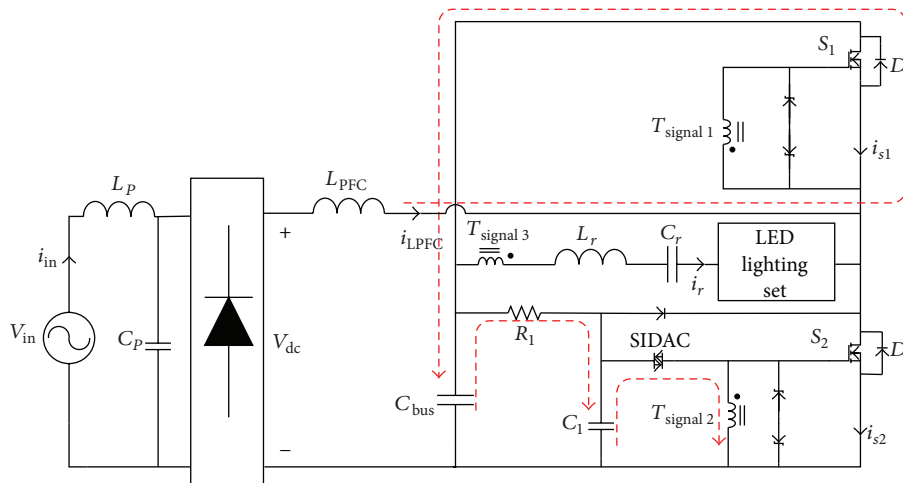


FIGURE 2: Current path of first trigger in self-excitation circuit.

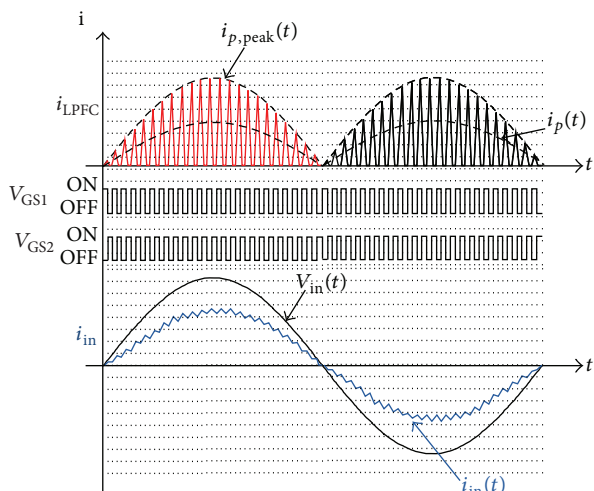


FIGURE 3: PFC inductor current waveform and input current waveform.

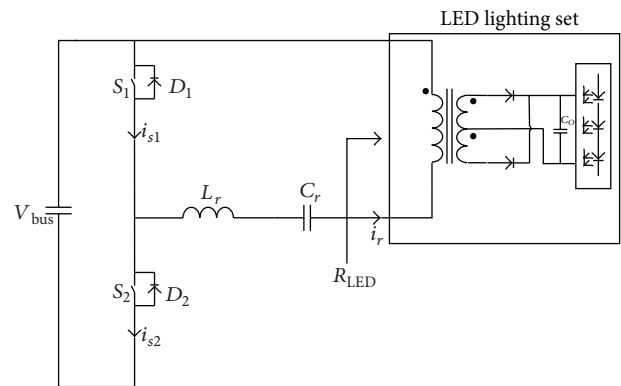


FIGURE 4: Half-bridge resonant converter.

demonstrates the current waveforms  $i_{s1}$  and  $i_{s2}$ . Zero-voltage switching is apparently observed.

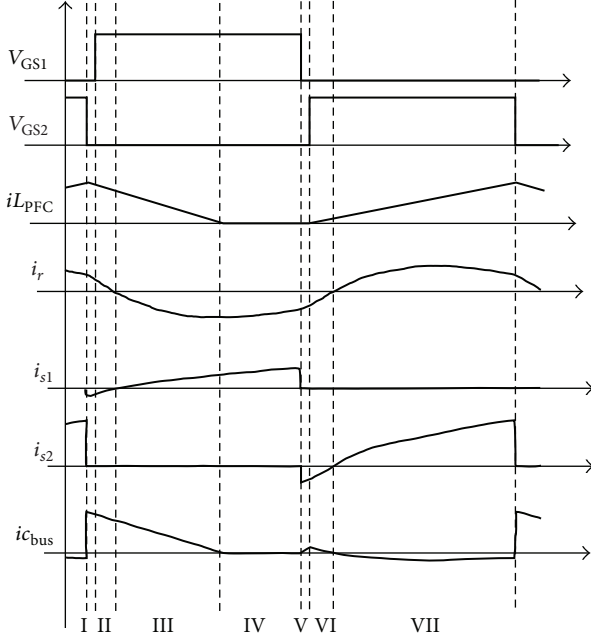


FIGURE 5: Triggering signals and current waveforms.

To simplify the parameter design and analyze the operation models, the following assumptions must be proclaimed in advance.

- (1) All diodes and switching devices are ideal.
- (2) Switching frequency is far greater than grid frequency.
- (3) The voltage  $V_{bus}$  on energy storage capacitor is looked upon as ideal voltage source. Resonant tank current  $i_r$  is viewed as ideal current source without ripple components.
- (4) Resonant quality factor is large enough to assume resonant to be sinusoidal.

**Operation Mode I.** By inspecting the triggering sequence and current waveforms in Figure 5, the triggering signals  $V_{GS1}$  and  $V_{GS2}$  are both under low state. Hence, the resonant current  $i_r$  does freewheeling through intrinsic diode  $D_1$  of switch  $S_1$  as demonstrated in Figure 6(a). Meanwhile, inductor  $L_{PFC}$  releases energy via intrinsic diode and energy storage capacitor  $C_{bus}$ .

**Operation Mode II.** The triggering signal  $V_{GS1}$  is in the high state. As shown in Figure 6(b), resonant current  $i_r$  passes through intrinsic diode  $D_1$  of switch  $S_1$  with freewheeling mechanism. Inductor  $L_{PFC}$  keeps on releasing energy via intrinsic diode and energy storage capacitor  $C_{bus}$ .

**Operation Mode III.** As shown in Figure 6(c), the resonant current  $i_r$  commutates; switch  $S_1$  turns on. Inductor  $L_{PFC}$  releases energy through resonant tank and capacitor  $C_{bus}$ .

**Operation Mode IV.** After energy storage inductor  $L_{PFC}$  releases energy completely, this mode starts as illustrated

in Figure 6(d). Merely resonant current  $i_r$  keeps on flowing through  $S_1$  till the next mode.

**Operation Mode V.** According to sequence waveforms shown in Figure 5, a dead time design is considered in the circuit for avoiding simultaneous conduction of power switches and possible damage. As displayed in Figure 6(e), both the triggering signals are at low state. Thus, resonant current  $i_r$  performs freewheeling through  $C_{bus}$  and intrinsic diode  $D_2$  of power switch  $S_2$ .

**Operation Mode VI.** The triggering signal  $V_{GS2}$  is at the high state in this stage as shown in Figure 6(f). Inductor  $L_{PFC}$  begins to store energy via resonant tank and energy storage capacitor  $C_{bus}$ . Resonant current  $i_r$  continues to do freewheeling through intrinsic diode  $D_2$ .

**Operation Mode VII.** In Figure 6(g), the resonant current  $i_r$  commutates and power switch  $S_2$  turns on. Inductor  $L_{PFC}$  is storing energy via  $S_2$ .

By utilizing the simple trigger signals to accomplish the operation of half-bridge resonant converter, the presented driving circuit also possesses the following advantages: (1) reducing EMI; (2) lowering low frequency noise; (3) providing zero-voltage switching.

#### 4. Circuit Analysis

Prior to the design of parameters, the specifications of circuit and load must be specified in advance. It includes input voltage  $V_{in}$ , switching frequency  $f_s$ , half-bridge resonant frequency  $f_r$ , input real power  $P_{in}$ , output real power  $P_{out}$ , lamp current  $i_r$ , lamp resistance  $R$ , duty cycle  $D$ , and allowable voltage ripple on energy storage capacitor. Afterwards, the design of circuit device parameter can be embarked on.

The proposed AC/DC converter is connected to and supplied by power grid. Thus, the source voltage can be written as

$$V_{in}(t) = V_m \sin(\omega t). \quad (1)$$

Because the switching frequency of half-bridge converter far exceeds the grid frequency as shown in Figure 3, the high frequency switching action will be accomplished within the grid frequency envelope. Thus,  $i_{p,peak}(t)$  can be expressed by (2). By solving out the triangle area of (2), the obtained result is described by  $i_p(t)$  as written in (3). Next,  $i_{p,peak}(t)$  is integrated over half period and the average value can be achieved, as shown in (4), where  $T_s$  is the switching period:

$$i_{p,peak}(t) = \frac{V_m \sin(\omega t) T_s}{2L_{PFC}}, \quad (2)$$

$$i_p(t) \cong \frac{1}{2} \times T_s \times i_{p,peak}(t), \quad (3)$$

$$i_{in}(t) \cong \frac{1}{T_s} \int_0^{T_s} i_p(t) \cdot d(t) = \frac{V_m T_s}{4L_{PFC}} \sin(\omega t). \quad (4)$$

Based on input voltage  $V_{in}(t)$  of (1) and input current  $i_{in}(t)$  of (4), the average input power  $P_{in}$  can be determined according to (5). With circuit efficiency being taken into

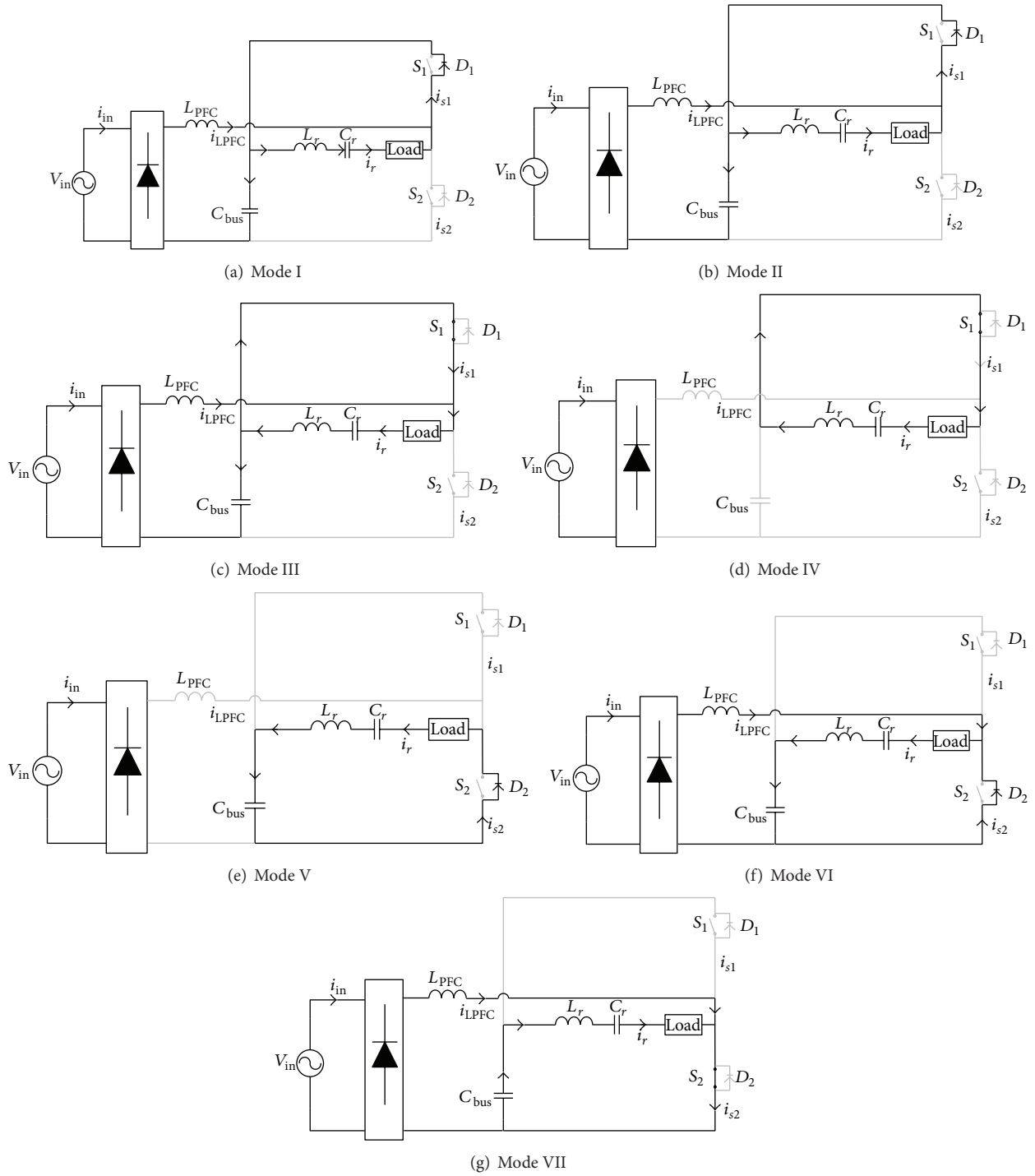


FIGURE 6: Current path of operation mode.

account, the output power  $P_{out}$  of converter can be expressed as in (6). By further mathematical calculation, the quantity of PFC inductor  $L_{PFC}$  can be written as in (7):

$$P_{out} = \eta \cdot P_{in} = \frac{\eta \cdot P_{in}}{8L_{PFC}f_s}, \quad (6)$$

$$L_{PFC} = \frac{\eta \cdot V_m^2}{8L_{PFC}f_s}. \quad (7)$$

$$P_{in} \cong \frac{1}{2\pi} \int_0^{2\pi} v_{in}(t) \cdot i_{in}(t) d(\omega t) = \frac{V_m^2}{8L_{PFC}f_s}, \quad (5)$$

Figure 7 shows the relationship of capacitor voltage with respect to capacitor input power. It is clearly seen that

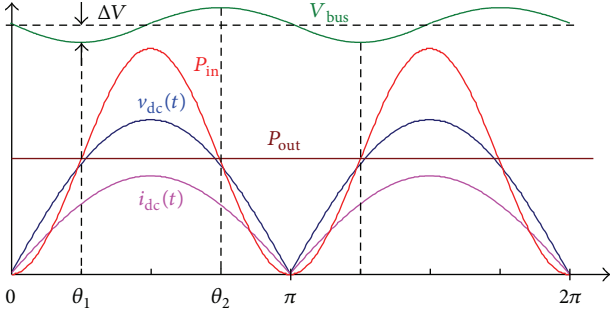


FIGURE 7: Capacitor voltage and electric energy relationship.

capacitor voltage  $V_{bus}$  lags capacitor input power with angle  $\theta$ . By integrating (8), capacitor input energy is derived as expressed by (9):

$$P_{C_{in}}(t) = V_{in}(t) \times i_{in}(t), \quad (8)$$

$$P_{out} = \frac{1}{2\pi} \int_0^{2\pi} P_{in}(t) dt = \frac{1}{2} V_m I_m. \quad (9)$$

According to energy conservation law, the energy stored on capacitor is identical to its output as expressed by (10). The solutions of  $\theta$  can obtain from (10). They are  $\theta = \pi/4$  and  $3\pi/4$ . Substitute  $\theta_1 = \pi/4$  and  $\theta_2 = 3\pi/4$  into integration form of (11) as lower and upper limit. The relationship among  $\Delta W$ ,  $\omega$ , and  $P$  can satisfy (10). Equation (13) is another form of  $\Delta W$ ; (11) and (12) are equal. Also, (11) can be expressed by (13), wherein  $2\Delta V/V_{bus}$  is the ripple factor. The reactance of energy storage capacitor is achieved and written as in (13):

$$V_m I_m \sin^2(\theta) = \frac{1}{2} V_m I_m, \quad (10)$$

$$\Delta W = \int_{\theta_1}^{\theta_2} V_m I_m \sin^2(\omega t) - \frac{1}{2} V_m I_m d\omega t \quad (11)$$

$$= \int_{\pi/4}^{3\pi/4} V_m I_m \sin^2(\omega t) - \frac{1}{2} V_m I_m d\omega t = \frac{P}{\omega},$$

$$\Delta W = \frac{1}{2} C [(V_{bus} + \Delta V)^2 - (V_{bus} - \Delta V)^2], \quad (12)$$

$$\Delta W = C \times V_{bus}^2 \times \frac{2\Delta V}{V_{bus}}, \quad (13)$$

$$C = \frac{P}{\omega \times V_{bus}^2 \times \text{ripple}}. \quad (14)$$

Figure 8 illustrates that the equivalent resonant circuit composed of resonant inductor  $L_r$  and resonant capacitor  $C_r$ . The associated parameters can be decided by using Ohm's law.

Firstly, the stored energy in the form of DC voltage on capacitor is converted to voltage  $V_{AB}$  on lower arm switch of half-bridge converter. The voltage across the lower arm switch  $V_{AB}$  can be calculated according to (15) by assigned conduction time  $d$  and dc bus voltage  $V_{bus}$ . By using resonant tank voltage of (15) and lamp current  $i_r$  mentioned above, the total load impedance  $Z_{total}$  can be achieved according

TABLE 1: Circuit specification.

|                           |              |
|---------------------------|--------------|
| Input voltage $V_{in}$    | 110 V, 60 Hz |
| Switching frequency $f_s$ | 50 kHz       |
| Output power $P_{out}$    | 28 W         |
| Lamp current $i_r$        | 0.35 A       |

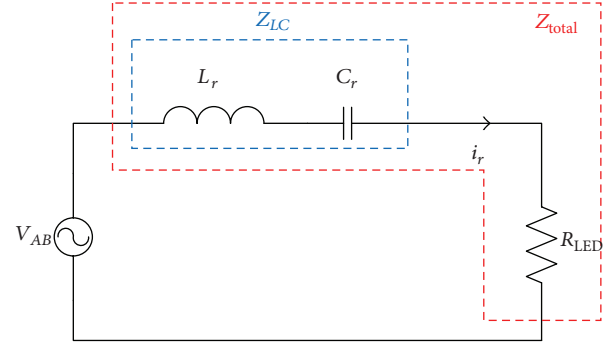


FIGURE 8: Equivalent circuit of resonant tank.

to Ohm's law as illustrated in (16). The relationship between lamp resistance  $R$  and reactance of resonant tank  $Z_{LC}$  can be expressed as in (17):

$$V_{AB} = V_{bus} \frac{\sqrt{2}}{\pi} \sin(\pi d), \quad (15)$$

$$Z_{total} = \frac{V_{AB}}{i_r}, \quad (16)$$

$$Z_{LC} = \sqrt{Z_{total}^2 - R^2}. \quad (17)$$

By substituting the assigned switching frequency and resonant tank impedance  $Z_{LC}$  determined by (17) into (18) and circuit design resonant frequency into (19), the parameters of resonant inductor  $L_r$  and resonant capacitor  $C_r$  will be obtained by solving the simultaneous equations (18) and (19):

$$Z_{LC} = 2\pi f_s L_r - \frac{1}{2\pi f_s C_r}, \quad (18)$$

$$f_r = \frac{1}{2\pi \sqrt{L_r C_r}}. \quad (19)$$

## 5. Experimental Results

This research employs the above-derived circuit parameters to implement a 28 W LED lighting driving circuit. The corresponding circuit specification is listed in Table 1.

Figure 9 displays the waveforms of input voltage  $V_{in}$ , input current  $i_{in}$ , and PFC inductor current  $i_{L_{PFC}}$ . By inspecting the relationship between input voltage  $V_{in}$  and input current, the small phase angle difference implies that high power factor is predictable. According to the measurement, the power factor is over 0.97.

Figure 10 demonstrates waveforms of triggering signals  $V_{GS1}$ ,  $V_{GS2}$ , and PFC inductor current  $i_{L_{PFC}}$ . It can be seen

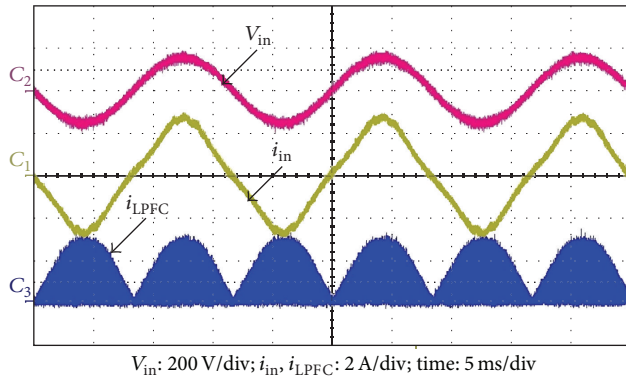


FIGURE 9: Input voltage, input current, and PFC inductor current waveform.

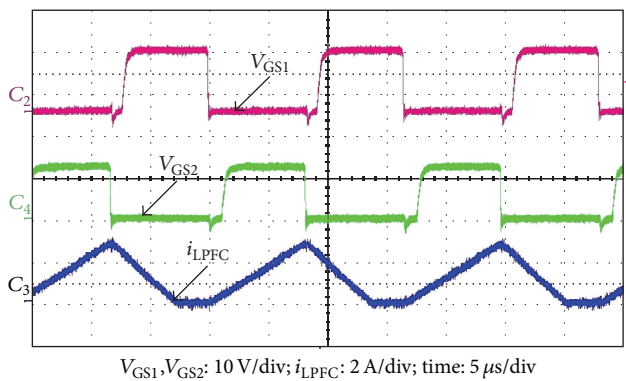


FIGURE 10: Switch triggering signal and PFC inductor current waveforms.

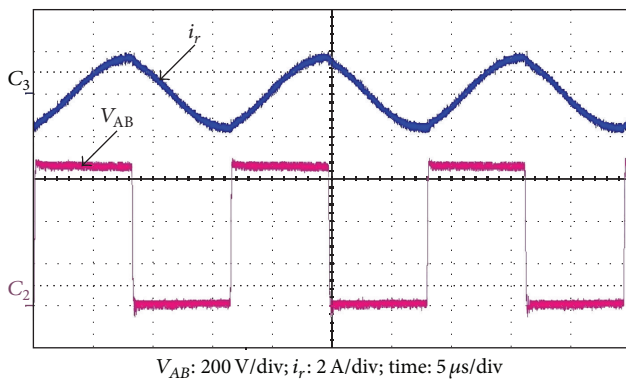


FIGURE 11: Waveforms with square wave voltage leading to resonant current.

that the PFC inductor begins to store energy after turning on switch  $V_{GS2}$ . On the contrary, the PFC inductor releases energy as the switch  $V_{GS2}$  turns off. The stored energy on PFC inductor ought to be released before next turn-on of  $V_{GS2}$ ; therefore, PFC must be operated with discontinuous conduction mode.

Figure 11 displays the resonant current and voltage waveforms. It can be observed that the resonant voltage  $V_{AB}$  leads resonant current  $i_r$ . The operation is controlled in the

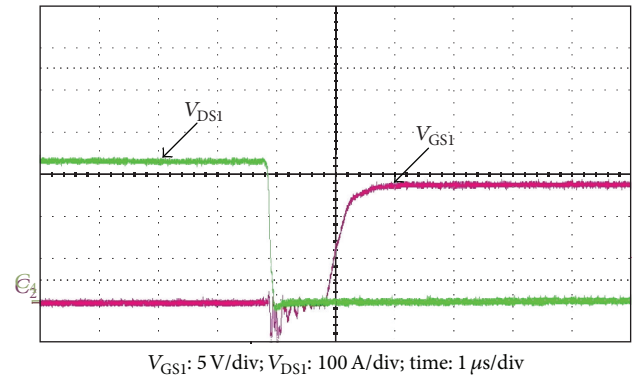


FIGURE 12: Zero-voltage-switching waveform.

inductive mode and furnishes the half-bridge resonant switch with zero-voltage-switching feature. Zero-voltage switching can effectively reduce the high frequency switching loss and, thus, promote the overall circuit operating efficiency.

Figure 12 illustrates that power transistor is triggered by  $V_{GS1}$  and then turns on, with  $V_{DS1}$  falling down to zero. If trigger signal  $V_{GS1}$  is high, the power switch is turned on and  $V_{DS1}$  falls down to zero. In this way, the simultaneous high states of  $V_{GS1}$  and  $V_{DS}$  are avoided. The switching actions are always completed when  $V_{DS1}$  is zero, that is, zero-voltage switching (ZVS).

## 6. Conclusion

This paper realizes a self-excitation single-stage high power factor driving circuit for LED lighting. Experimental results validate the availability of this circuit configuration. The presented self-excitation single-stage high power factor driving circuit can effectively avoid the IC cost, achieve high power factor over 0.97, and promote power efficiency to over 85%. In consequence, this paper has successfully realized a self-excitation single-stage high power factor driving circuit for LED lighting.

## Conflict of Interests

The author declares that there is no conflict of interests regarding the publication of this paper.

## References

- [1] C. Y. Chen, T. H. Yang, C. H. Hsu, and C. C. Sun, "High-efficiency white LED packaging with reduced phosphor concentration," *IEEE Photonics Technology Letters*, vol. 25, no. 7, pp. 694–696, 2013.
- [2] Z. Chen, Q. Zhang, F. Jiao et al., "Study on the reliability of application-specific LED package by thermal shock testing, failure analysis, and fluid-solid coupling thermo-mechanical simulation," *IEEE Transactions on Components, Packaging and Manufacturing Technology*, vol. 2, no. 7, pp. 1135–1142, 2012.
- [3] Z. Liu, S. Liu, K. Wang, and X. Luo, "Optical analysis of phosphor's location for high-power light-emitting diodes," *IEEE*

*Transactions on Device and Materials Reliability*, vol. 9, no. 1, pp. 65–73, 2009.

- [4] C. A. Cheng, H. L. Cheng, C. W. Ku, and T. Y. Chung, “Design and implementation of a single-stage acoustic-resonance-free HID lamp ballast with PFC,” *IEEE Transactions on Power Electronics*, vol. 29, no. 4, pp. 1966–1976, 2014.
- [5] H. L. Cheng, C. S. Moo, C. S. Yang, and C. K. Huang, “Analysis and implementation of an HPF electronic ballast for HID lamps with LFSW voltage power conversion conference-nagoya,” *IEEE Transactions on Power Electronics*, vol. 27, no. 11, pp. 4584–4593, 2012.
- [6] T. J. Liang, C. M. Huang, and J. F. Chen, “Two-stage high-power-factor electronic ballast for metal-halide lamps,” *IEEE Transactions on Power Electronics*, vol. 24, no. 12, pp. 2959–2966, 2009.
- [7] International electromechanical commission IEC 555-2 standards: Disturbances in supply systems caused by household appliances and similar electrical equipment. Part 2: Harmonics, 1982.
- [8] Y. C. Chuang, C. S. Moo, H. W. Chen, and T. F. Lin, “A novel single-stage high-power-factor electronic ballast with boost topology for multiple fluorescent lamps,” *IEEE Transactions on Industry Applications*, vol. 45, no. 1, pp. 323–331, 2009.
- [9] C. S. Moo, Y. J. Chen, and W. C. Yang, “An efficient driver for dimmable LED lighting,” *IEEE Transactions on Power Electronics*, vol. 27, no. 11, pp. 4613–4618, 2012.
- [10] H. S. Athab, D. D. C. Lu, A. Yazdani, and B. Wu, “An efficient single-switch quasi-active PFC converter with continuous input current and low DC-Bus voltage stress,” *IEEE Transactions on Industrial Electronics*, vol. 61, no. 4, pp. 1735–1749, 2014.
- [11] F. L. Tofoli, E. A. A. Coelho, L. C. de Freitas, V. J. Farias, and J. B. Vieira Jr., “Proposal of a soft-switching single-phase three-level rectifier,” *IEEE Transactions on Industrial Electronics*, vol. 55, no. 1, pp. 107–113, 2008.
- [12] J. W. Kolar and T. Friedli, “The essence of three-phase PFC rectifier systems. Part I,” *IEEE Transactions on Power Electronics*, vol. 28, no. 1, pp. 176–198, 2013.
- [13] H. S. Athab, D. D. C. Lu, and K. Ramar, “A single-switch AC/DC flyback converter using a CCM/DCM quasi-active power factor correction front-end,” *IEEE Transactions on Industrial Electronics*, vol. 59, no. 3, pp. 1517–1526, 2012.
- [14] Y. S. Roh, Y. J. Moon, J. C. Gong, and C. Yoo, “Active power factor correction (PFC) circuit with resistor-free zero-current detection,” *IEEE Transactions on Power Electronics*, vol. 26, no. 2, pp. 630–637, 2011.
- [15] B. Akin and H. Bodur, “A new single-phase soft-switching power factor correction converter,” *IEEE Transactions on Power Electronics*, vol. 26, no. 2, pp. 436–443, 2011.
- [16] T. J. Liang and C. M. Huang, “Interleaving controlled three-leg electronic ballast for dual-HID-lamps,” *IEEE Transactions on Power Electronics*, vol. 23, no. 3, pp. 1401–1409, 2008.
- [17] A. E. Aroudi, R. Haroun, A. Cid-Pastor, and L. Martínez-Salameiro, “Suppression of line frequency instabilities in PFC AC-DC power supplies by feedback notch filtering the pre-regulator output voltage,” *IEEE Transactions on Circuits and Systems I: Regular Papers*, vol. 60, no. 3, pp. 796–809, 2013.
- [18] H. L. Cheng, C. A. Cheng, C. C. Fang, and H. C. Yen, “Single-switch high-power-factor inverter driving piezoelectric ceramic transducer for ultrasonic cleaner,” *IEEE Transactions on Industrial Electronics*, vol. 58, no. 7, pp. 2898–2905, 2011.
- [19] S. Y. Chen, Z. R. Li, and C. L. Chen, “Analysis and design of single-stage AC/DC LLC resonant converter,” *IEEE Transactions on Industrial Electronics*, vol. 59, no. 3, pp. 1538–1544, 2012.

## Research Article

# Optimization of Biohydrogen Production with Biomechatronics

Shao-Yi Hsia<sup>1</sup> and Yu-Tuan Chou<sup>2</sup>

<sup>1</sup> Department of Mechanical and Automation Engineering, Kao Yuan University, Kaohsiung 821, Taiwan

<sup>2</sup> Department of Applied Geoinformatics, Chia Nan University of Pharmacy & Science, Tainan 717, Taiwan

Correspondence should be addressed to Shao-Yi Hsia; syhsia@cc.kyu.edu.tw

Received 10 February 2014; Accepted 19 February 2014; Published 26 March 2014

Academic Editor: Teen-Hang Meen

Copyright © 2014 S.-Y. Hsia and Y.-T. Chou. This is an open access article distributed under the Creative Commons Attribution License, which permits unrestricted use, distribution, and reproduction in any medium, provided the original work is properly cited.

Massive utilization of petroleum and natural gas caused fossil fuel shortages. Consequently, a large amount of carbon dioxide and other pollutants are produced and induced environmental impact. Hydrogen is considered a clean and alternative energy source. It contains relatively high amount of energy compared with other fuels and by-product is water. In this study, the combination of ultrasonic mechanical and biological effects is utilized to increase biohydrogen production from dark fermentation bacteria. The hydrogen production is affected by many process conditions. For obtaining the optimal result, experimental design is planned using the Taguchi Method. Four controlling factors, the ultrasonic frequency, energy, exposure time, and starch concentration, are considered to calculate the highest hydrogen production by the Taguchi Method. Under the best operating conditions, the biohydrogen production efficiency of dark fermentation increases by 19.11%. Results have shown that the combination of ultrasound and biological reactors for dark fermentation hydrogen production outperforms the traditional biohydrogen production method. The ultrasonic mechanical effects in this research always own different significances on biohydrogen production.

## 1. Introduction

Because hydrogen is clean and sustainable and has high thermal energy, research on hydrogen energy has recently been emphasized in academia and industry. Traditional hydrogen production methods include the thermochemical and electrochemical methods, which are highly energy intensive, resulting in expensive and polluting production. However, the biological method applies anaerobic microorganism (primarily clostridium bacteria) to wastewater treatment, simultaneously converting the organic matter in wastewater into usable hydrogen. This method not only solves the problem of environmental pollution but also develops clean hydrogen energy and is an economic and competitive method of hydrogen production.

Reviewing the previous development of destructive ultrasound biological effects, Coakley et al. [1] discovered the cavitation of Amoebae under the ultrasonic effects with the frequency 1 MHz and the intensity 515 W/cm<sup>2</sup> in 1971, when the number of cells obviously decreased after the irradiation. Coakley and Dunn [2], in the same year, discovered

the irrelative relationship between the extraction of DNA with the irradiation of frequency 1 MHz and intensity 200–288 W/cm<sup>2</sup> and transient cavitation, but the molecular weight of DNA reduced with the increasing transient cavitation when the energy exceeded 500 W/cm<sup>2</sup>. Coakley et al. [3] studied the ultrasonic cavitation effects on the inactivation of enzymes in 1973 and found out the less influence of cavitation effects on catalase under the continuous irradiation of 20 kHz ultrasound but the inactivation of alcohol dehydrogenase and lysozyme with increasing exponential rate. Ahmed and Russell [4] explored the death of microorganisms with ultrasound and hydrogen peroxide in 1975. Dooley et al. [5] irradiated mice's thymocytes suspension with continuous and pulsed ultrasound under the frequencies of 0.5 MHz and 1 MHz in 1983 and argued that the ultrasound transducer used in medicine did not reveal absolute correlations with the damage of suspension cells. Van [6] discussed the flow of cysts and oocytes of protozoa by irradiating with ultraviolet and ultrasound in 2002. Broda [7] reduced the bacillaceae attached in the test tubes or on the resin by increasing the temperature and adding high-acid disinfectants as well as

increasing the temperature and adding ultrasound irradiation to study and observe the survival rate of the bacteria in 2007.

Regarding biohydrogen production, Lin [8] performed hydrogen production on wastewater sludge and developed an immobilized cell system for programming sludge in hydrogen production and immobilizing cells with different materials and hydrogen production, thus identifying the optimal method for producing repeated batches of immobilized cell hydrogen. Chen [9] cultivated anaerobes using carbohydrate and waste-water sludge via CSTR (the reaction volume 4l) to generate hydrogen. Wang [10] combined mixed bacteria with starch and starch hydrolysis as the carbon source to design a dark fermentation hydrogen production system and found starch hydrolysis to have a higher hydrogen production rate than starch. Hydrolyzing starch thus was the key to biohydrogen production cost in developing hydrolyzing amylase. Modigell et al. [11] designed a high-efficiency and low-energy consumption biohydrogen production method with membrane contact and nonporous polymer membranes that not only could effectively absorb the byproduct, carbon dioxide, but also could prevent high pressure and high fodder in the polluted natural liquid under aseptic conditions during hydrogen production and enable harmful materials, like monoethanolamine (ethanolamine), being the carrier liquid to pass the test of different membranes and be optimized and commercially applied. Antonopoulou et al. [12] developed sweet sorghum with glucose as the material under distinct hydraulic retention time in which both glucose-fermentation hydrogen production and fermented waste liquid were utilized to generate methane. The experiment proved that the highest hydrogen production rate (2550 mLH<sub>2</sub>/d) appeared at the retention time of 6 hrs, while the highest amount (10.4 LH<sub>2</sub>/kg) appeared at the glucose retention time of 12 hrs. To optimize methane generation, about 29l CH<sub>4</sub>/kg glucose was required during fermentation. The research outcomes also demonstrated that using glucose for hydrogen production could efficiently generate methane. In this case, using gas to replace fossil fuels became an ideal method. Kotay and Das [13] also mentioned the important contribution of biohydrogen production to renewable energy in the future, which was particularly suitable for smaller scale and scattered systems. Additionally, the combination of agricultural and industrial activities and waste treatment facilities for biohydrogen production was essential in maintaining global electricity supply, and it was considered a substitute for fossil fuels and a fuel with multiple applications. Manish and Banerjee [14] considered hydrogen a reliable energy since various methods could be established to promote the development of renewable energy. For instance, light and dark fermentation, or a combination of the two, could provide a feasible method of biohydrogen production and confirm various related techniques and design parameters. The results of using such biological methods for hydrogen production and sugar cane juice for nutrient showed that byproducts increased with biohydrogen production efficiency. In terms of the biological experiment designed using the Taguchi Method, Su [15] planned ultrasonic mechanical effect exposure and light source adjustment to hatch fairy shrimps

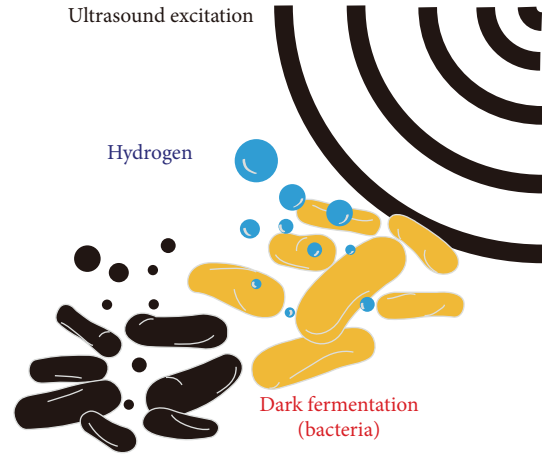


FIGURE 1: Sketch map of biohydrogen production with biomechanics.

and optimize the parameters. The outcomes identify optical wavelength as the main influence on hatchability.

Research on the effects of ultrasound exposing bacillaceae has not been discussed. This study thus attempted to develop a suitable medium composition and perform dark fermentation hydrogen production with biological reactors and ultrasonic mechanical effect shown on Figure 1, where the Taguchi Method was combined to discuss the optimal hydrogen production conditions in the process, and aimed to further understand the effects of ultrasound on microorganisms.

## 2. Basic Theory

In response to depleting fossil fuel energy and to meet pollution reduction targets, it is necessary to develop new energy technologies that match modern demand. Among all emerging energy sources, hydrogen appears to have the fewest side effects and pose the least environmental harm. Looking at traditional thermochemical methods and electrochemical methods reveals that hydrogen production exhibits strengths and weaknesses in stability, security, and production; however, biohydrogen production represents a natural and potential hydrogen production method. Generally, anaerobe (primarily bacillaceae-clostridium) can transform organic matter into usable hydrogen during wastewater treatment via the biological method and also contributes to reducing pollution. Biological dark fermentation hydrogen production thus is considered a favorable choice as anaerobes can decompose organic compounds to generate hydrogen without a light source and are easily incorporated into waste-water treatment so that a practical form of renewable energy can be developed while processing environmental pollution. When the Taguchi Method is applied to optimize hydrogen production it becomes an economical hydrogen production method. Focused on ultrasound, biological effect, and the Taguchi Method, this chapter further discusses the correlations in this study. Figure 2 plotted the flowchart of the biohydrogen production experiment.

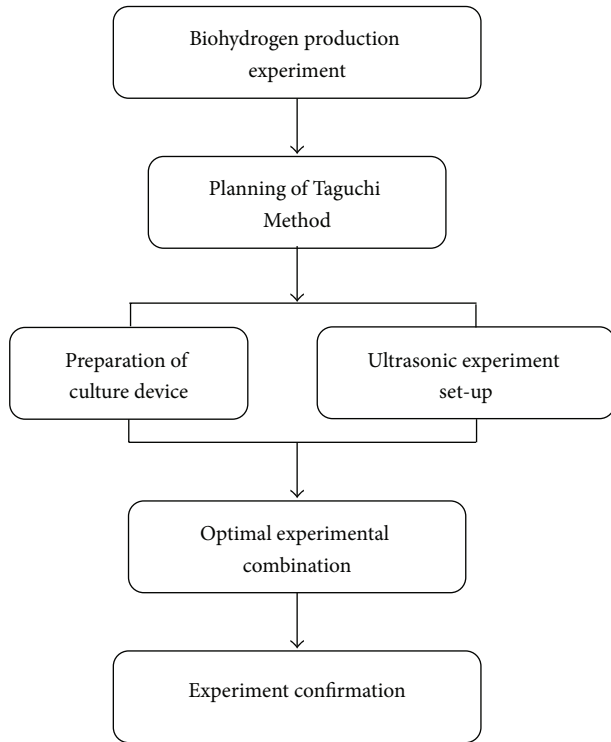


FIGURE 2: Flowchart of the biohydrogen production experiment.

**2.1. Principles Underlying the Biological Application of Ultrasound.** Ultrasound has been applied to real world applications in recent decades and has been utilized to improve human life. Compared with certain animals, such as bats and whales, people still learn from the biosphere to improve production and life quality. Research on animal behavior models could provide improvements in mechanical design and logistic processing models. Consequently, it becomes necessary to understand the effects of ultrasound on organisms. Ultrasound communicates in transmission media and can generate a series of effects and influences, including organism-related thermal and nonthermal effects. The latter are further divided into mechanical effects and empty-hole effects.

**2.1.1. Thermal Effect.** When transmitting through viscous substances, ultrasonic energy is partially absorbed by friction and relaxation among molecules or lattices. The energy thus absorbed is transformed into heat and increases the temperature of the substance involved. As seen for physiological tissues, heat effects can boost metabolism but harm physiological tissues with these different effects depending on ultrasonic intensity and exposure time on physiological tissues. Thermal effect refers to micromassage causing tissues to generate ultrasonic efficacy and thus produce different heat energy and also refers to the increased heat production by the body after eating owing to the metabolic energy cost of digestion. It is considered diet-induced thermogenesis.

**2.1.2. Nonthermal Effect.** The nonthermal effects of ultrasound include radiation pressure, radiation force, acoustic

torque, acoustic streaming effect, and cavitation. The basic source of these effects is the peripheral pressure change caused by ultrasound. The cavitation produces the largest effect and thus can break the cell structure, collapse aerosol cells, or tear solid physiological tissues. Rayleigh-Plesset announced the mathematical movement model for the inner cavitation vibration of incompressible liquid in 1949 [16]. Applying such a theory to calculate the appearance of dark fermentation rod hydrogen producing bacteria and the internal tissue could result in the natural frequency in the physical activation so as to observe the activation effects by setting different pulse intensity for the vibration. The radius  $R_0$ , surface tension  $\sigma$ , heat capacity ratio  $\gamma$ , density  $\rho$ , viscosity coefficient  $\eta$ , and pressure  $P_0$  of the bacteria are substituted for the following equation to calculate the natural frequency:

$$(\omega'_r)^2 = \frac{1}{\rho R_0^2} \left[ 3\gamma \left( P_0 + \frac{2\sigma}{R_0} \right) - \frac{2\sigma}{R_0} \right] - \left( \frac{2\eta}{\rho R_0^2} \right)^2. \quad (1)$$

Collapse of cavity cells can cause high pressure and temperature change and hence biochemical reactions. Generally, the nonthermal effect can be separated into the mechanical effect and empty-hole effect.

**(a) Mechanical Effect.** The mechanical oscillation effect describes ultrasound generating extendable change in tissues via a process similar to massage and is also called micromassage. During transmission in media, oscillation of spatial particles in the ultrasonic path is induced so that particles present faster movement, displacement of acoustic pressure, tensile stress, compressive stress, and expansion or contraction.

**(b) Empty-Hole Effect.** When applying strong ultrasound in liquid, excessive pressure and negative pressure occur because ultrasound is a compressional wave. Negative pressure breaks the liquid, causing empty holes and cavitation. Such bubbles comprise liquid steam or gas in the liquid. Bubbles are unlikely to break when the radius reaches a certain size. Some bubbles might break during oscillation, resulting in shock waves and high temperature through which cavitation causes various physical or chemical actions in the liquid.

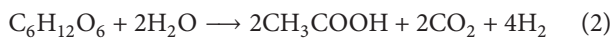
**2.1.3. Effects of Ultrasound on Cells.** Ultrasound can increase cell membrane permeability (permeability is the ability of water to pass through a material; water passes more easily through materials with good permeability and cannot pass easily through those with poor permeability). The experimental findings showed that constant and pulse ultrasound change tissue internal and external osmotic pressure (osmosis refers to the ability of a matter to pass through the membrane or not) and that cell stimulation needs to be changed to enhance the metabolism and reaction process and change the pH of the human body.

Ultrasound enhances tissue regeneration and the effects of peripheral nerves and significantly influences the conduction velocity of peripheral nerves. The major factor is the diathermanous effect of ultrasound. Higher intensity

ultrasound generates a transmission area that proves the sensibility of nervous tissues toward ultrasound.

**2.2. Biohydrogen Production Method and Classification.** Generally, based on nutrient category and the distinct formula, hydrogen production methods can be classified as thermochemical, electrochemical, and biological. The thermochemical and electrochemical methods have some weaknesses, such as large energy consumption and instability. Biohydrogen production can transform organic waste into energy via biodegradation and biotransformation. This method not only can solve environmental pollution and generate hydrogen energy but is also considered the best method of energy production for achieving sustainable environmental protection and commercial value. Biohydrogen production can use numerous microorganisms, for example, green algae, cyanobacteria, photosynthetic bacteria, and fermentation bacteria. The biological method includes photosynthesis, light fermentation, and dark fermentation. The dark fermentation applied in this study utilizes anaerobic bacteria to decompose organic matters, which is considered the traditional anaerobic fermentation method.

Regarding the organic matter in wastewater, the anaerobic bacteria contain hydrolytic bacteria, hydrogen production acetic acid bacteria, acetic acid synthetic hydrogen production bacteria, and methane bacteria. In the traditional anaerobic digestion process, the organic matter converts into methane and carbon dioxide, and hydrogen is generated using acid production metabolism, but acetic acid bacteria and methane bacteria consume hydrogen so that hydrogen becomes the intermediary in the metabolic pathway. In this case, the concentration of hydrogen accumulated was lower than in the traditional anaerobic digestion process. In terms of anaerobic hydrogen production bacteria, clostridium bacteria is common and merely needs preprocessing sludge to inhibit or destroy methane bacteria activity, which can be achieved through heat or acid-alkali treatment. Having glucose as the substrate, the equation for hydrogen production of anaerobic bacteria is as follows:



where  $\text{C}_6\text{H}_{12}\text{O}_6$  is glucose,  $\text{CH}_3\text{COOH}$  is acetic acid, and  $\text{C}_3\text{H}_7\text{COOH}$  is butyrate.

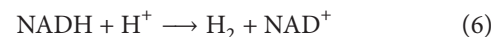
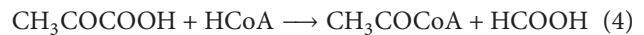
The traditional anaerobic digestion process hydrolyzed complex organisms (cellulose polysaccharide or protein) into small molecules (carbohydrate amino acid) which were converted into hydrogen, carbon dioxide, acetate, propionate, butyrate, and alcohols through fermentation. The propionate, butyrate, and alcohols were converted into hydrogen, carbon dioxide, and acetate through fermentation, while the hydrogen and carbon dioxide were converted into acetate by acetic bacteria and the acetate was further converted into gas by methane bacteria. The process using anaerobic bacteria yields a better hydrogen rate if the main metabolite is organic acid than if it is alcohols or ketones. Electrons are transferred to higher reduced form outcomes such as alcohols or ketones, thus resulting in a low hydrogen rate.

### 2.3. Hydrogen Production Strains and Metabolism Path

**2.3.1. Introduction to Bacillaceae.** Short stemmed bacillaceae is one of the bacteria that are best able to produce hydrogen. Under anaerobe, the best production occurs at 25~60°C and neutral pH, and it forms endospore and becomes dormant in an unsuitable environment. Bacillaceae is spore-producing with a particular structure and grows in thalli. Each thallium can grow a spore at its end that is wider at the end and also differs from other thalli.

Spore formation is a severe physiological and biochemical change for thalli. Both thalli and spores exhibit two nuclei and form two cell membranes, as the precursor spores. When the cells take the first step, they merely form endospores only when the thick wall of precursor forms is complete. The entire process lasts about 8~10 hours.

**2.3.2. Anaerobic Fermentation Metabolic Pathway.** According to Wang [10], increasing the contents of formate, pyruvate, and nicotinamide adenine dinucleotide reduced form (NADH) enhances hydrogen production. Tanisho and Das reported increased NADH and hydrogen. Consider



### 2.4. Taguchi's Optimization Experiment

**2.4.1. Taguchi's Orthogonal Array.** Taguchi's Orthogonal Array describes the creation of a pair of parameters from all levels at two column intervals in the experimental table, where each composition exhibits the same frequency. The Classical Orthogonal Array is named after  $L_a(b^c)$  and presents that the experiment contains  $c$  factors, each of which has  $b$  levels for an experiment. Orthogonal Array compromises on experimental cost and precision, and fewer experiments are needed to achieve useable statistical information. Nevertheless, Orthogonal Array experiments are not Full Factorial experiments. The "bias" cannot be fully eliminated but is acceptable since not all levels of compositions appear on the Orthogonal Array. The optimal composition therefore might not occur in the experimental group.

**2.4.2. Signal-to-Noise Ratio (S/N Ratio).**  $S/N$  ratio is frequently used as the quality index in the Taguchi Method, demonstrating the effects of errors at the process or product level. According to different quality characteristics, various  $S/N$  ratio formulas are formed, including Nominal-the-best, Smaller-the-better, and Larger-the-better. Both Smaller-the-better and Larger-the-better were applied in this study, and the Smaller-the-better  $S/N$  ratio is shown as follows:

$$\frac{S}{N_{SB}} = -10 \log \left[ \frac{\sum_{i=1}^n (y_i)^2}{n} \right] = -10 \log (\bar{y}^2 + S_n^2). \quad (7)$$

The larger-the-better  $S/N$  ratio is shown as

$$\frac{S}{N_{LB}} = -10 \log \left[ \frac{\sum_{i=1}^n (1/(y_i)^2)}{n} \right], \quad (8)$$

where  $y_i$  shows the experimental values,  $\bar{y}$  the mean experimental value,  $S_n$  the standard deviation, and  $n$  the number of experimental times.

This study combined the mechanical effect generated by ultrasound and biohydrogen production technology and applied the Taguchi Method to design the experiment and analyze the parameter relations to optimize the effect. In the process, dark fermentation was utilized for hydrogen production based on several advantages as follows.

- (1) Fermented strains have rapid hydrogen metabolism.
- (2) It could rapidly and continuously produce hydrogen from organic matter.
- (3) It shows a favorable growth rate on general microbial systems.

For these reasons, dark fermentation hydrogen production appears to obtain better benefits in terms of microorganism quality and quantity than does photosynthesis bacteria hydrogen production. Regarding the mechanical effect of ultrasound on dark fermentation, frequency, energy, number of exposures, and duration are the changeable parameters. Additionally, pH, temperature, nutrient content, starch, and stir speed can be adjusted to match specific organisms. The experiment designed three parameters for ultrasonic mechanical effect using the Taguchi Method, namely, frequency, intensity, and exposure time, to observe and analyze the effects on biohydrogen production.

### 3. Experimental Method and Procedures

**3.1. Experimental Method.** The ultrasonic system and biohydrogen production equipment utilized for this experiment are described as follows.

**3.1.1. Ultrasonic System.** The experimental structure in which ultrasound was used for hydrogen production is shown in Figure 3. In the research, the physical parameters of microorganisms covered surface tension  $\sigma = 72.75 \text{ dyn/cm}$ , heat capacity ratio  $\gamma = 1.4$ , water density  $\rho = 1 \text{ g/cm}^3$ , viscosity coefficient  $\eta = 9.197 \times 10^{-3} \text{ g/cm} \cdot \text{sec}$ , pressure  $P_0 = 760 \text{ torr}$ , and the size  $I_0 = 5\text{--}8 \text{ }\mu\text{m}$  [17]. Such parameters are substituted for (1) to acquire the natural frequencies 0.5 MHz and 0.96 MHz of the hydrogen producing bacteria. Hence, this study selected the single-crystal straight-beam longitudinal-wave immersion transducer with natural frequencies of 0.5 and 1.0 MHz, while 5 MHz is selected as the nonnatural frequency transducer for the comparison. After completing the required nutrient and strains, the proportion of 10:1 was placed in the reactor, as shown in Figure 3. Meanwhile, the thermostatic water bath was filled with water whose temperature was controlled at  $33^\circ\text{C}\text{--}40^\circ\text{C}$  by a temperature controlling machine. To ensure even distribution of the

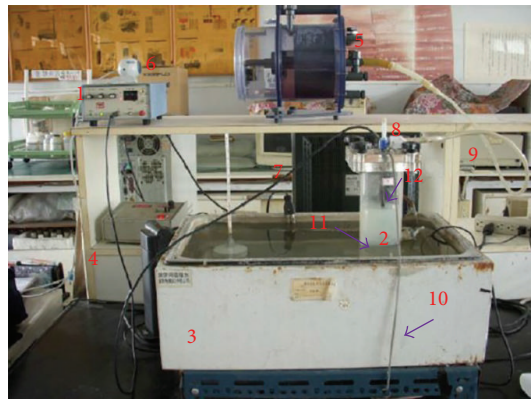


FIGURE 3: Experimental structure: 1: ultrasonic pulser, 2: reactor, 3: thermostatic bath, 4: thermostat, 5: flowmeter, 6: video camera, 7: computer, 8: sampling tube, 9: gas tube, 10: stirrer, 11: stirring stone, and 12: ultrasonic transducer.

measured liquid, a stirring rock was placed in the reactor, which was covered to create a closed space. The reactor was then placed in the thermostatic water bath with a stirrer beneath it to power the stirring stone for mixing nutrient and strains. Following the preparation, an ultrasonic transducer was connected to the pulse transmitter with the reactor lid and was soaked in the fermentation liquid. The other two empty holes on the reactor lid were placed in soft tubes for sampling and delivery of gas to the flowmeter. The ultrasonic pulser was further connected to an oscilloscope, leading to the incident and reflected waves being shown on the oscilloscope display for storage in a computer.

#### 3.1.2. Biohydrogen Production System

**(1) Strains and Nutrients.** The experimental strains were taken from the wastewater in the end sedimentation tank of sewage treatment plants. This wastewater was mixed with bacterial strains, primarily bacillaceae. Numerous methods could be used for strain treatment, and this experiment adopted high temperature treatment. First, the bacteria liquid was placed in a beaker with a cover to prevent airborne competitors from entering the bacteria liquid. Second, the beaker, separated using an iron net, was heated to boiling on the heating plate. The boiled bacteria liquid was then stored for cooling. This process aimed to eliminate competitors to prevent them from generating other gases during the reaction.

Regarding the nutrient content, potato starch was used as the carbon source, ammonium hydrogen phosphate ( $\text{NH}_4\text{H}_2\text{PO}_4$ ) as the nitrogen source, and dibasic sodium phosphate as the buffer salt for acid change, and all these materials included some microelements, as shown in Table 1. Proper carbon source, nitrogen source, buffer salt, and microelements were stirred in a pot with 1 L RO water and then heated to boiling point. In the process, the solution was evenly stirred to prevent precipitation causing uneven nutrient concentration. The buffer salt served to stabilize the system pH. During the metabolism in dark fermentation hydrogen production, the generation of acid and alcohols

TABLE 1: Nutritional composition and formula.

| Composition                                    | Concentration mg/L   |
|--|----------------------|
| Carbon source                                  | 10 g/L–20 g/L–30 g/L |
| NH <sub>4</sub> H <sub>2</sub> PO <sub>4</sub> | 4500                 |
| Na <sub>2</sub> HPO <sub>4</sub>               | 11867                |
| K <sub>2</sub> HPO <sub>4</sub>                | 125                  |
| MgCl <sub>2</sub> • 6H <sub>2</sub> O          | 100                  |
| MnSO <sub>4</sub> • 6H <sub>2</sub> O          | 15                   |
| FeSO <sub>4</sub> • 7H <sub>2</sub> O          | 25                   |
| CuSO <sub>4</sub> • 5H <sub>2</sub> O          | 5                    |
| CoCl <sub>2</sub> • 5H <sub>2</sub> O          | 0.125                |

could reduce system pH and further change the metabolism path of hydrogen production or even limit the fermentation for hydrogen production. The most commonly utilized buffer salts are NH<sub>4</sub>H<sub>2</sub>PO<sub>4</sub> and Na<sub>2</sub>HPO<sub>4</sub>, which could increase hydrogen production and reduce the CO<sub>2</sub>/H<sub>2</sub> ratio.

(2) *Analysis.* H<sub>2</sub> and CO<sub>2</sub> are the main gases produced in dark fermentation. This study thus selected Gas Chromatography analysis using a thermal conductivity detector. The separation column is a high-molecule ball with fixed length of 1.5 m; the temperature at the injection port and detector was 100°C, and the separation column temperature was 50°C. Volatile acid and alcohols performed Gas Chromatography analysis with a flame ionization detector. The mobile gas was argon, which could separate methane, hydrogen, oxygen, carbon monoxide, and carbon dioxide. A spectrophotometer was utilized to measure the fermentation solution following ultrasonic exposure to understand the starch concentration of the fermented liquid. Iodine reagent caused the starch solution to appear blue violet. The main function was that amylase in starch formed a hollow helix to hold iodine molecules, causing the color change. Under certain starch concentrations, the concentration change was linearly related to the optical absorbance and could test starch decomposition in fermentation. The spectrophotometer, Shimadzu UV-1201, with the radiation wavelength 550 nm was used in this experiment.

(3) *Fermentation Hydrogen Production Simulation.* The modified Gompertz equation (9) was used to stimulate hydrogen production. Hydrogen production was simulated over time using the modified Gompertz equation, where the dynamic parameters (H<sub>max</sub>, R<sub>max</sub>, and λ) were established using the nonlinear regression function Sigma Plot [1]. Consider

$$H = H_{\max} \exp \left\{ - \exp \left[ \frac{R_{\max, H_2} \times e}{H_{\max}} (\lambda - t) + 1 \right] \right\}, \quad (9)$$

where H represents accumulated produced hydrogen (mL), T represents fermentation duration (h), H<sub>max</sub> represents maximum hydrogen production potential (mL), R<sub>max</sub> represents maximum hydrogen production rate (mL/h), and λ represents lag time (h).

(4) *Calculation of Hydrogen Production Efficiency.* Under the traditional process of transforming organic anaerobe into

methane, carbon dioxide, and acids (including acetic acid, propanoic acid, and butyric acid), 1 mole sugar could produce 2 moles acetic acid, 4 moles hydrogen, and 2 moles carbon dioxide, as shown in (2). The actual hydrogen produced differed from the theoretical calculation, and the hydrogen production efficiency was represented as follows:

$$\text{Efficiency (\%)} = \left( \frac{\text{Actual H}_2 \text{ volume}}{\text{Theoretical H}_2 \text{ volume}} \right) \times 100\%. \quad (10)$$

Theoretical hydrogen production could be shown as

$$\begin{aligned} & \text{Theoretical H}_2 \text{ volume} \\ &= \frac{(\text{starch} \times 0.9 \times 0.7 \times 4 \times 0.08205 \times 298)}{162}. \end{aligned} \quad (11)$$

Substituting (10) for (11), the experimental efficiency was

$$\begin{aligned} & \text{Efficiency (\%)} \\ &= \left\{ \frac{\text{Actual H}_2 \text{ volume}}{[(\text{starch} \times 0.9 \times 0.7 \times 4 \times 0.08205 \times 298) / 162]} \right\} \\ & \times 100\%, \end{aligned} \quad (12)$$

where Actual H<sub>2</sub> volume represents hydrogen actually received in the experiment (liter), Theoretical H<sub>2</sub> volume represents hydrogen volume received according to chemical theory (liter), Starch represents starch concentration (g/L) used in the experiment, 0.9 represents 1 g starch containing 0.1 g water and so the actual starch was 0.9 g, 0.7 represents that the work volume of the reaction tank was just 0.7 L, 4 represents that 1 mole sugar could produce 4 moles hydrogen, 0.08205 represents idea gas (constant), 298 represents absolute temperature, and 162 represents calculated number of units of starch.

3.2. *Experimental Procedure.* The experimental framework is shown in Figure 3. Ultrasound was applied to dark fermentation biohydrogen production to understand the mutual effects in the hydrogen production process, and the Taguchi Method was utilized to plan the experiment groups and times. The experimental procedure was as follows.

3.2.1. *Parameter Selection.* Orthogonal Array L<sub>9</sub>(3<sup>4</sup>) in the Taguchi Method was applied to plan the experiment groups. Before determining the controlling factors and levels, experiments were performed using various controlling factors and levels to determine their effects on dark fermentation hydrogen production. Since the effects of ultrasound in exposing bacillaceae have not been studied and discussed, the number of controlling factors and levels for this study was as listed in Table 2.

- (a) Ultrasonic exposure energy was first used as the controlling factor to clarify its effects on biohydrogen production. As the ultrasonic pulser could be adjusted to 2, 4, and 8 joules, the three values were the adjustable level numbers.

TABLE 2: Experiment planning table.

| Factors | Specifics                                 | Level 1 | Level 2 | Level 3      |
|---------|---|---------|---------|--------------|
| A       | Power energy (joules)                     | 2       | 4       | 8            |
| B       | Exposure time<br>(exposure/stop, min/min) | 15/30   | 15/15   | All the time |
| C       | Frequency (MHz)                           | 0.5     | 1       | 5            |
| D       | Starch concentration (g/L)                | 10      | 20      | 30           |

- (b) Distinct ultrasonic exposure time periods were selected as the second controlling factor. The exposure time periods were 15 min exposure followed by 30 min rest, 15 min exposure followed by 15 min rest, and continuous exposure for full time.
- (c) The third controlling factor was frequency of transducer exposure. The exposure frequency was changed to discuss the effects of ultrasound on biohydrogen production, and the adopted frequencies included 0.5 MHz, 1 MHz, and 5 MHz.
- (d) The effect of various starch concentrations on biohydrogen production was further discussed. Wang [10] found that hydrogen production peaked at starch concentration 20 g/L, and the volume production rate reached 106 mL/h. Complying with the level selection in the Taguchi Method, the present experimental parameters were considered the standard and varied by one unit in each direction. Consequently, 10, 20, and 30 g/L starch were selected as the changed levels of nutrient concentration.

3.2.2. *Experiment.* By following Table 2 using the Taguchi Method, dark fermentation hydrogen production was combined with ultrasound to adjust the number of controlling factors and levels for the experiment.

- (a) Strains were first boiled to delete the competitor and then cooled.
- (b) Nutrient was prepared by mixing suitable starch, buffer salt, microelements, and 1 L boiled water that was being cooled.
- (c) Strains and nutrient were placed in the reaction tank in a ratio of 1:10, and argon was infused for about 10 minutes to expel the air in the reaction tank.
- (d) The external temperature of the reaction tank was controlled at 36°C. A stirrer was placed under the reaction tank to drive the stirring rock to evenly mix the reaction tank liquid.
- (e) Proper control conditions, as listed in Table 2, were added to the cultivation process.

3.2.3. *Data Analysis.* To increase the experiment reliability, nine sets of Taguchi's Orthogonal Arrays  $L_9(3^4)$  were applied to acquire the maximum hydrogen production, hydrogen production rate, and lag time. The analyses are described below.

- (a) *S/N* ratio, Response Table, or Response Diagram could be utilized to optimize the experimental conditions. Four quality characteristics, namely, experimental efficiency, hydrogen production rate, starch surplus ratio, and lag time, were analyzed in this study. The former two were Larger-the-better as the larger experimental efficiency and faster hydrogen production rate were better, while the latter two were Smaller-the-better as the lower starch surplus ratio indicated more starch use, and the shorter lag time helped reduce the fermentation time.
- (b) The *S/N* ratio result was used to determine the mean of the corresponding quality characteristics. Response Diagram could be applied to determine the required optimization conditions. In the process, the importance of different controlling factors in hydrogen production was also discussed.

3.2.4. *Experiment Confirmation.* The factor from *S/N* ratio could reduce experiment variability. The factor in quality characteristics could then control the hydrogen production experiment being preceded under the optimal condition. *S/N* ratio showed distinct optimization results from quality characteristics. Having compared the differences and selected the most suitable result for confirming the experiment, the verification demonstrated the best experimental combination of hydrogen production technology and mechanical effect.

## 4. Results and Discussions

To select the number of controlling factors and levels using the Taguchi Method, one of the curve diagrams of the experimental results after three repetitions is shown in Figure 4. The horizontal axis (*x*-axis) represented the reaction time (h) while the vertical axis (*y*-axis) represented the hydrogen production (mL). According to Taguchi's Orthogonal Array  $L_9(3^4)$ , nine experiments and nine different symbols represented each experimental result. Table 3 represented the curve in Figure 4 showing the results of maximum hydrogen production, hydrogen production rate, and lag time. The maximum hydrogen production efficiency could be calculated from (10)–(12), and the rest (hydrogen production rate and lag time) could be directly analyzed without calculation. The fermented liquid could be measured for the starch surplus ratio. This experiment thus examined four quality characteristics, namely, hydrogen production efficiency, hydrogen production rate, starch surplus ratio, and lag time. Hydrogen production efficiency and hydrogen production rate were Larger-the-better, while lag time and starch surplus ratio were Smaller-the-better. The optimization process was divided into two steps. The first step reduced the variability, namely, to maximize *S/N* ratio, while the other maximized the hydrogen production efficiency. Aiming at distinct optimization processes, the experimental results were further discussed.

The experimental results in Table 3 were repeated three times to obtain the mean hydrogen production efficiency, hydrogen production rate, starch surplus ratio, lag time, and

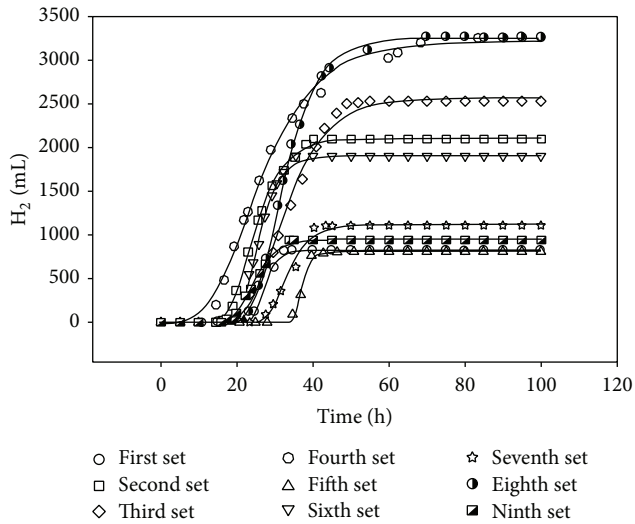


FIGURE 4: The curve diagram showing the first experimental results using the Taguchi Method.

TABLE 3: The effects of biological  $H_2$  production using the Taguchi Method.

| Experimental sets | $H_{max}$ (mL) | $R_{max}$ (mL/h) | $\lambda$ (h) |
|-------------------|----------------|------------------|---------------|
| 1                 | 889.79         | 118.93           | 24.08         |
| 2                 | 2126.58        | 147.42           | 17.72         |
| 3                 | 2785.89        | 115.27           | 22.12         |
| 4                 | 3141.07        | 119.35           | 12.50         |
| 5                 | 811.02         | 185.28           | 185.28        |
| 6                 | 2087.64        | 164.75           | 20.09         |
| 7                 | 1370.16        | 86.55            | 27.54         |
| 8                 | 3199.82        | 198.66           | 24.16         |
| 9                 | 1079.55        | 79.31            | 18.81         |

$S/N$  ratio. All the values were listed in Table 4. The second to the fifth columns represented the variability of the controlling factors and levels corresponding to the nine experiments in Taguchi's Orthogonal Array. To reduce the variability, Table 5 shows the factor Response Table of hydrogen production efficiency  $S/N$  ratio calculated using the experimental results in Table 4. The level values under column A presented the effects of variability, and the variability among different levels could be regarded as the effect of controlling factors on  $S/N$ . The range in the table showed the maximum range of variability, where the larger variability in Rank is more important. As the  $S/N$  ratio was expected to be Larger-the-better, the optimal experimental settings for hydrogen production efficiency showed the conditions of A2B2C1D3. This implied ultrasonic exposure energy 4 joules, exposure time 15 min/stop for 15 min, transducer frequency 0.5 MHz, and starch concentration 30 g/L. The Response Table of  $S/N$  ratio showed that starch concentration (factor D) was the most significant factor in the experimental results, followed by exposure intensity, frequency, and time. In this case, the ultrasonic exposure intensity was 72.46% significance when compared with the starch concentration that was always used

by the traditional biohydrogen production method. Table 6 showed the  $S/N$  ratio of hydrogen production rate. Similar to the optimization results of hydrogen production efficiency, the optimal results occurred with ultrasonic energy at level 2, exposure time at level 2, transducer frequency at level 1, and starch concentration at level 3. Starch concentration was also the main controlling factor.

By analyzing the starch surplus ratio, Table 7 listed the optimal settings for  $S/N$  ratio as ultrasonic exposure energy at level 2, exposure time at level 1, transducer frequency at level 2, and starch concentration at level 2. Comparing hydrogen production efficiency and hydrogen production rate revealed that the exposure energy had the same level, while the other three controlling factors were different. With the four controlling factors, starch concentration showed the largest effect on starch surplus ratio, followed by exposure frequency. By analyzing the lag time, the optimal settings for  $S/N$  ratio, as listed in Table 8, included ultrasonic energy at level 2, full-time exposure at level 3, transducer frequency at level 2, and starch concentration at level 2. From the table, the transducer frequency showed the strongest effect on lag time, followed by starch concentration.

According to Tables 5–8, besides hydrogen production efficiency and hydrogen production rate sharing a common optimal level with various controlling factors and starch surplus ratio and lag time exhibiting different exposure times, the other factors exhibited the same optimal level. In the reaction of controlling factors, all experiments obtained the largest  $S/N$  ratio from the controlling factors when the ultrasonic energy totaled 4 joules, and the level number selected by the other three controlling factors was distinct for different quality characteristics. Starch concentration was considered crucial in three quality characteristics, while the key factor was the transducer frequency under the lag time. Since the four quality characteristics were not consistent in the variability analysis of reducing  $S/N$  ratio, hydrogen production efficiency and rate were first considered during the second optimization phase. The quality characteristics were shown in Figures 5 and 6, where the  $x$ -axis A1 represented the reaction given controlling factor A and level number 1. The  $y$ -axis represented the hydrogen production efficiency and rate. From Figure 5, starch concentration showed the largest change, followed by exposure energy, exposure frequency, and exposure time. In Figure 6, the extent of the influences of exposure energy and exposure time switched so that the largest influence remained starch concentration, but the smallest effect was exposure energy. Figures 3 and 4 also identify the experimental parameters for hydrogen production efficiency and hydrogen production rate optimization as being

$$A2, B2, C1, D3. \quad (13)$$

The determined parameters corresponded to Tables 5 and 6, and thus the optimal hydrogen production efficiency and hydrogen production rate confirmed the experiment results when reduced variability was first considered. Table 9 showed the comparison between the confirmation experiment based on (13) as the optimization and the maximum value of the

TABLE 4: Experiments examining the effect of ultrasonic influences on hydrogen production.

| Exp. | A | B | C | D | Production efficiency |          | Production rate |          | Starch surplus ratio |          | $\lambda$ (h) |          |
|------|---|---|---|---|-----------------------|----------|-----------------|----------|----------------------|----------|---------------|----------|
|      |   |   |   |   | Average (%)           | S/N (dB) | Average (mL/h)  | S/N (dB) | Average (%)          | S/N (dB) | Average (h)   | S/N (dB) |
| 1    | 1 | 1 | 1 | 1 | 18.94                 | 18.94    | 85.40           | 37.81    | 10.27                | -20.31   | 22.54         | -27.45   |
| 2    | 1 | 2 | 2 | 2 | 22.66                 | 26.50    | 131.47          | 42.10    | 7.77                 | -17.86   | 16.35         | -24.44   |
| 3    | 1 | 3 | 3 | 3 | 23.02                 | 27.10    | 164.77          | 43.60    | 8.32                 | -18.51   | 22.03         | -26.91   |
| 4    | 2 | 1 | 2 | 3 | 27.11                 | 28.46    | 142.18          | 42.87    | 7.43                 | -17.54   | 15.68         | -24.03   |
| 5    | 2 | 2 | 3 | 1 | 21.82                 | 26.67    | 127.01          | 40.10    | 9.40                 | -19.60   | 30.18         | -29.65   |
| 6    | 2 | 3 | 1 | 2 | 26.76                 | 28.17    | 149.62          | 43.40    | 8.38                 | -18.54   | 17.32         | -25.10   |
| 7    | 3 | 1 | 3 | 2 | 21.12                 | 25.23    | 129.84          | 40.20    | 7.73                 | -18.18   | 24.47         | -28.10   |
| 8    | 3 | 2 | 1 | 3 | 26.68                 | 28.34    | 218.88          | 46.70    | 9.04                 | -19.30   | 22.10         | -26.91   |
| 9    | 3 | 3 | 2 | 1 | 20.23                 | 25.82    | 66.23           | 36.04    | 9.50                 | -19.61   | 20.69         | -26.87   |

TABLE 5: Hydrogen production efficiency for different S/N ratios.

|         | A     | B     | C     | D     |
|---------|-------|-------|-------|-------|
| Level 1 | 26.26 | 26.29 | 27.23 | 25.89 |
| Level 2 | 27.77 | 27.17 | 26.93 | 26.63 |
| Level 3 | 26.46 | 27.03 | 26.33 | 27.97 |
| Range   | 1.50  | 0.88  | 0.90  | 2.07  |
| Rank    | 2     | 4     | 3     | 1     |

TABLE 6: Hydrogen production rate for different S/N ratios.

|         | A     | B     | C     | D     |
|---------|-------|-------|-------|-------|
| Level 1 | 41.17 | 40.29 | 42.64 | 37.98 |
| Level 2 | 42.12 | 42.97 | 40.34 | 41.90 |
| Level 3 | 40.98 | 41.01 | 41.30 | 44.39 |
| Range   | 1.14  | 2.67  | 2.30  | 6.41  |
| Rank    | 4     | 2     | 3     | 1     |

TABLE 7: Starch surplus ratio for different S/N ratios.

|         | A      | B      | C      | D      |
|---------|--------|--------|--------|--------|
| Level 1 | -18.89 | -18.68 | -19.38 | -19.84 |
| Level 2 | -18.56 | -18.92 | -18.34 | -18.19 |
| Level 3 | -19.03 | -18.89 | -18.76 | -18.45 |
| Range   | 0.47   | 0.25   | 1.05   | 1.65   |
| Rank    | 3      | 4      | 2      | 1      |

TABLE 8: Lag time for different S/N ratios.

|         | A      | B      | C      | D      |
|---------|--------|--------|--------|--------|
| Level 1 | -26.27 | -26.53 | -26.49 | -27.99 |
| Level 2 | -26.26 | -27.00 | -25.11 | -25.88 |
| Level 3 | -27.29 | -26.29 | -28.22 | -25.95 |
| Range   | 1.03   | 0.71   | 3.11   | 2.11   |
| Rank    | 3      | 4      | 1      | 2      |

nine experiments in Taguchi's Orthogonal Array (Table 4). In terms of hydrogen production efficiency, the optimal combination of quality characteristics and S/N ratio was 19.11% better than the maximum value obtained from the nine experiments in Taguchi's Orthogonal Array. Regarding

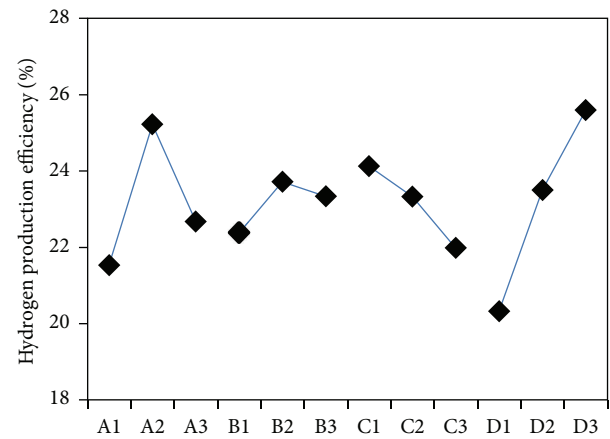


FIGURE 5: The Response Diagram of hydrogen production efficiency for different levels.

the hydrogen production rate, the optimal settings from the nine experiments in Taguchi's Orthogonal Array was 23.82% better. To summarize the above optimization and confirmation experiments, the optimal settings were A2, B2, C1, and D3 when considering the maximum hydrogen production efficiency and rate. That is, the best hydrogen production occurred with ultrasonic energy 4 joules, exposure for 15 min followed by no exposure for 15 min, transducer 0.5 MHz, and starch concentration 30 g/L.

## 5. Conclusion

Introducing the Taguchi Method, the number of experiments could be significantly reduced by the Orthogonal Array, which is determined from controlling factors and parameters. Two steps in optimization process are accomplished. The variability of experiment is reduced and then the hydrogen production efficiency and rate are maximized. For verifying the analyzed results, the experiment is performed as follows.

- (1) The optimal hydrogen production efficiency is 32.29%, which is 19.11% higher than the maximum in Taguchi's Orthogonal Array.

TABLE 9: The results of the confirmation experiment.

| Quality indicators        | Orthogonal Array | Optimal condition | Improvement (%) |
|---------------------------|------------------|-------------------|-----------------|
| Production efficiency (%) | 27.11            | 32.29             | 19.11           |
| Production rate (mL/h)    | 218.88           | 271.01            | 23.82           |

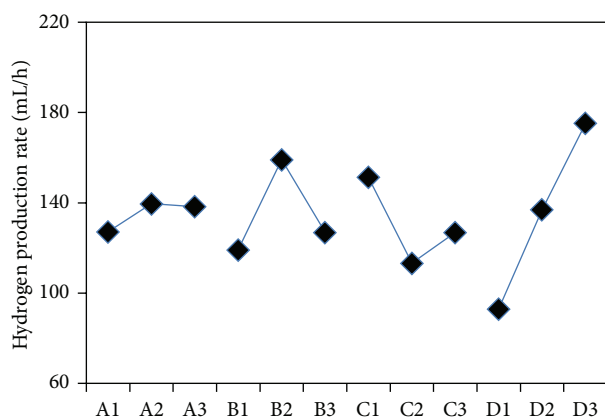


FIGURE 6: The Response Diagram of hydrogen production rate for different levels.

- (2) The optimal hydrogen production rate is 271.01 mL/h, which is 23.82% higher than in Taguchi's Orthogonal Array.
- (3) Hydrogen production efficiency and hydrogen production rate are optimized given ultrasonic energy 4 joules, 15 min exposure followed by 15 min rest, transducer 0.5 MHz, and starch concentration 30 g/L.
- (4) Within the four controlling factors, starch concentration most strongly affects the experimental results. For hydrogen production efficiency, exposure intensity ranks second, while for exposure time hydrogen production rate ranks second.
- (5) The ultrasonic mechanical effects always own different significances on biohydrogen production. For example, the ultrasonic exposure intensity possesses 72.46% significance when compared with the starch application on the consideration of hydrogen production efficiency. At the same time, the ultrasonic frequency shows the strongest effect on the concentration of the lag time.

Besides developing a suitable medium composition, this study also combines ultrasonic mechanical effects with biological reactors to perform dark fermentation hydrogen production. The Taguchi Method is also utilized to discuss the relationship among parameters in the hydrogen production process and is expected to optimize the hydrogen production conditions and further understand the effects of ultrasound on microorganisms.

## Conflict of Interests

The authors declare that there is no conflict of interests regarding the publication of this paper.

## Acknowledgments

This work was partially supported by the National Science Council, Taiwan, under Grant NSC-99-2221-E-244-004. Ted Knoy is appreciated for his editorial assistance.

## References

- [1] W. T. Coakley, D. Hampton, and F. Dunn, "Quantitative relationships between ultrasonic cavitation and effects upon amoebae at 1 MHz," *Journal of the Acoustical Society of America*, vol. 50, no. 6, pp. 1546–1553, 1971.
- [2] W. T. Coakley and F. Dunn, "Degradation of DNA in high-intensity focused ultrasonic fields at 1 MHz," *Journal of the Acoustical Society of America*, vol. 50, pp. 1539–1545, 1971.
- [3] W. T. Coakley, R. C. Brown, C. J. James, and R. K. Gould, "The inactivation of enzymes by ultrasonic cavitation at 20 kHz," *Archives of Biochemistry and Biophysics*, vol. 159, no. 2, pp. 722–729, 1973.
- [4] F. I. K. Ahmed and C. Russell, "Synergism between ultrasonic waves and hydrogen peroxide in the killing of micro organisms," *Journal of Applied Bacteriology*, vol. 39, no. 1, pp. 31–40, 1975.
- [5] D. A. Dooley, S. Z. Child, E. L. Carstensen, and M. W. Miller, "The effects of continuous wave and pulsed ultrasound on rat thymocytes *in vitro*," *Ultrasound in Medicine and Biology*, vol. 9, no. 4, pp. 379–384, 1983.
- [6] D. W. Van, "The effect of ultraviolet light, cavitation flow and ultrasound on protozoan cysts and oocysts, bacteriophages and Clostridium," *Water SA*, vol. 28, pp. 16–22, 2002.
- [7] D. M. Broda, "The effect of peroxyacetic acid-based sanitizer, heat and ultrasonic waves on the survival of *Clostridium estertheticum* spores *in vitro*," *Letters in Applied Microbiology*, vol. 45, no. 3, pp. 336–341, 2007.
- [8] C. N. Lin, *Hydrogen Production with Immobilized Cells [M.S. dissertation]*, Feng Chia University, Taichung, Taiwan, 2002.
- [9] C. C. Chen, *Hydrogen production in an anaerobic Continuous-flow Stirred Tank Reactor (CSTR) System [Ph.D. dissertation]*, Feng Chia University, Taichung, Taiwan, 2002.
- [10] C. H. Wang, *Fermentation strategies for biomass hydrogen production using anaerobic bacterial microflora [Ph.D. dissertation]*, Feng Chia University, Taichung, Taiwan, 2006.
- [11] M. Modigell, M. Schumacher, V. V. Teplyakov, and V. B. Zenkevich, "A membrane contactor for efficient CO<sub>2</sub> removal in biohydrogen production," *Desalination*, vol. 224, no. 1–3, pp. 186–190, 2008.
- [12] G. Antonopoulou, H. N. Gavala, I. V. Skiadas, K. Angelopoulos, and G. Lyberatos, "Biofuels generation from sweet sorghum:

- fermentative hydrogen production and anaerobic digestion of the remaining biomass,” *Bioresource Technology*, vol. 99, no. 1, pp. 110–119, 2008.
- [13] S. M. Kotay and D. Das, “Biohydrogen as a renewable energy resource-Prospects and potentials,” *International Journal of Hydrogen Energy*, vol. 33, no. 1, pp. 258–263, 2008.
- [14] S. Manish and R. Banerjee, “Comparison of biohydrogen production processes,” *International Journal of Hydrogen Energy*, vol. 33, no. 1, pp. 279–286, 2008.
- [15] C. L. Su, *The biological activation of fairy shrimp cyst induced by ultrasound exposure and light [M.S. thesis]*, National Sun Yat-sen University, Kaohsiung, Taiwan, 2011.
- [16] G. Cum, G. Galli, R. Gallo, and A. Spadaro, “Role of frequency in the ultrasonic activation of chemical reactions,” *Ultrasonics*, vol. 30, no. 4, pp. 267–270, 1992.
- [17] R. Pratt, “Studies on *Chlorella vulgaris*. XI. Relation between surface tension and accumulation of chlorellin,” *American Journal of Botany*, vol. 35, no. 9, pp. 634–637, 1948.